Early-stage adhesion of microbes onto oral biomaterials at the nanoscale

Sebastian Daniel Aguayo

Submitted for the degree of Doctor of Philosophy

University College London

2017

Department of Biomaterials and Tissue Engineering

UCL Eastman Dental Institute

Declaration

I, Sebastian Daniel Aguayo, confirm that the work presented in this thesis is my own. Where information has been derived from other sources, I confirm it has been clearly indicated in the thesis.

Acknowledgements

Firstly, I would like to thank my primary supervisor Dr. Laurent Bozec for his constant support and motivation throughout these past three years of PhD, and for the long and encouraging discussions regarding my research and career development. Also, I would like to thank my secondary supervisors Prof. Nikos Donos and Prof. Dave Spratt for putting their insight into my research, and for providing great suggestions on to how to improve my project.

Secondly, I would like to thank my colleagues from the UCL Eastman Dental Institute that provided direct and indirect support regarding my work (and many hours of social entertainment). Special thanks to Adam, Tarek, Angelica, Vanessa, Dimitra, Mehmet, Dallas and Jacob for your great company and chats at the Eastman and during meetings all across the world (sorry to the many others that I have probably forgotten!). Also, a big thank you to Dr. Helina Marshall for her huge support in microbiology and countless hours in the AFM lab during both successful and failed experiments, to Dr. Richard Thorogate for his continuous technical AFM support, and all the collaborators that in one way or another have been part of the publications that have resulted from my research. And of course, huge thanks to all my friends from London and back home in Chile for putting up with me during these last years!

Finally and most importantly, this thesis is dedicated to my loving family, as nothing of this would have been possible without them!

Abstract

Despite much progress, the infection of oral biomaterials by bacterial and fungal cells remains an important problem in the clinic, affecting millions of patients worldwide. Although biofilm formation comprises a series of stages, the initial cell-surface interaction is crucial in determining infection of the biomaterial surface. By employing single-cell force spectroscopy (SCFS) and nanoindentation with the atomic force microscope (AFM), the biophysics of the bacteria-biomaterial surface interaction has been characterised for *Streptococcus sanguinis*, *Staphylococcus aureus* and *Candida albicans*. Initially, the development and optimisation of a protocol to harvest and immobilise living bacterial and fungal cells for AFM experimentation is described. In a next step, SCFS was utilised to explore the influence of implant surface nanotopography on the colonisation of *S. aureus,* utilising an in vitro polycarbonate implant model. Although nanotopography was not found to influence bacterial elasticity, it did increase the adhesion of *S. aureus* to the surface at early time points. Subsequently, the interaction between clinically relevant titanium (Ti) implant substrates and *S. aureus* and *S. sanguinis* cells was studied, which demonstrated strain-dependent differences in the unbinding patterns observed in AFM experiments. Worm-like chain (WLC) modelling of unbinding events was used to predict the length of the bacterial adhesins involved in the Ti-bacteria interaction, which were found to be different for *S. aureus* and *S. sanguinis.* Finally, the attachment of *C. albicans* to acrylic surfaces at the single-cell level was explored with AFM. *C. albicans* was found to exhibit morphology-

dependent adhesion onto acrylic, with adhesion being increased in hyphal tubes compared to yeast cells. Also, experiments suggest a potential correlation between strain virulence and increased adhesion to surfaces. Future work should focus on utilising this in vitro AFM model to explore novel antiadhesive and antimicrobial approaches at the single-cell level.

List of Figures

List of Tables

Table of Contents

CHAPTER 1

INTRODUCTION

1. Biomaterials in medicine and dentistry

1.1. Overview

Biomaterials have been traditionally defined as materials utilised to augment or replace missing or damaged tissues in the human body for medical purposes (Ratner & Bryant 2004; Huebsch & Mooney 2009). Currently, biomaterials are also expected to integrate and interface with the surrounding tissues and to exert some degree of biological activity (i.e. to promote osteogenic differentiation) (O'Brien 2011). In recent years, the study and development of biomaterials has acquired a vital importance for the modern biomedical field, and today they are utilised to replace diseased body parts such as artificial heart valves and shoulder, knee, hip and dental implants, greatly improving the quality of life for thousands of patients worldwide (Logan & Brett 2013). Furthermore, greater life expectancies have inclined population demographics towards older age groups, and it has been predicted that the number of patients requiring implant placement will suffer an important increase throughout the next years (Tang & Hu 2005).

Although no 'ideal' material for the elaboration of artificial implants has been established, certain properties such as high biocompatibility, increased wear resistance, mechanical properties similar to host tissues and improved

osseointegrative capacities are desirable **(Figure 1.1)** (Geetha et al. 2009). Biocompatibility is understood to be the absence of adverse effects for the host starting at implantation, and should be maintained at both short and long-term time points. Upon installation, an implant is expected to induce a biological response in the surrounding tissues that favours integration (Sakiyama-Elbert & Hubbell 2001). Surface characteristics such as chemical properties and topography of the implant have been shown to influence this biomaterial-host interaction. Most importantly, the future success or failure of the treatment is highly determined by the initial interaction between the implanted biomaterial and the attached tissue (Geetha et al. 2009; Rupp et al. 2006; Khan et al. 2012).

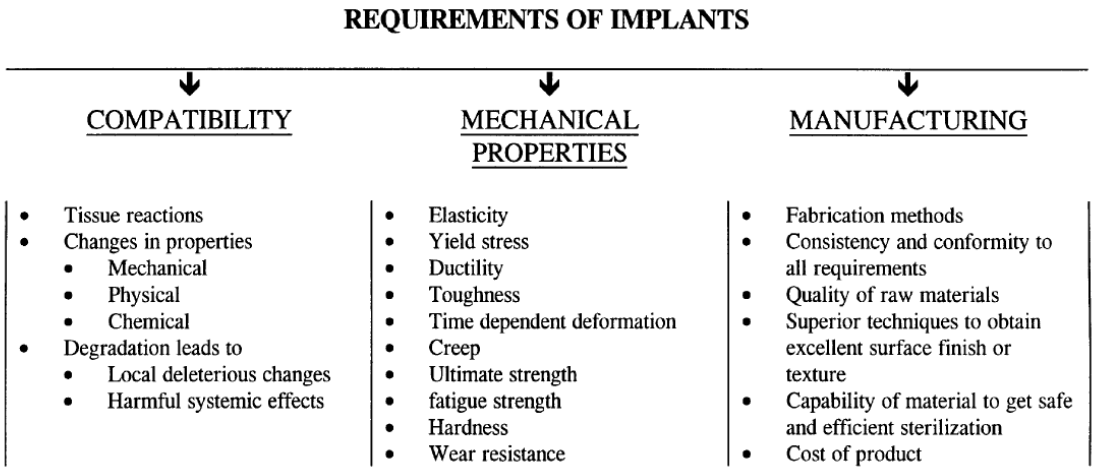

Figure 1.1: Desirable requirements for implant biomaterials (Adapted from *Titanium alloys in total joint replacement: a materials science perspective.* Long and Rack, 1997).

1.2. Biomaterial properties and surface characteristics

Although different biomaterials -such as stainless steel and cobalt-chromium alloys- have been utilised, titanium (Ti) and its different alloys (e.g. Ti-6Al-4V) are still considered as the 'gold standard' for fabrication of orthopaedic and dental

implants (Wall et al. 2009). Ti holds many advantages as a biomaterial such as high biocompatibility, great capacity to integrate with both soft and hard tissues, increased strength, and enhanced resistance to corrosion (Zhao et al. 2007; Alcheikh et al. 2013). Also, Ti also has a similar elastic modulus to bone, giving it an improved biological behaviour when placed in osseous tissue (Long & Rack 1998). Other chemical modifications, such as the incorporation of vanadium and nickel into Ti alloys, have been performed in hopes of enhancing both chemical and mechanical properties (Sykaras et al. 2000), although concerns still exist on the possible toxic effects and long-term health risks of these materials (Long & Rack 1998). Another important characteristic of Ti is the presence of an oxide layer on the surface of the material (Ananth et al. 2015). The presence of the oxide layer activates the material surface and increases the adsorption of extracellular fluid, proteins and cells from adjacent tissues. Furthermore, this oxide layer is crucial for osseointegration as its contamination has been shown to directly impact the survival of titanium implants (Zhao et al. 2005).

There are a series of events that take place *in-vivo* upon installation of an artificial implant into human bone (Anderson et al. 2008). The primary response is the adsorption of water onto the surface of the implant, followed by the interaction with proteins from the surrounding tissue, blood and serum (Olivares-Navarrete et al. 2011). These events give place to subsequent migration and attachment of cellular components from the host, primarily in the form of multipotent progenitor cells (Subramani et al. 2009). Ideally, an artificial implant should have the ability to influence mesenchymal cells into differentiating towards an osteogenic lineage and

induce bone formation. It has been demonstrated that implant surface topography plays an important role in this process, since micro-roughened surfaces have shown increased osteoblast proliferation and activity compared to smooth surfaces (Metavarayuth et al. 2016).

In dentistry, it has been widely accepted that the placement of dental implants is an efficacious way of replacing missing teeth, considering the high survival rates shown consistently in clinical trials over the years (Setzer & Kim 2014). The introduction of 'osseointegrated' implants was a major breakthrough for dentistry, as it has provided clinicians with a predictable long-term outcome treatment for the replacement of single or multiple missing teeth (Esposito et al. 1998). The concept of osseointegration has had many modifications throughout the years; however, it can currently be defined as the direct histological bone-to-implant contact found in an implant that has been functionally loaded (Marco et al. 2005), and is the final desired outcome for any implanted artificial device in osseous tissue. Many surface modifications have been developed to enhance the biological and mechanical properties of dental implants. Smooth or machined Ti surfaces have been replaced by surface-treated implants with hopes of improving osseointegration and soft-tissue response (Cooper 2000; Shalabi et al. 2006; Wennerberg & Albrektsson 2009).

Several animal models and human clinical studies have shown a positive relationship between surface roughness and bone-to-implant contact (BIC). Franchi et al. employed an *in-vivo* animal model to demonstrate that rough implant surfaces

increase deposition of new osseous tissue around the implant when compared to smooth titanium (Franchi et al. 2004). Another animal model study by Cochran et al. compared titanium plasma-sprayed and blasted/etched surfaces and reported significantly higher BIC in the second group (Cochran et al. 1998), furthermore, Wennerberg et al. reported increased BIC in sandblasted compared to smooth implants (Wennerberg et al. 1998). Although the role of surface topography in osseointegration is still not fully understood, it has been shown that rough surfaces have an increased ability to induce mesenchymal stem cell (MSC) differentiation into an osteogenic lineage and promote bone healing (Logan & Brett 2013). Controlled patterning of the biomaterial surface at the nanoscale level has been shown to directly influence human stem cell proliferation and differentiation, giving it important advantages compared to uncontrolled topographies and smooth surfaces **(Figure 1.2)** (Estevez et al. 2015; Dalby et al. 2007). One of the possible explanations for this effect is the increased surface area generated by the nanopatterned surfaces, which allow increased numbers of cell-surface contacts. Furthermore, it is also believed that mechanoreceptors on the cell surface are able to sense topographic cues at the nanoscale, leading to promotion of attachment and differentiation (Dalby et al. 2007). However, although increasing surface roughness in beneficial for osseointegration, it also favours bacterial colonisation and infection (Esposito et al. 2007; Grossner-Schreiber et al. 2001).

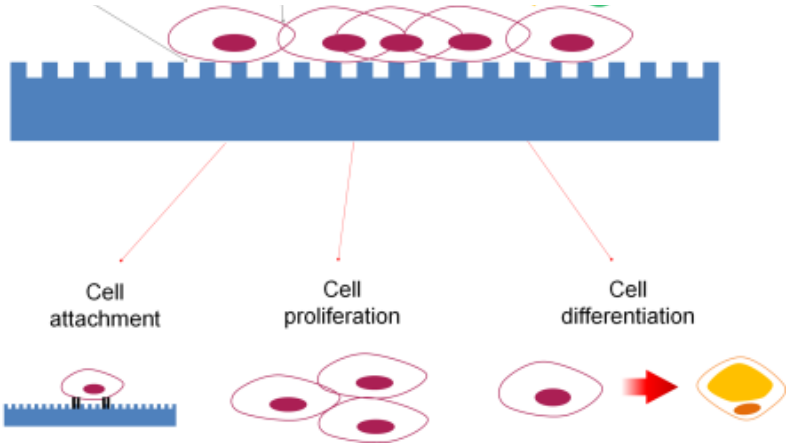

Figure 1.2: Controlled nanopatterning on biomaterial surfaces has shown to improve cell adhesion and proliferation (Adapted from *Stem cell responses to nanotopography.* Park and Im, 2014).

2. Bacterial attachment and biofilm formation

Bacteria are prokaryotic microorganisms that can be found living on virtually every environment present on Earth. Bacteria are usually found bound to surfaces or as part of an established biofilm, from where they are able to migrate to other places and colonise new surfaces (Winkelströter et al. 2013). The ability of bacteria to attach to natural and artificial substrates is one of the most important factors for their high survival capacities observed in nature (Zhao et al. 2013). These biofilms are of great interest to researchers in biomedicine, as they can be found on medical devices, catheters, orthopaedic and dental implants and heart valve replacements (Subramani et al. 2009; Abe et al. 2012; Schmidlin et al. 2013). However, biofilms in

the human body are not confined to artificial surfaces: they are also found on hard and soft tissues, and the establishment of these biofilms throughout the body cause a wide range of chronic diseases that can be very difficult to control and treat (McConnell et al. 2010). Therefore, many fields of research are currently looking for novel approaches to enhance or inhibit the adhesion of bacteria to surfaces, in hopes of improving industrial applications of biofilms or reducing the prevalence of bacterial infections in the population.

Despite much research and progress in the field, the control of biofilm-mediated diseases continues to be highly problematic (Geetha et al. 2009; Svensson et al. 2014; Arciola et al. 2012). *Pseudomonas aeruginosa* biofilm infection continues to be a threat to cystic fibrosis patients (Hassett et al. 2010), and peritoneal catheters are prone to colonisation and infection with *Staphylococcus epidermidis* that in some cases can be impossible to eradicate (Pihl et al. 2013). Furthermore, over the years it has been demonstrated that tooth decay and periodontitis- arguably the two most frequent oral diseases in humans- are caused and maintained by the establishment of a specific biofilm on the surface of the tooth (Jakubovics et al. 2014), and more specifically, the presence of certain bacteria such as *Porphyromonas gingivalis*, *Treponema denticola and Tanerella Forsythia* in dental biofilm is strongly related to periodontal disease severity (Schmidlin et al. 2013; Socransky et al. 1998).

2.1. Process of biofilm development

Biofilms are considered highly organized populations of adhered bacteria embedded in an extracellular polysaccharide and protein matrix (Costerton et al. 1995; Hassett et al. 2009). These bacterial populations comprise many different species of microorganisms strongly intercommunicated and related with each other (Díaz et al. 2007). Biofilms give bacteria strong evolutionary advantages compared to individual bacterial cells such as the capacity to grow and survive in severe hostile environments, increased resistance to antibiotic treatment and mechanical removal, and a constant dispersion of bacterial cells into the surroundings for colonisation (Hall-Stoodley & Stoodley 2009; Van Acker et al. 2014). Furthermore, bacteria secrete extracellular polymeric matrix that grant biofilms with protection against host immunological responses and facilitates communication and cohesion between different species (Bar-Zeev et al. 2012; Ahimou et al. 2007).

The development of biofilms involves a series of stages, starting with the adhesion of single bacterial cells to a surface and followed by the subsequent binding of secondary colonisers **(Figure 1.3)** (Otto 2013; Balaban et al. 2003). This consecutive co-aggregation of species changes the composition, phenotype and pathogenic properties of the residing bacteria in order to adapt to the established biofilm setting (Zhao et al. 2013; Hojo et al. 2009). This process, however, must be initiated by the attachment of early bacterial colonisers to the surface (Waar et al. 2005), and therefore, the adhesion of bacteria to surfaces can be considered the crucial initial factor for the formation and maturation of a biofilm (Park et al. 2001). Bacteria have been reported to interrelate with artificial surfaces, host cells and tissues, and other bacteria from the same or different species (Hamada et al. 1998).

Important factors influencing the adhesion of bacteria to surfaces are cellular geometry, substrate roughness and elastic properties of the cell (Oh et al. 2009).

Figure 1.3: Biofilm formation on biological surfaces

2.2. Oral biofilm formation

Inside the oral cavity, most bacterial species can be found in a planktonic state; however, under adequate conditions they can adhere to solid surfaces present in the mouth -tooth enamel, restorations, dental implants- and initiate the formation of an oral biofilm (Wessel et al. 2014). In this context, *Streptococci sp.* and *Actinomyces sp.* have frequently been described as initial colonisers in the early phases of oral biofilm development (Hojo et al. 2009). This initial attachment creates a favourable environment for the subsequent adhesion of late pathogenic

colonisers such as *Fusobacterium nucleatum* and *Porphyromonas gingivalis* (Renvert et al. 2008).

Similar to what occurs on tooth surfaces, biofilm accumulation and maturation on the surface of dental implants can produce an inflammatory response in the surrounding tissues and impact the long-term stability and success of the treatment (Grossner-Schreiber et al. 2001; Swierkot et al. 2012). According to the Sixth European Workshop on Periodontology, peri-implant diseases can be defined as the infectious reactions surrounding an implant (Lindhe & Meyle 2008), which can be divided into *peri-implant mucositis,* describing the inflammation of surrounding mucosa without bone loss; and *peri-implantitis*, where mucosal inflammation is accompanied by bone loss around the implant (Fürst et al. 2007). Current estimates suggest the prevalence of peri-implantitis to be around 5% at 10-year follow-up (Albrektsson et al. 2012), when implants are placed in ideal conditions by well-trained clinicians in healthy patients. However, in the regular clinical situation the prevalence seems to be higher, reaching 80% and 56% for peri-implant mucositis and peri-implantitis, respectively (Lindhe & Meyle 2008; Lundgren et al. 2008; Setzer & Kim 2014).

2.3. Species involved in oral biofilm-mediated diseases: Staphylococcus aureus and Candida albicans

Although many species are found to be present in oral biofilms, certain strains have been directly related to the development of disease when found attached to oral biomaterials. *Staphylococcus aureus* -a species not traditionally described in

dental biofilm- has been isolated from failing dental implant sites (Lee & Wang 2010). *S. aureus* is a well-known Gram-positive pathogen involved in a vast number of human infections (Roberts et al. 2006). The presence of microbial surface components recognising adhesive matrix molecules, MSCRAMMs, on the membrane of *S. aureus* is a key factor for recognition and adhesion to surfaces (Buck et al. 2010). *S. aureus* has shown an increased likelihood to colonise and infect implants in humans and its presence is related to negative clinical prognosis (Arciola et al. 2012; Lee & Wang 2010; Harris et al. 2002). Furthermore, in recent years *S. aureus* has demonstrated increased antibiotic resistance and as a result, novel antibacterial and anti-adhesive approaches are currently being explored in hopes of developing new strategies against biomaterial surface infection (Loskill et al. 2014; McKendry 2012; Francius et al. 2008).

Candida albicans is a commensal Gram-positive yeast found living on skin and mucosal surfaces; however, it also has the capacity of causing opportunistic surface or deep tissue infections in immunocompromised patients (Kabir et al. 2012; Salvatori et al. 2016), and it has further been associated to infection of medical devices in diverse parts of the body (Nett et al. 2010). Among these devices, denture surface infection with *C. albicans* biofilm continues to be a major problem, particularly when patients fail to maintain good denture hygiene **(Figure 1.4)** (Barbeau et al. 2003).

Figure 1.4: Clinical manifestations of denture-related stomatitis, according to the Newton classification. (I) Dispersed petequiae throughout mucosa, (II) erythema without hyperplasia and (III) erythema with popular hyperplasia.

Typically, *C. albicans* exists as a polymorphic fungus, which means it has the capacity to grow in either yeast or filamentous form **(Figure 1.5)** (Veses & Gow 2009). Filamentous forms, also known as hyphae, are tubular growths of *C. albicans* cells associated with tissue penetration and invasion (Thomson et al. 2016). Overall, *C. albicans* transition towards hyphae forms is considered one of the most important virulence factors of this particular strain (Jackson et al. 2014). Adhesion of *C. albicans* to denture surfaces is necessary in order to initiate the process of infection and biofilm formation (Park et al. 2008). Once established, this candida biofilm is associated to the onset of denture-associated stomatitis, a chronic inflammatory form of oral candidiasis that can affect up to 70% of denture wearers **(Figure 1.4)** (Cao et al. 2010; Izumida et al. 2014; Nett et al. 2010). Clinically, this disorder can

sometimes give rise to pain or irritation of the oral mucosa (Yarborough et al. 2016). Also, it can be a potential source of systemic candida infection in immunocompromised individuals, and together with any accompanying bacterial colonisation, a possible reservoir for respiratory infection (O'Donnell et al. 2016). The presence of high counts of hyphae in the biofilm has been related to the severity of the disease (Park et al. 2008). There remains no specific therapy for treating this disorder, although typical strategies are physical cleaning of the dentures and topical use of antimicrobials such as chlorhexidine and/or antifungals such as miconazole (Yarborough et al. 2016).

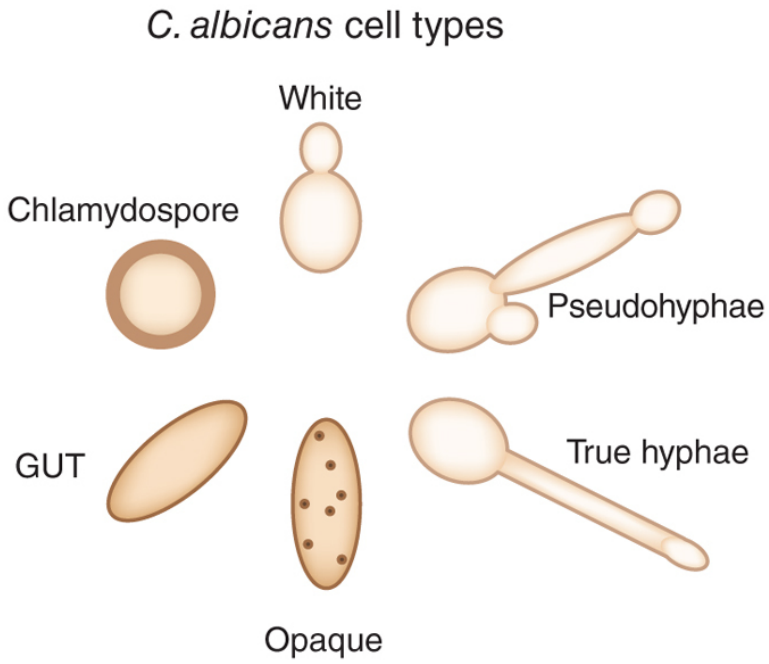

<u>Figure 1.5</u>: Phenotypic forms of *Candida albicans*, with different roles in commensalism and pathogenesis. True hyphae are associated to tissue invasion and penetration, while White-phase and GUT forms are mostly present during commensalism (Adapted from *A developmental program for Candida commensalism.* Gow, 2013).

Gram-positive cells are characteristically surrounded by a rigid cell wall (Navarre & Schneewind 1999). In the case of bacteria, the bulk of the cell wall is mostly composed by peptidoglycan, while in fungi it consists of chitin and β-glucans (**Figure 1.6**); however, in both cases adhesins - which are present on the exterior part of the cell wall - are considered as the main contributors to adhesion (de Groot et al. 2013; Sullan et al. 2015).

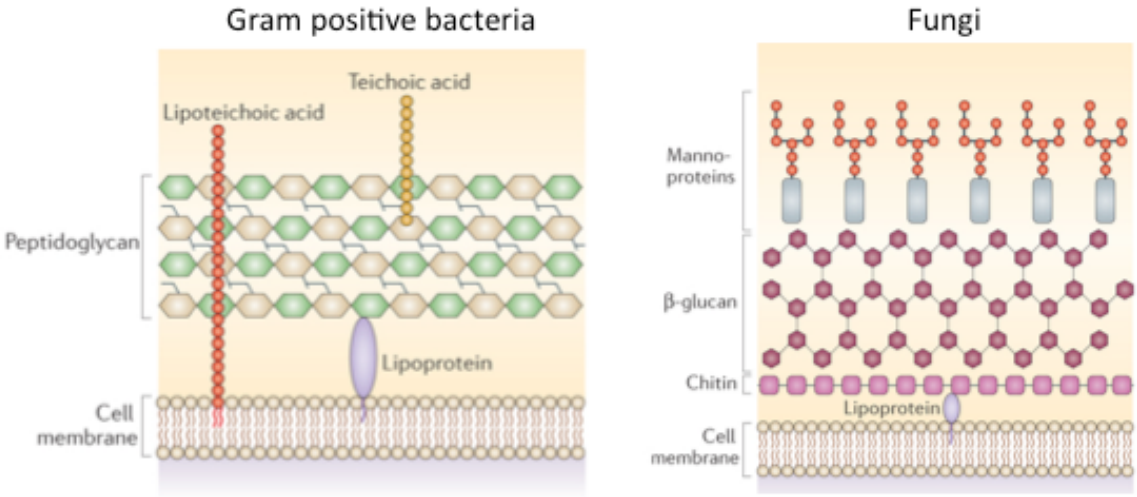

Figure 1.6: **Composition of the cell wall of Gram-positive bacteria and fungi** *(*Adapted from "*Through the wall: extracellular vesicles in Gram-positive bacteria, mycobacteria and fungi".* Brown et al, 2015).

2.4. Biophysics of the bacteria-substrate interaction

From a biophysical point of view, bacterial adhesion to substrates can be considered a two-stage process: the long-range docking phase and the short-range locking phase (F. Pinar Gordesli & Abu-Lail 2012; Katsikogianni & Missirlis 2004) **(Figure 1.7)**. When a planktonic bacterium comes into close proximity with a surface, there is an initial predominance of non-specific forces such as attractive van

der Waals and repulsive electrostatic forces (Harimawan et al. 2013). The interplay of both of these forces determines the likelihood of the bacterial cell to come into direct contact with the substrate. If the attractive forces overweigh the repulsive ones, the bacterium will tend towards the surface and allow the adhesion process to continue. The *Derjaguin, Landau, Vervey, and Overbeek (DLVO) theory*, originating from colloidal particle physics, is useful to understand the influence of both of these physicochemical interactions occurring in this initial docking phase (Abu-Lail & Camesano 2003; Hermansson 1999).

Subsequently, once a bacterium is immediately adjacent to the surface, specific and close-range interactions are produced as a result of ligand-receptor coupling (Eskhan & Abu-Lail 2014). In this secondary locking stage, molecules on the bacterial surface and appendages interact directly with the host surface generating strong and irreversible binding (An & Friedman 1998). At this point, bacteria can only be removed from the surface by mechanical or chemical treatment. This adhesion process between a microbial cell and surface depends on several factors which include bacterial structure and species, the physicochemical properties of bacteria and substrate, and surrounding environment (Bushnak et al. 2010). Furthermore, bacterial appendages -such as pili and fimbriae- and specific surface proteins -such as adhesins and microbial surface components recognizing adhesive matrix molecules (MSCRAMMs)- have been shown to be important players during this phase **(Figure 1.7)** (Dorobantu et al. 2009; Buck et al. 2010).

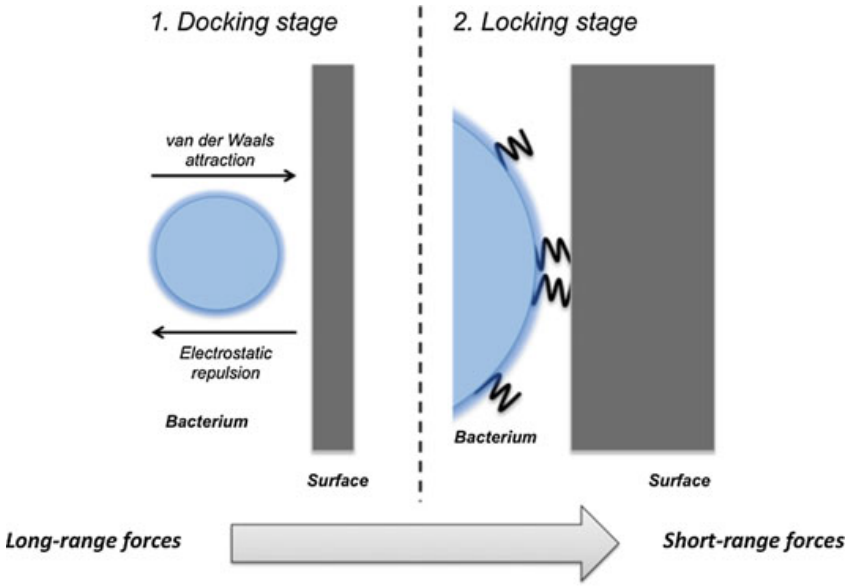

Figure 1.7: Forces determining the attachment of bacteria to surfaces. (Adapted from *Mechanics of bacterial cells and initial surface interaction.* Aguayo and Bozec, 2016).

3. Atomic force microscopy of microbial cells:

3.1. Configuration of an Atomic Force Microscope (AFM)

Atomic force microscopy (AFM) has been a valuable tool for the study of living bacterial samples. Introduced initially as an imaging tool (Binnig et al. 1986), the AFM has evolved into a highly specialised instrument to probe into both cellular and sub-cellular mechanics (Aguayo et al. 2015). The main components of an AFM setup are illustrated in **Figure 1.8a**. The basic setup on which the atomic force microscope is configured is simple yet very effective. The tip or probe of the AFM is scanned over the sample either in direct contact or in the close vicinity of the surface (Heinisch et al. 2012). The tip is attached to the end of a silicon-nitride cantilever; hence variations on the surface height and topography will cause some

degree of vertical deflection on the cantilever (Vukosavljevic et al. 2014). To perceive this deflection the AFM reflects a laser beam from the backside of the cantilever directly towards a position-sensitive photodiode; therefore, any bending in the cantilever will change the position of the laser beam on the detector (Dufrene & Pelling 2013). Finally, the signal difference between the four quadrants of the photodiode is transduced into either an image or mechanics data depending on the experiment being carried out by the researcher (Núñez et al. 2005).

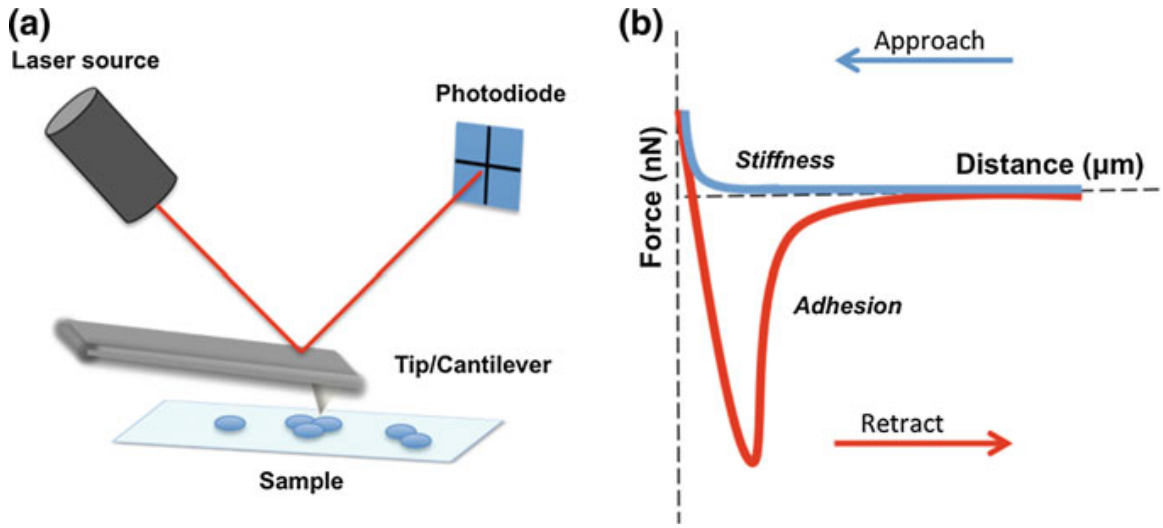

Figure 1.8: Setup of an Atomic Force Microscope (AFM). (a) The basic components of an AFM are the tip and cantilever, laser beam and photodiode. The tip is scanned over the sample of interest, and deflections occurring on the cantilever due to surface characteristics (i.e. topography and chemistry) will generate a change in the position of the laser beam on the photodiode. (b) When performing AFM force-spectroscopy, force curves are obtained that reflect the stiffness and adhesion of the sample (Adapted from *Mechanics of bacterial cells and initial surface interaction.* Aguayo and Bozec, 2016).

Currently, there are many different AFM systems available on the covering a vast number of applications ranging from conventional imaging and nanomechanics to high-speed AFM systems (Ando et al. 2013; Jalili & Laxminarayana 2004). The ability of the AFM to interact directly with substrates can be used to study the nanomechanical properties of bacterial cells, giving it an important advantage compared to traditional microscopy techniques such as electron microscopy (Pillet et al. 2014). Perhaps one of the most important advantages for microbiology is that the AFM allows measurements to be performed in liquid with little to no sample preparation, and therefore viable bacteria can be studied under physiological conditions (Helenius et al. 2008; Gaboriaud & Dufrêne 2007). Employed buffers can be further modified by the addition of antibacterial solutions to study the impact of these substances on bacterial morphology, aggregation, cell-wall mechanics or adhesion. The applicability of AFM mechanics in microbiology goes beyond the use of bacterial cells, as the fabrication of single-molecule coated AFM tips can be utilised to probe the mechanic behaviour of sub-cellular bacterial structures with piconewton sensitivity (Hwang et al. 2015; Méndez-Vilas et al. 2007). The use of AFM allows researchers to *a)* obtain high resolution images of biological samples, *b)* acquire information on the nanomechanical properties of samples (i.e. elasticity), and *c)* measure adhesive forces between cells and surfaces (Pinzón-Arango et al. 2010; T. Zhang et al. 2011).

3.2. Exploring sample nanomechanics with AFM

When employing the AFM to study the mechanical properties of samples, a force curve representing the relationship between force and distance is obtained **(Figure 1.8b)**. Initially, the tip/cantilever is situated at a distance from the sample, and is slowly approached towards the surface until a given loading force is reached (**Figure 1.8b,** blue curve). After a user determined contact time, the probe is retracted from the sample surface and brought back to the initial resting point (Taubenberger et al. 2014). The adhesion occurring between the tip and surface is observed as a dip towards negative force values during this retraction phase: therefore, adhesive forces are usually expressed as negative force values (**Figure 1.8b,** red curve). When dealing with bacteria however, retraction curves tend to be more complex as they display a series of unbinding events, which can be further analysed to characterise the corresponding cell-surface interaction (**Figure 1.9**) (Muller et al. 2009).

Figure 1.9: Characteristic force curve for cell-surface unbinding

How are force values obtained from the cantilever deflection? As the tip/cantilever behaves as a spring, force (F) values can be obtained according to Hooke's Law

$$F = -k \times d \qquad \text{(Equation 1)}$$

where k is the cantilever spring constant and d is vertical deflection of the cantilever (Schaer-Zammaretti & Ubbink 2003; Bolshakova et al. 2004). Previous calibration of each cantilever before experimentation is essential in order to obtain correct spring constant values, as variations can be found even within cantilevers from the same batch (Sheng et al. 2007). Several different methodologies for calibration, such as thermal tuning and pushing the cantilever against a calibrated reference lever, have been developed in hopes of providing precise and consistent spring constant measurements. Most commercially available AFM systems incorporate reliable built-in tuning software, many of which are highly automated and user friendly, and some companies also provide researchers with pre-calibrated cantilevers that simplify the process even further. These advantages that AFM brings to the field of microbiology allows researchers to design and perform a broad array of experiments to characterise the mechanic behaviour of single-bacterial cells (Wu & Zhou 2010).

3.3. Nanoindentation: probing the elasticity of samples

Firstly, the AFM can be used to understand the elasticity of bacterial cells and how certain environmental and antibacterial factors can influence these parameters (Vadillo-Rodriguez et al. 2004). Upon indenting a sample with a determined loading force, it will respond by deforming its surface by a given amount. This stress/strain relationship can be utilised to determine stiffness of a sample, which is also applicable to bacterial indentation experiments. However, more useful to researchers is the elastic modulus, which can be obtained by determining values for Young's modulus according to several elastic models (Dokukin et al. 2013). Traditionally, the Hertzian model for spherical indentation has been applied to cell indentation data mainly because of simplicity, and can be expressed by the relationship between force (F) and indentation (δ)

$$F = \frac{4ER^{1/2}\delta^{3/2}}{3(1-\nu^2)} \qquad \text{(Equation 2)}$$

where E is the Young's modulus, R is the radius of the indenter and ν is the Poisson's ratio of the indented sample (which for cells and biological samples is usually considered at 0.5). This approach, however, has several considerations that make it not appropriate for the interpretation of bacterial indentation experiments (Glaubitz et al. 2014). Firstly, the Hertzian model assumes no adhesive interaction

between the indenter and the surface, which is not the case for bacterial cells as their adhesive behaviour allows attachment to cantilevers (coated or un-coated) during indentation experiments. Furthermore, Hertzian modelling assumes that the indented surface is infinitely thick compared to the indenter, and therefore indentation should only occur on the surface of the sample and not affect the bulk material. As bacterial cells are compliant in nature, it is safe to assume that a load sufficient enough to deform the cell wall can also cause a certain degree of deformation of underlying cellular structures. These limitations have taken researchers to consider the application of more appropriate models such as the Derjaguin-Muller-Toporov (DMT) or Oliver-Pharr models for indentation, which also take into account adhesion between the bacterial sample and indenter and are therefore more suitable for the real experimental situation (Loskill et al. 2014; Strange et al. 2017). Modern AFM setups are progressively incorporating these models into their analysis software to facilitate data analysis and interpretation in a user-friendly manner. As values of bacterial elastic modulus vary according to many factors – i.e. cell wall structure and integrity, surrounding osmotic pressure – nanoindentation of bacteria is an efficient way of understanding how they respond to changes in their internal or external environments. As certain antibiotics can target cell wall synthesis, reduced Young's modulus values have been observed for bacteria after treatment with antibacterial drugs (Formosa et al. 2012; Wu & Zhou 2009). Furthermore, this approach is not limited to individual bacterial cells as it can also be utilised to study the mechanical behaviour of biofilms at different stages

of development (Abe et al. 2011) and before and after chemical treatment (Powell et al. 2013).

3.4. Force-spectroscopy: exploring microbial adhesion at the nanoscale

In vitro, it is possible to probe into the world of bacterial adhesion to surfaces with AFM. Techniques such as single-cell force spectroscopy (SCFS) of bacterial cells and molecules have contributed enormously to comprehend the fundamental forces behind bacterial adhesion to surfaces (Touhami et al. 2006; Ivanov et al. 2011). However, for force measurements to have significance in microbiology, an AFM tip must be functionalised with bacterial cells by means of an immobilising agent (Beaussart & El-Kirat-Chatel 2014). Immobilisation is the key element for effective cell-based AFM work, and must not only ensure correct attachment of the bacterium to the cantilever tip but also maintain cell viability throughout experimentation. This ensures stability throughout force-spectroscopy measurements, as ineffective immobilisation may lead to incorrect measurements due to lateral displacement or complete bacterial detachment. Some substances previously employed for cell immobilization in AFM nanomechanic experiments include glutaraldehyde, poly-L-lysine and polyethyleneimine (Dorobantu & Gray 2010; Ovchinnikova et al. 2013; van der Mei et al. 2000; Beckmann et al. 2006; Da Silva & Teschke 2003). These agents confer a positive charge to the cantilever surface to which negatively charged bacteria can bind non-specifically (Louise Meyer et al. 2010; A Beaussart et al. 2013). Another interesting and promising

alternative for cantilever functionalization is the use of probes coated with the bio-inspired adhesive polymer poly-dopamine (poly-DOPA) (Lee et al. 2007; Kang & Elimelech 2009; Dreyer et al. 2012; Harimawan et al. 2013).

Recently, researchers raised some concerns about viability of bacteria attached directly onto silicon-nitride cantilevers (Audrey Beaussart et al. 2013), and therefore performed attachment of glass micro beads to tip-less cantilevers under which bacterial cells were immobilised. This approach allowed better control of the bacteria-substrate contact area and maintained cell viability throughout experimentation. Furthermore, the use of poly-DOPA did not interfere with adhesion measurements during force probing of single cells. Further work carried out by Herman et al. employing *Staphylococcus epidermidis* confirmed these findings (A Beaussart et al. 2013).

In SCFS a cell-modified cantilever is approached, placed into contact and retracted from a surface of interest to explore the adhesive behaviour between the bacteria and the substrate (Ubbink & Schär-Zammaretti 2005). Therefore, the most important information is obtained from the retraction segment of the resulting force curves. The approach segment of the curve usually displays a smoothened slope, consistent with the viscoelastic behaviour of the bacterium being gently pressed against the surface. The retraction segment, however, displays a great amount of information regarding the bacterium-surface interaction. Initially, a major unbinding peak representing the largest negative value in the vertical axis can be observed, from which the maximum adhesion force (F_{max}) can be obtained. F_{max} is

usually the most reported parameter in SCFS experiments and is mainly representative of non-specific adhesion between the bacteria and substrate. Another relevant parameter known as adhesion work (Adh_{work}) can be extracted by integrating the retraction curve, obtaining an area under the curve indicative of the amount of energy needed to fully unbind the bacterium-surface interaction. Adh_{work} involves both the major peak and minor unbinding events, and therefore reflects the influence of both the non-specific and specific surface adhesion **(Figure 1.10)** (Taubenberger et al. 2014).

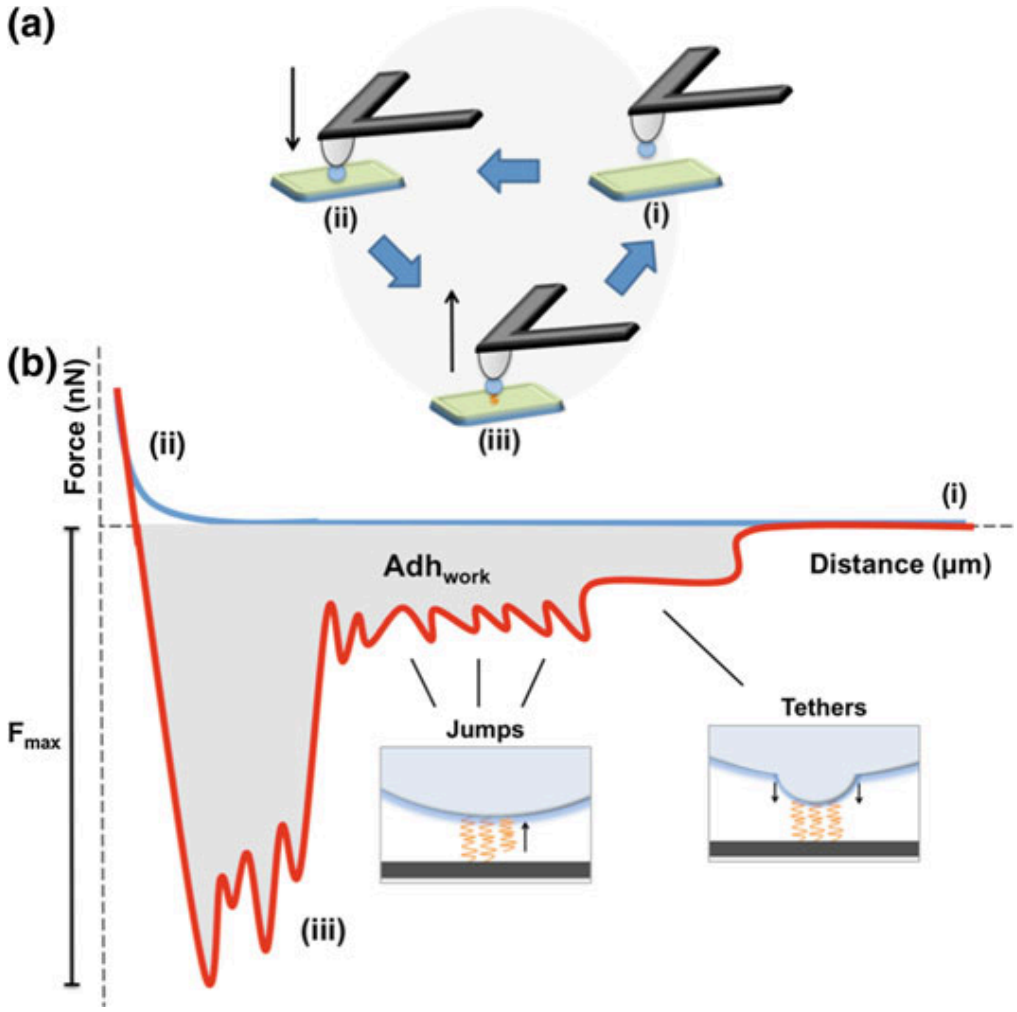

Figure 1.10: Representation of a bacterial single-cell force spectroscopy (SCFS) experiment. (a) A functionalised bacterial probe is initially away from the surface (i) and approached until contact with the surface is established (ii). After a user-defined contact time, probe is retracted back to the original starting point. (b) Diagram of a typical force curve obtained during bacterial unbinding. Corresponding probe positions (i), (ii) and (iii) are shown. Insets represent the biological significance of jumps and tethers (Adapted from *Mechanics of bacterial cells and initial surface interaction.* Aguayo and Bozec, 2016).

Furthermore, the analysis of minor unbinding events observed in the retraction curve can give insight on the dynamic behaviour of bacterial adhesion molecules (Evans & Calderwood 2007). Two distinct minor unbinding patterns can be detected throughout bacterial retraction curves. The most commonly observed are jumps that represent the unbinding of single-adhesive units and which sometimes are described in the literature as sawtooth-like patterns (Yongsunthon & Lower 2006; Lower et al. 2005). Tethers, which represent the stretching of the cellular membrane before unbinding (Krieg et al. 2008), are not observed frequently in bacterial SCFS retraction curves as many bacteria are surrounded by structures (i.e. cell wall, capsule) that do not allow significant elongation of the cell before receptor unbinding.

An important parameter that can be controlled is the dwelling time, also known as surface delay, which represents the contact time between the bacterium and the surface before retracting the probe. As bacteria are dynamic cells, the influence of contact time on all previously mentioned adhesion parameters can be studied in great detail (Kashef & Franz 2015). Most importantly, control of the

dwelling time allows researchers to simulate different stages of the physiological process of bacterial adhesion. Short dwelling times are representative of the early interaction between the bacterium and surface, while increased times can be used to simulate changes in adhesion forces once bacteria have settled on the surface. Many bacterial receptors have shown time-dependent bond strengthening at increasing contact times, effect which has been reported extensively in the literature (Vadillo-Rodriguez et al. 2004; Mei et al. 2009).

3.5. Force-extension and worm-like chain (WLC) modeling

The applicability of the AFM in microbiology is not only limited to the nanoindentation of microbial cells or to the probing of forces driving bacterial attachment to surfaces. The modeling of bacterium-surface unbinding events can yield important information on the length and nature of the specific molecules involved in adhesion to biological and non-biological surfaces. Several models have been reported to describe the stretching of elastic polymers during AFM experimentation (Storm & Nelson 2003; Francius et al. 2009).

For the case of protein unfolding, force-extension data can be modeled according to the worm-like chain (WLC) equation as

$$F(x) = \frac{k_b T}{l_p}\left[\frac{1}{4}\left(1-\frac{x}{L}\right)^{-2} + \frac{x}{L} - \frac{1}{4}\right] \qquad \text{(Equation 3)}$$

where F is force (N), k_b is the Boltzmann constant (J/kelvin), T is temperature (K), x is molecular extension (m), l_p is the persistence length and L the total contour length of the molecule. The WLC model considers polypeptides as elastic molecules conformed by smaller indivisible units (persistence length, l_p), which add up to give the total length of the molecule (contour length, L) (Marszalek & Dufrêne 2012). Instead of only being flexible between l_p segments, proteins are continuously flexible throughout the entire length of the molecule (**Figure 1.11**). For fitting purposes, l_p is usually considered as the length of a single aminoacid (~0.36nm) for polypeptide force-extension experiments (Herman et al. 2014).

Polysaccharides, on the other hand, are better fitted by the freely jointed chain (FJC) model, which can be used to probe the adhesion of lectins and other polysaccharide microbial molecules (Francius et al. 2009; Marszalek & Dufrêne 2012). The FJC model considers the total length of a molecule as

$$L = n \times l \qquad \text{(Equation 4)}$$

where L is the total unfolded length, n is the number of monomers and l is the length of a single monomer. Contrary to the WLC model, monomers are considered rigid units and thus molecules can only bend between segments (**Figure 1.11**). In literature, both of these force-extension models have been employed to model the stretching of bacterial appendages and proteins, and more recently, to describe the

unbinding of bacterial cell probes from surfaces during SCFS experiments (Beaussart & El-Kirat-Chatel 2014; Aguayo et al. 2015; Jacquot et al. 2014; Rangel et al. 2013).

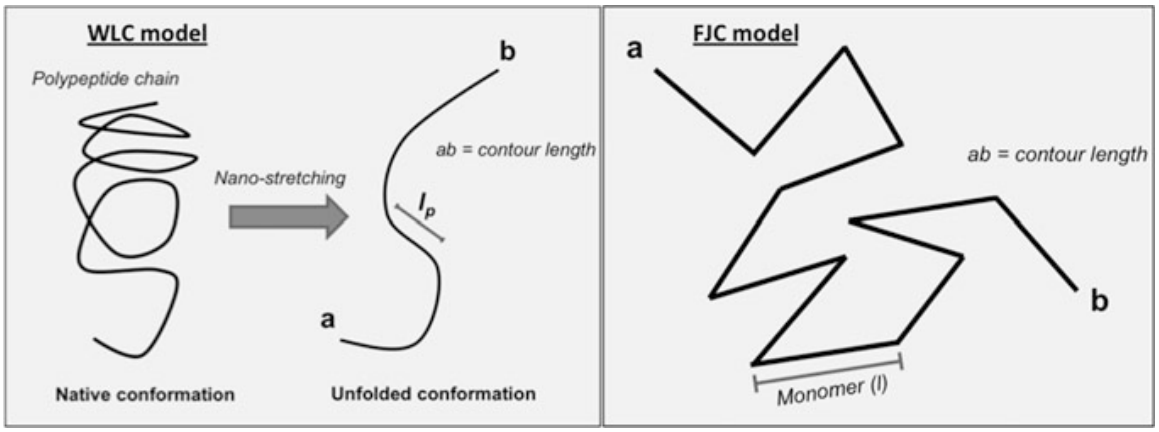

Figure 1.11: Force-extension analysis of receptor stretching, according to the worm-like chain (WLC) and freely-jointed chain (FJC) models (Adapted from *Mechanics of bacterial cells and initial surface interaction.* Aguayo and Bozec, 2016).

3.6. Poisson analysis

Finally, a mathematical approach known as Poisson analysis can also be applied to the minor unbinding events found in the retraction curve to deconstruct each minor peak into the corresponding short range and long range force components, as previously discussed in literature (Chen et al. 2011). This approach assumes that short-range adhesion forces are constituted by the sum of a limited number of individual bonds, and therefore, the total bacterium-substrate adhesion force (F) can be expressed as:

$$F = (f_{SR} \times k) + F_{LR} \qquad \text{(Equation 5)}$$

where f_{SR} is the value of a single-bond, k is the number of formed bonds and F_{LR} the value for long-range interactions. At very close distances (such as the ones observed during AFM force measurements), values for F_{LR} are minimal compared to F_{SR} and therefore it is safe to assume that variance in adhesion forces are mainly due to variations in the occurrence of bonds, k. As the distribution of unbinding forces between bacterial probes and surfaces usually follow a Poisson distribution, it is possible to plot a linear regression from which both F_{LR} and F_{SR} can be determined (Mei et al. 2009). F_{LR} is mostly representative of van der Waals and electrostatic interactions while F_{SR} reflects the value of specific bacterium-surface adhesion, and therefore decoupling bacterial adhesion into these two categories allows for deeper understanding of the specific mechanisms behind the adhesion of different bacterial strains. As an example, Abu-lail and Camesano have suggested that in many cases the formation of hydrogen bonds, with an individual bond value of ~0.13nN, are key players of bacterial adhesion to hydrophilic surfaces (Abu-Lail & Camesano 2006). Lastly, it is important to consider that contrary to F_{SR} which is always positive, values for F_{LR} can be either positive or negative depending on if the overall force is repulsive or attractive, respectively.

3.7. Application of AFM nanomechanics in microbiology

Despite significant progress in microbiological research, bacterial colonization and biofilm-related pathologies continue to challenge the fields of food science, orthopaedics, medicine and dentistry (Barros et al. 2013; Postollec et al. 2006; Ammendolia et al. 2014), and therefore the characterization of bacterial virulence factors (i.e. adhesion) and development of antibacterial substrates and agents remains a priority. Concerns also exist regarding the rise of antimicrobial resistant (AMR) bacterial strains such as MRSA (methicillin-resistant *Staphylococcus aureus*) and VRE (vancomycin-resistant *Enterococcus*) (McKendry 2012). Also, current reports of broadly and totally AMR strains of *Mycobacterium tuberculosis* pose a major threat for healthcare systems around the world (Ford et al. 2013; Hu et al. 2014). Most alarmingly, many bacteria have now displayed AMR to a vast number of antibiotics accessible in the market, and the availability of new drugs for therapies against non-susceptible strains is very limited for years to come (Ansari et al. 2014).

Several studies have successfully determined the elastic and hardness properties of living bacterial cells. Mechanical properties of *Escherichia coli* membranes were characterized by probing the cell surface with an AFM cantilever by Longo et al (Longo et al. 2012). Nanoindentation was also employed to correlate the macroscopic aggregation of seven bacterial strains with their microscopic mechanical properties (Wang et al. 2012). Indentation nanomechanics were also used to demonstrate the effect of two antibacterial agents, ticarcillin and

tobramycin, on the cell wall of *P. aeruginosa* (Formosa et al. 2012). Subsequently, the same authors determined the mechanism of action of a novel antibacterial agent on the cell wall of resistant strains of *P. aeruginosa* (Formosa et al. 2012). In another *in-vitro* study, researchers investigated the effect of a low-molecular weight alginate oligosaccharide (*OligoG*) on the mechanics of *Acinetobacter baumannii* and *P. aeruginosa* biofilms (Powell et al. 2013). Similarly, Wu and Zhou employed nanoindentation essays to evaluate the Young's modulus of *Mycobacterium sp* before and after treatment with antimycobacterial agents ethambutol and isoniazid (Wu & Zhou 2009), providing new understandings on the biomechanical interactions between antimycobacterial drugs and *Mycobacterium* cell wall components.

Regarding bacterial adhesion to surfaces, Loskill et al. carried out a study to investigate the adhesion force of *Staphylococcus carnosus* towards hydrophobic and hydrophilic silicon wafers (Loskill et al. 2014). In another study, Zhang et al. evaluated the binding of *E. coli* to corundum and hematite nanoparticles (W. Zhang et al. 2011). Younes et al. compared the adhesion forces between lactobacilli and *S. aureus* to the forces mediating staphylococcal co-aggregation (Younes et al. 2012). Ophthalmological devices have also been studied with AFM force spectroscopy, where adhesion strength of *Pseudomonas aeruginosa*, *S. aureus* and *Serratia marcescens* to contact lens (CL), polypropylene and Ag-impregnated cases was evaluated. In a similar study, authors studied the adhesion of nine bacterial strains to contact lenses and polypropylene lens-cases (Qu et al. 2013; Qu et al. 2012). Other interesting applications of SCFS include mapping of individual receptor-ligand

sites for the antibiotic drug vancomycin on *Lactococcus lactis* (Gilbert et al. 2007), measuring the interaction of pig gastric mucin (PGM) and *L. lactis* (Le et al. 2013), evaluating the interaction between *Staphylococcus epidermidis* and *Candida albicans* (A Beaussart et al. 2013) and characterization of bacterial footprints (El-Kirat-Chatel, Boyd, et al. 2014; El-Kirat-Chatel, Beaussart, et al. 2014).

Overall, the introduction and development of AFM force-spectroscopy techniques for bacterial nanomechanics has opened new insights for future biomedical research (Dufrêne 2008). Future approaches of bacterial nanoscopy are focusing on potential use of AFM cantilevers as nanomechanical biosensors, which could offer real-time antibacterial assays with high sensitivity (Fritz et al. 2000; McKendry 2012; Ndieyira et al. 2008). Current research is also being applied in the field of food sciences as a new method for describing the adhesive behaviour of common food-borne pathogens (Fatma Pinar Gordesli & Abu-Lail 2012; Goulter-Thorsen et al. 2011). Despite this recent progress several methodological difficulties must be addressed. The AFM continues to be a highly complex tool which non-experts may find difficult to operate. Adhesion measurements with cell-spectroscopy are usually non-parametrical and tend to have large standard deviations making it difficult to extract significant conclusions from the data (van der Mei et al. 2010). Additional efforts should be directed towards developing standardized protocols in hopes of homologating data acquisition, processing and interpretation. It is important to stress that bacterial force-spectroscopy remains an in vitro technique which results may not always be consistent with in vivo behaviour of bacterial cells, therefore, further headway must be made towards

effectively translating experimental findings of bacterial force spectroscopy into *in-vivo* implications and significances.

In the field of dentistry, AFM bacterial probes have been utilized to evaluate interactions between oral bacteria and hard tooth surfaces with SCFS. To study the nature of the forces responsible for bond-strengthening of four oral *Streptococci* strains to saliva-coated enamel surfaces, Mei et al. employed Poisson analyses of adhesion-force distribution obtained by AFM nanomechanic probing (Mei et al. 2009). A later study by Wessel et al. employed AFM bacterial probes to measure the interaction of microbial cells to saliva-coated enamel surfaces (Wessel et al. 2014). These findings give new insights on the importance of initial bacteria-surface interactions for bacterial adhesion and colonization of hard surfaces leading to dental biofilm formation in the oral cavity. However, not much research exists on the use of living AFM probes to study the interaction between cells and oral biomaterials of interest, and therefore it remains important to develop a reproducible approach to study the colonisation of these biomaterials at the single-cell level.

4. Research question

Is it possible to use an AFM-based approach to evaluate the adhesion between single-cells and dental biomaterials at the nanoscale level?

5. General objectives:

- To develop a reproducible AFM-based model to study the adhesion of oral microbes to dental biomaterial surfaces
- To determine the influence of biomaterial surface characteristics on the early-colonisation of bacterial cells
- To study strain-dependent differences in the microbial colonisation of oral biomaterials
- To determine if strain characteristics such as phenotype and virulence play a role in early-stage adhesion

CHAPTER 2

Development of a non-destructive immobilisation protocol for Atomic Force Microscopy imaging and nanomechanics of living oral bacteria and fungal cells*

---

1. Introduction

Despite significant progress in microbiological research, bacterial colonisation of medical devices and biofilm-related pathologies continue to challenge the fields of food science, orthopaedics, medicine and dentistry (Postollec et al. 2006; Barros et al. 2013; Ammendolia et al. 2014). The use of AFM allows researchers to obtain high-resolution images of bacterial samples, acquire information on the nanomechanical properties of microbial cells as well as measuring the adhesive forces between cells and surfaces (Pinzón-Arango et al. 2010; T. Zhang et al. 2011). However, since the AFM tip comes into direct (or very-close) contact with the sample, it remains necessary to effectively immobilise the bacterial cells to the substrates, to avoid cell detachment during imaging or nanomechanics. This immobilisation must allow experimentation in buffer environments, to keep bacteria in their viable and physiological state without disrupting native morphology and properties (Yang et al. 2010). In this part of my thesis, the development of a simple and effective protocol to immobilize living microbial cells for AFM experimentation is described.

* TEM sample preparation and imaging was carried out together with Dr. Helina Marshall

2. Aim

The aim of this investigation was to develop a non-destructive and simple approach to immobilize living bacterial and fungal cells for AFM imaging and nanomechanics in buffered solution.

3. Objectives

- Determine the ideal growth conditions for strains of *Staphylococcus aureus*, *Streptococcus sanguinis* and *Candida albicans,* in order to facilitate immobilization for AFM experiments.
- Characterise the morphology of *Staphylococcus aureus*, *Streptococcus sanguinis* and *Candida albicans* by employing electron microscopy and AFM imaging.
- Evaluate the effectiveness of different immobilisation agents (gelatin, poly-L-lysine and poly-dopamine) on the attachment of bacterial and fungal cells for AFM investigation.
- Fabricate functionalised AFM cantilevers to allow immobilisation of viable bacteria, and study the adhesion between *S. aureus* and *S. sanguinis* and biomaterial surfaces of interest.

4. Materials and Methods

4.1. Bacterial stocks

For this research, all bacterial experiments were carried out with stocks of *Streptococcus sanguinis* (ATCC 10556) and *Staphylococcus aureus* (8325-4). Both

strains were stored at -80°C (15% glycerol in BHI broth); and for experiments, bacteria were grown on agar plates for 24 hours. *S. sanguinis* was cultured on BHI Agar (Oxoid Ltd, UK) whereas *S. aureus* was maintained on TSB Agar plates (Oxoid Ltd, UK). For experiments, colonies of *S. sanguinis* were freshly harvested from agar plates and inoculated into BHI nutrient broth (Oxoid Ltd, UK) for 16hrs at 37°C and 5% CO_2. *S. aureus* was prepared for experiments by growing in TSB broth (Oxoid Ltd, UK) for 16 hours at 37°C.

4.2. Fungal strains

C. albicans ATCC 10231 and a clinical isolate of *C. albicans* (C1, Royal Free Hospital, London) were utilised throughout the study. From frozen stocks, *C. albicans* were grown in *Sabouraud* broth (Oxoid Ltd, UK) for 16hrs at 37°C and aeration to obtain the yeast cell phenotype. For hyphal differentiation of *C. albicans*, three different approaches were assessed. *C. albicans* were grown at 37°C and aeration in either a) BHI broth (Oxoid Ltd, UK) for 3hrs, b) BHI for 18hrs or c) DMEM (Sigma, UK) for 18hrs. Subsequently and for all cases, 100µl of fungal suspension was diluted into 1ml final concentration of phosphate-buffer saline (PBS 1x, Lonza, Belgium) and harvested at 5000rpm for 1min (Eppendorf 5417R, UK). Resulting pellets were re-suspended in 1mL PBS and transferred immediately to the AFM for experiments.

4.3. Electron microscopy characterisation of microbial strains

Initial characterization and morphology of *S. sanguinis*, *S. aureus* and *C. albicans* cells was obtained by scanning electron microscopy (SEM) using a Philips XL30 FEG

(FEI, Eindhoven, Netherlands) microscope. Briefly, a droplet of obtained microbial culture was placed onto a sterile glass coverslip, and covered with 500µl glutaraldehyde 4% for 10min. Subsequently, samples were rinsed in a series of ethanol dilutions at 50, 70, 90 and 100%, critically point dried, mounted on SEM stubs and sputter-coated with gold for SEM imaging. Images were obtained with an acceleration voltage of 5kV, at both low and high magnification at representative areas of each sample.

In the case of *S. sanguinis* and *S. aureus*, transmission electron microscopy (TEM) characterisation was also obtained. For TEM, pelleted bacteria were re-suspended in PBS and incubated at 37°C for 30min. After two washes with PBS, samples were then fixed with 1ml 1% paraformaldehyde for 1hr at 4C. Following centrifugation, samples were re-suspended in 1.5% low gelling temperature agarose (Sigma, UK) in 0.1M phosphate buffer, and incubated overnight at room temperature. The resulting agarose plugs were then cut to be approximately $1mm^2$ and incubated on ice in a solution consisting of 2% formaldehyde, 2.5% glutaraldehyde, 0.075% ruthenium red, 0.075M lysine acetate and cacodylate buffer (0.1M cacodylate trihydrate, pH 7.4, 3% sucrose, 0.1% CaCl) for 20 minutes. Bacteria were then washed twice in cacodylate buffer with 0.075% ruthenium red and re-incubated in 2% formaldehyde, 2.5% glutaldehyde, and 0.075% ruthenium red in cacodylate buffer for 3 hours on ice. After two subsequent washes, samples were then fixed with 1% osmium in cacodylate buffer and 0.075% ruthenium red for 1hr on ice. Samples were then washed twice (cacodylate buffer, 0.075% ruthenium red) prior to sequential ethanol dehydration -with 10, 20, 50, 70, 90 and 100%- for 30min each,

on ice. Sections were then incubated in 1-part LR White Resin (Sigma, UK) to 1-part ethanol for 2hrs on ice, and then overnight in 2-parts LR White Resin to 1-part ethanol. Following this procedure, samples were incubated in 100% LR White Resin for 3 days at 4C, changing resin every 12 hours. Ultimately, sections were baked in gelatin capsules at 65C in LR White Resin for 24 hours prior to cutting 70nm sections and mounting onto copper grids. Sections were visualised using a Jeol 1010 Transmission Electron Microscope (Jeol Ltd, Japan).

4.4. Substrate preparation for bacterial immobilization

To immobilise microbial cells for AFM imaging and nanomechanics, a 100µl droplet of either gelatin (Sigma-Aldrich, UK), poly-L-lysine (PLL) (P4707, Sigma-Aldrich, UK) or a solution of 4mg/ml dopamine hydrochloride in 10mM TRIS buffer, pH 8.0 (Dopamine Hydrochloride, Sigma-Aldrich, Germany) was placed on the surface of a sterile glass slide (Select Micro Slides, Solmedia, UK; 20 minute sterilization cycle, BR-506, UVC Light Products, UK). After 1hr incubation, surfaces were rinsed 3 times with sterile/filtered dH_2O and dried under N_2 airflow. All surfaces were stored at 4°C until experiments were carried out **(Figure 2.1).**

For bacterial attachment, 500µl aliquots of overnight *S. sanguinis* and *S. aureus* stocks were diluted into 500µl of dH_2O, and cells were harvested by centrifugation at 5000rpm during 1min (Eppendorf 5417R, UK), washed and re-suspended into 1ml of PBS to remove growth media components. This process was repeated three times, and the final pellet was diluted into 1ml of PBS. Finally, a 50µl droplet of 10-fold diluted bacterial suspension was incubated for 15min on each

pre-treated surface and washed three times with PBS to remove any unattached cells. For *C. albicans*, 100µl of fungal suspension was diluted into 1ml final concentration of phosphate-buffer saline and harvested at 5000rpm for 1min. Resulting pellets were re-suspended in 1mL PBS and transferred immediately to the AFM for experiments. AFM measurements were carried out immediately in buffer to avoid dehydration and preserve bacterial viability throughout experiments **(Figure 2.1).**

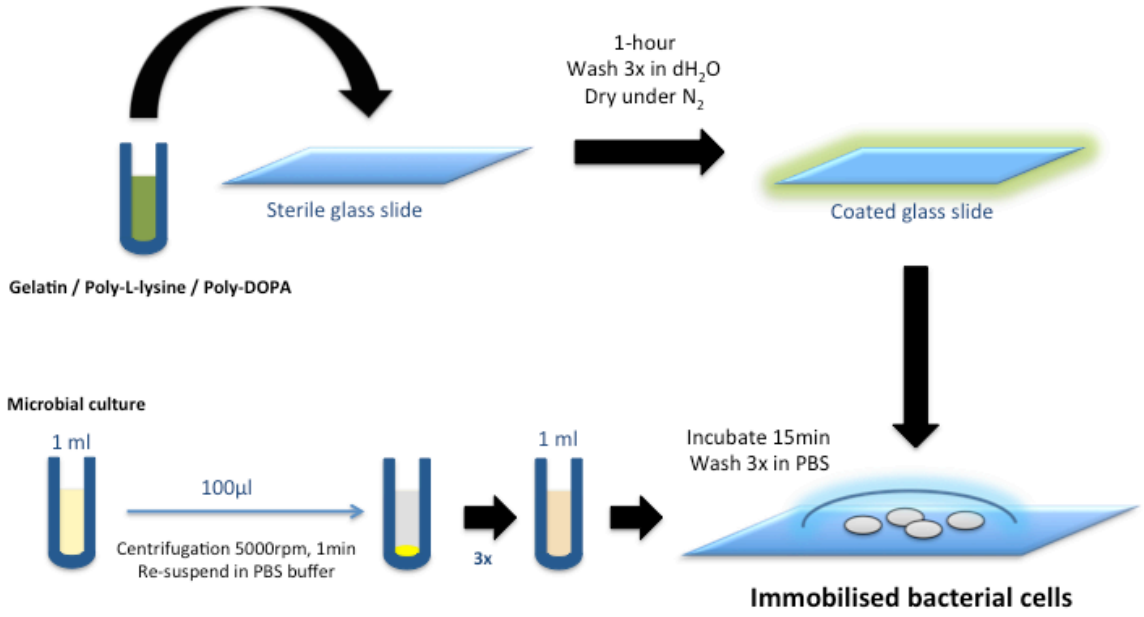

<u>Figure 2.1</u>: Diagram representing the protocol to immobilise living bacteria on functionalised glass slides for AFM experiments.

4.5. Bacterial viability assays

To assess viability of *S. aureus* and *S. sanguinis* cells before AFM measurements, a bacterial live/dead stain was employed (Live/Dead Baclight, Life

Technologies, USA). Briefly, 1.5µl of SYTO 9 nucleic acid stain (Component A) was mixed with 1.5µl of propidium iodide (Component B) and added to 1ml of prepared bacterial suspension. After a 15min incubation period (covered from light), bacteria were immobilized to coated surfaces for 15min and rinsed to remove unattached bacteria. Viability was confirmed by green fluorescence of bacteria upon attachment and throughout measurements, whereas red fluorescence was used as an indicator of bacterial death.

4.6. Live cell imaging with AFM

Bacteria immobilised onto coated glass cover slips were imaged employing a JPK NanoWizard AFM (JPK Instruments, Germany) mounted on an Olympus IX71 (Olympus, Japan) inverted microscope, in intermittent contact mode at room temperature (20°C). Bacterial cells were imaged in TRIS buffer (Sigma, UK) while *C. albicans* was imaged in PBS. MSNL-10 cantilevers (Bruker, Santa Barbara, USA) tuned to a drive frequency of ~46 kHz (nominal resonant frequency 25-50 kHz) were employed with a constant line rate of 0.3Hz. Gain parameters and setpoint were adjusted according to each sample. Thermal resonance calibration yielded a cantilever spring constant of 0.11N/m (nominal value 0.1N/m). After focusing on an area of interest, images were obtained at different magnifications with 256x256 pixels at random sites of each sample, and processed with the JPK Data Processing Software v.5.1.8 (JPK Instruments, Germany).

4.7. Functionalisation of AFM cantilevers for force spectroscopy

Glass microspheres of ~10µm diameter (Whitehouse Scientific, UK) were

attached to NP-O10 tip-less cantilevers (Bruker, Santa Barbara, USA) by employing the NanoWizard/inverted microscope setup. Firstly, cantilevers were mounted on the AFM and slowly approached towards a thin layer of UV-curable glue (Loctite, UK) spread on a glass slide. After a 5s contact with the glue, cantilevers were retracted before being placed carefully over an individual glass microsphere and approached until contact was established. After a dwelling time of ~3min, the cantilever-microsphere array was retracted and cured in a UV chamber for 10min (2UV Transilluminator, UVP, USA). Both optical microscopy and SEM imaging confirmed adequate attachment of a single glass micro-bead on each cantilever.

For the immobilisation of living bacteria, modified colloidal probes were coated with a solution of 4mg/ml dopamine hydrochloride (Sigma, UK) in 10mM TRIS buffer (pH 8.0) for 1 hour, rinsed 3 times with sterile/filtered dH_2O and dried under N_2. A 50µl droplet of 10-fold diluted bacterial suspension was placed onto a cover slip before placing the probe in contact with a bacterial cell for ~3mins. All this process was carried out in TRIS buffer, avoiding dehydration of probes and surfaces during preparation and throughout measurements. Probes were used immediately or otherwise stored at 4°C until experimentation.

5. Results and Discussion

5.1. Characterisation of fungal and bacterial cell morphology and aggregation

Previous to any AFM experiments, morphological characterization of *S. aureus* and *S. sanguinis* was obtained with standard electron microscopy techniques. *S.*

aureus was mainly observed in diplococcal form, although it was also possible to observe clusters of >3 cells **(Figure 2.2)**. Cells presented a regular rounded shape with an average diameter of ~0.7-1µm, and morphology was found to be consistent with other studies (Barros et al. 2017; Zengin & Baysal 2014). TEM imaging allowed for the visualisation of the cell wall, where it was possible to observe the presence of a microcapsule surrounding certain areas of the bacterial cell **(Figure 2.2C and 2.2D)**. This observation was consistent across all *S. aureus* cells visualised under TEM. In the case of *S. sanguinis*, cells were observed in chain-like formations of variable lengths (~2-8 cells), and visually appeared more oval in shape compared to *S. aureus* **(Figure 2.3A and 2.3B)** (Evans et al. 2014). There were also less individual and diplococcic cells than observed in the case of *S. aureus*; furthermore, *S. sanguinis* cells were smaller in size with an average diameter of 0.5µm (Hao et al. 2010). TEM sectioning demonstrated the presence of a capsule surrounding the bacterial cell, which was much larger in size than the one observed in *S. aureus*. The presence of surface capsule on streptococci is well described in the literature, and its believed to play an important role in immune evasion and adhesion to surfaces (Hyams et al. 2010; Tsunashima et al. 2012). In the case of *S. aureus*, microcapsule has been previously described, although some authors debate that strain 8325-4 effectively expresses the phenotype (Kneidinger et al. 2003; Wann et al. 1999). Overall, the selected sample preparation protocol preserved the capsule on the surface of the bacteria and allowed correct visualisation under TEM.

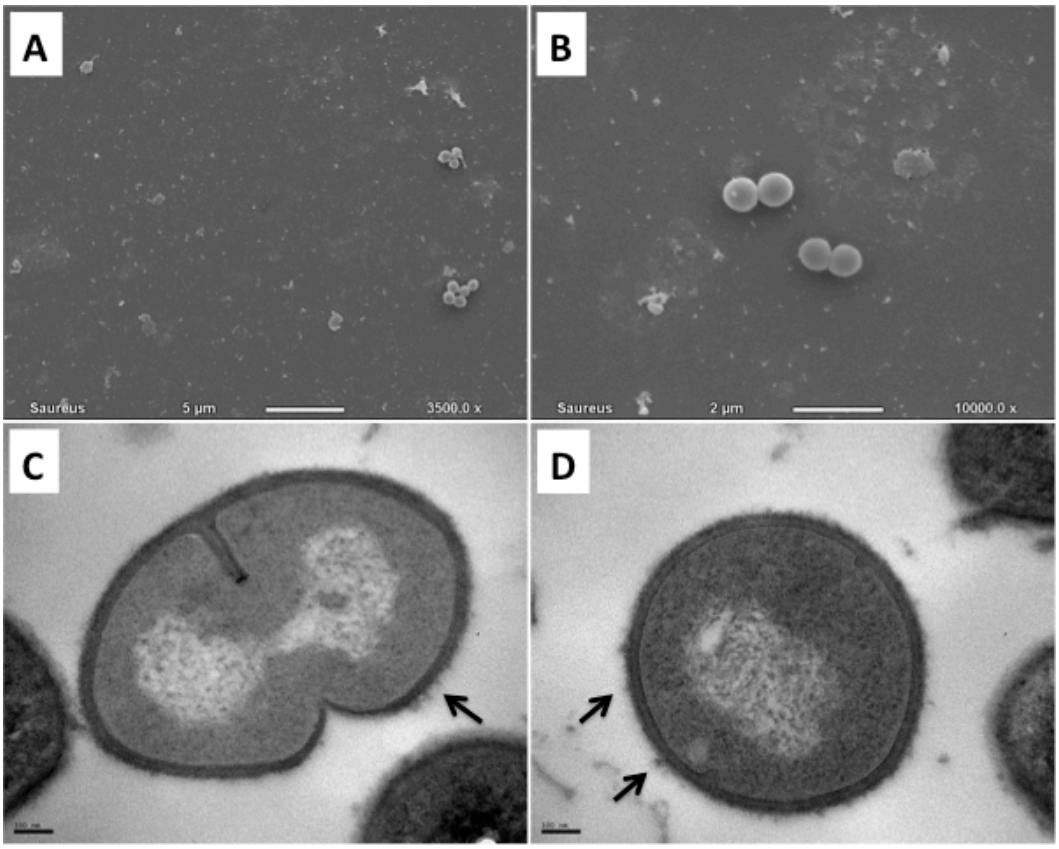

Figure 2.2: **Electron microscopy characterisation of *Staphylococcus aureus* cells.** (A) 3500x and (B) 10000x magnification SEM images of *S. aureus*, observed mainly as rounded, diplococcal cells on the surface. TEM sectioning of a (C) diplococcal and (D) single *S. aureus* cell, in which the cell wall and can be observed (scale bars 100nm). The presence of microcapsule is highlighted with arrows.

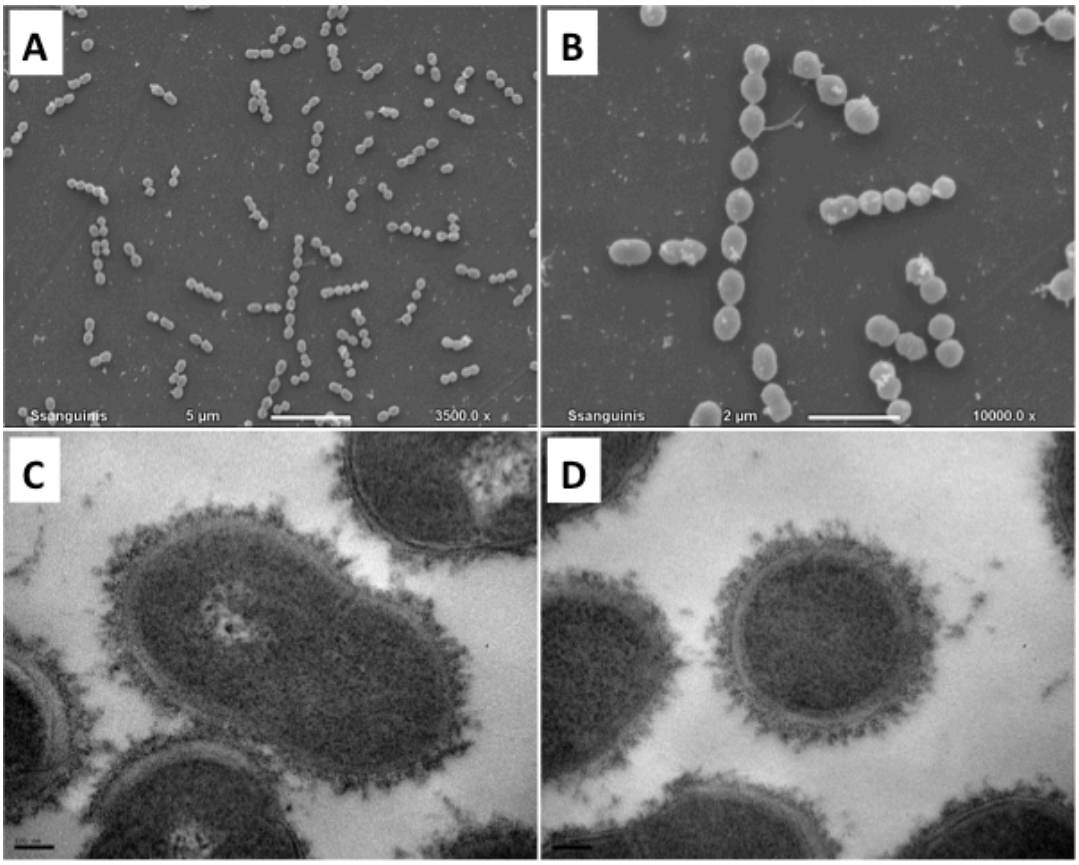

Figure 2.3: Electron microscopy characterisation of *Streptococcus sanguinis* cells. (A) 3500x and (B) 10000x magnification SEM images of *S. sanguinis*, in which the typical chain-like configuration of the strain can be observed. (C) and (D) TEM sectioning of *S. sanguinis* cells, which demonstrate the presence of capsule surrounding the cell wall (scale bars 100nm).

SEM imaging was also utilised to characterise the morphology and phenotype of *C. albicans* cells. It is well known that *C. albicans* is a polymorphic yeast that can express both a yeast cell and hyphae phenotype, depending – amongst other factors - on the surrounding growth conditions (Sudbery 2011; Thomson et al. 2016). Several growth methods were assessed to favour either yeast cell or hyphae

expression. In the case of yeast cell expression, it was obtained by growing *C. albicans* in Sabouraud broth for 16hrs at 37°C **(Figure 2.4)**. Yeast cells are observed as rounded or ovoid structures, some of which show the presence of budding scars on the surface **(Figure 2.4B and 2.4C)**. Cell size is increased compared to the bacterial cells, with diameters typically between 2-5µm. Although a reduced number of pseudo-hyphae can be observed in this sample, *C. albicans* are mostly expressing yeast cell morphology consistent with previous reports in literature **(Figure 2.4A and 2.4D)** (Staniszewska et al. 2013).

To determine an effective approach to obtain true hyphal differentiation, *C. albicans* were grown in BHI broth for either 3hrs or 18hrs or in DMEM for 18hrs. Both BHI and DMEM are nutrient-rich media, which provide *Candida* with similar conditions as if they were invading a host. Growth in BHI for 3hrs was found to be the optimal protocol to induce the presence of hyphae in the sample. Hyphae were observed as a single tube germinating from a *C. albicans* cell, with no constriction at the point of origin and no septa observed throughout the prolongation **(Figure 2.5A and 2.5B)** (Krasowska et al. 2009). Increasing the incubation time to 18hrs yielded absence of hyphae, which suggests phenotypic reversal induced by the lack of nutrient availability in the media after longer growth periods **(Figure 2.5C and 2.5D).** Growth in DMEM for 18hrs generated clusters of large hyphae, which is not optimal for AFM experiments as it is does not allow the presence of individual hyphae on the surface for probing **(Figure 2.5E and 2.5F)**.

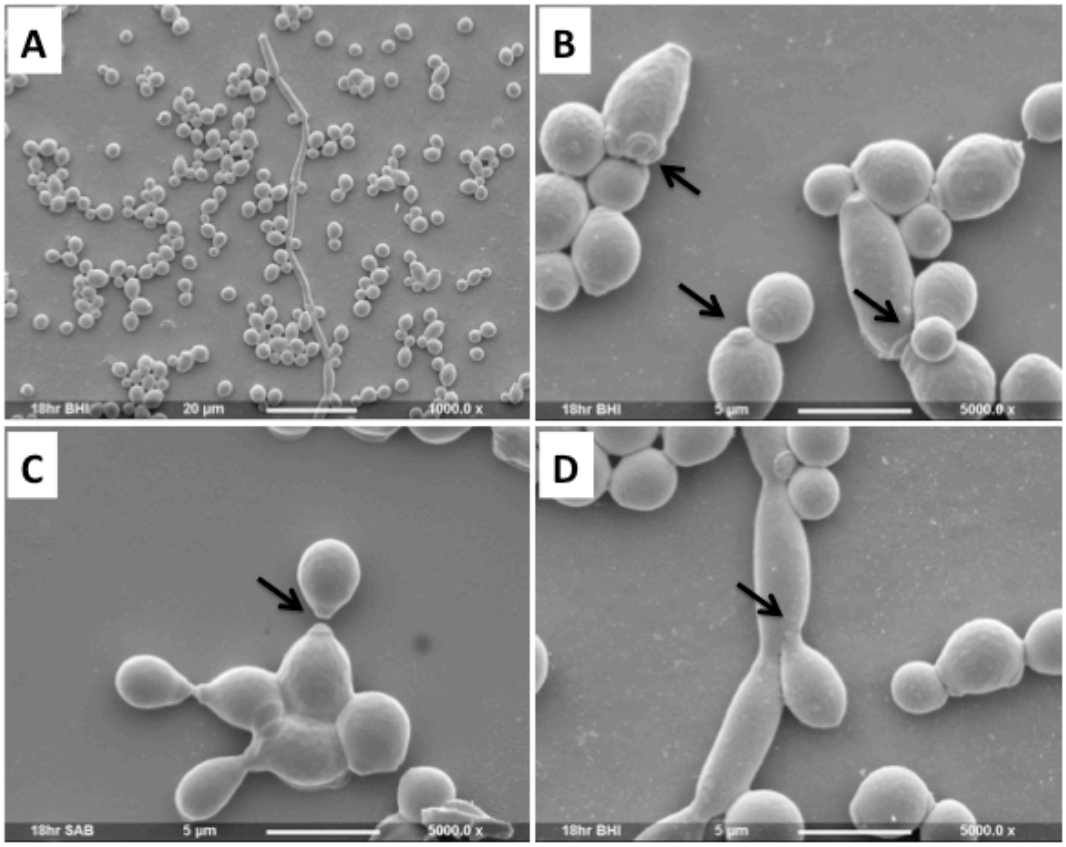

Figure 2.4: SEM characterisation of *C. albicans* yeast cells and pseudohyphae in Sabouraud media. (A) 1000x field of *C. albicans* yeast cells and a single pseudohyphae. (B) and (C) represent 5000x magnification images of yeast cells, demonstrating morphologies ranging from spherical to ovoid. Budding scars observed on the surface of *C. albicans* are represented by the inset arrows. (D) 5000x image of a daughter *C. albicans* cell budding off the pseudohyphae (arrow).

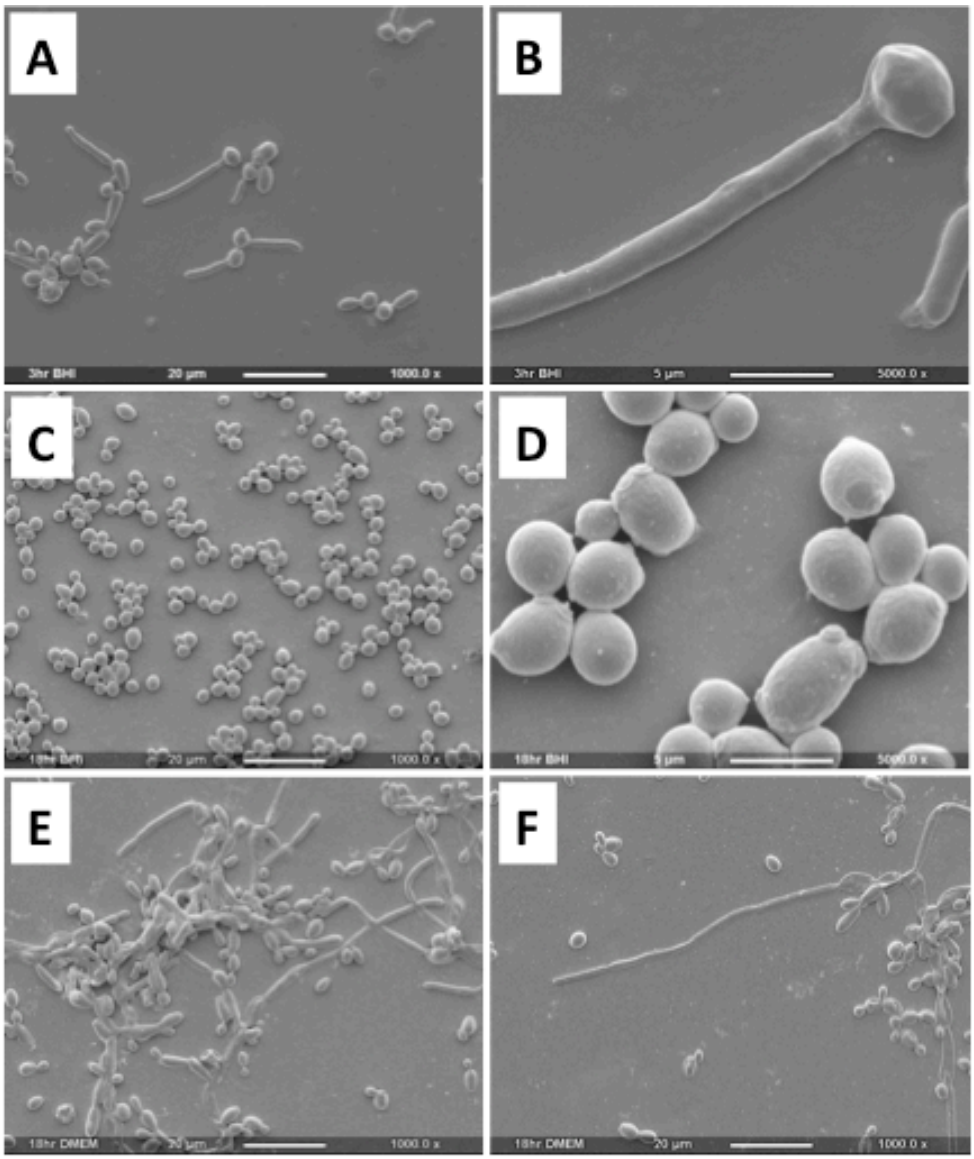

Figure 2.5: Assessment of *C. albicans* hyphal induction utilising three different growth conditions. (A) and (B) represent growth in BHI for 3hrs. Hyphal differentiation is observed, and resulting hyphae are individualised and consistent with the expected phenotype. (C) and (D) represent growth in BHI for 18hrs, where hyphal differentiation is reversed and only the yeast cell phenotype is present. (E) and (F) represent growth in DMEM for 18hrs. Hyphae are large in size and cluster on the surface, making them not optimal for AFM force-spectroscopy experimentation.

5.2. Immobilisation protocols for AFM study of live bacteria

To assess the effectiveness of gelatin, PLL and poly-DOPA for immobilizing bacterial cells to a substrate for AFM imaging and nanomechanics, high-resolution imaging of *S. sanguinis* and *S. aureus* in dH_2O was attempted **(Table 2.1)**. These three immobilising agents were selected, as they have been described in literature as non-destructive, by conferring a positive charge to the surface allowing negatively-charged bacteria to covalently bind (Louise Meyer et al. 2010; A Beaussart et al. 2013). Gelatin coated surfaces were not effective for immobilization under buffer conditions as cells became rapidly detached during scanning; however, when removing excess buffer from the system, both *S. sanguinis* and *S. aureus* cells could be imaged. Thus, as it is vital to ensure that cells are maintained hydrated to minimise sample destruction, this approach has not been pursued any further. As with gelatin, PLL coated slides did not yield immobilisation of either *S. aureus* or *S. sanguinis*. These results are consistent with previous reports by Doktycz et al., who were also unable to image bacteria attached to PLL surfaces (Doktycz et al. 2003). These authors, however, were able to image *S. aureus* on gelatin-coated surfaces, although their protocol did not specify if cells were maintained hydrated throughout the entire preparation process.

In contrast, poly-DOPA was found to be the only substance to effectively immobilize *S. aureus* and *S. sanguinis* cells for intermittent contact imaging under liquid conditions (Dreyer et al. 2012; Harimawan et al. 2011; Lee et al. 2007; Kang & Elimelech 2009). Contact mode imaging was not possible, as the increased lateral forces exerted during scanning either detached the cells from the surface, or

induced imaging artefacts as a result of the AFM tip deforming the soft bacterial sample. With intermittent contact imaging, high-resolution imaging of individual and groups of cells was possible, and very seldom did bacteria cells detach from the DOPA-coated surface even during consecutive scanning. All imaging was performed in TRIS buffer since imaging in PBS resulted mostly in detachment of cells. This can be explained mostly by the stronger ionic charge of PBS compared to TRIS buffer, as immobilization of cells onto gelatin, PLL and poly-DOPA is strongly dependent on the effective interaction between the negative-charged bacterial wall and the positive-charged surface created (Louise Meyer et al. 2010; Webb et al. 2011).

Table 2.1: Summary of agents utilised to immobilise *S. aureus*, *S. sanguinis* and *C. albicans* for AFM imaging and experimentation.

Strain	Gelatin	Poly-L-lysine	Poly-DOPA
***S. aureus* 8325-4**	no	no	no
***S. sanguinis* ATCC 10556**	no	no	no
***C. albicans* (yeast cells)** **	—	yes	no
***C. albicans* (hyphae)** **	—	no	yes

** *for both C. albicans strains*

For *C. albicans*, AFM intermittent contact imaging allowed for high-resolution imaging of yeast cells, pseudohyphae and hyphae in PBS buffer **(Figure 6)**. Thus, it was possible to obtain images with no previous sample preparation (i.e. fixation,

dehydration), and therefore minimise sample alteration and ensure viability. Both yeast cells and hyphae are clearly distinguishable in the AFM images. Furthermore, smaller structures such as dividing septa and cell-wall topography can be clearly resolved **(Figure 2.7A)**. It is also possible to obtain high-resolution images of budding scars at higher magnifications, in which a central elevation of the cell wall can be observed surrounded by a ring-like structure **(Figure 2.7B, C and D)**. Budding scars were only observed on the surface of *C. albicans* yeast cells and pseudohyphae, and were absent in hyphae. Overall, all morphologies of *C. albicans* observed with AFM were consistent with previous observations reported in literature (Formosa & Dague 2015; Braga & Ricci 2011; Chopinet et al. 2013).

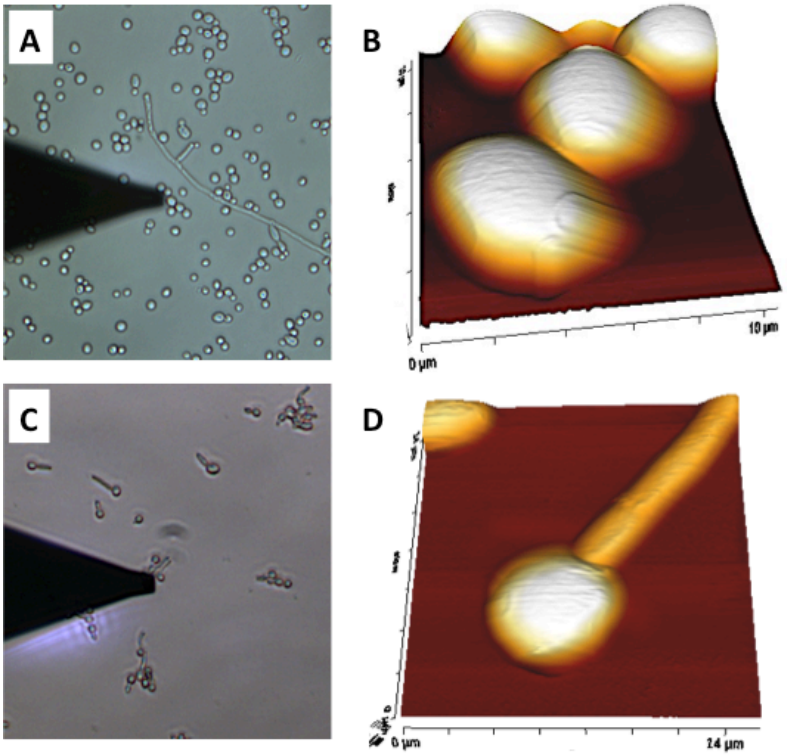

Figure 2.6: AFM imaging of living *C. albicans* yeast cells and hyphae immobilised to PLL and poly-DOPA coated surfaces in PBS buffer. Optical microscopy images obtained during AFM scanning of (A) yeast cells and (C) hyphae. The AFM tip can be observed to the left of each image. (B) 3D height reconstruction image of *C. albicans* yeast cells immobilised onto PLL, in which budding scars can also be resolved. (D) 3D height reconstruction image of *C. albicans* hyphae immobilised onto a poly-DOPA coated slide.

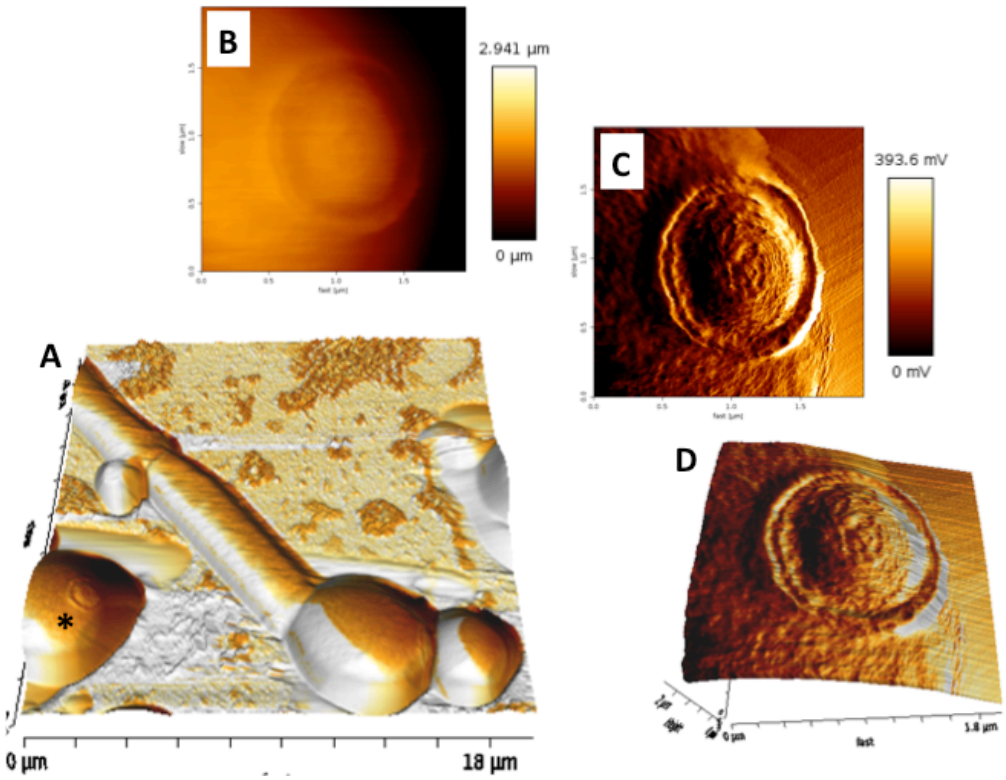

Figure 2.7: High-resolution AFM imaging of living *C. albicans* cell surface topography in buffer. (A) 3D height reconstruction image of *C. albicans* yeast cells and pseudohyphae immobilised onto PLL coated glass slides, in which budding scars can be resolved (star). High-resolution (B) topography image, (C) amplitude image and (D) 3D height/amplitude overlay image (2x2 µm) of the bud scar highlighted in (A). It is possible to resolve the structure of the budding scar in great detail.

5.3. Functionalization of tipless cantilevers for bacterium force spectroscopy

To allow for the study of adhesive forces generated between bacterial cells and biomaterial surfaces, functionalised probes were constructed from commercially available tipless AFM cantilevers. By employing the AFM as a micromanipulator, it was possible to effectively attach ~10μm diameter glass microspheres to the end of a tipless cantilever (**Figure 2.8**). This process of cantilever functionalisation was proven to be highly reproducible and yielded consistent placement of glass microspheres. The UV-curable glue allowed control of the process without premature hardening, and kept the microsphere correctly placed until the curing process was completed. In few occasions did the microsphere detach from the cantilever after curing, in which case the probe was discarded. This approach is similar to what has been reported so far in the literature by other groups (Audrey Beaussart et al. 2013; Beaussart & El-Kirat-Chatel 2014; Herman et al. 2013).

Once microspheres were attached, it was necessary to coat them with an immobilisation agent in order to allow the attachment of bacteria for AFM force-spectroscopy experiments. Poly-DOPA was the agent of choice, as it was previously successful at immobilising both *S. aureus* and *S. sanguinis* for AFM imaging. Poly-DOPA coating was effectively obtained by placing a droplet of immobilising agent onto the end of the AFM cantilever and incubating for a 1hr period. Subsequently, the probe was approached to individual bacterial cells, which were allowed to attach to the coated glass microsphere for ~3min while keeping the loading force to a minimum. Successful attachment of bacterial cells was observed during probe

retraction, as bacteria were removed from the focal plane together with the cantilever. SEM images also confirmed attachment of bacteria to the coated microsphere surface (**Figure 2.9C**).

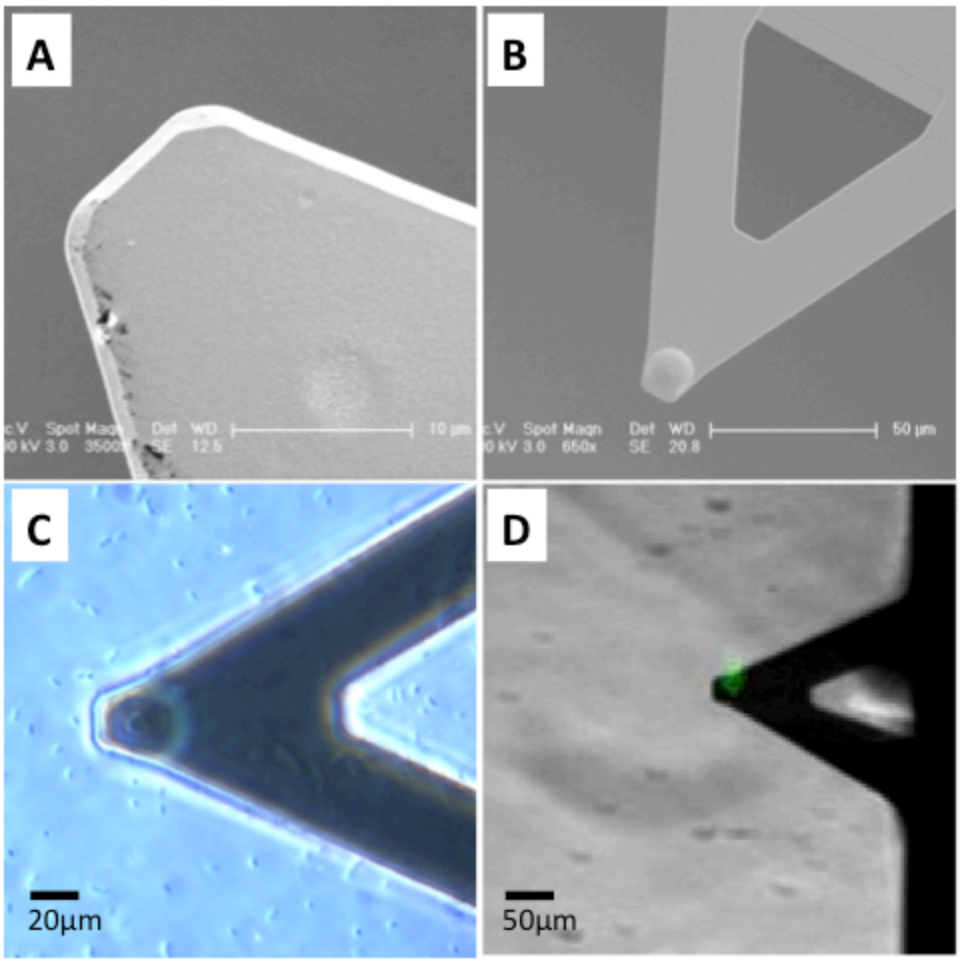

Figure 2.8: Protocol for the fabrication of functionalised AFM cantilevers for force-spectroscopy experiments. (A) SEM image of a tipless cantilever as purchased from the manufacturer. (B) After coating the tip of the cantilever with UV-curable glue, a glass microsphere was attached. (C) Optical microscopy image of a functionalised AFM cantilever being placed atop a *S.*

sanguinis cell in solution. (D) Live/Dead staining, demonstrating the viability of the cell probe after fabrication, as long as it is maintained in buffer.

5.4. Determination of cell viability and optimal probing forces for force-spectroscopy

To evaluate the viability of poly-DOPA immobilised *S. sanguinis* and *S. aureus* cells, a Live/Dead staining was employed (Herman et al. 2013). Bacterial viability was assessed for both surface-bound bacteria and cells attached to functionalised AFM probes after 1hr of immobilisation in buffer (**Figure 2.9A**). As observed, surface-bound bacteria remain viable, confirming that poly-DOPA immobilisation is a non-destructive method for cell attachment (**Figure 2.9A**) (Kang & Elimelech 2009). Minor changes may occur in poly-DOPA bound bacteria, however, the lack of morphological alterations and preserved viability make this highly unlikely. In the case of functionalised probes, attachment of bacteria to coated microspheres also preserves cell viability (**Figure 2.9B**). Interestingly, viability of bacteria attached directly onto the metallic cantilever surface is decreased, confirming previous reports that cantilever-bound cells are likely to die due to overheating by the incident laser (Audrey Beaussart et al. 2013).

As a final step before AFM force-spectroscopy experimentation, the 'optimal' loading force of the bacterium against the surface was determined. As it has been demonstrated that loading forces can influence the adhesion between bacteria and surfaces (Chen et al. 2014), it is important to utilise a loading force that minimises cell deformation when cells are approached to the surface. In nature, bacterial

adhesion occurs by the initial positioning of a bacterium to the close vicinity of a surface, which is mainly governed by physical interactions. Therefore, to effectively represent the physiological conditions leading towards bacterial adhesion to surfaces, bacteria must not be excessively compressed during experiments. To do so, bacterial cells were immobilised onto a poly-DOPA glass slide and probed with increasing loading forces of 0.5, 1.5 and 3.0nN. If the applied force is sufficient to effectively deform the sample, a stiffness pixel map representing the underlying bacterial cell is obtained (**Figure 2.10,** 1.5 and 3.0nN loading forces). In contrast, decreased forces unable to deform the bacterial cell only generate deflection of the cantilever, in which case a stiffness pixel map is not generated (**Figure 2.10**, 0.5nN loading force). By employing this force of 0.5nN, minimal mechanical deformation was exerted on the bacterial surface during experiments.

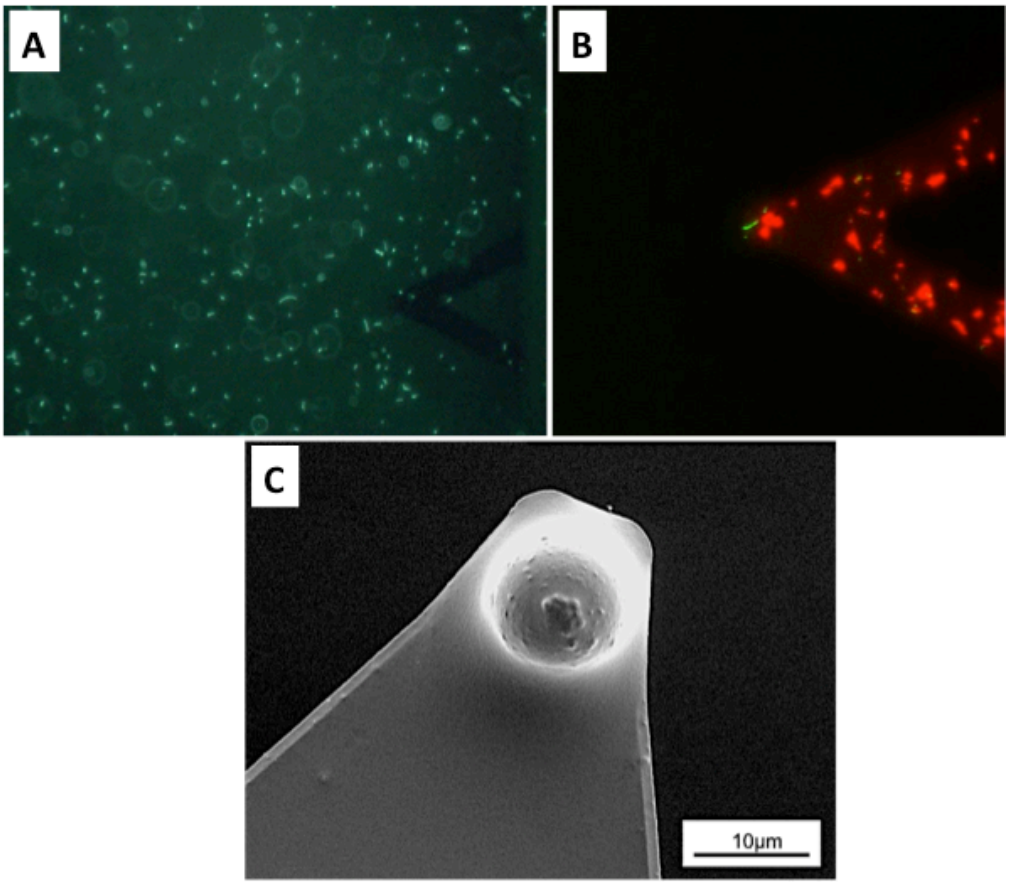

Figure 2.9: Viability of poly-DOPA bound bacterial cells on coated glass slides and functionalised AFM cantilevers. (A) *S. sanguinis* cells immobilised onto a poly-DOPA coated glass slide in PBS, after a 1hr incubation time. Cell viability is maintained throughout the sample. (B) *S. sanguinis* immobilised onto a functionalised AFM cantilever. Note how only cells immobilised onto the microsphere are viable, and cells attached directly to the cantilever are dead. (C) SEM image of *S. aureus* cells attached to a functionalised cantilever, confirming the correct placing of cells on the coated microsphere and absence of cells on the surrounding cantilever surface.

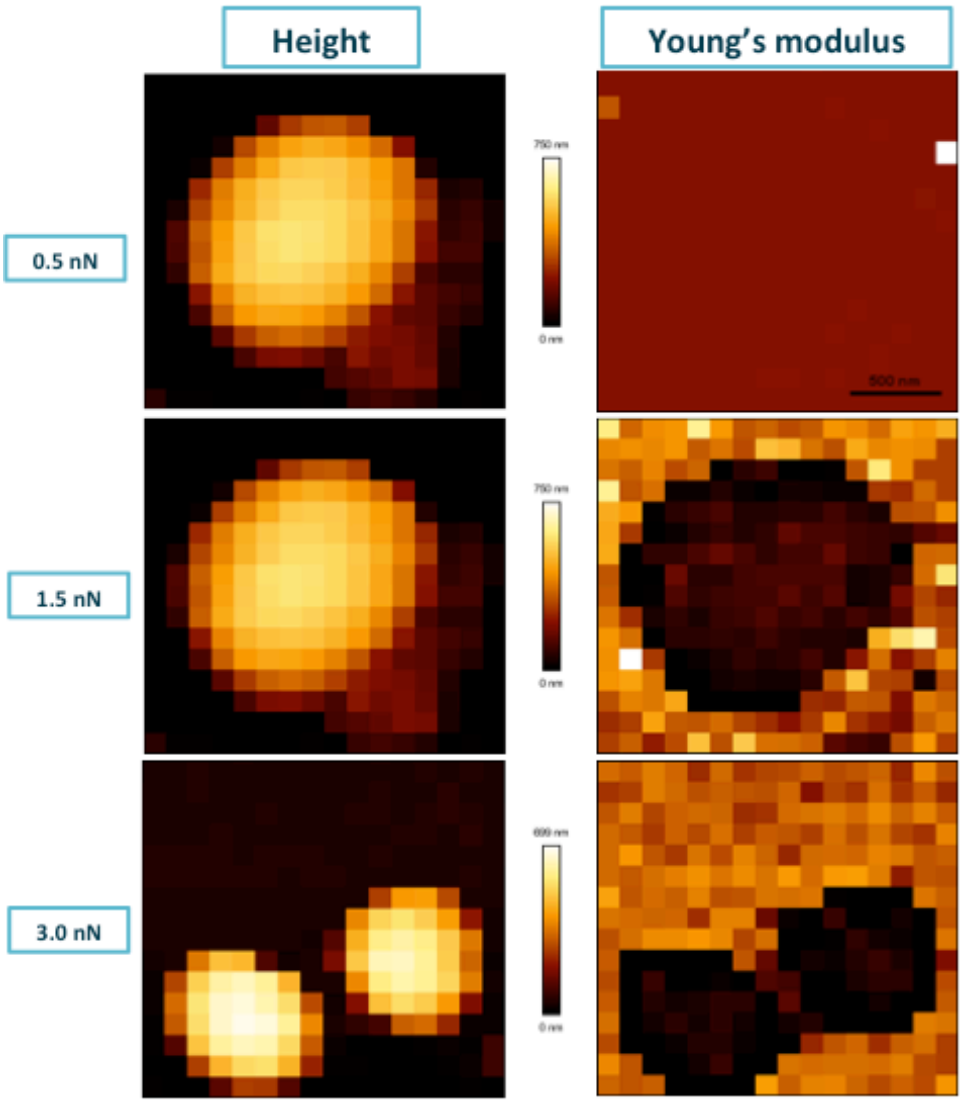

<u>Figure 2.10</u>: Determining optimal loading force for AFM force-spectroscopy experiments. Height (nm) and stiffness pixel maps of *S. aureus* cells immobilised onto a poly-DOPA coated surface, where lighter pixels represent increased values. Bacteria were indented with loads of 0.5, 1.5 and 3nN to determine an optimal loading force that will not deform the cell upon probing. Forces of 1.5 and 3.0nN cause indentation of the bacterial cell, as observed in the corresponding stiffness pixel map. However, forces of 0.5nN only cause deflection of the AFM cantilever

(hence, no cell deformation) as observed in the pixel map, and therefore was selected as loading force for AFM force-spectroscopy experiments.

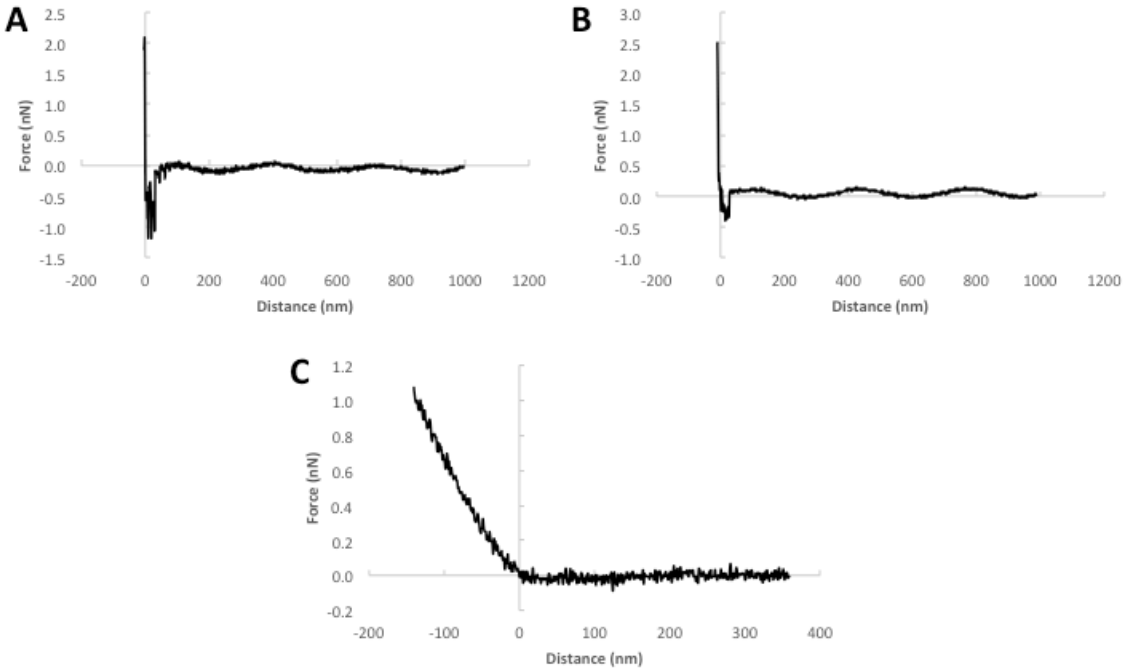

<u>Figure 2.11</u>: Representative control force-curves obtained on functionalised glass surfaces. Retraction segment of force-curves obtained with functionalised probes on (A) glass slide, (B) poly-DOPA coated glass and (C) PLL coated glass at increased contact times (30s). The presence of a small unbinding peak is observed in the case of glass and poly-DOPA, with very short rupture distance and lacking the presence of specific unbinding events.

Finally, control force-curves were obtained for uncoated functionalised probes, and for poly-DOPA and PLL coated-surfaces **(Figure 2.11)**. The presence of a major unbinding peak (<1nN) is only observed in the case of glass surfaces and poly-DOPA,

while PLL shows no adhesive behaviour. However, in all cases there is a lack of specific unbinding events, even after a 30s contact time with the surface. Therefore, it is believed that the adhesive effect of immobilisation agents during SCFS experiments can be neglected.

6. Summary:

In this chapter, a reproducible and effective method for immobilisation of living *S. aureus*, *S. sanguinis* and *C. albicans* cells for AFM imaging and nanomechanic experiments has been described. In summary:

- The optimal growth condition to induce hyphal formation of *C. albicans* for AFM experimentation was found to be incubation in BHI broth for 3hrs. Extended incubation times generated reversal towards the yeast cell phenotype.
- Regarding immobilisation techniques, poly-DOPA was found to be the most effective agent to attach *S. aureus*, *S. sanguinis* and *C. albicans* hyphae. In the case of *C. albicans* yeast cells, the optimal immobilising agent was PLL. Cell viability was ensured, as long as cells were kept in buffer and experimentation times were kept within 1hr.
- High-resolution AFM imaging of living bacterial and fungal cells was possible in buffer. Low-ionic charge buffers are favoured in the case of imaging bacterial cells, as they have the tendency to detach due to lateral shear forces generated during scanning.
- Utilising the AFM, it was possible to modify cantilevers with glass microspheres and functionalise them with living *S. aureus* and *S. sanguinis* cells. Bacteria immobilised onto glass microspheres remain viable for ~1hr, allowing adequate experimentation times.

- The optimal loading force – that generates effective contact between bacterial probes and surface, without deforming the cell and promoting adhesion – was found to be 0.5nN.

CHAPTER 3

Influence of controlled nano-scale roughness on early-stage bacterial adhesion to biomaterial surfaces

---

1. Introduction

Now that we have established a protocol to study bacterial colonisation with the AFM, we will examine the effect of biomaterial surface roughness on bacterial adhesion at the single-cell level. In modern medicine, biomaterials are being employed for the augmentation or replacement of missing or diseased tissues (Huebsch & Mooney 2009; Ratner & Bryant 2004). In recent years, many surface modifications have been incorporated into the design of biomaterials in the hope of improving their biological activity and host tissue integration (O'Brien 2011). Among these, controlled nanopatterning of the biomaterial surface has been considered a promising approach, as it has the potential to directly influence human stem cell proliferation and differentiation (Dalby et al. 2007; Izquierdo-Barba et al. 2015). Despite these positive effects on eukaryotic cell integration, the effect of biomaterial nanopatterning on bacterial attachment and surface colonisation remains unknown (Jahed et al. 2014). As implant surface infection is unfavourable for biomaterial-host tissue integration and can lead to complications such as chronic infection or replacement surgery, there is a strong current interest on understanding the process of bacterial adhesion to biomaterial surfaces (Svensson et al. 2014). One of the most medically important biomaterial colonisers is

Staphylococcus aureus, as its presence on the implant surface is associated to negative clinical prognosis (Arciola et al. 2012; Lee & Wang 2010; Harris et al. 2002). Additionally, increased antibiotic resistance has been observed for many strains of *S. aureus* and as a result, new strategies against biomaterial surface colonisation are being studied in hopes of reducing post-surgical implant infection (Loskill et al. 2014; McKendry 2012; Francius et al. 2008). Utilising AFM techniques, it is possible to assess the elastic properties of surface-bound bacteria by indenting the bacterial surface with an AFM cantilever (Webb et al. 2011) and by employing approaches such as single-cell force spectroscopy (SCFS), bacterial adhesion to biological and non-biological surfaces can be studied in the nano- and pico-meter ranges (Taubenberger et al. 2014; Audrey Beaussart et al. 2013; Sullan et al. 2015). Although several studies have used AFM to probe the nanomechanics of *S. aureus* and its adhesion to substrates and other cells (Ovchinnikova et al. 2012; Aguayo et al. 2015; Peters et al. 2012), little remains known regarding the influence that biomaterial nanopatterning exerts on *S. aureus* adhesion and early-colonisation of the implant surface.

The work in this chapter has been published as **"Influence of biomaterial nanotopography on the adhesive and elastic properties of *Staphylococcus aureus* cells." RSC Advances, 6.92 (2016): 89347-89355.**

2. Aim:

The aim of this study was to determine the influence of surface nanopatterning on early-stage *S. aureus* biomaterial infection, by utilising AFM nanoindentation and single-cell force spectroscopy (SCFS) techniques.

3. Objectives:

- Characterise the topography and surface chemistry of smooth and nanopatterned polycarbonate (PC) surfaces
- Determine the influence of underlying roughness on the elasticity of surface-bound *S. aureus* cells.
- Study the dynamics of early-stage *S. aureus* adhesion onto smooth and nanopatterned PC surfaces, by employing force-spectroscopy, worm-like chain (WLC) modeling and Poisson analysis.

4. Materials and methods:

4.1. *Polycarbonate surface characterisation*

Two distinct engineered polycarbonate (PC) surfaces were employed throughout this present study. Nanopatterned PC surfaces, consisting of 120nm pits with 300nm centre-centre separation in a square arrangement (SQ), were obtained with a previously reported protocol (Dalby et al. 2007). A flat PC surface (PL) was employed as a smooth control. To remove any surface contamination, nanopatterned surfaces were prepared and cleaned by sonication in dH_2O for 5mins, washed with 70% ethanol and dried under N_2 airflow. Characterisation of

surface topography was obtained by AFM imaging (Dimension 3100, Bruker, Santa Barbara, USA) employing intermittent contact mode in air, utilising MSNL-10 (Bruker, USA) cantilevers with a scanning rate of 1.0Hz. Average surface roughness (R_a) was determined using height images obtained during AFM scanning (n = 3), and processed using the proprietary NanoScope Analysis 1.5 software (Bruker, USA). Surface hydrophilicity was determined by contact angle measurements with deionised water (dH_2O), utilising a Cam 200 Optical Contact Angle Meter (Biolin Scientific, Germany). To do so, a single 5µl droplet was applied to the surfaces, and the average angle of contact over 10 seconds was measured and recorded (n = 3). Previous to any bacterial experiments, surfaces were placed in a UV-chamber and sterilised with a 20min cycle (BR-506, UVC Light Products, UK).

4.2. *Bacterial cultures*

Bacterial cells were obtained by incubating stocks of *S. aureus* (strain 8325-4) in TSB for 16hrs at 37°C and aeration. Subsequently, 100µl of bacterial suspension was diluted 10-fold in PBS (PBS 1x, Lonza, Belgium) and harvested at 5000rpm for 1min (Eppendorf 5417R, UK). Resulting pellets were re-suspended in 1mL PBS and transferred immediately to the AFM for experiments.

4.3. *Sample preparation for scanning electron microscopy-focused ion beam (SEM-FIB) milling and imaging.*

To visually characterise the interaction between *S. aureus* and PC surfaces, a 500µl droplet of bacterial suspension was incubated on each surface for 10min, rinsed with PBS to remove unattached cells, and fixed immediately with 4%

glutaraldehyde for 30min. Samples were then dehydrated with 10min serial washes in 50, 70, 90 and 100% ethanol, and sputter coated with gold. Imaging was carried out with an XB1540 (Carl Zeiss, Germany) SEM-FIB system with an acceleration voltage of 10kV at magnifications of 50,000x and 100,000x. FIB milling was carried out with a 30kV:20mA gallium beam probe, by tilting the sample 54° and performing serial linear millings on *S. aureus* cells until exposing the bacterial-surface interface.

4.4. *AFM imaging and bacterial nanomechanics*

To attach single *S. aureus* cells onto substrates for imaging and nanomechanics, a 20µl droplet of final bacterial suspension was deposited onto each PC surface and incubated for 10min. For imaging, samples were washed after incubation with dH_2O and softly dried under N_2 airflow. For nanoindentation experiments, samples were washed with PBS to remove unattached cells, and re-suspended with 100µl of TRIS buffer (Sigma-Aldrich, UK). For all nanomechanic experiments, bacterial cells were maintained submerged in TRIS buffer throughout experimentation to preserve cell viability.

Both imaging and force-volume mapping of the bacterial surface of *S. aureus* were obtained witha JPK Nanowizard system (JPK Instruments, Germany) mounted on an inverted optical microscope (Olympus IX71, Olympus, Japan). Imaging was carried out with a NCS35 cantilever (MikroMasch, USA) in intermittent contact mode in air, tuned at ~110KHz. Images were obtained at 512x512pixels with an average scanning rate of 0.5Hz, optimising setpoint and gain parameters during

scanning. For force-volume mapping, MSNL-10 cantilevers with a spring constant of ~0.1N/m were used. After locating an isolated attached bacterium, force-curves were obtained at random points of the cell centre and perimeter of each bacterium, with a constant speed of 2μm/s and a maximum loading force of 3nN. Six independent *S. aureus* cells were indented and analysed per PC surface. As minimal adhesion between the cantilever and bacterial cell was recorded and an indentation depth of ~50nm was obtained, Young's modulus (YM) was determined from the extension curve by applying the Hertzian model as previously described in the literature (Formosa et al. 2012).

4.5. *Single-cell force spectroscopy (SCFS)*

For SCFS experiments, customised colloidal probes were fabricated in order to immobilise *S. aureus* cells by emplying the protocol described in the previous chapter. All cantilevers were calibrated using thermal tuning (~0.3N/m spring constants), and stored at 4°C until AFM experiments. To functionalise colloidal probes with living *S. aureus* cells, cantilevers were mounted onto the AFM and submerged into a 20μl droplet of bacterial suspension. The probe was then brought into contact with an isolated cell, with a loading force of 0.5nN for ~3mins until attachment was observed. Cantilevers were then retracted, transferred above the PC surface submerged in TRIS buffer. Experiments were carried out with a loading force of 0.5nN, a constant speed of 2μm/s, and surface delay times of 0s and 1s. Each of the *S. aureus* functionalised probes were utilised only for a single experiment and discarded thereafter. Four independent *S. aureus* probes were utilised for each surface (for a total of 8 probes).

4.6. *Data analysis:*

All obtained images and force-curves were analysed using the JPK Data Processing Software v.5.1.8 (JPK Instruments, Germany). For bacterial nanomechanics results, histograms and median (Mdn) values were obtained for each surface at the studied contact times, and significance was determined with the Mann-Whitney test ($p<0.05$). For SCFS, values for maximum adhesion force (nN) and overall adhesion work (aJ) were obtained from resulting force-curves. Unbinding peaks observed during retraction were fitted with the worm-like chain (WLC) model as previously described assuming a persistent length of 0.36nm (corresponding to the length of a single amino-acid) (Herman et al. 2014). Finally, a Poisson analysis of *S. aureus*-PC unbinding was performed employing a previously published approach, to decouple adhesion into short-range (F_{SR}) and long-range (F_{LR}) forces (Chen et al. 2011).

5. Results and discussion:

5.1. *Characterisation of bacterial adhesion onto PC surfaces*

Initial AFM characterisation of PC substrates demonstrated different topographies for the PL and SQ surfaces. SQ exhibited a distinct nanoscale pattern, with clearly defined rounded nanopits at regular intervals consistently throughout the surface, which contrasted strongly with the smooth topography observed for PL **(Figure 3.1)**. Furthermore, AFM surface cross-sections of SQ nanopits showed an average diameter of 99±6nm and a depth of ~70nm (n=20) **(Figure 3.2)**. Differences were found in R_a measurements, as SQ surfaces presented an increased value of 13.7±0.8nm compared to PL with 0.4±0.0nm. Despite these differences, no significant differences were found in surface wettability, with values for PL and SQ at 80.6±2.7° and 80.3±1.5° respectively **(Figure 3.2)**. In literature, surface contact angle values under 90° have previously been associated to hydrophilic behaviour, which has been previously shown to favour staphylococcal attachment (Boks et al. 2008). Therefore, this data suggests that both PC surfaces are slightly hydrophilic and may possibly enhance *S. aureus* adhesion.

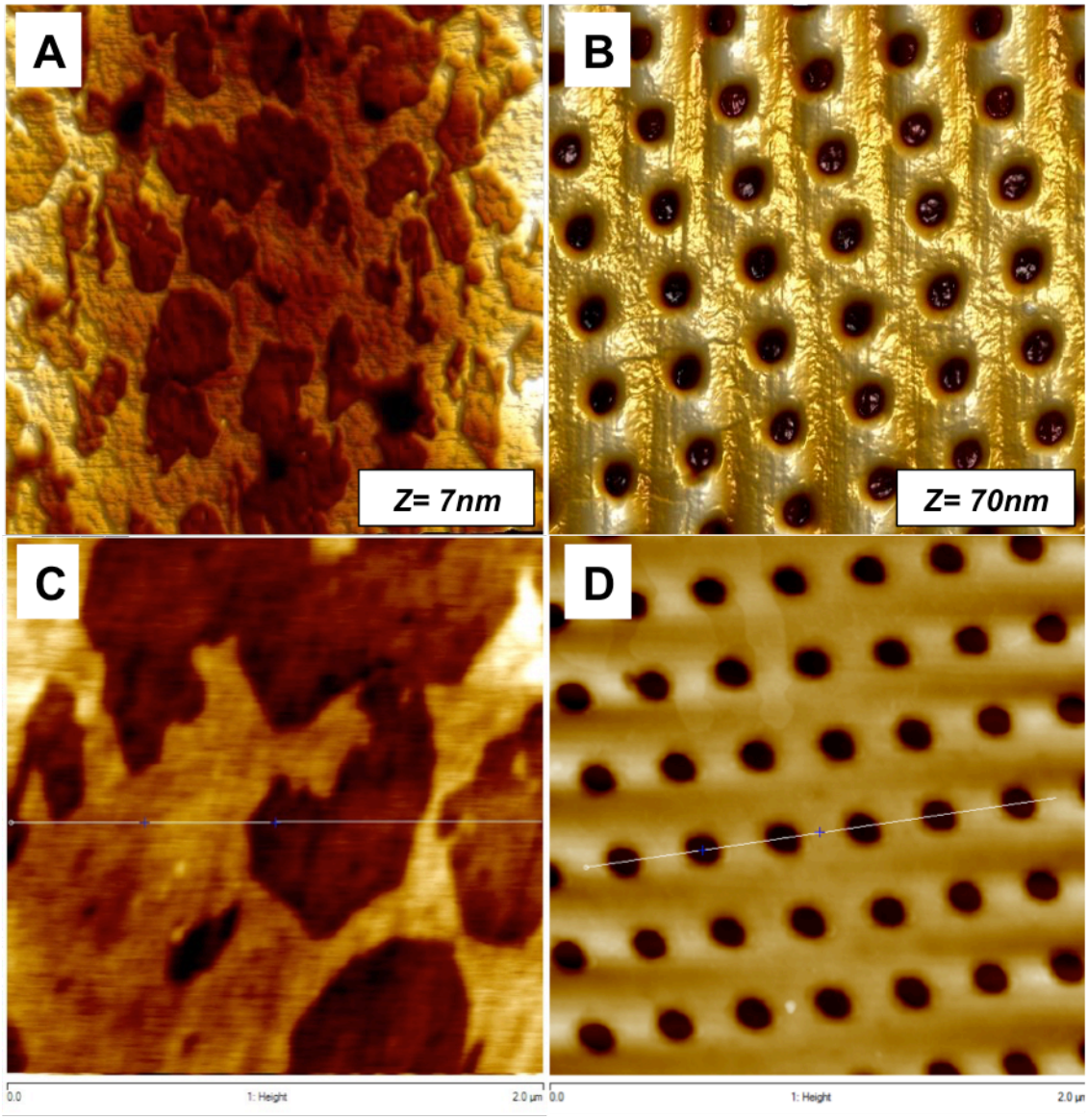

Figure 3.1: AFM imaging of planar (PL) and nanopatterned (SQ) polycarbonate (PC) surfaces. 2x2µm AFM 3D reconstruction images of (A) PL and (B) SQ demonstrate marked topographical differences between both surfaces. (C) and (D) correspond to AFM height scans for PL and SQ respectively, from which surface cross sections were obtained (observed in Figure 2).

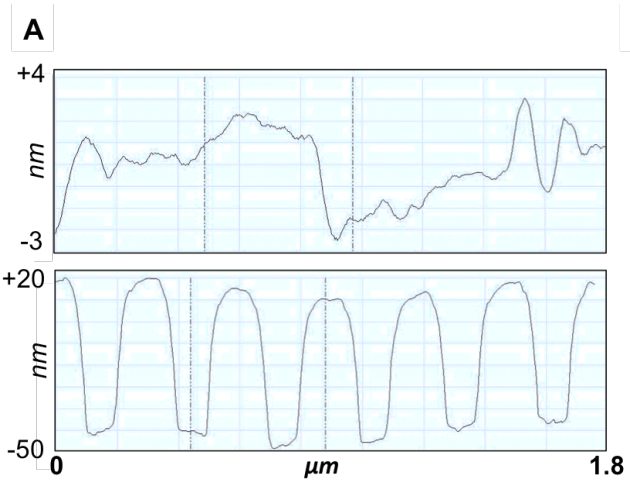

B

	R_a (nm)	C. angle (°)
PL	***0.4*** *± 0.0*	***80.6*** *± 2.7*
SQ	***13.7*** *± 0.8**	***80.3*** *± 1.5*

**p<0.05, t-test*

Figure 3.2: **Polycarbonate surface topography and chemistry characterisation**. (A) AFM surface cross-sections (corresponding to the lines drawn on Figure 1, (C) and (D)). For the SQ surface, it is possible to measure nanopit depth, diameter and spacing in the nanometre range. (B) Although surface roughness was increased in patterned (SQ) compared to planar (PL) surfaces, no significant differences were found regarding surface wettability (*p<0.05, t-test) (n=3).

AFM images of surface-bound *S. aureus* cells were successfully obtained with intermittent contact mode. Imaging suggests the presence of a microcapsule surrounding the *S. aureus* cell **(Figure 3.3A and B)**. This area appears to not only border the bacterial cell but to also cover its surface partially, consistent with previous AFM observations which employed a similar *S. aureus* strain (Tollersrud et al. 2001). Phase contrast imaging, which has been previously used to differentiate

cell from capsule in streptococcal species (Rukke et al. 2012), was used to demonstrate differences in physico-mechanical properties between the bacterial cell and adjacent structure, suggesting that this structure is different in composition than the bacterial cell wall **(Figure 3.3C).** Height images obtained with force-volume mapping in buffer are also consistent with this bacterial morphology, and although resolution is not as high as with intermittent contact imaging, the surrounding capsule-like structure can still be clearly observed in the corresponding pixel map **(Figure 3.4D)**. As force-mapping techniques mainly involve vertical movement of the AFM cantilever (in the z-axis), lateral shear forces are minimal and thus softer structures -such as the bacterial capsule- are preserved during scanning. Interestingly, previous research suggests that although *S. aureus* strain 8325-4 carries a serotype-5 capsule gene, it is defective in capsule expression (Wann et al. 1999; Kneidinger et al. 2003). However, Coldren and colleagues found very similar morphological characteristics in a serotype-8 capsule-positive *S. aureus* strain when imaged with AFM under comparable conditions (Coldren et al. 2009). TEM imaging of *S. aureus* in the previous chapter also demonstrates the presence of possible microcapsule remnants on the bacterial surface (**Figure 2.2**). Serotype-5 and serotype-8 bacterial capsules are considered to have similar characteristics (Wann et al. 1999), and therefore it is possible that the strain is effectively expressing a minimal amount of capsule-like structure.

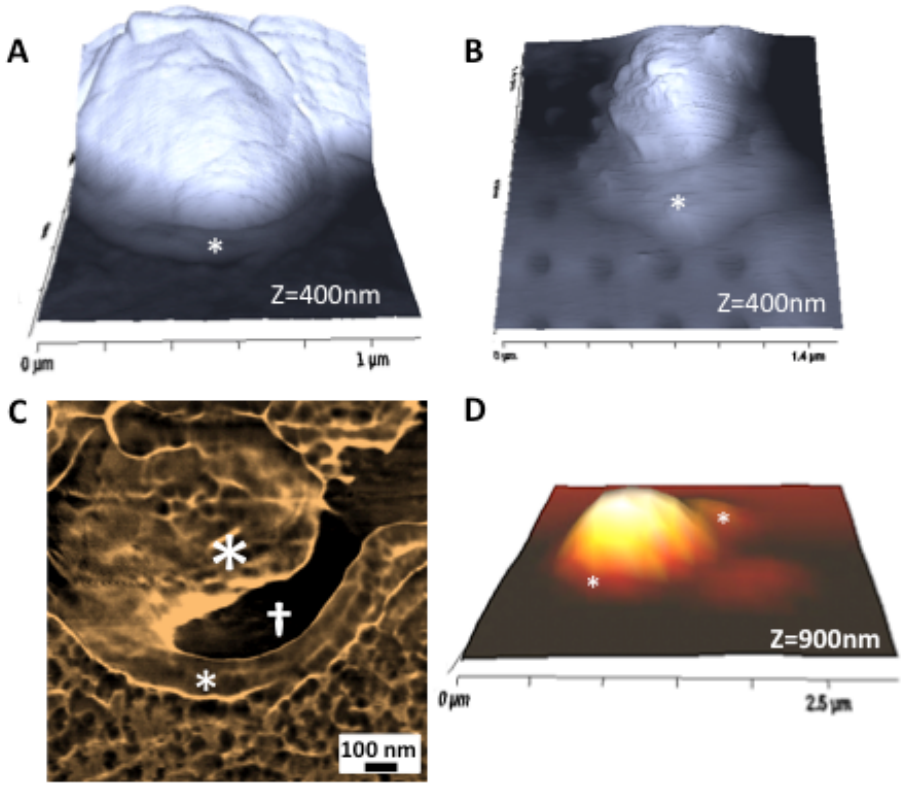

Figure 3.3: AFM intermittent contact imaging of *S. aureus* 8325-4 adhered to PL and SQ surfaces in buffer solution. 3D reconstruction images of S. *aureus* attached to (A) PL and (B) SQ surfaces. It is possible to observe the S. *aureus* cell surrounded by capsule-like structure (stars). (C) Phase-contrast image obtained for the bacterium imaged in (A), which evidences distinct structural composition for both the *S. aureus* cell (cross) and capsule (stars). (D) 3D reconstruction image obtained during a *S. aureus* force-volume map, in which both the bacterial cell and capsule-like structure (stars) can be observed.

Although careful preparation was used, it was not possible to observe the *S. aureus* microcapsule under the SEM-FIB, suggesting that it is destroyed or lost during sample preparation **(Figure 3.4)**. As SEM preparation involves a series of steps (i.e. fixation, dehydration and metal coating), it remains likely that any soft structures surrounding the bacterial cell would be removed during this process. Subsequently, upon exposing the *S. aureus*-PC interface with FIB milling, only minor contact between bacteria and surface could be observed and therefore it is believed that the bacteria-substrate interaction is mostly mediated by capsule rather than by the bacterial cell. Overall, imaging suggests that *S. aureus* capsule does not only account for a significant part of bacterial size observed in AFM imaging, but most importantly, it also increases the effective contact area between the bacterium and PC surface during surface attachment.

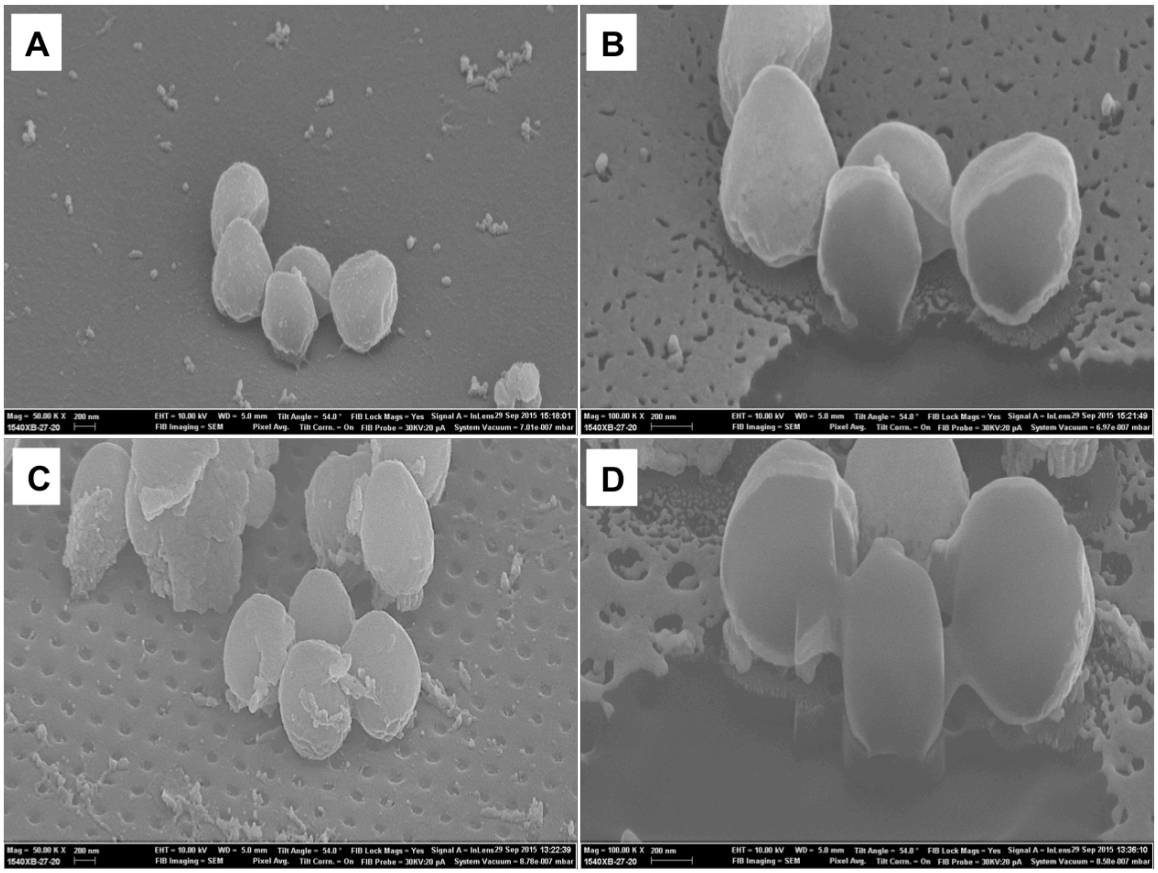

Figure 3.4: SEM-FIB imaging and milling of the *S. aureus*-PC interface. Imaging of *S. aureus* cells attached to PL (A, B) and SQ (C, D) surfaces before and after FIB milling, respectively (A and C, 50,000x; B and D, 100,000x). *S. aureus* capsule is absent suggesting it was destroyed during sample preparation; nevertheless, a minor degree of interaction can still be observed between bacterial cells and PC surfaces after FIB milling.

5.2. *Underlying substrate topography does not influence the nanomechanical properties of surface-bound S. aureus*

The elastic properties of surface-bound *S. aureus* were obtained in force-volume mode by performing nanoindentation on the bacterial surface. Two distinct

mechanical behaviours were observed for *S. aureus*, consistent with the presence of a stiffer cell body surrounded by capsule of decreased stiffness **(Figure 3.5B)**. This observation was consistent throughout measurements for *S. aureus* cells attached to both studied PC surfaces. YM for the bacterial cell was found to be 2.20MPa for PL and 4.14MPa for SQ, in the range of previously reported values for *S. aureus* 8325-4 elasticity (Chen et al. 2012). However, surrounding the central bacterium, an area with significantly reduced YM of 116.58kPa for PL and 92.89kPa for SQ was observed ($p<0.05$) **(Figure 3.5B and C)**.

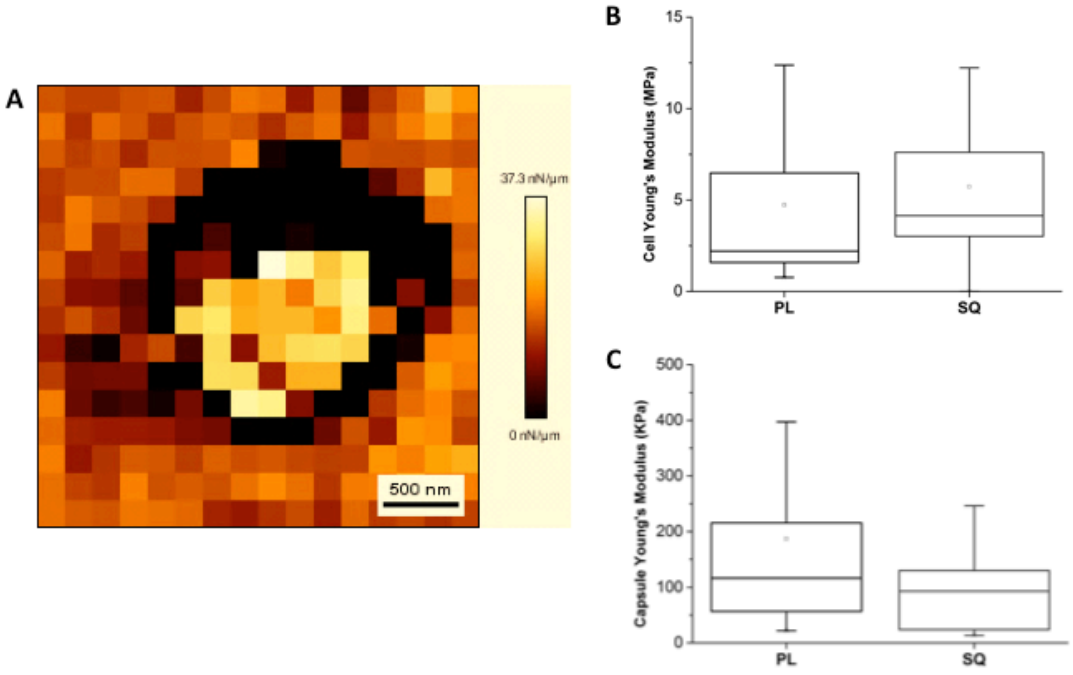

<u>Figure 3.5:</u> Nanomechanics of surface-bound *S. aureus* cells attached to PL and SQ in buffer. (A) 16x16pixel stiffness map on the surface of an immobilised *S. aureus* cell attached to a PL surface. An area of decreased stiffness can be observed surrounding the central bacterial cell (darker pixels represent softer areas of the sample). Values for Young's modulus (YM) obtained with the Hertzian model for (B)

the bacterial cell and (C) capsule-like structure are shown (n=6 independent cells, 30 force curves per cell). A marked difference is observed between the two regions, with the bacterial cell showing values in the MPa range, and surrounding area being in the kPa range. No significant differences in YM were found between PL and SQ, suggesting that surface nanotopography does not influence the mechanics of *S. aureus* cells ($p>0.05$, Mann-Whitney).

Regarding the influence of the underlying surface on of *S. aureus* nanomechanics, no significant differences were found in YM between bacteria bound to PL and SQ substrates ($p>0.05$). As AFM imaging demonstrated that a typical *S. aureus* cell directly interacts with a number of nanopits on the SQ surface, any effect that nanotopography may have on bacterial cell elasticity should be clearly noticeable at the single-cell level. However, both *S. aureus* cell and capsule nanomechanics were not affected by the presence or absence of surface nanopatterning. It is also possible that nanopatterning may only exert a localised effect on elasticity in the vicinity of the bacteria-nanopattern interface, and therefore it cannot be explored by solely indenting the top region of attached *S. aureus* cells.

5.3. *Adhesion forces between S. aureus-PC surfaces are increased by the presence of surface nanopatterning*

To study the effect of surface nanopatterning on the early colonisation of *S. aureus*, SCFS was performed with functionalised AFM bacterial probes were constructed and probed against PC surfaces at 0s and 1s contact times **(Figures 3.6 and 3.7)**. Adhesion forces and work between *S. aureus* and PL surfaces were found

to be <0.05nN and <0.05aJ at 0s surface contact times delays. However, increasing the contact time to 1s raised these values to 0.11nN and 5.01aJ respectively ($p<0.0001$). Adhesion forces between *S. aureus* and SQ surfaces was increased at both time points compared to PL, with values of 0.10nN at 0s and 0.23nN at 1s surface delay times ($p<0.0001$). A similar increase was observed for adhesion energy, with values of 4.28aJ and 18.75aJ for 0s and 1s respectively ($p<0.0001$). Altogether, these results suggest that both contact time and surface nanopatterning influence the early-adhesion of *S. aureus* to PC surfaces. In literature, the same strain of *S. aureus* 8325-4 has been employed to measure adhesion with *Candida albicans* hyphae and yeast cells, and attachment to fibronectin-functionalised AFM cantilevers (Ovchinnikova et al. 2012; Xu et al. 2008). In both these cases, adhesion forces were found to be higher than the ones observed between *S. aureus* and PC. These two studies examined specific receptor-ligand interactions between *S. aureus* and biological substrates (*Candida* and fibronectin). Therefore, it remains possible that the reduced adhesion forces observed for the unbinding of *S. aureus*-PC, irrespective of patterning, is a reflection of a lack of specificity between the bacterial cell and surface. It also remains possible that increased loading forces were employed in these studies, which has been shown to promote bacterial adhesion to substrates (Chen et al. 2014). In the present work, loading forces between *S. aureus* and PC were kept to a minimum (0.5nN) to avoid this effect (as discussed in Chapter 2).

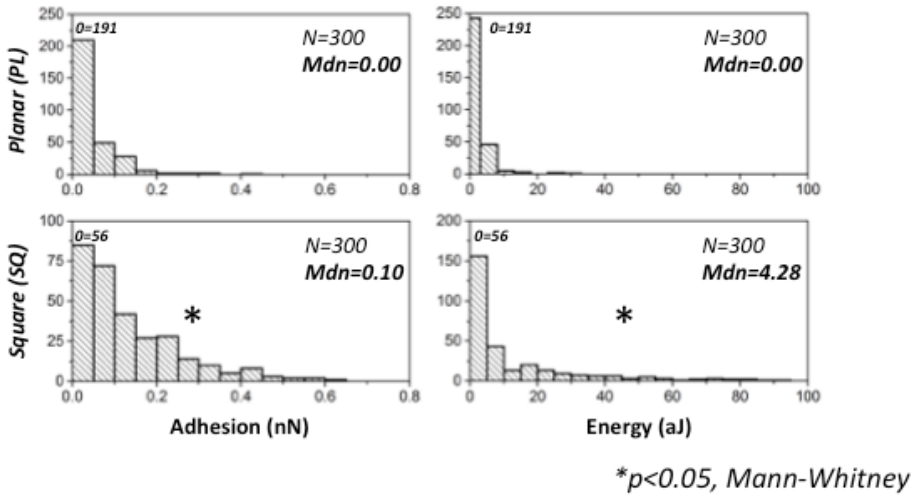

Figure 3.6: Adhesion forces and energy between living *S. aureus* and PC surfaces at short contact times. Histograms for adhesion forces and energy recorded between *S. aureus*-functionalised AFM probes and PL and SQ surfaces at 0s contact times. Both parameters were significantly increased in SQ compared to PL surfaces ($p<0.05$). The number of non-adhesive events per group is indicated in the upper left corner of each histogram (n=4 cell probes, 300 total force curves).

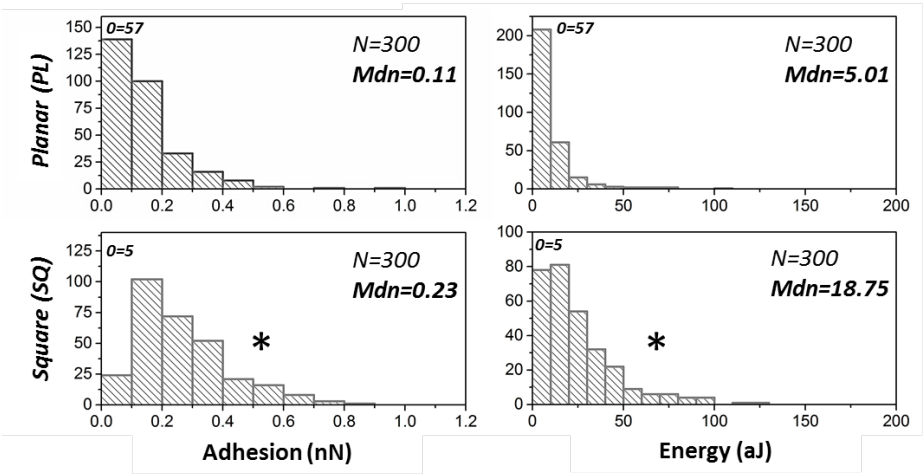

Figure 3.7: Adhesion forces and energy between living *S. aureus* and PC surfaces at increased contact times. Histograms for adhesion forces and energy recorded between *S. aureus*-functionalised AFM probes and PL and SQ surfaces at 1s contact times. Increased contact times raised adhesion forces and energy in both studied surfaces ($p<0.05$). Similar to 0s contact times, both parameters were also found to be increased in SQ compared to PL surfaces ($p<0.05$) (n=4 cell probes, 300 total force curves).

Images of representative force-curves obtained for the unbinding of *S. aureus* from PL and SQ surfaces can be found in **Figure 3.8A**. In both cases, unbinding peaks indicative of specific adhesion between the probe and surface (also known as 'saw-tooth' events) were clearly observed throughout measurements. Peaks were fitted with the WLC model, yielding contour length values predominantly in the range of 50-400nm. The number of unbinding peaks found for SQ (n=942) was slightly increased compared to PL (n=889). Interestingly, PL surfaces displayed peaks at 140nm, 270nm and 358nm; while SQ surfaces were also found to have comparable peaks at lengths of 147nm, 253nm, and 380nm, respectively **(Figure 3.8B)**. As both PC surfaces showed comparable surface chemistry, it is believed that these contour length values suggest similar bacterial surface receptors are being recruited for *S. aureus* attachment to PL and SQ.

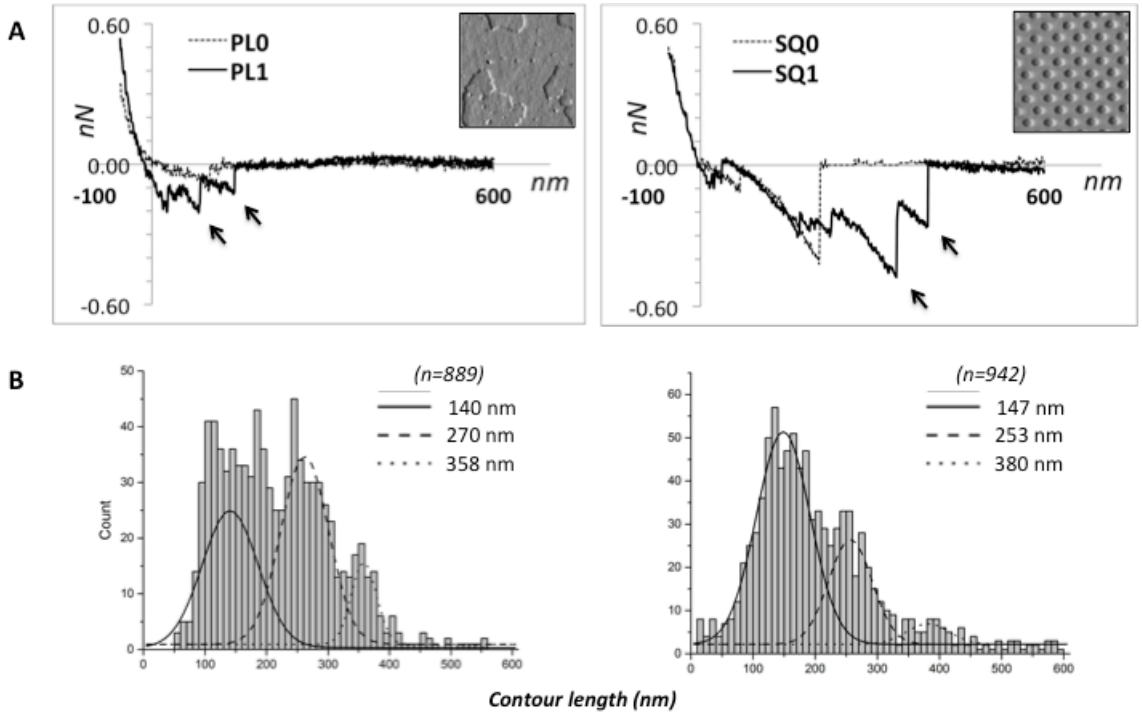

Figure 3.8: Worm-like chain (WLC) modelling of force-extension peaks observed during *S. aureus*-PC unbinding. (A) Representative retraction curves observed during between *S. aureus* probes and PL and SQ surfaces. Single unbinding events can be observed in both cases, as indicated by the arrows. Insets represent AFM deflection images of each surface (2x2µm scans). (B) WLC modelling yielded multiple peaks for contour lengths in both PL and SQ, as observed in the corresponding histograms.

As a final step, Poisson analysis of *S. aureus*-PC unbinding was carried out to decouple overall adhesion forces into short-range (F_{SR}) and long-range (F_{LR}) forces. PL surfaces were found to have a F_{SR} of -0.08±0.02nN, while SQ surfaces showed an

increased value of -1.42±0.02nN (**Table 3.1**). Interestingly, F_{LR} for PL surfaces was found to be a positive value of 0.38±0.25nN, indicating that the overall long-range forces acting between *S. aureus* and PL are repulsive in nature. Biophysically, increased F_{SR} between *S. aureus*-SQ surfaces paired with a repulsive F_{LR} in *S. aureus*-PL may help explain the reduced adhesion force and work observed in the latter case.

Table 3.1: Poisson analysis of *S. aureus* unbinding from PL and SQ surfaces

Surface	**Specific (F_{SR})**		**Non-specific (F_{LR})**	
	Mean (nN)	*SE*	*Mean (nN)*	*SE*
PL	**-0.08**	***0.02***	**0.38**	*0.25*
SQ	**-1.42**	***0.02***	**-0.23**	*0.01*

Overall, the use of SCFS was an effective approach to study the early-colonisation of *S. aureus* onto PC surfaces. Early bacterial colonisers are believed to come into contact with the biomaterial surface with minimal to no external loading force. High loading forces would therefore not effectively recreate the physiological process of bacterial adhesion, as they would be promoting the interaction between bacteria and surface. Therefore, in this PC-based model of biomaterial nanopatterning, loading forces for *S. aureus* probes were reduced (0.5nN) to avoid deformation of the bacterial cell during probing **(Figure 2.10)**. By utilising this 'zero-force contact'

approach, it is believed that the influence of AFM probing on adhesion values can be kept to a minimum. This correlation between loading force and adhesion was recently demonstrated by Chen et al, who found that the attachment of *S. aureus* strain 8325-4 to a glass surface was proportional to the loading force applied (Chen et al. 2014).

Amongst other functions, the bacterial capsule has been considered to play an active role in bacterial attachment to biomaterial surfaces (An & Friedman 1998; Baselga et al. 1994). Considering the early contact times utilised in this study (0 and 1s), it is believed that adhesion between *S. aureus* 8325-4 and PL and SQ surfaces at these time points is mainly mediated by the interaction between the microcapsule and substrate. In the past, surfaces with nanoscale topographies have been found to possess improved antibacterial properties against *S. aureus*, when bacteria are cultured for <1hr and macro-scale bacterial attachment assays such as fluorescence microscopy and spread plate methods were employed (Jahed et al. 2014; Huo et al. 2013; Puckett et al. 2010; Anselme et al. 2010). However, these results suggest that nanopatterning increases the colonisation of biomaterial surfaces at early contact times (0 and 1s). Although bacterial adhesion to surfaces is a crucial initial phase (Whitehead et al. 2005), it does not account on its own for the entire process of biomaterial colonisation (Anselme et al. 2010). It remains possible that although attachment of *S. aureus* to nanopatterned surfaces is initially increased at very short time points, bacteria may not be able to effectively colonise the surface due to reduced proliferation capabilities or decreased capsule secretion at later contact times. Therefore, it remains possible that even if bacteria favour early-attachment

onto nanopatterned surfaces, these substrates counteract biofilm formation in the long term. Furthermore, although contact times of ≤1s may be short in relation to the lifetime of a biomaterial infection process, early-colonising bacteria could potentially become a 'base-layer' for the attachment of secondary bacteria at increased time points (Otto 2013). Future efforts should focus on further understanding the in-vivo relevance of early biomaterial colonisation by *S. aureus*, and if promoting or inhibiting this initial bacterium-surface interaction can aid in the search for novel ways to control biofilm formation without compromising the increased biological properties of nanopatterned surfaces.

6. Summary:

Throughout this chapter, the effect of biomaterial nanoscale patterning on bacterial nanomechanics has been discussed. In summary:

- Nanoindentation and SCFS were found to be powerful tools to study the nanomechanics of living *S. aureus* cells in buffer conditions.
- Imaging of surface bound *S. aureus* suggested the presence of a microcapsule surrounding the central bacterial cell. AFM nanomechanics demonstrated both areas to have distinct elastic properties; however, no differences in bacterial elasticity were observed between cells attached to PL or SQ surfaces.
- SCFS with *S. aureus* functionalised probes demonstrated increased adhesion force and energy between bacteria and SQ surfaces, compared to PL surfaces. WLC modelling predicted the length of receptors involved to be in the range of 50-400nm. Poisson analysis suggests that this is due to higher short-range forces between *S. aureus*-SQ and repulsive long-range forces between *S. aureus*-PL.
- Overall, surface nanotopography was found to influence *S. aureus* attachment to PC surfaces at early time points (0 and 1s), and further research is necessary to evaluate is this effect is observable at increased contact times.

CHAPTER 4

Nanoscale adhesion of *Staphylococcus aureus* and *Streptococcus sanguinis* to titanium implant surfaces

---

1. Introduction:

After studying the effect of surface roughness on bacterial adhesion, in this chapter we will characterise the adhesion of *S. sanguinis* and *S. aureus* to dental implant surfaces at the single-cell level, to explore the influence of strain-specific differences in early-adhesion to biomaterial surfaces.

In dentistry, it is widely accepted that the placement of dental implants is an efficacious treatment considering the high survival rates shown in clinical trials over the years (Setzer & Kim 2013). The introduction of osseointegrated implants was a major breakthrough for dentistry, and ever since, it has provided clinicians with predictable long-term outcome treatments for the replacement of single/multiple missing teeth (Esposito et al. 1998). Despite the fact that titanium (Ti) implants are regarded as gold standard, surface infection remains a frequent complication that increases failure rates and patient morbidity (Zhao et al. 2014). CHX is one of the most widely used agents for the non-surgical treatment of infected dental implant surfaces (Valderrama et al. 2014); however, little is known about the effect this substance has on the early adhesion of oral streptococci and staphylococci, or how this substance can affect the attachment of bacteria at later stages.

Oral biofilm formation on hard surfaces comprises a series of stages, starting with the initial adhesion of early colonising species (Hojo et al. 2009) and continued by the attachment of secondary and increasingly pathogenic bacteria that can lead to disease (Renvert et al. 2008). In this context, *S. sanguinis* has been consistently reported as an initial coloniser in the process of oral biofilm and titanium implant colonisation (Rodríguez-Hernández et al. 2011). Attachment of *S. sanguinis* to substrates is mostly mediated by adhesins present on the bacterial cell wall surface (Yamaguchi et al. 2006), with some studies even describing the existence of bacterial appendages such as pili as contributing factors in adhesion (Okahashi et al. 2010). Another important coloniser is *S. aureus*, a well-known Gram-positive pathogen involved in a vast number of human infections (Roberts et al. 2006). The presence of microbial surface components recognising adhesive matrix molecules, MSCRAMMs, on the membrane of *S. aureus* is a key factor for recognition and adhesion to surfaces (Buck et al. 2010). It has been shown that *S. aureus* has an increased affinity to Ti substrates, being found consistently adhered to the surface of implants (Izquierdo-Barba et al. 2015). Interestingly, *S. aureus* is frequently isolated from failing dental implant sites and associated to poor clinical outcomes (Lee & Wang 2010). Although bacterial adhesion to implant surfaces has been studied with traditional techniques (i.e. electron and fluorescence microscopy), there currently remains limited literature regarding the use of AFM to study the adhesion of bacteria onto Ti implant surfaces.

This work has been published as **"Nanoadhesion of *Staphylococcus aureus* onto titanium implant surfaces." Journal of Dental Research, 94.8 (2015):**

1078-1084; and **"Probing the nanoadhesion of *Streptococcus sanguinis* to titanium implant surfaces by atomic force microscopy." International Journal of Nanomedicine, 11 (2016): 1443.**

2. Aim

The aim of this research was to utilise SCFS to characterise the adhesion between *S. sanguinis* and *S. aureus* and Ti implant surfaces, and suggest an approach for evaluating the adhesion of bacteria to implant surfaces in the presence and absence of antibacterial agents.

3. Objectives

- Characterise the topography and surface chemistry of Ti implant surfaces
- Evaluate the adhesion forces between *S. aureus* and *S. sanguinis* and Ti surfaces at the nanoscale, and analyse the biophysics of the bacteria-substrate interaction
- Predict the molecular length of bacterial receptors involved in the attachment to Ti implant surfaces, by employing the worm-like chain (WLC) model
- Evaluate the effect of chlorhexidine (CHX) on the early-stage adhesion of bacteria to Ti surfaces

4. Materials and Methods:

4.1. *Titanium substrates*

For this study, sterile 15mm-diameter Ti discs provided by Straumann (Basel, Switzerland) were employed, as they are analogous to implants utilised in the clinical setting. Two distinct surfaces were characterised: a 'smooth' machined and a sandblasted/acid-etched 'SLA' surface. To evaluate surface morphology of Ti discs, a Philips XL30 FEG-SEM scanning electron microscope was employed with an acceleration voltage of 5kV, and AFM characterisation (NanoWizard, JPK Instruments, Germany) was performed in contact mode employing NP-S10 probes (Bruker, Santa Barbara, USA) with a spring constant of 0.3N/m at a scanning rate of 1.0Hz. Surface roughness values (R_a) were obtained by conventional profilometry (Scantron, Proscan 1000, UK), with 10x10μm size scans on three independent samples. Surface wettability was calculated by employing an optical contact angle meter with a deionised water droplet (KSV Instruments, CAM 200, USA). All measurements were performed on three discs per sample group

4.2. *Bacterial cultures*

Cultures of *Straphylococcus aureus* (8325-4) were grown in TSB broth (Oxoid Ltd, UK) for 16hr at 37°C and aeration, while *Streptococcus sanguinis* (ATCC-10556) cells were obtained by growth in BHI broth (Oxoid Ltd, UK) for 16hr at 37°C and aeration. Previous to AFM experiments, a 20-fold dilution of bacterial cells was obtained by centrifugation for 1min at 5000rpm (Eppendorf 5417R, UK), washed three times and resuspended in TRIS-buffer pH7.4 (Sigma-Aldrich, UK). Finally, a

50µl aliquot of resulting bacterial dilution was transferred to a sterile glass slide for cell probe preparation.

4.3. *Functionalisation of AFM cell probes*

Construction of functionalised colloidal probes was performed by attaching ~10µm diameter glass microspheres (Whitehouse Scientific, UK) to NP-O10 tip-less cantilevers (Bruker, Santa Barbara, USA) by employing a thin layer of UV-curable glue (Loctite, UK). Optical microscope and SEM confirmed adequate attachment of a single microsphere on each cantilever. Thermal calibration yielded spring constant values of ~0.3N/m. Subsequently, colloidal probes were coated with a poly-DOPA solution for 1hr, rinsed and dried under N_2. Probes were then placed into contact with isolated bacterial cells for ~3min until attachment was observed, and subsequently positioned over the titanium substrate for force measurements. All constructed cell probes were utilised immediately for force-spectroscopy experiments. A minimum of three independent probes per cell was utilised for analysis.

4.4. *SCFS force-measurements*

SCFS of *S. sanguinis* was performed with a NanoWizard AFM system (JPK Instruments, Germany) mounted on an Olympus IX71 (Olympus, Japan) inverted microscope. All SCFS measurements were carried out in TRIS-buffer at room temperature immediately after cell probe construction. To minimise the influence of surface topography, multiple force curves were recorded for each cell probe at representative areas of the sample. Measurements were performed with reduced

surface delays of 0 and 1s and an increased surface delay of 60s, with a loading force of 500pN and a constant speed rate of 2.0μm/sec. Optimal loading force was determined by applying increasing loading forces to immobilised *S. aureus* cells with a MSNL-10 cantilever until indentation was observed. Control force-curves for both glass microspheres and DOPA were also obtained. A minimum of three probes from independent bacterial cultures were employed. As a model to evaluate the effect of a commonplace implant disinfection solution, a 2mg/ml concentration of chlorhexidine (CHX) (Sigma, UK) in TRIS buffer was added to the system, immersing the probe for 5min before force-curves were recorded at 60s surface delays.

4.5. *Data extraction and statistical analysis*

Maximum adhesion force and adhesion work values were collected from resulting force-curves (Francius et al., 2009) and processed with the JPK Data Analysis software v4.2.61 (JPK Instruments, Germany). Results were expressed as mean±SE, and further analysed with the Kruskall-Wallis test for non-parametric variables considering significance at p <0.05. Data from increased dwelling times (60s) was modelled according to the worm-like chain (WLC) model previously described (Storm & Nelson 2003) to yield predicted contour length values for individual peaks. Five independent probes were employed for WLC modelling. Persistence length, l_p, was assumed to be 0.36nm (approximate length of a single amino-acid), thus obtaining values for molecular contour length (L). Decoupling of bacterial adhesion forces was obtained by Poisson analysis by employing a previously reported approach (Chen et al. 2011) yielding both short-range (F_{SR}) and long-range-force (F_{LR}) components for bacterial adhesion.

5. Results and discussion:

5.1. *Characterisation of Ti substrates*

Initial topography characterisation of smooth and SLA discs was obtained with SEM imaging. SEM imaging proved to be a valuable technique for assessing the surface topography of both titanium substrates, and confirmed the increased surface roughness of SLA compared to smooth Ti **(Figure 4.1)**. Interestingly, at the micro and nanoscale levels, smooth Ti surfaces display grooves and ridges consistent with the machining process. The average surface roughness for smooth and SLA and Ti surfaces was 0.61 and 1.70μm respectively, which are comparable to previous reports in the literature for implant surfaces (Sykaras et al. 2000). Furthermore, contact angle measurements demonstrated the highly hydrophobic nature of SLA (149.9 ± 3°) when compared to smooth Ti (67.0 ± 5°) **(Figure 4.2)**.

Regarding AFM, high-resolution imaging was only possible on smooth Ti samples, as the high surface roughness of SLA titanium did not allow for correct scanning of the surface. Although some AFM images were obtained for SLA **(Figure 4.1E and F)**, they do not represent the true topography of the surface and only correspond to the highest areas present in the substrate. It is well known that AFM techniques are limited to samples with decreased surface roughness, thus the imaging of SLA surfaces (20-40μm micropits) is not possible (Zhao et al. 2005). The two main issues found regarding the SLA surface were a) the difficulty of the AFM tip to come into contact with the surface, due to the presence of large 'peaks' and 'valleys' on the substrate, and b) the incapacity of scanning the sample when contact

was obtained due to large z-range offsets. After a large number of efforts to correctly approach the SLA surface, only a couple attempts yielded contact between the AFM tip and substrate. Therefore, as force-spectroscopy techniques require contact between the bacteria-coated AFM probe and surface, SLA surfaces were not employed for SCFS experiments with *S. aureus* and *S. sanguinis*.

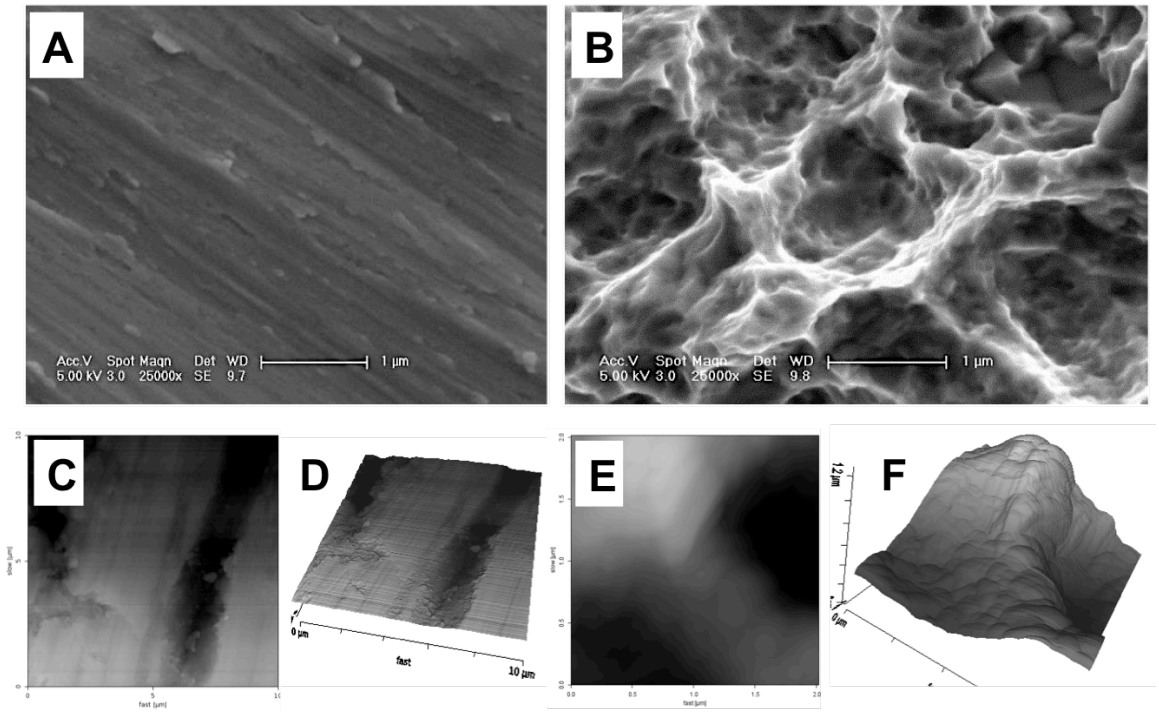

<u>Figure 4.1</u>: Topography characterisation of smooth and SLA Ti surfaces with SEM and AFM. SEM images of (A) smooth and (B) SLA discs, which demonstrate the distinct surface topography obtained by sandblasting and acid etching the Ti substrate. (C) Height and (D) 3D reconstruction AFM images of smooth Ti (10x10µm, z=580nm). (E) Height and (F) 3D reconstruction AFM images of SLA Ti

(2x2µm, z=1.4µm). It was not possible to obtain larger scan areas for SLA due to increased surface roughness.

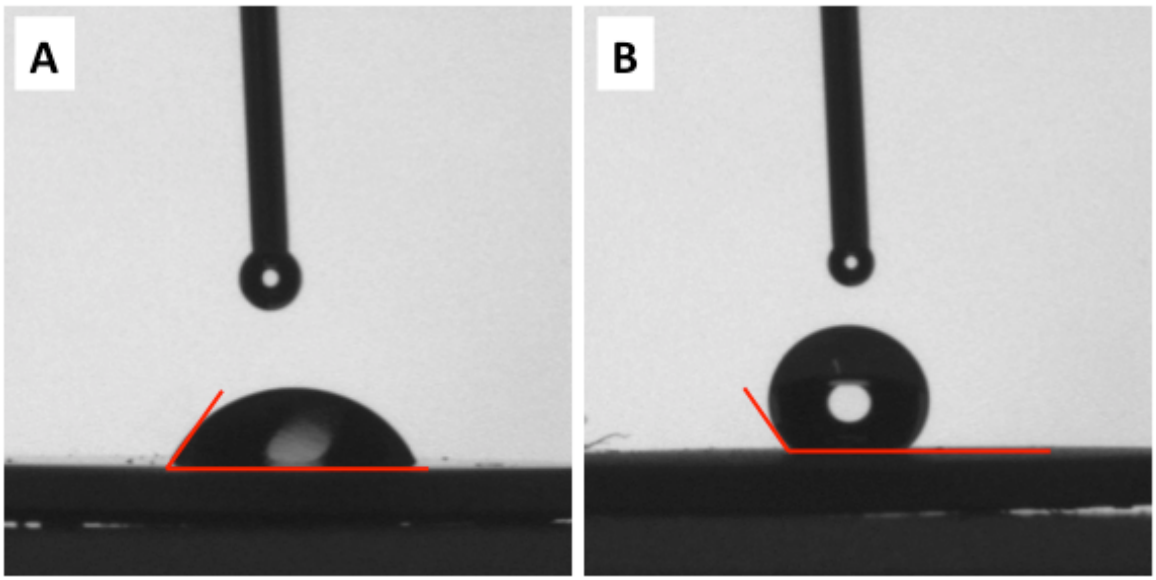

Figure 4.2: Surface chemistry measurements of smooth and SLA titanium discs. dH_2O droplets on (A) smooth and (B) SLA titanium (Ti) discs. Average contact angle for smooth Ti was 67.0 ± 5°, while values for SLA were 149.9 ± 3° demonstrating increased hydrophobicity compared to the smooth surface (n=3).

5.2. *Deciphering the bacteria-Ti nanoadhesive interaction*

5.2.1. Adhesion between S. aureus and smooth Ti

Mean adhesion forces and adhesion work values measured between *S. aureus* and smooth Ti are presented in **Figure 4.3.** Maximum adhesion forces for *S. aureus* were found to increase from 0s to 60s surface delays (-0.27±0.30nN and -9.15±0.78nN, respectively), with similar results observed for total adhesion work (7.39±2.38 and 988.06±117.08aJ, respectively). Utilising similar approaches, Mei et al observed similar effects for nine different strains of oral Gram-positive bacteria when

increasing surface delays from 0 to 120s (Mei et al. 2009). Furthermore, retraction curve patterns and force values at 1s surface delays (-1.48±0.08 nN) are consistent with previous reports in literature for *S. aureus* and other Gram-positive strains (Herman et al. 2013). We found, however, that reduced surface delays (0s and 1s) showed no significant difference in adhesion forces between poly-DOPA-coated probes and bacterial probes. Despite similar adhesion force values, there were major differences in force curve architecture, demonstrating that indeed *S. aureus* probes presented specific adhesive events during unbinding **(Figure 4.3A).** These observations highlight the importance of not relying only on the adhesion force parameter study attachment, as this value alone may lead to confusion and erroneous conclusions when comparing different conditions.

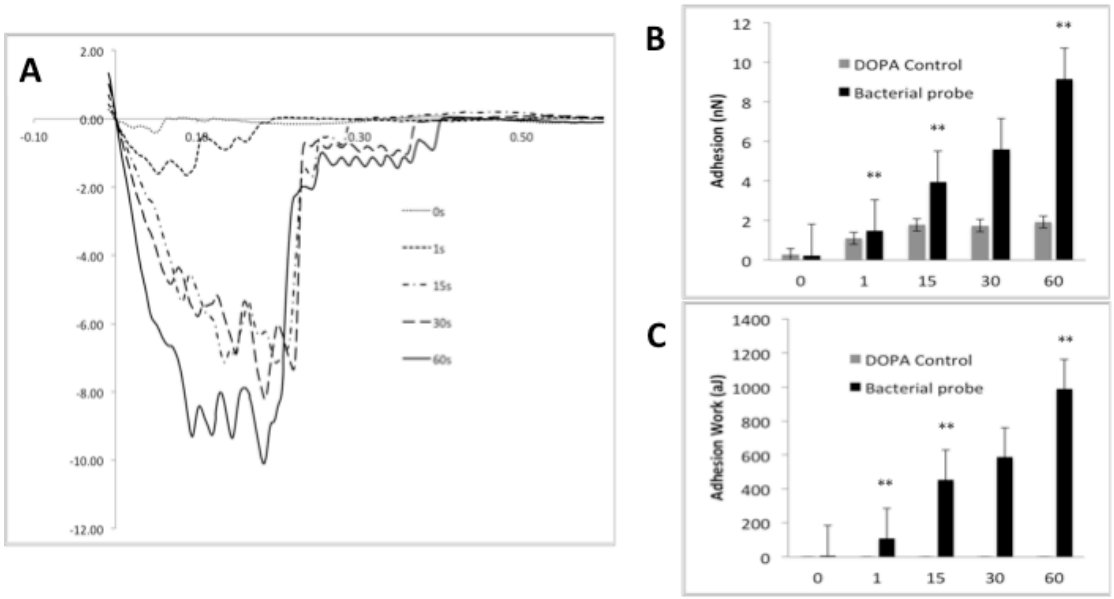

Figure 4.3: Adhesion between *Staphylococcus aureus* and smooth Ti surfaces observed by AFM force-spectroscopy. (A) Representative force-curves at increasing surface delays of 0, 1, 15, 30 and 60s. X-axis values represent distance in µm, and Y-axis

represents force in nN. (B) Mean adhesion forces and (C) adhesion work are shown for *S. aureus* probes observed at all studied surface delays. Data represents three bacterial probes obtained in three independent experiments. Note that adhesion increases for bacterial probes as a function of contact time (*** p<0.05, Kruskall-Wallis*) (n=3 cell probes).

Force curves obtained at increased contact times (>1s) showed characteristic unbinding patterns described previously in literature as 'jumps' which describe the unbinding of single adhesive units on the surface of the cell (Taubenberger et al. 2014) (**Figure 4.3A**). These single-unbinding events were observed towards the right of the major adhesion peak at Z distances usually over >150nm. At increased surface contact, two main variations of unbinding patterns were found repeated throughout SCFS measurements. For about 50% of resulting force curves, ~5-8 consecutive detachment peaks were observed at regular intervals, whereas in remaining force curves unbinding events seemed to follow a more irregular pattern (**Figure 4.4A**). Regardless, no significant differences in rupture force or predicted contour length values were found between the two scenarios, and therefore it is believed that these differences reflect the dynamic nature of the interaction of *S. aureus* with Ti surfaces.

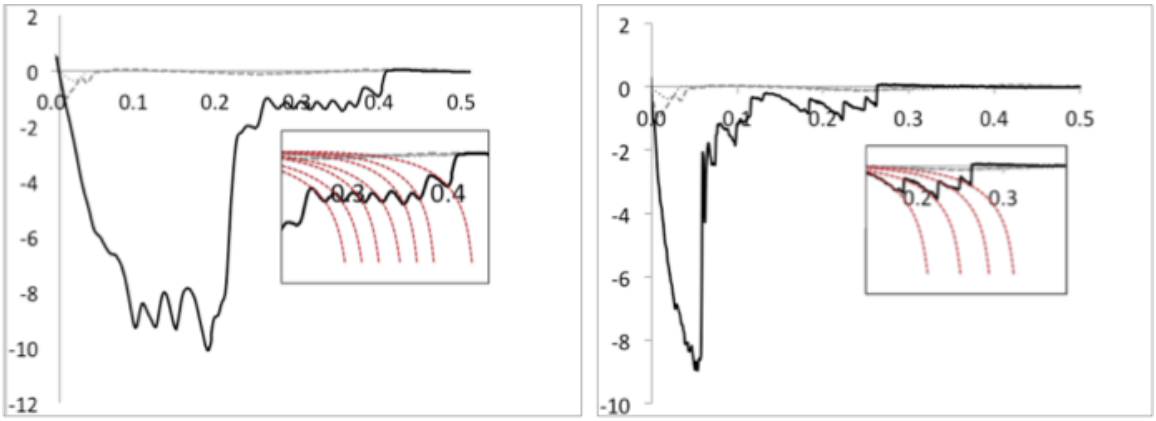

<u>Figure 4.4:</u> Force-curve architecture for the unbinding of *S. aureus* from smooth Ti surfaces. Two main unbinding patterns were observed throughout experiments; however, no significant differences were observed in contour length predictions. Insets correspond to diagrammatic representations demonstrating how WLC modelling was performed. X-axis values represent distance in μm, and Y-axis represents force in nN.

Unbinding-events were observed in 8-10% of force-curves at 1s contact time; however, surface delays of 60s increased this occurrence to 91%, which is consistent with time-dependent binding mediated by surface proteins. Similarly to our approach, Yongsunthon and Lower observed 'sawtooth-like' unbinding events in 2-3% of recorded force-curves between *S. aureus* and silica and polystyrene beads in buffer at ~1s surface delays, which they attributed to protein-mediated binding (Yongsunthon & Lower 2006). Average rupture force for single-unbinding events between cell probes and Ti surfaces at 60s contact time was found to be -0.95±0.04nN, which is similar to previous reports in literature. Liu et al. reported rupture values of ~-1nN between *Staphylococus epidermidis* probes and a coated

fibrinogen (Fg) substrate (Liu et al. 2008), and Boks et al. found average rupture values for four staphylococcal strains probed against a glass substrate at ~-1.05nN (Boks et al. 2008).

5.2.2. Adhesion between *S. sanguinis* and smooth Ti

As in the case of *S. aureus*, functionalisation of colloidal probes with *S. sanguinis* was possible with the use of poly-DOPA as an immobilisation agent, similar to what has been previously reported for different strains of bacteria and yeast cells (Dufrene 2015). It is important to consider however, that as *S. sanguinis* is usually found in chain conformation, it is very difficult to immobilise a unique bacterium onto the microsphere **(Figure 2.9B)**. Nevertheless, this did not seem to affect SCFS measurements as all cell probes presented similar unbinding behaviour that allowed for successful comparison and statistical analysis. As the colloidal geometry of the microsphere only allows a reduced area of contact to occur with the Ti surface, the probed adhesive interactions are limited only to a single or reduced number of bacterial cells and therefore similar behaviour was observed for all probes. *S. sanguinis* probes remained viable for about 1 hour during measurements, as observed by Live/Dead fluorescence staining. Experiments for each probe were carried out well under this time limit, and for this reason a reduced number of increased surface delay force-curves (60s) were obtained compared to shorter contact times (0s and 1s). As minimal differences were found between contact times of 15, 30 and 60s in *S. aureus* **(Figure 4.3A)**; *S. sanguinis* were only probed against the Ti surface at contact times of 0, 1 and 60s for comparison.

As observed in **Figure 4.5**, increasing contact time between the *S. sanguinis* probe and Ti surface generated important changes in the architecture of resulting force- curves. Force-curves obtained at 60s showed increased parameters for maximum adhesion, number of minor-unbinding events and rupture lengths compared to shorter contact times. Adhesion forces for the *S. sanguinis* probe were found to be 0.32±0.00nN, 1.07±0.06nN and 4.85±0.56nN for 0s, 1s and 60s contact times respectively. However, similarly to what was observed for *S. aureus*, only 60s contact times demonstrated a significant difference in maximum adhesion forces when compared to the poly-DOPA control probe ($p<0.05$). Adhesion work, represented by the integrated area under the retraction curve, was found to be 19.28±2.38aJ, 104.60±7.02aJ and 1317.26±197.69aJ for 0s, 1s and 60s respectively.

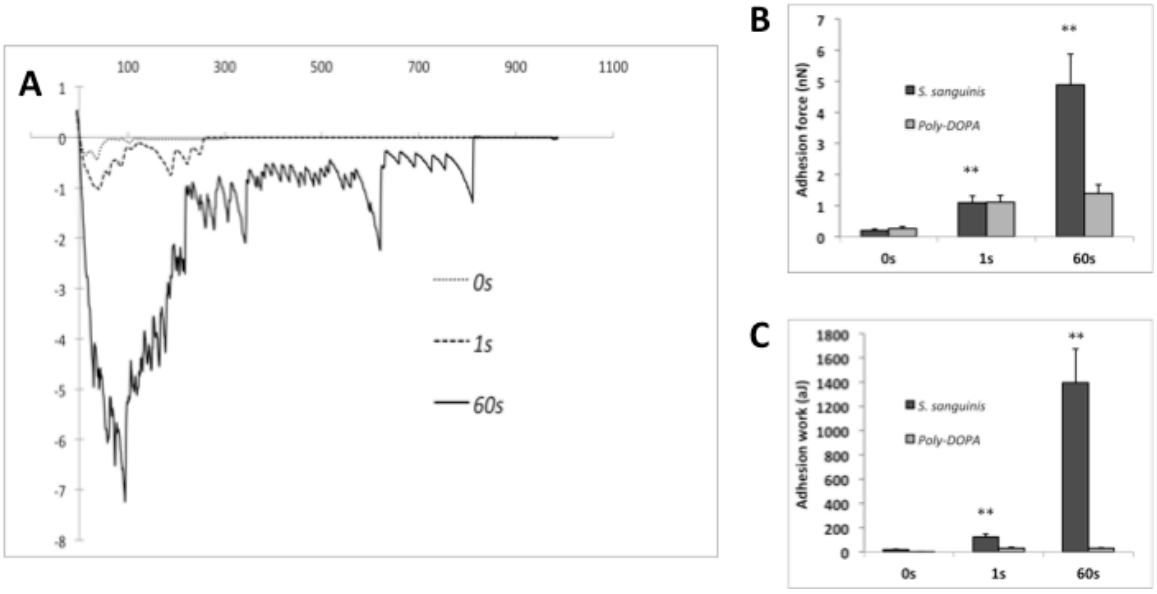

Figure 4.5: *S. sanguinis*-Ti adhesive interactions probed by atomic force microscopy. (A) Representative force-curves for the unbinding of *S. sanguinis*

bacterial probes after 0s, 1s and 60s surface contact times. (B) Adhesion force and (C) adhesion work for bacterial probes and the poly-DOPA coated probes (controls) at each time point for both studied parameters (n=3 independent probes) *(*p<0.05, Kruskal-Wallis).*

For both studied parameters, higher contact times resulted in increased values compared to decreased surface delays. As cells are compliant in nature, it is believed that longer contact times allow the bacterium to effectively adapt to the geometry and topography of the substrate, generating an increased contact area that allows a higher number of specific interactions to occur between bacteria and Ti surface. Similar results have been previously observed for other streptococcal strains (Mei et al. 2011; Mei et al. 2009). Additionally, these results further demonstrate that bacteria such as *S. aureus* and *S. sanguinis* can attach directly onto titanium surfaces without the existence of a previously formed biological pellicle. This observation is in line with a recent study by Lorenzetti et al which also observed direct adhesion of Escherichia coli onto non-treated and treated titanium surfaces (Lorenzetti et al. 2015).

5.3. *WLC modelling as a tool for predicting the length of bacterial surface adhesins*

Furthermore, it was possible to model the single-unbinding events observed for both *S. aureus* and *S. sanguinis*, according to the worm-like chain (WLC) model. In the case of *S. aureus*, molecular contour-length predictions where clustered around three peaks of 148, 334 and 624nm (**Figure 4.6A**). The contour length given by the

WLC model is representative of the total length of a completely unfolded molecule or protein (Chan et al. 2010). Interestingly, these predicted lengths are in the range of several important *S. aureus* surface-anchored adhesins that have been extensively described in literature (O'Neill et al. 2008). By considering the length of a single amino acid to be ~0.36nm (Herman et al. 2014) we can obtain the contour length for important *S. aureus* adhesins such as *protein A* (~183nm) (Uhlen et al. 1984), clumping factor *ClfA* (~336nm) (Hartford et al. 1997), fibrinogen-binding proteins *FnBPA* and *FnBPB* (~366nm) (Keane et al. 2007) and *cna* (~426nm) (Patti et al. 1992). Interestingly, FnBPA has been shown to express strongly in *S. aureus* 8325-4, the strain of choice in the present study. Although WLC modelling is not regularly applied to bacterial unbinding in literature, many studies do report the maximum rupture length between the cell probe and substrate, with values of 50-600nm for adhesin-Fg complexes (Herman et al. 2014), >200nm for bacterial pairs (Younes et al. 2012), and 400-600nm between oral streptococci and stainless steel surfaces (Mei et al. 2009). Therefore, it is believed that contour lengths obtained with the WLC model, with most values in the 150-400nm range, are a result of receptor-surface interactions between living *S. aureus* cells and Ti substrates.

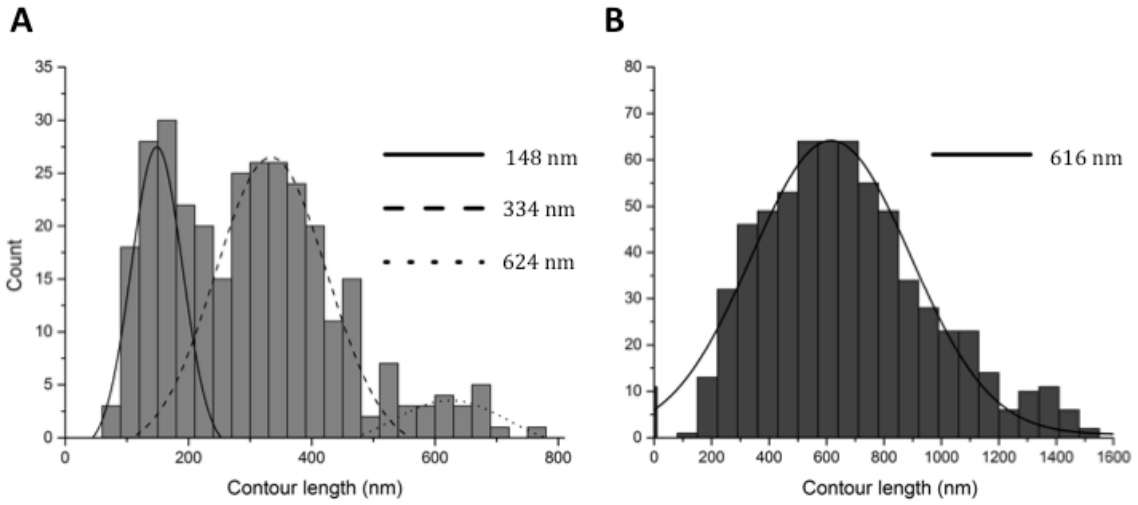

Figure 4.6: Worm-like chain (WLC) modelling of single-rupture events observed between *Staphylococcus aureus* and *Streptococcus sanguinis* and smooth Ti surfaces. (A) Distribution of predicted contour lengths for *S. aureus*, which were clustered around three peaks at 148, 334 and 624nm (n=5 independent cell probes, 319 unbinding peaks). (B) Distribution of predicted contour lengths for *S. sanguinis*, which predominantly clustered at a single peak of 616nm (n=3 independent cell probes, 661 unbinding peaks). For both cases, persistence length was considered to be 0.36nm.

Interestingly, the average contour length predicted for *S. sanguinis* corresponds to 616 (n=661 unbinding events across three independent probes), which is higher than the contour lengths predicted for *Staphylococcus aureus* **(Figure 4.6B)**. Not many reports are available in the literature regarding SCFS experiments with *S. sanguinis*, and thus it remains difficult to compare these

findings with others. There are, however, some studies that have examined the adhesion of other streptococcal strains to surfaces that allow for some discussion. Sullan et al (Sullan et al. 2015) observed that the unbinding of *S. mutans* from surfaces coated in salivary agglutinin (SAG), fibronectin and collagen had rupture lengths up to ~6000nm, ~2000nm and ~5000nm, respectively. These values are increased compared to the ones observed between *S. sanguinis* and Ti surfaces, which could be explained by the presence of extensible biomolecule coatings that increase the retraction distance before rupture of the bacteria-biomolecule bond. In contrast, as the smooth Ti substrates employed are non-coated, it is believed that the values reported for the unbinding of *S. sanguinis* are predominantly the result of the unfolding of cell wall proteins, without any participation of the surface. In another study, Francius et al. found the unbinding length between *S. thermophilus* and an abiotic surface to be up to 800nm, which is comparable to the values reported in the present work (Francius et al. 2013).

5.4. *Poisson analysis of unbinding events to decouple adhesion forces*

Additionally, Poisson analysis of adhesion forces was used to divide minor adhesion peaks into F_{SR} and F_{LR} components as described previously in literature (Chen et al. 2011). By plotting a linear regression between mean adhesion force (nN) and variance (nN^2) of the minor unbinding peaks observed between independent bacterial probes and substrate, it was possible to determine values for F_{SR} and FLR **(Figure 4.7)**. In the case of *S. aureus*, five-independent probes were utilised, yielding F_{SR} values of -0.75±0.04nN and F_{LR} of -0.58±0.15nN **(Table 4.1)**.

Both short and long-range-forces we found to be attractive in nature, which may help explain the affinity observed between *S. aureus* and Ti surfaces in previous studies. Similar values were reviewed by Chen et al. for several Gram-positive strains (Chen et al. 2011), and Boks et al. reported average values of -0.7nN contribution for short-range interactions between *S. epidermidis* and glass surfaces (Boks et al. 2008). F_{SR} can be considered to reflect the value of hydrogen bonding between the bacterial cell and surface. Ti surfaces employed in this study were slightly hydrophilic in nature, with R_a and contact angle values of 0.61μm and 67.0±5°, respectively, which correspond with previous literature (Logan et al. 2015). It is known that bacteria have higher tendencies to form hydrogen bonds with hydrophilic surfaces, which have also been shown to strengthen at prolonged contact times. Interestingly, F_{SR} between *S. aureus* and smooth Ti were found to be increased compared to the ones observed for smooth polycarbonate surfaces **(Table 3.1)**, suggesting that the increased hydrophobicity of polycarbonate may be limiting the amount of hydrogen bonding between bacteria and surface. Abu-lail and Camesano reported rupture forces for individual hydrogen bonds at around -0.13nN (Abu-Lail & Camesano 2006), and therefore it is possible to hypothesise that several hydrogen bond bridges are involved in a single *S. aureus*-Ti adhesive unit (~5-6 bonds).

A

Probe	Mean Adhesion (nN)	Variance	Number of peaks
1	-1.72	1	101
2	-0.82	0.22	78
3	-0.74	0.31	43
4	-0.42	0.08	85
5	-0.47	0.08	46
Total			**353**

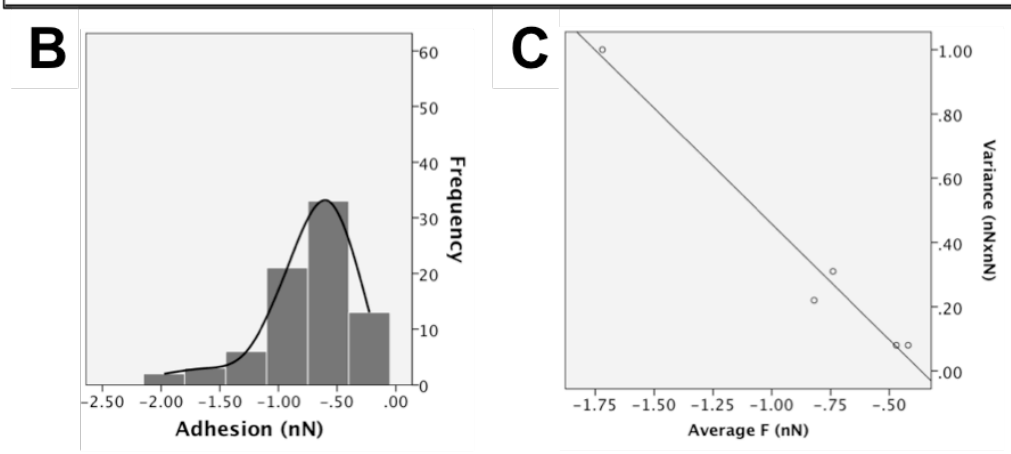

Figure 4.7: Poisson analysis of *S. aureus* functionalised probes. (a) Mean adhesion values and variance (nN^2) of single-unbinding peaks observed for five independent *Staphylococcus aureus* cell probes. (b) Histogram of minor detachment forces, which follow a Poisson distribution. (c) Plotting force v/s variance yields a linear fit, from which short-range and long-range adhesion components can be determined utilising the slope of the curve (R^2 linear = 0.97).

For *S. sanguinis*, mean value for minor-detachment events was -1.84±0.64nN, with an F_{SR} component of -1.60±0.34nN and a F_{LR} component of -0.55±0.47nN **(Table 4.1)**. The negative value observed for F_{LR} reflects an overall attractive nature of the long-range forces affecting *S. sanguinis* attachment to Ti. Interestingly, F_{SR} values were higher than the ones observed for *S. aureus*. Considering that bacterial attachment to hydrophilic surfaces has been suggested to be predominantly

mediated by hydrogen bonding, with an individual bond force of approximately -0.13nN, it is possible to hypothesise that a minimum of ~12 hydrogen bonds are formed between the *S. sanguinis* cell probe and the surface during AFM probing. This increased bond formation capacity in *S. sanguinis* compared to *S. aureus* could help explain the increased early-colonising behaviour of this strain towards hard surfaces in the oral cavity.

Table 4.1: Poisson analysis of *S. aureus* and *S. sanguinis* adhesion to smooth Ti surfaces.

Strain	Specific (F_{SR})		Non-specific (F_{LR})	
	Mean (nN)	*SE*	*Mean (nN)*	*SE*
S. aureus	**-0.75**	***0.04***	**-0.58**	*0.15*
S. sanguinis	**-1.60**	***0.34***	**-0.55**	*0.47*

5.5. *Effect of 2mg/ml chlorhexidine on early bacterial attachment*

To evaluate the effect of CHX on the adhesion of *S. aureus* and *S. sanguinis* to Ti surfaces, AFM force-spectroscopy was carried out in a solution of 2mg/ml CHX in TRIS buffer. Our experiments also showed that CHX increases both adhesion force (19.51±2.48nN) and adhesion work (2850.96±670.10aJ) of *S. aureus* at 60s surface

delays ($p<0.05$, Kruskall-Wallis) **(Figure 4.8)**. Significant changes in attachment behaviour was also observed in *S. sanguinis* for both adhesion force and work, as values increased to 47.93±5.26nN and 10473.10±1472.59aJ respectively after exposure to the CHX solution **(Figure 4.9)**. Similar observations were made by Kishen et al. who found that nanoadhesion of *Enterococcus faecalis* was increased on dentin surfaces after treatment with a 2%CHX solution (Kishen et al. 2008).

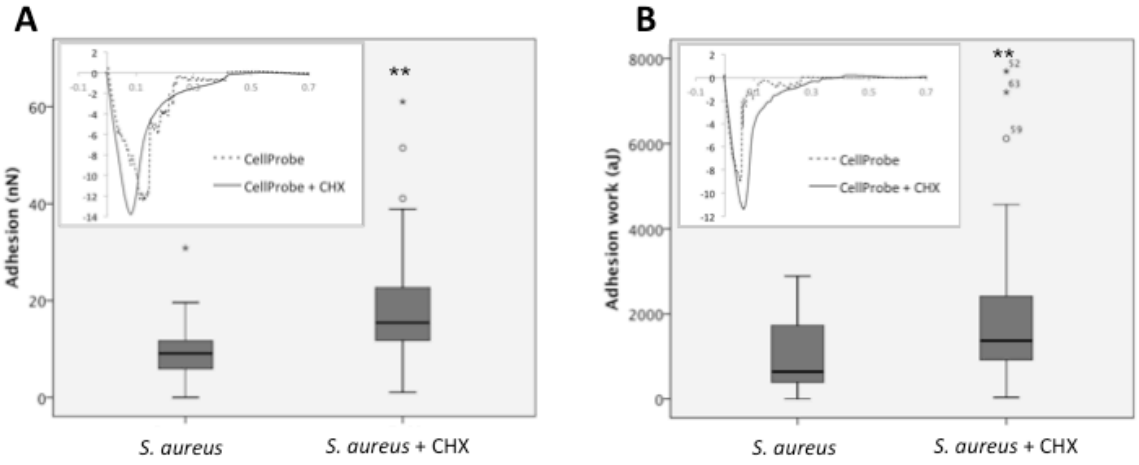

<u>Figure 4.8</u>: Addition of 2mg/ml chlorhexidine (CHX) to the buffer solution modifies S. aureus adhesion. (a) Adhesion force and (b) adhesion work observed for *S. aureus* in buffer solution and after addition of 2mg/ml CHX. Insets illustrate the change in force-curve patterns for 2 independent *S. aureus* cell probes *(**p<0.05, Kruskall-wallis).*

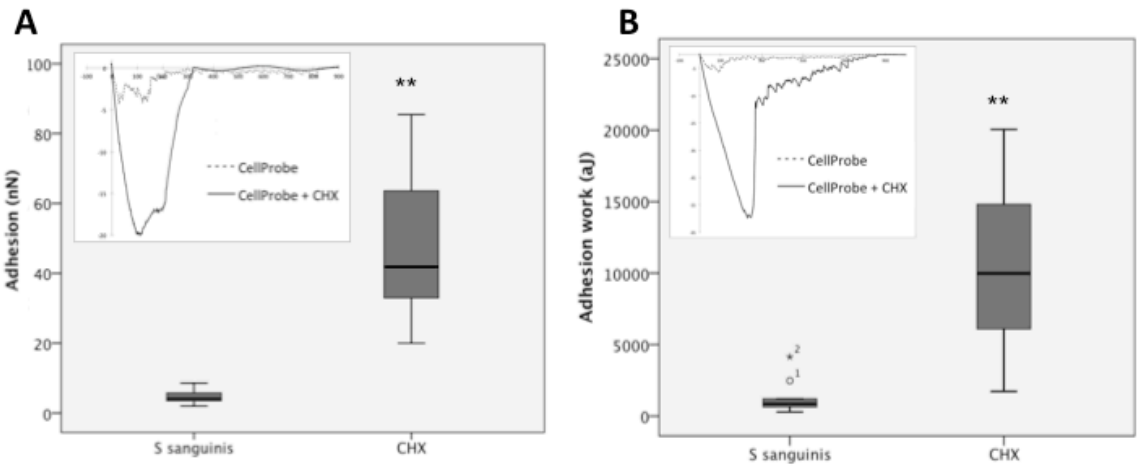

Figure 4.9: Addition of 2mg/ml chlorhexidine (CHX) to the buffer solution modifies *S. sanguinis* adhesion. (a) Adhesion force and (b) adhesion work observed for *S. sanguinis* in buffer solution and after addition of 2mg/ml CHX. Insets illustrate the change in force-curve patterns for 2 independent *S. aureus* cell probes *(**p<0.05, Kruskall-wallis).*

The increase in adhesion observed after the application of CHX could be explained by two possible mechanisms. Firstly, CHX is a positively charged molecule with the ability to bind to substrates and negatively charged bacterial surfaces (Valderrama et al. 2014), and therefore its presence may increase the binding affinity between the probe and Ti surface. Secondly, CHX exposure has been shown to alter the mechanical properties of the bacterial cell and cause membrane damage (Edmiston et al. 2013; Mcdonnell & Russell 1999), which could also lead to increased adhesion due to increased compliance of the bacterium against the surface during probing. This effect could also be a result of loss of integrity of the bacterial wall due to CHX

accumulation (Gilbert & Moore 2005). Nevertheless, further research is necessary to clarify the specific mechanism of CHX-mediated increase in *S. aureus* and *S. sanguinis* nanoadhesion to Ti surfaces, and to determine the clinical significance this effect could potentially have on biofilm formation post-implant disinfection with CHX. Furthermore, these results suggest that this AFM approach could potentially be employed as a tool to evaluate the impact of anti-adhesive surfaces, coatings or solutions on the attachment of a diverse number of bacterial strains to implant surfaces, in hopes of preventing surface colonisation and infection.

6. Summary:

Throughout this chapter, the adhesion between *S. sanguinis* and *S. aureus* and Ti implant surfaces has been studied employing AFM force-spectroscopy. In summary:

- Clinically analogous smooth and SLA Ti substrates were characterised in terms of surface topography and hydrophobicity. Although both surfaces demonstrated marked differences, only smooth Ti was considered suitable for AFM experiments, due to the increased surface roughness of the SLA surface.
- Differences in adhesive behaviour towards smooth Ti was observed between *S. aureus* and *S. sanguinis*. Although *S. aureus* demonstrated increased maximum adhesion forces, Poisson analysis indicates that *S. sanguinis* binds to the Ti surface with increased F_{SR}, which suggests improved specific binding between this strain and substrate.
- WLC modelling predicted receptor length of *S. aureus* to be in the range of ~150-400nm, while receptors in *S. sanguinis* were found to be increased at ~600nm. This data suggests that strain-specific receptors are involved in the interaction between bacteria and Ti surfaces.
- Addition of 2mg/ml CHX increases the adhesion force and energy between smooth Ti and both *S. aureus* and *S. sanguinis*. However, further research is necessary to clarify the specific mechanism of CHX-mediated increase in bacterial adhesion to Ti surfaces

CHAPTER 5

Candida albicans adhesion onto poly-methyl methacrylate (PMMA) denture surfaces at the nanoscale†

---

1. Introduction

In this final results chapter, we will show how a modified version of the previously described AFM approach allows us to study the adhesion *Candida albicans* and oral biomaterial surfaces with high morphological precision.

C. albicans is a commensal yeast found living on skin and mucosal surfaces; however, it also has the capacity of causing opportunistic surface or deep tissue infections in immunocompromised patients (Kabir et al. 2012; Salvatori et al. 2016), and it has further been associated to infection of medical devices in diverse parts of the body (Nett et al. 2010). Typically, *C. albicans* exists as a polymorphic fungus, which means it has the capacity to grow in either yeast or filamentous form (Veses & Gow 2009). Filamentous forms -also known as hyphae- are tubular growths of *C. albicans* cells associated with tissue penetration and invasion (Thomson et al. 2016), and transition towards hyphae is considered one of the most important virulence factors of this particular strain (Jackson et al. 2014).

† The ex-vivo growth in blood and C3 Compliment Binding Assay was carried out together with Dr. Helina Marshall (UCL Respiratory)

The use of non-implant retained acrylic dentures remains one of the most commonly used methods to rehabilitate partially or fully edentulous patients (PAN et al. 2015). Most denture bases are constructed using poly-methyl methacrylate (PMMA) as a main structural component (Uzunoglu et al. 2014). Nevertheless, denture surface infection with *C. albicans* biofilm continues to be a major problem, particularly when patients fail to maintain good denture hygiene (Barbeau et al. 2003). Once established, this candida biofilm is associated to the onset of *denture-associated stomatitis*, a chronic inflammatory form of oral candidiasis that can affect up to 70% of denture wearers (Nett et al. 2010; Izumida et al. 2014; Cao et al. 2010). Clinically, this disorder can sometimes give rise to pain or irritation of the oral mucosa (Yarborough et al. 2016). It can also be a potential source of systemic candida infection in immunocompromised individuals, and a possible reservoir for respiratory infection (O'Donnell et al. 2016; Wu et al. 2015). There remains no specific therapy for treating this disorder, although typical strategies are physical cleaning and topical use of antimicrobials or antifungals (Yarborough et al. 2016). In the case of *Candida*, some AFM-based studies have analysed its attachment onto both bacterial cells and abiotic surfaces (Ovchinnikova et al. 2013; Alsteens et al. 2009; Formosa et al. 2015; Hwang et al. 2015). However, there remain no studies evaluating the nanoscale adhesion of *C. albicans* onto clinically relevant biomaterial surfaces such as PMMA.

The work in this chapter was published as *"**Candida albicans*** **adhesion onto acrylic surfaces at the nanoscale." Journal of Dental Research, Apr 1:22034517706354.**

2. Aim

The aim of this research was to investigate the adhesion between *C. albicans* yeast cells and hyphae and PMMA surfaces at the single-cell level, in hopes of understanding the crucial initial yeast-denture interaction and thereby provide insight into effective methods or preventing and/or treating this common disorder.

3. Objectives:

- Develop specialised PMMA-microsphere AFM probes to study the adhesion forces between different phenotypes of *C. albicans* and acrylic denture substrates.
- Evaluate the adhesion forces and energy between *C. albicans* yeast cells and hyphae and PMMA surfaces.
- Determine the virulence of both a laboratory and a clinical strain of *C. albicans*, and correlate it with differences in adhesive behaviour observed in-vitro.

4. Materials and methods:

4.1. *C. albicans strains*

C. albicans ATCC 10231 and a clinical isolate of *C. albicans* (C1, isolated from the Royal Free Hospital, London) were utilised throughout the study, and maintained in 15% glycerol in Sabouraud broth (Oxoid Ltd, UK) at -80°C. From frozen stocks, *C. albicans* were grown in *Sabouraud* broth for 16hrs at 37°C and aeration to obtain the yeast cell phenotype. For hyphal differentiation, *C. albicans* were grown in BHI broth (Oxoid Ltd, UK) for 3hrs at 37°C and aeration. Subsequently and for both cases, 100µl of fungal suspension was diluted into 1ml final concentration of phosphate-buffer saline (PBS 1x, Lonza, Belgium) and harvested at 5000rpm for 1min (Eppendorf 5417R, UK). Resulting pellets were re-suspended in 1mL PBS and transferred immediately to the AFM for experiments, carefully maintaining cells submerged in buffer throughout the process.

4.2. *Non-destructive fungal immobilisation for AFM imaging and nanomechanics in buffer*

To allow effective immobilisation of *C. albicans* yeast and hyphae for AFM experimentation, glass cover slides were coated with either a 100µl droplet of poly-L-lysine (PLL, P4707, Sigma-Aldrich) or a 100µl droplet of 4mg/ml dopamine hydrochloride in 10mM TRIS buffer, pH8.0 (poly-DOPA, Sigma-Aldrich). After drying for 2hrs, surfaces were washed with dH_2O, dried with N_2 airflow and stored at 4°C until experimentation. PLL-coated slides were utilised to immobilise *C. albicans*

yeast cells, while poly-DOPA was the preferred method to attach hyphal forms of the strains.

4.3. *Fabrication of PMMA-functionalised AFM probes*

For single-cell force spectroscopy (SCFS), customised AFM probes were constructed in order to explore the adhesion of PMMA to surface immobilised *C. albicans*. Probe functionalisation was obtained by utilising a JPK Nanowizard system (JPK Instruments, Germany) mounted on an inverted optical microscope (Olympus IX71, Olympus, Japan). Tipless AFM cantilevers (NP-O10, Bruker, USA) were brought into contact with a thin layer of UV-curable glue (AA 350, Loctite, UK) spread out on a glass slide for 10s. Each cantilever was then approached to a 10μm PMMA microsphere (Cospheric, USA) for 1min to allow attachment to the glue-covered surface. Subsequently, functionalised cantilevers were UV-cured for 10mins, and correct placing of the microsphere was assessed by optical and SEM imaging. Finally, each PMMA-functionalised cantilever was calibrated utilising the JPK proprietary tuning software (~0.3N/m spring constants) before experimentation.

4.4. *AFM nanomechanics setup*

All AFM nanomechanic experiments were carried out with a JPK Nanowizard system. SCFS experiments were carried out with a loading force of 1nN, a constant speed of 2μm/s, and surface delay times of 0, 1, 5, 10 and 30s. For yeast cells and budding cells, force curves were obtained on the centre of the cell as observed with the optical microscope **(Figure 5.1)**. For hyphal tubes, force curves were performed in the middle portion of the tube **(Figure 5.1)**. All SCFS experiments were carried

out in PBS buffer, maintaining probes and *C. albicans*-coated surfaces fully hydrated throughout the whole process. Force curves obtained over a total of 7 independent yeast cells and hyphae were utilised for data analysis.

4.5. *Ex-vivo growth in blood*

Human blood was obtained with written consent from healthy human volunteers under ethical approval granted by the local University College London ethics committee (application 3076/001). Blood clotting was prevented by the addition of 300IU/50ml of heparin sodium solution. Growth in blood was investigated using an inoculum of approximately $5x10^6$ CFU/ml. Samples were then incubated at 37°C for 4 hours before serial dilution and plating onto Sabouraud agar plates.

4.6. *Complement C3 binding assay*

Pooled human serum was obtained from healthy human volunteers and stored in single use aliquots at -70°C. Binding to *C. albicans* after incubation in human serum was measured by means of a well-described flow cytometry assay (Brown et al. 2002), using a fluorescein isothiocyanate (FITC)-conjugated polyclonal anti-human C3 antibody (MP Biomedicals). Markers for identifying positive cells were set using *C. albicans* incubated in PBS and then C3 antibody. Results of the assay are presented as a fluorescence index (FI, percentage of positive bacteria multiplied by the geometric mean MFI of C3 binding) in arbitrary units.

4.7. *AFM data analysis:*

Resulting force curves were analysed using the JPK Data Processing Software v.5.1.8 (JPK Instruments, Germany). Maximum adhesion force, expressed in nN, was determined as the lowest negative value during the retraction phase; and energy of adhesion, expressed in aJ, was obtained by integrating the area under the retraction curve. Data was graphed as mean±SE and significance was determined with the Mann-Whitney test ($p<0.05$).

5. Results and discussion:

5.1. *Construction of PMMA-modified AFM cantilevers*

For the study of *C. albicans* adhesion to PMMA, an alternative approach to the method used for bacterial cells was explored. As *S. aureus* and *S. sanguinis* cells are rounded and consistent in shape and size (<1µm), it was possible to immobilise them to AFM cantilevers for force-spectroscopy measurements. However, *C. albicans* are larger in size and can be present in different phenotypes (yeast cells and hyphae); thus, immobilisation to the cantilever tip is not possible. Therefore, it was necessary to develop a protocol in which the surface of interest – PMMA- was approached towards *C. albicans* attached to a glass substrate **(Figures 5.1 and 5.2)**.

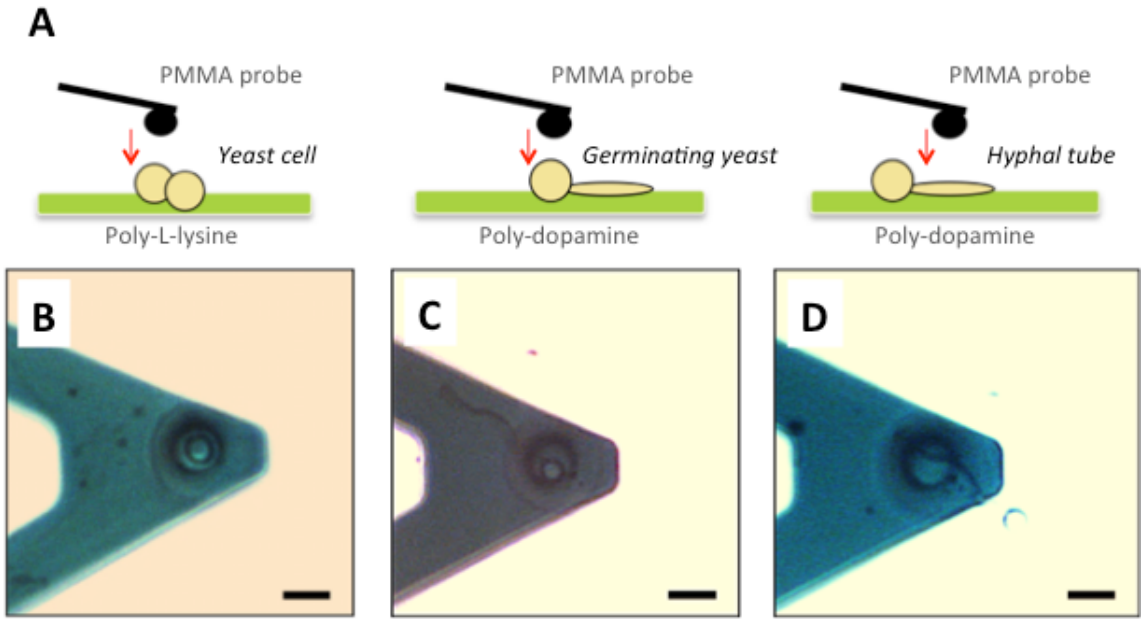

Figure 5.1: Overview of the single-cell force spectroscopy (SCFS) setup for studying adhesion between a poly-methyl methacrylate (PMMA) functionalised AFM probe and living *C. albicans* cells. (A) Diagrammatic representation of the setup used to study adhesion between a PMMA-functionalised cantilever and *C. albicans* yeast cells, germinating yeast and hyphal tubes in buffer. Cells were immobilised onto glass substrates by covalent binding to poly-L-lysine (PLL) in the case of yeast cells or poly-dopamine (DOPA) for hyphae. (B), (C) and (D) are optical images depicting probe positioning atop *C. albicans* yeast cells, germinating yeast and hyphal tubes, respectively (scale bar 10µm).

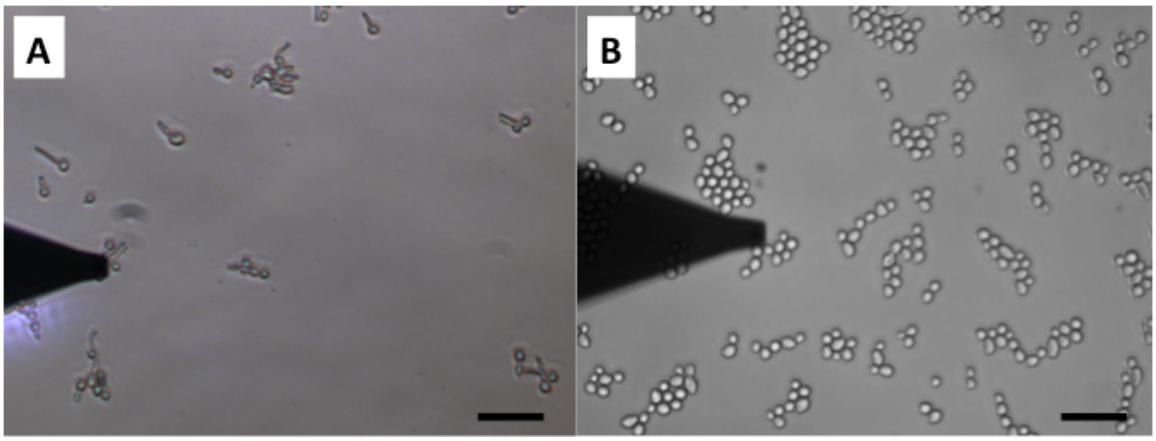

Figure 5.2: Immobilisation of *C. albicans* onto biopolymer-coated glass slides. (A) *C. albicans* hyphae attached to a poly-DOPA coated surface. (B) *C. albicans* yeast cells immobilised onto PLL coated glass slides (scale bar 30µm).

For this approach, 10µm PMMA microspheres were attached to the end of a tipless AFM cantilever, by employing a similar protocol than the one previously

utilised with glass microspheres **(Figures 2.8A and 2.8B)**. This technique allowed consistent placement of PMMA microspheres, which did not detach from the tip during preparation or force-spectroscopy experimentation. Immobilisation of *C. albicans* was found to be determined by phenotype, as yeast cells were easily attached to PLL coated surfaces; however, immobilisation of hyphae was more effective by employing poly-DOPA **(Figure 5.2)**. Positioning of the PMMA microsphere was easily observable with both optical and electron microscopy **(Figure 5.3)**. More importantly, this approach facilitated the selective placement of the PMMA surface atop the area of interest of the *C. albicans* yeast cell and hyphae, with micrometre precision **(Figure 5.1A, B and C)**. Therefore, consistent force-curves were obtained on either the yeast cell, hyphae tube or budding cell.

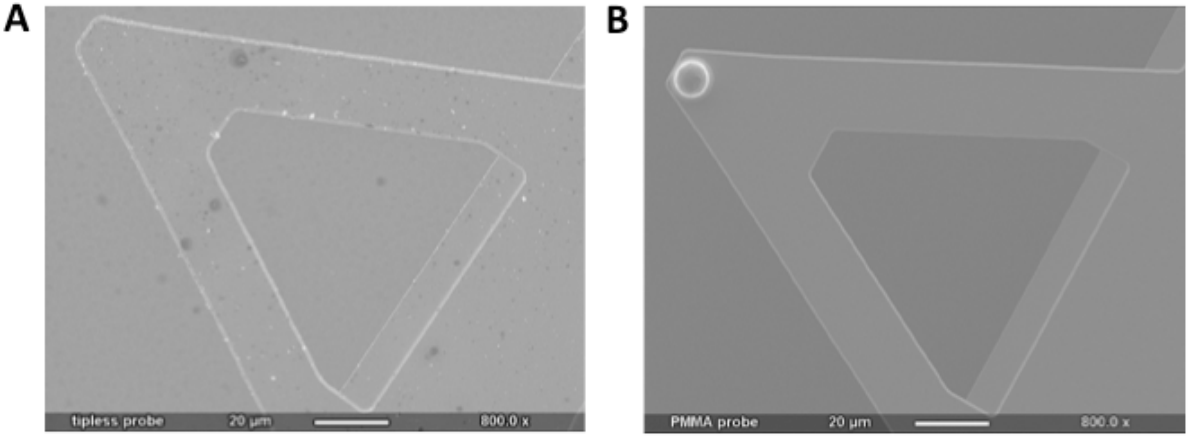

Figure 5.3: Construction of PMMA-functionalised probes. SEM images of a tipless AFM cantilever (A) before and (B) after a PMMA microsphere is attached by employing the AFM as a micromanipulator.

5.2. *PMMA-C. albicans nanoscale interaction is morphology dependent*

SCFS of living *C. albicans* in buffer was possible by immobilisation to PLL and poly-DOPA surfaces **(Figure 5.1)**. As previously discussed, PLL was only found to be effective for immobilising yeast cells; and therefore poly-DOPA was the selected agent for the attachment of hyphae, as it was able to maintain stability by resisting the lateral shear forces generated by the AFM tip during scanning. Cells and hyphae remained immobilised throughout measurements in PBS buffer, and detachment from surfaces was rarely observed. This positioning was consistent for different cells, and therefore reproducible results were observed across independent cells and hyphae (n=7 *C. albicans* cells). Representative retraction patterns for the unbinding of PMMA from *C. albicans* yeast cells and hyphae are shown in **Figure 5.4** and **Figure 5.5**, respectively.

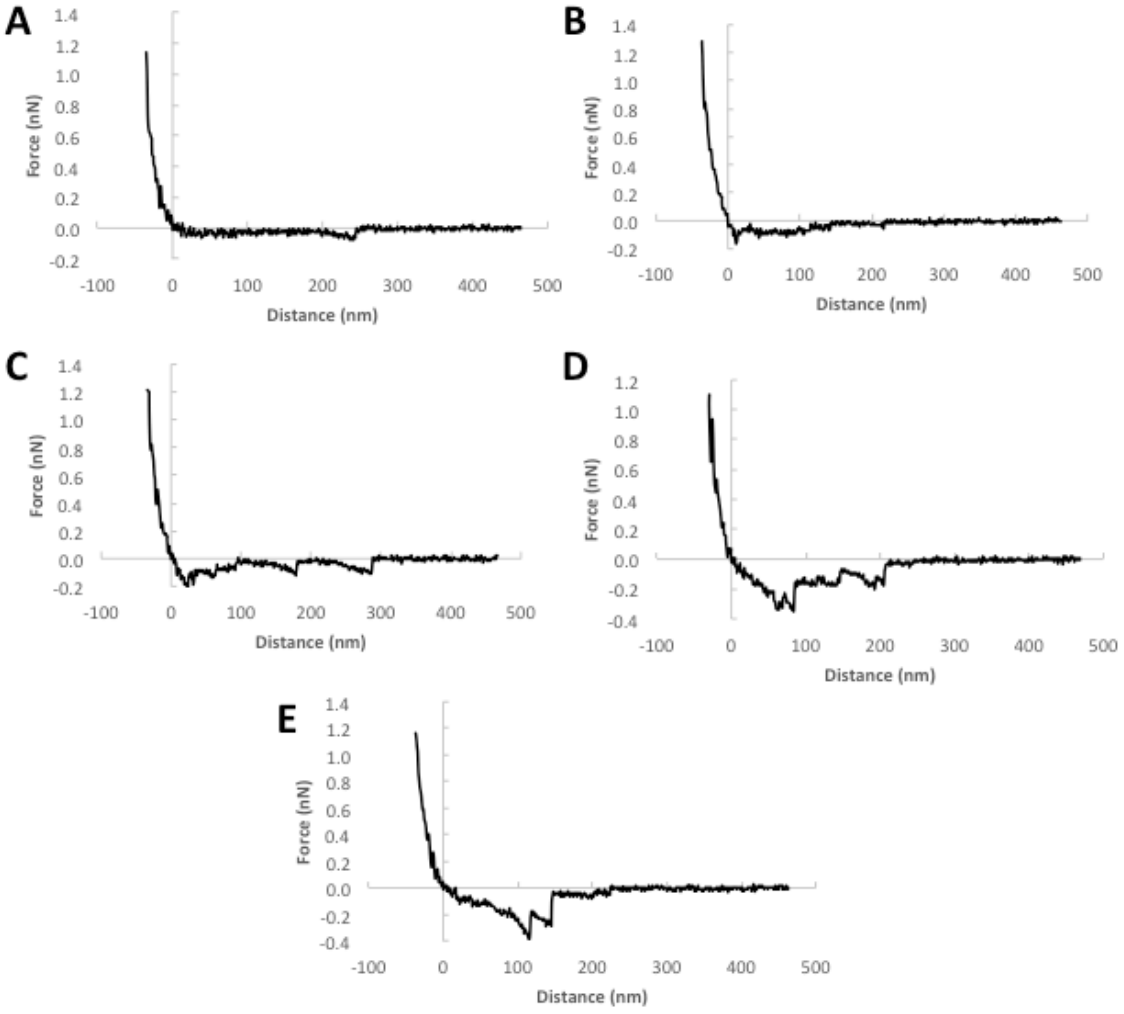

<u>Figure 5.4:</u> SCFS of the *C. albicans* C1 yeast cell-PMMA interaction. Representative retraction force-curves obtained at (A) 0s, (B) 1s, (C) 5s, (D) 10s and (E) 30s contact times.

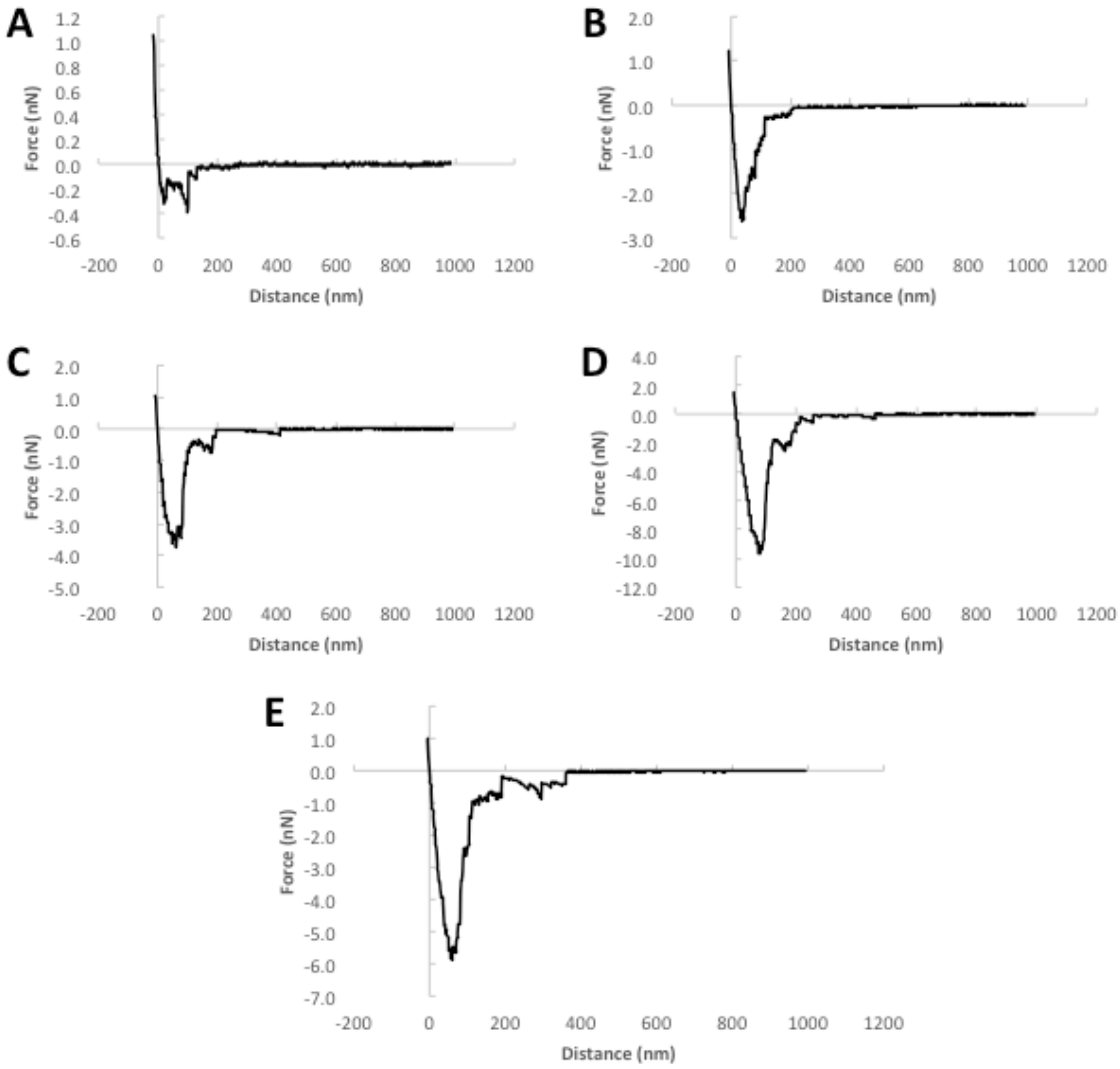

<u>Figure 5.5:</u> SCFS of the *C. albicans* C1 hyphae-PMMA interaction. Representative retraction force-curves obtained at (A) 0s, (B) 1s, (C) 5s, (D) 10s and (E) 30s contact times. Adhesion forces are increased compared to the yeast cell-PMMA interaction.

In the case of yeast cells, the mean adhesion forces between *C. albicans* C1 and PMMA were found to be 0.12±0.0nN, 0.24±0.0nN, 0.43±0.0nN, 0.45±0.0nN and 0.29±0.0nN for 0, 1, 5, 10 and 30s respectively **(Figure 5.6)**. A similar time-

dependent increase was also found for the adhesion energy **(Figure 5.7)**. Interestingly, adhesion forces between PMMA and hyphal tubes were found to be increased at every time point compared to yeast cells, with values of 0.34±0.0nN, 1.68±0.1nN, 2.47±0.1nN, 3.71±0.2nN and 6.09±0.4nN for 0, 1, 5, 10 and 30s respectively. Thus, PMMA-hyphae adhesion was found to be increased by an order of magnitude compared to the PMMA-yeast cell forces. At a maximum contact time of 30s, adhesion forces between PMMA-hyphae are nearly twenty times higher than those of PMMA-yeast cell. However, the budding yeast cell was found to have adhesion forces of ≤0.05±0.0nN (50pN). As these force values are in the range of the system detection limit (20-40pN), adhesion between PMMA and this portion of the hyphae can be considered non-existent. This is similar to what was described previously in the case of mother budding yeast cells, which were also found to be non-adherent (Formosa et al., 2015a), and further demonstrates the plasticity of *C. albicans* adhesin expression. The same morphology-dependent adhesion between PMMA and *C. albicans* was also found to be present in the ATCC 10231 strain; however, forces between PMMA-hyphae were only four times higher than between PMMA-yeast cells at 30s contact times **(Figure 5.8)**. Also, increasing the contact time was found to have a greater influence in the case of hyphae, suggests the presence of increased numbers of surface adhesins available for interacting with biomaterial surfaces (de Groot et al. 2013; Beaussart et al. 2012).

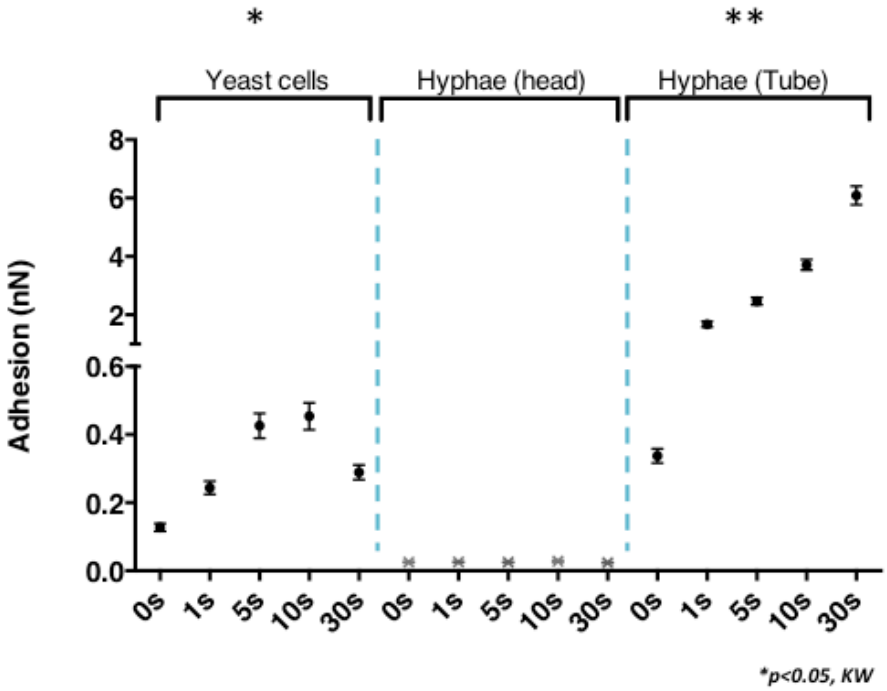

Figure 5.6: Adhesion forces (nN) observed between *C. albicans* C1 and PMMA functionalised AFM probes. Comparison between adhesion forces observed between PMMA and yeast cells, budding cells (hyphae head) and hyphal tube. Adhesion forces between PMMA and hyphal tubes were found to be 10 times higher than the ones probed between PMMA and yeast cells (n=7).

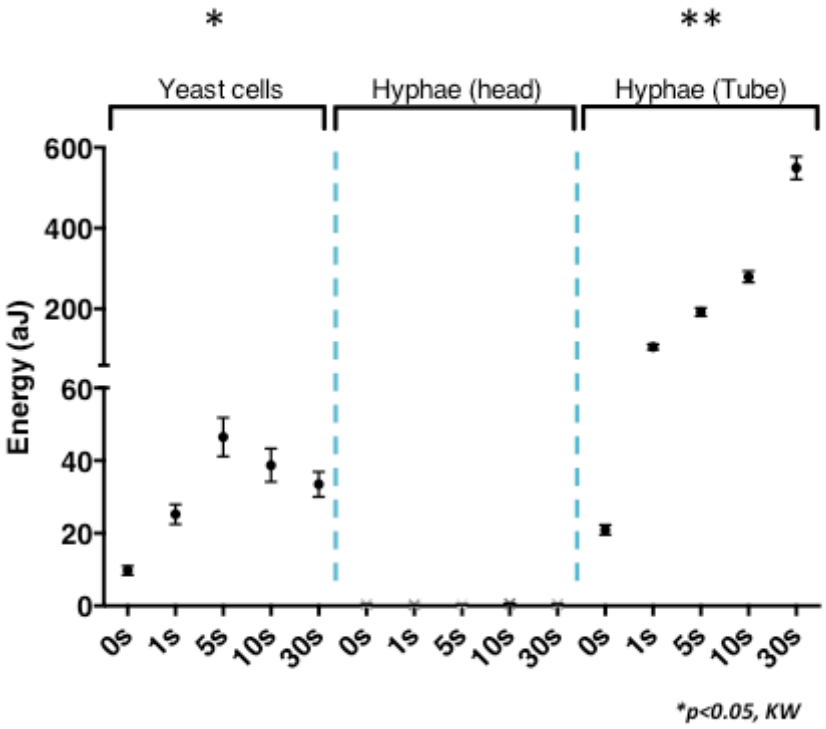

Figure 5.7: Adhesion energy (aJ) observed between *C. albicans* C1 and PMMA functionalised AFM probes. Comparison between adhesion energy measurements observed between PMMA and yeast cells, budding cells (hyphae head) and hyphal tube (n=7).

It is well known that candidal hyphal differentiation is a key factor in pathogenicity as it promotes invasiveness and tissue penetration (Naglik et al. 2014). Our results back these previous observations, as it was observed that adhesion forces between PMMA the tube portions of *C. albicans* hyphae were significantly increased compared to yeast cells (**Figures 5.6 and 5.7**). This supports the notion that polarised growth observed in *C. albicans* hyphae is indeed a mechanism to increase adhesion and penetration to host tissues (Brand 2012). It also appears that adhesion within the hyphae is morphology-selective, as the

budding cell portion is non-adhesive, displaying attachment forces that are even lower than the ones observed for yeast cells. This suggests that during hyphal differentiation, adhesin expression is limited to the growing tube and is not a generalised mechanism throughout the entire length of the hyphae. Also, similar to what has been observed in bacterial SCFS experiments (Aguayo et al. 2015), higher contact times between *C. albicans* and PMMA yield increased adhesion forces between the substrate and cell (**Figure 5.5**). This effect was much more pronounced in the clinical strain, where increasing contact time from 0s to 30s raised adhesion to PMMA by 20-fold. This effect could be due to either a time-dependent cell wall-surface contact area, or adhesin bond strengthening after the initial surface-receptor coupling has occurred (Ovchinnikova et al. 2012). These results also demonstrate the ability of *C. albicans* to rapidly attach to PMMA surfaces after only a few seconds of contact, without the presence of an acquired pellicle or existing biofilm.

5.3. *Adhesion of C. albicans to PMMA is strain specific and suggests correlation to strain virulence*

To compare the adhesion forces between a laboratory and a clinical strain, SCFS experiments were carried out by using *C. albicans* ATCC 10231 and *C. albicans* C1 strains. Interestingly, adhesion forces and energy were increased in the clinical strain for both yeast cells and hyphae. In the case of hyphal tubes, adhesion between PMMA and the clinical strain was found to be ~10 times higher compared to *C. albicans* ATCC 10231 **(Figure 5.8)**.

To evaluate a possible relationship between candida virulence and attachment to PMMA surfaces, growth in blood and C3 complement binding assays were performed for both *C. albicans* strains. After a 4hr incubation period, *C. albicans* C1 demonstrated a 49.83±4.3% survival in blood, compared to only a 33.33±2.4% observed for strain 10231 **(Figure 5.9)**. Furthermore, C3 complement binding showed an increased opsonisation of strain 10231 compared to C1, with fluorescence Index values of 67710±2778 and 48700±798, respectively **(Figure 5.10)**. According to these results, the increased capacity of *C. albicans* C1 to evade the immune system and survive in blood is correlated to its ability to adhere to and colonise biomaterial surfaces at the nanoscale (Mayer et al. 2013). In the case of candida infection, increased adhesion capabilities at early time points could favour the formation of biofilm on the surface of biomaterials, and the capacity of evading the host immune response would be a crucial factor in creating a scenario of chronic inflammation as observed in patients with denture-related stomatitis (Shirley et al. 2015). Furthermore, increased adhesion capabilities of the clinical strain are more pronounced for hyphae compared to yeast cells **(Figure 5.8)**, which further supports the idea that increased adhesion forces between *C. albicans* and PMMA are correlated to virulence.

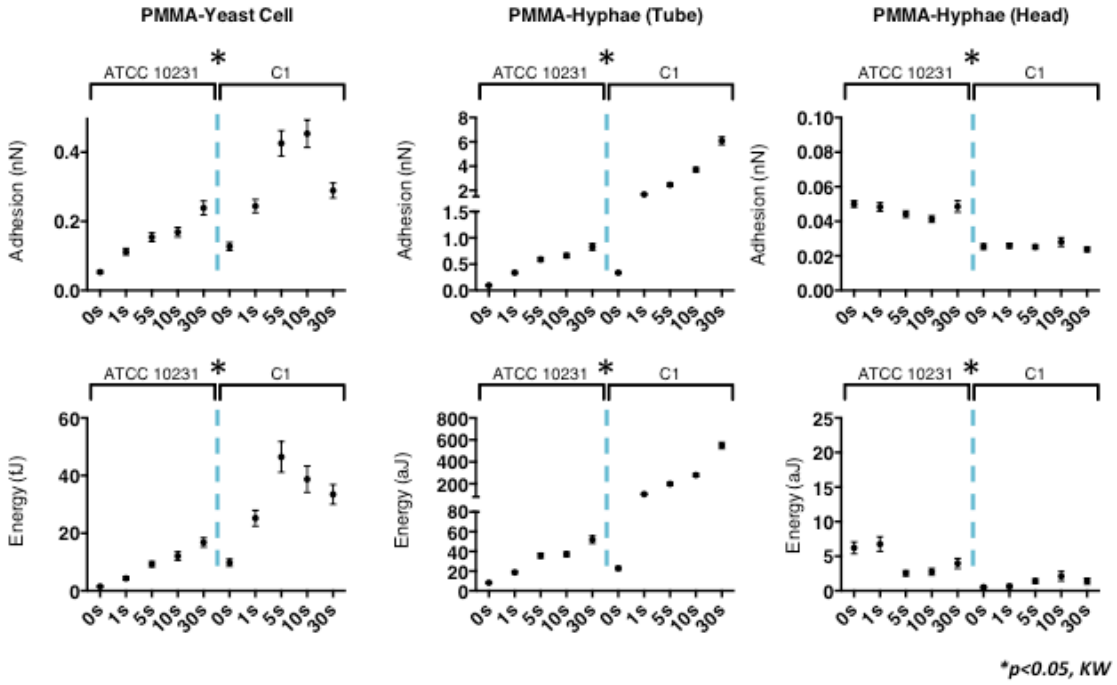

<u>Figure 5.8</u>: Comparison between the adhesion of *C. albicans* 10231 and *C. albicans* C1 to PMMA-functionalised probes at increasing contact times (0-30s). Overall, the clinical *C. albicans* strain demonstrated increased adhesion forces to PMMA compared to 10231 ($p<0.05$, Kruskall-wallis). The hyphal head was also non-adherent for *C. albicans* 10231 (n=7).

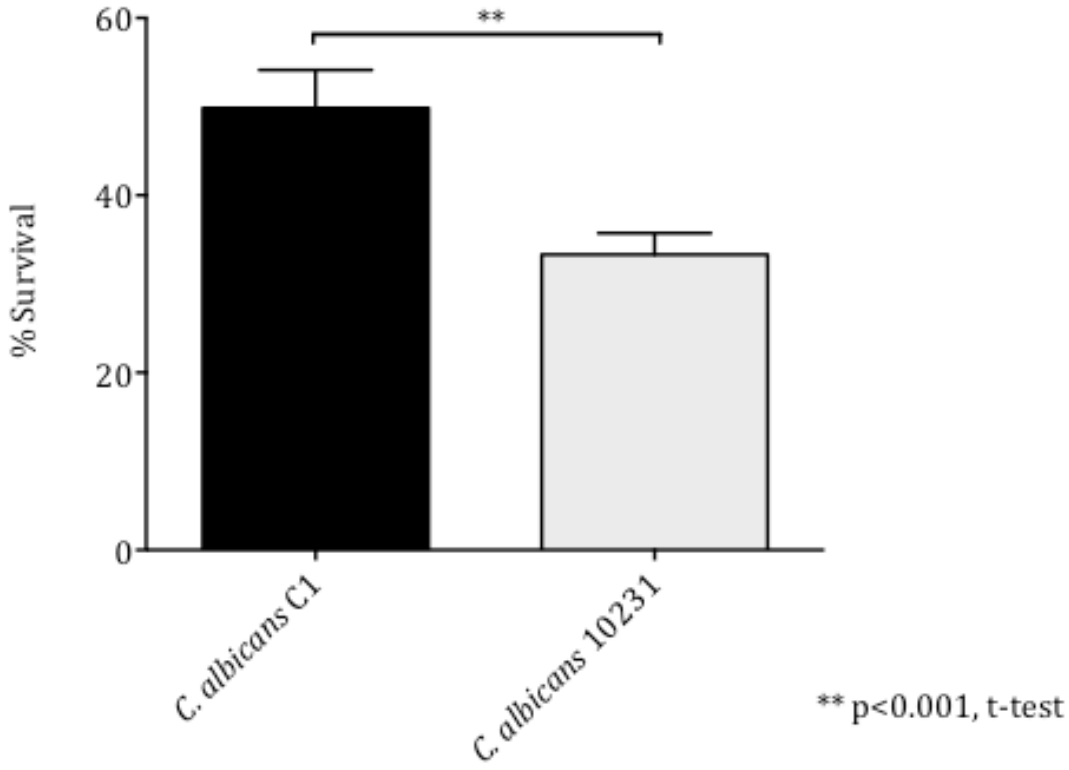

Figure 5.9: *C. albicans* 10231 and C1 survival in blood. Incubation in human blood for 4hrs showed increased survival of *C. albicans* C1 compared to 10231 (**p<0.001, t-test) (n=4).

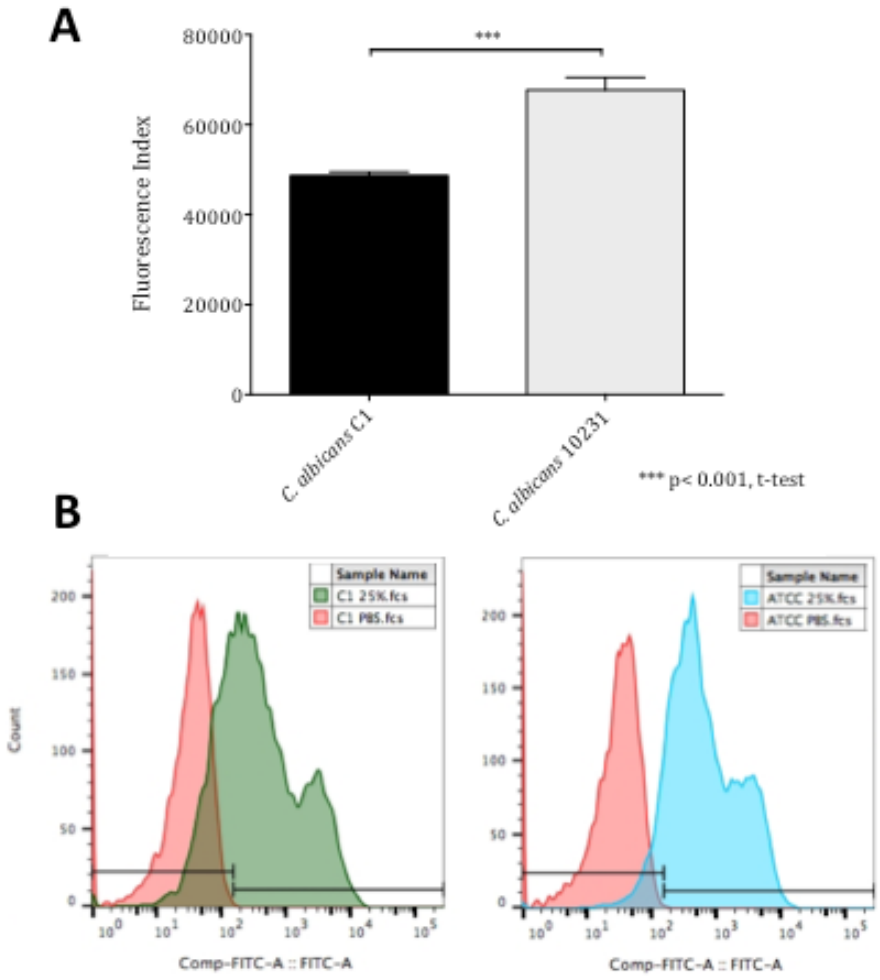

<u>Figure 5.10</u>: *C. albicans* 10231 and C1 in-vitro complement binding assay. (A) A decreased degree of opsonisation was found in *C. albicans* C1, suggesting improved immune evasion properties compared to 10231. (B) Corresponding FIT-C histograms for both *C. albicans* C1 and 10231, respectively. PBS control curves are shown in red (***p<0.001, t-test) (n=4).

Overall, the present AFM-based approach to obtain PMMA-modified probes facilitated the correct positioning of the bead on the end of the tipless cantilever, and allowed effective approach of the PMMA surface onto the *C. albicans* surface with great precision **(Figure 5.1)**. In the case of hyphae, this approach allowed specific positioning of PMMA onto each morphological region (budding cell and tube) to obtain adhesion forces in the nano- and pico- newton range. Although this work is centred on PMMA as an important surface colonised by *C. albicans*, further studies are necessary in order to focus on unravelling the interactions between this pathogen and other materials and biological surfaces of interest in the oral cavity, as well as aiding in the search for novel anti-adhesive and antifungal molecules.

6. Summary:

The use of PMMA microspheres to selectively probe the adhesion of polymorphic *C. albicans* has been employed here for the first time to characterise fungal attachment to biomaterial surfaces at the nanoscale level. In summary:

- Specific positioning of the probe was crucial to understand the adhesion forces driving attachment of PMMA to each region of *C. albicans.*
- PMMA adhesion was found to be higher for the tube region of hyphae, compared to yeast cells where forces were decreased by an order of magnitude. Also, the budding cell region of hyphae was found to be non-adherent at all studied contact times and for both strains.
- Adhesion forces and energy between PMMA and the clinical strain of *C. albicans* were significantly increased compared to the lab strain, which suggests a possible correlation between virulence and adhesion to acrylic surfaces.
- This customised AFM cantilever approach is an effective method to study attachment between *C. albicans* and biomaterial surfaces with high morphological precision, and could potentially be utilised with different materials and fungal strains to support the development of strategies that can prevent or treat this common clinically relevant disorder.

CHAPTER 6

CONCLUSIONS AND FUTURE WORK

As presented throughout this thesis, an AFM force-spectroscopy approach has been developed that allows the study of microbial cell adhesion at the single-cell level. This approach was highly reproducible and was effective for both bacteria and fungal strains. Utilising this protocol, we were able to explore the effect of a number of variables on the adhesion of microbes such as surface roughness, strain differences, and phenotype expression and strain virulence.

Regarding the protocol development, bacterial strains such as *S. sanguinis* and *S. aureus*, and different fungal strains of *C. albicans* were immobilised for AFM experimentation, though it was found that the effectiveness of the immobilisation substance was very different for each strain **(Table 2.1)**. This is an interesting observation, as all studied substances are positively charged, which interact with the negatively charged microbial wall ensuring immobilisation (Louise Meyer et al. 2010). This strain-dependent variability in attachment could potentially be explained either by differences in cell wall charges between the strains, a weak interaction between the cell and coated substrate, or by strain-specific enzymes that are able to degrade the immobilisation agent. This issue was responsible for quite a number of delays regarding the protocol setup, and therefore it should be considered when setting up bacterial AFM experiments, as the use of new and different strains will most likely involve some trial and error before effective immobilisation is ensured.

Despite the effectiveness of AFM nanomechanical techniques, there are a couple limitations that still need to be addressed mainly regarding data analysis and interpretation, and that should be considered for future work. This still holds true in literature, as there is not yet a consensus regarding the parameters being reported by different groups working in bacterial nanomechanics (Beaussart & El-Kirat-Chatel 2014; Chen et al. 2011; Dufrêne 2008). To date, the most reported value in force-spectroscopy measurements is F_{max}, which as discussed previously, is only representative of non-specific adhesion and does not consider potential unbinding events observed during force-spectroscopy experiments. In cases of increased unbinding lengths, such as seen between *S. sanguinis* and Ti **(Figure 4.5)**, values of F_{max} underestimate adhesion and could potentially lead to interpretation bias. In these cases, utilising parameters such as work of adhesion, which include all unbinding events, seems to be more appropriate and should be encouraged in future studies (Taubenberger et al. 2014).

Another limitation of this particular model is the absence of a salivary or serum pellicle on the surface of the biomaterial, as it would be expected in vivo (Hojo et al. 2009). As this model detects forces at the nano- and pico-Newton range, the presence of a wide range of proteins and molecules between the surface and bacterium can lead to high variability in measurements, with inconsistent force values. Therefore, the interactions probed within this work are mostly non-specific interactions - such as Van der Waals forces and hydrogen bonds – between microbial cells and biomaterials. Thus, future work should focus on developing ways to incorporate bio-pellicles (i.e. saliva, serum, simulated body fluid) into the model

while maintaining control over the reproducibility of the system. By utilising protein coatings, further insights of the specific receptor-ligand interactions occurring between cell and pellicle can be studied, such as interactions with fibronectin and fibrinogen (Herman et al. 2013).

Utilising the AFM based approach described above, we were able to demonstrate that surface roughness, strain-specific differences and phenotype conditions influence the adhesion of microbes to biomaterials at the nanoscale level. Although surface roughness is known to increase bacterial adhesion at the microscale (Gallo et al. 2014), no data was available on the effect of nanoscale roughness on this process. We have shown in this work that patterning the surface at the nanoscale level yields increased adhesion of *S. aureus* compared to smooth surfaces (**Figure 3.6 and 3.7**); however, other authors have reported an antibacterial effect of nanopatterning surfaces when observed at the macroscale at longer growth times (Jahed et al. 2014; Puckett et al. 2010). This data supports the idea that bacteria behave differently at the single-cell level compared to biofilm level (Kara et al. 2006), as increased early-stage adhesion does not seem to directly correlate to the long-term adhesion between *S. aureus* and surfaces.

Regarding strain-specific variations, we observed that *S. aureus* and *S. sanguinis* demonstrate clear adhesion differences when probed against the same smooth Ti substrate (**Figure 4.3 and 4.4**). However, we were not able to study adhesion against SLA titanium due to its increased roughness, and therefore it was not possible to compare attachment differences between these two Ti surfaces. Both

studied strains were found to have similar cell shape and sizes (**Figure 2.2 and 2.3**), and therefore it is believed that the differences observed between *S. aureus* and *S. sanguinis* are not due to geometric factors, but instead reflect strain-specific surface adhesins interacting with the Ti substrate. This is supported by WLC modelling, which demonstrates differences in the contour length predictions between both strains of bacteria. Although there is quite some literature on *S. aureus* adhesins (O'Neill et al. 2008), which we were able to correlate with contour length predictions, little information regarding *S. sanguinis* was found for comparison. Future work, ideally utilising knockout mutant strains of bacteria, should focus on determining which are these specific receptors involved in Ti surface adhesion for both *S. aureus* and *S. sanguinis*.

Additionally, it was observed that adhesion was strongly dependent on the type of buffer in which experiments took place. Immobilisation of both bacterial strains was very sensitive to PBS, and the strong ionic charge of this particular buffer did not allow bacterial adhesion to occur (Webb et al. 2011). However, this was not the case for *C. albicans*, as both imaging and nanomechanics were possible in PBS. We believe that this can be explained by the larger size of *C. albicans*, which allows an increased contact area with the immobilisation agent that ensures a strong interaction with the substrate. Furthermore, the presence of CHX in the buffer was found to significantly increase the adhesion of both *S. aureus* and *S. sanguinis* to Ti surfaces (**Figure 4.8 and 4.9**), and represents a potential approach to study antiseptic effectiveness at the single-bacterium level.

As a final step, we utilised *C. albicans* to explore the effect of phenotypic differentiation and virulence on biomaterial adhesion. To do so it was necessary to modify the protocol used for bacterial attachment, by attaching a PMMA sphere to the AFM tip while maintaining the yeast cells immobilised to the substrate. We observed that hyphal induction potentiated adhesion to the acrylic surface, although adhesion within the hyphae was different for germinating cell and hyphal tube. Also, we demonstrate a potential correlation between *C. albicans* virulence and nanoscale adhesion, although further experiments with increased number of strains would be ideal to confirm this observation. These results demonstrate that our AFM-based approach is not only useful to explore cell adhesion to different surfaces, but also sensitive enough to probe differences at the nano-newton level, with the capacity of placing the probe on a specific area of the hyphae (germinating cell or tube) with micrometer precision.

Overall, the present research has focused on developing an in vitro model to study bacterial adhesion to oral biomaterials of interest; however, there are many potential avenues for future work. Firstly, as this model allows different substrates to be placed under the AFM in an exchangeable way, the antiadhesive effect of novel modified implant or dental material surfaces could be studied with high-throughput. Secondly, the technique can also be employed in the search of new antibacterial molecules, as a stand-alone or complimentary technique to measure effects at the single-cell level. These approaches are already being utilised in other fields, and the potential applications in dental research could include testing the anti-biofilm properties of new dental implant surfaces (Arciola et al. 2012; Ananth et al. 2015),

or aid in the search for novel antibacterial substances for endodontic treatment (Kishen et al. 2008; Beyth et al. 2013; Dai et al. 2011) or restorative dentistry (Yang et al. 2014; Weng et al. 2010; Weng et al. 2012) . Moreover, this model could aid in the fight against antimicrobial resistant strains and 'superbugs', which are currently threatening healthcare systems all over the globe (McKendry 2012). Although this approach is promising, by no means should it be considered the sole method of choice to study bacterial adhesion in vitro. It would be greatly beneficial to compare these results to other bacterial attachment techniques such as flow chamber measurements (Waar et al. 2005; Rangel et al. 2013; Le et al. 2013) to observe interactions occurring under both static and shear conditions. Other well described and established approaches may include scanning electron microscopy, fluorescence microscopy and CFU counting, which would compliment the data by providing information on adhesion at later stages (hours to days after initial attachment). Altogether, it remains important to complement AFM bacterial spectroscopy with these other approaches, and future work should focus on finding novel ways to correlate findings from these different techniques.

Furthermore, as this model can also be modified to study cell-cell interactions, it could also be useful to study aggregation of known oral biofilm species with each other (Hojo et al. 2009), as well as their interaction to hard (i.e. enamel, dentin) and soft (i.e. mucosa) tissues in the oral cavity. The interaction between oral pathogens and epithelial cells is of great interest in periodontology (Lamont et al. 1995; Tribble & Lamont 2010), and could be studied in vitro by minimally modifying our current protocol. As this approach is not limited to

bacterial cells, there is considerable potential to employ this technique to study the interaction between human cells (i.e. stem cells, fibroblasts) and implant surfaces to study the process of osseointegration (Logan & Brett 2013).

Finally, variations of our model are currently being employed by collaborators in nanomedicine to study the nanomechanics of collagen tissue (Strange et al. 2017) **(Appendix 2)**; in conservation science to explore the adhesion between nanoparticles and canvas; in regenerative medicine to characterise roughness of polymer microspheres (Wright et al. 2015) **(Appendix 3)**, and in Microbiology to study the mechanics of oral biofilms and the adhesive and elastic properties between different strains of respiratory pathogens. These avenues further highlight the high transferability of this technique into other fields of research.

References

Abe, Y. et al., 2012. Cohesiveness and hydrodynamic properties of young drinking water biofilms. *Water Research*, 46(4), pp.1155–1166.

Abe, Y. et al., 2011. Elasticity and physico-chemical properties during drinking water biofilm formation. *Biofouling*, 27(7), pp.739–50. Available at: http://www.ncbi.nlm.nih.gov/pubmed/21762041.

Abu-Lail, N.I. & Camesano, T.A., 2003. Role of ionic strength on the relationship of biopolymer conformation, DLVO contributions, and steric interactions to bioadhesion of pseudomonas putida KT2442. *Biomacromolecules*, 4(4), pp.1000–1012.

Abu-Lail, N.I. & Camesano, T.A., 2006. Specific and nonspecific interaction forces between escherichia coli and silicon nitride, determined by poisson statistical analysis. *Langmuir*, 22(17), pp.7296–7301.

Acker, H., Van Dijck, P. & Coenye, T., 2014. Molecular mechanisms of antimicrobial tolerance and resistance in bacterial and fungal biofilms. *Trends in Microbiology*, 22(6), pp.326–333.

Aguayo, S. et al., 2015. Nanoadhesion of Staphylococcus aureus onto Titanium Implant Surfaces. *Journal of dental research*, 94(8), pp.1078–84. Available at: http://www.ncbi.nlm.nih.gov/pubmed/26130256.

Ahimou, F. et al., 2007. Effect of protein, polysaccharide, and oxygen concentration profiles on biofilm cohesiveness. *Applied and Environmental Microbiology*, 73(9), pp.2905–2910.

Albrektsson, T., Buser, D. & Sennerby, L., 2012. Crestal Bone Loss and Oral Implants. *Clinical Implant Dentistry and Related Research*, 14(6), pp.783–791.

Alcheikh, A. et al., 2013. PolyNaSS grafting on titanium surfaces enhances osteoblast differentiation and inhibits Staphylococcus aureus adhesion. *Journal of Materials Science: Materials in Medicine*, 24(7), pp.1745–1754.

Alsteens, D. et al., 2009. Unfolding individual Als5p adhesion proteins on live cells. *ACS Nano*, 3(7), pp.1677–1682.

Ammendolia, M.G. et al., 2014. Listeria monocytogenes Behaviour in Presence of Non-UV-Irradiated Titanium Dioxide Nanoparticles. *PLoS ONE*, 9(1).

An, Y.H. & Friedman, R.J., 1998. Concise review of mechanisms of bacterial adhesion to biomaterial surfaces. *Journal of biomedical materials research*, 43(3), pp.338–348.

Ananth, H. et al., 2015. A review on biomaterials in dental implantology. *International Journal of Biomedical Science*, 11(3), pp.113–120.

Anderson, J.M., Rodriguez, A. & Chang, D.T., 2008. Foreign body reaction to biomaterials. *Seminars in Immunology*, 20(2), pp.86–100.

Ando, T., Uchihashi, T. & Kodera, N., 2013. High-speed AFM and applications to biomolecular systems. *Annual review of biophysics*, 42(March), pp.393–414. Available at: http://www.ncbi.nlm.nih.gov/pubmed/23541159.

Ansari, M.A. et al., 2014. Gum arabic capped-silver nanoparticles inhibit biofilm formation by multi-drug resistant strains of Pseudomonas aeruginosa. *Journal of Basic Microbiology*, 54(7), pp.688–699.

Anselme, K. et al., 2010. The interaction of cells and bacteria with surfaces structured at the nanometre scale. *Acta Biomaterialia*, 6(10), pp.3824–3846.

Arciola, C.R. et al., 2012. Biofilm formation in Staphylococcus implant infections. A review of molecular mechanisms and implications for biofilm-resistant materials. *Biomaterials*, 33(26), pp.5967–5982.

Balaban, N. et al., 2003. Prevention of Staphylococcus aureus biofilm on dialysis catheters and adherence to human cells. *Kidney International*, 63(1), pp.340–345.

Bar-Zeev, E. et al., 2012. Revised paradigm of aquatic biofilm formation facilitated by microgel transparent exopolymer particles. *Proceedings of the National Academy of Sciences of the United States of America*, 109(23), pp.9119–24. Available at: http://www.pubmedcentral.nih.gov/articlerender.fcgi?artid=3384133&tool=pmcentrez&rendertype=abstract.

Barbeau, J. et al., 2003. Reassessing the presence of Candida albicans in denture-related stomatitis. *Oral Surgery, Oral Medicine, Oral Pathology, Oral Radiology,*

and Endodontics, 95(1), pp.51–59.

Barros, J. et al., 2013. A modular reactor to simulate biofilm development in orthopedic materials. *International Microbiology*, 16(3), pp.191–198.

Barros, J. et al., 2017. Staphylococcus aureus and Escherichia coli dual-species biofilms on nanohydroxyapatite loaded with CHX or ZnO nanoparticles. *Journal of Biomedical Materials Research Part A*, 105(2), pp.491–497. Available at: http://dx.doi.org/10.1002/jbm.a.35925.

Baselga, R., Albizu, I. & Amorena, B., 1994. Staphylococcus aureus capsule and slime as virulence factors in ruminant mastitis. A review. *Veterinary Microbiology*, 39(3–4), pp.195–204.

Beaussart, A. et al., 2013. Single-cell force spectroscopy of probiotic bacteria. *Biophysical Journal*, 104(9), pp.1886–1892.

Beaussart, A. et al., 2013. Single-cell force spectroscopy of the medically important Staphylococcus epidermidis-Candida albicans interaction. *Nanoscale*, 5(22), pp.10894–10900. Available at: http://pubs.rsc.org/en/content/articlepdf/2013/nr/c3nr03272h.

Beaussart, A. et al., 2012. Single-molecule imaging and functional analysis of Als adhesins and mannans during candida albicans morphogenesis. *ACS Nano*, 6(12), pp.10950–10964.

Beaussart, A. & El-Kirat-Chatel, S., 2014. Quantifying the forces guiding microbial cell adhesion using single-cell force spectroscopy. *Nature protocols*, 9(5), pp.1049–55. Available at: http://www.ncbi.nlm.nih.gov/pubmed/24722404%5Cnhttp://www.nature.com/nprot/journal/v9/n5/abs/nprot.2014.066.html.

Beckmann, M.A. et al., 2006. Measuring cell surface elasticity on enteroaggregative Escherichia coli wild type and dispersin mutant by AFM. *Ultramicroscopy*, 106(8–9), pp.695–702.

Beyth, N. et al., 2013. Rapid kill-novel endodontic sealer and Enterococcus faecalis. *PloS one*, 8(11), p.e78586. Available at: http://journals.plos.org/plosone/article?id=10.1371/journal.pone.0078586.

Binnig, G., Quate, C. & Gerber, C., 1986. Atomic Force Microscope. *Physical Review*

Letters, 56(9), pp.930–933. Available at: http://link.aps.org/doi/10.1103/PhysRevLett.56.930%5Cnpapers2://publication/uuid/551F6513-EAC6-4BC0-A144-AB381B706D40.

Boks, N.P. et al., 2008. Bond-Strengthening in Staphylococcal Adhesion to Hydrophilic and Hydrophobic Surfaces Using Atomic Force Microscopy. *Langmuir*, 24(22), pp.12990–12994.

Bolshakova, A. V., Kiselyova, O.I. & Yaminsky, I. V., 2004. Microbial surfaces investigated using atomic force microscopy. *Biotechnology Progress*, 20(6), pp.1615–1622.

Braga, P.C. & Ricci, D., 2011. Thymol-induced alterations in Candida albicans imaged by atomic force microscopy. *Methods in molecular biology (Clifton, N.J.)*, 736, pp.401–410.

Brand, A., 2012. Hyphal growth in human fungal pathogens and its role in virulence. *International Journal of Microbiology*.

Brown, J.S. et al., 2002. The classical pathway is the dominant complement pathway required for innate immunity to Streptococcus pneumoniae infection in mice. *Proceedings of the National Academy of Sciences of the United States of America*, 99(26), pp.16969–74. Available at: http://www.pnas.org/content/99/26/16969.

Buck, A.W. et al., 2010. Bonds between fibronectin and fibronectin-binding proteins on staphylococcus aureus and lactococcus lactis. *Langmuir*, 26(13), pp.10764–10770.

Bushnak, I. a et al., 2010. Adhesion of microorganisms to bovine submaxillary mucin coatings: effect of coating deposition conditions. *Biofouling*, 26(4), pp.387–97. Available at: http://www.ncbi.nlm.nih.gov/pubmed/20182931.

Cao, Z. et al., 2010. Rechargeable infection-responsive antifungal denture materials. *Journal of dental research*, 89(12), pp.1517–1521. Available at: http://jdr.sagepub.com.libproxy.uml.edu/content/89/12/1517.full.pdf+html.

Chan, Y., Haverkamp, R.G. & Hill, J.M., 2010. Force-extension formula for the worm-like chain model from a variational principle. *Journal of Theoretical Biology*, 262(3), pp.498–504.

Chen, Y. et al., 2014. Nanoscale cell wall deformation impacts long-range bacterial adhesion forces on surfaces. *Applied and Environmental Microbiology*, 80(2), pp.637–643.

Chen, Y. et al., 2011. Statistical Analysis of Long-and Short-Range Forces Involved in Bacterial Adhesion to Substratum Surfaces as Measured Using Atomic Force Microscopy. *Applied and environmental microbiology*, 77(15), pp.5065–5070.

Chen, Y. et al., 2012. under External Loading Bacterial Cell Surface Deformation under External Loading. *mBio*, 3(6), pp.1–7.

Chopinet, L. et al., 2013. Imaging living cells surface and quantifying its properties at high resolution using AFM in QI™ mode. *Micron (Oxford, England : 1993)*, 48, pp.26–33. Available at: http://www.ncbi.nlm.nih.gov/pubmed/23522742.

Cochran, D.L. et al., 1998. Bone response to unloaded and loaded titanium implants with a sandblasted and acid-etched surface: A histometric study in the canine mandible. *Journal of Biomedical Materials Research*, 40(1), pp.1–11.

Coldren, F.M. et al., 2009. Encapsulated Staphylococcus aureus strains vary in adhesiveness assessed by atomic force microscopy. *Journal of Biomedical Materials Research - Part A*, 89(2), pp.402–410.

Cooper, L.F., 2000. A role for surface topography in creating and maintaining bone at titanium endosseous implants. *Journal of Prosthetic Dentistry*, 84(5), pp.522–534.

Costerton, J.W. et al., 1995. Microbial biofilms. *Annual review of microbiology*, 49, pp.711–45. Available at: http://www.annualreviews.org/doi/abs/10.1146/annurev.mi.49.100195.003431.

Dai, L. et al., 2011. The effect of QMix, an experimental antibacterial root canal irrigant, on removal of canal wall smear layer and debris. *Journal of Endodontics*, 37(1), pp.80–84.

Dalby, M.J. et al., 2007. The control of human mesenchymal cell differentiation using nanoscale symmetry and disorder. *Nature Materials*, 6(5), pp.407–413.

Díaz, C. et al., 2007. Nano/microscale order affects the early stages of biofilm formation on metal surfaces. *Langmuir*, 23(22), pp.11206–11210.

Doktycz, M.J. et al., 2003. AFM imaging of bacteria in liquid media immobilized on gelatin coated mica surfaces. *Ultramicroscopy*, 97(1–4), pp.209–216.

Dokukin, M.E., Guz, N. V. & Sokolov, I., 2013. Quantitative study of the elastic modulus of loosely attached cells in AFM indentation experiments. *Biophysical Journal*, 104(10), pp.2123–2131.

Dorobantu, L.S. et al., 2009. Analysis of force interactions between AFM tips and hydrophobic bacteria using DLVO theory. *Langmuir*, 25(12), pp.6968–6976.

Dorobantu, L.S. & Gray, M.R., 2010. Application of atomic force microscopy in bacterial research. *Scanning*, 32(2), pp.74–96.

Dreyer, D.R. et al., 2012. Elucidating the structure of poly(dopamine). *Langmuir*, 28(15), pp.6428–6435.

Dufrene, Y.F., 2015. Sticky microbes: Forces in microbial cell adhesion. *Trends in Microbiology*, 23(6), pp.376–382.

Dufrêne, Y.F., 2008. Atomic force microscopy and chemical force microscopy of microbial cells. *Nature Protocols*, 3(7), pp.1132–1138. Available at: http://www.ncbi.nlm.nih.gov/pubmed/18600218%5Cnhttp://www.nature.com/doifinder/10.1038/nprot.2008.101.

Dufrene, Y.F. & Pelling, A.E., 2013. Force nanoscopy of cell mechanics and cell adhesion. *Nanoscale*, 5(10), pp.4094–4104. Available at: http://dx.doi.org/10.1039/C3NR00340J%5Cnhttp://pubs.rsc.org/en/content/articlepdf/2013/nr/c3nr00340j.

Edmiston, C.E. et al., 2013. Reducing the risk of surgical site infections: Does chlorhexidine gluconate provide a risk reduction benefit? *American Journal of Infection Control*, 41(5 SUPPL.).

El-Kirat-Chatel, S., Beaussart, A., et al., 2014. Single-cell and single-molecule analysis deciphers the localization, adhesion, and mechanics of the biofilm adhesin LapA. *ACS Chemical Biology*, 9(2), pp.485–494.

El-Kirat-Chatel, S., Boyd, C.D., et al., 2014. Single-molecule analysis of pseudomonas fluorescens footprints. *ACS Nano*, 8(2), pp.1690–1698.

Eskhan, A.O. & Abu-Lail, N.I., 2014. A new approach to decoupling of bacterial adhesion energies measured by AFM into specific and nonspecific components.

Colloid and Polymer Science, 292(2), pp.343–353.

Esposito, M. et al., 1998. Biological factors contributing to failures of osseointegrated oral implants. (I). Success criteria and epidemiology. *European journal of oral sciences*, 106(1), pp.527–551.

Esposito, M. et al., 2007. Interventions for replacing missing teeth: Management of soft tissues for dental implants. *Cochrane Database of Systematic Reviews*, (3).

Estevez, M. et al., 2015. Adhesion and migration of cells responding to microtopography. *Journal of Biomedical Materials Research - Part A*, 103(5), pp.1659–1668.

Evans, E. a & Calderwood, D. a, 2007. Forces and bond dynamics in cell adhesion. *Science (New York, N.Y.)*, 316(5828), pp.1148–53. Available at: http://www.ncbi.nlm.nih.gov/pubmed/17525329.

Evans, K. et al., 2014. Systematic study of genes influencing cellular chain length in Streptococcus sanguinis. *Microbiology (United Kingdom)*, 160(PART 2), pp.307–315.

Ford, C.B. et al., 2013. Mycobacterium tuberculosis mutation rate estimates from different lineages predict substantial differences in the emergence of drug-resistant tuberculosis. *Nature genetics*, 45(7), pp.784–90. Available at: http://www.pubmedcentral.nih.gov/articlerender.fcgi?artid=3777616&tool=pmcentrez&rendertype=abstract.

Formosa, C. et al., 2015. Multiparametric imaging of adhesive nanodomains at the surface of Candida albicans by atomic force microscopy. *Nanomedicine: Nanotechnology, Biology, and Medicine*, 11(1), pp.57–65.

Formosa, C. et al., 2012. Nanoscale analysis of the effects of antibiotics and CX1 on a Pseudomonas aeruginosa multidrug-resistant strain. *Scientific Reports*, 2, p.575. Available at: http://www.ncbi.nlm.nih.gov/pmc/articles/PMC3418629/.

Formosa, C. & Dague, E., 2015. Imaging Living Yeast Cells and Quantifying Their Biophysical Properties by Atomic Force Microscopy. In T. E. S. Dahms & K. J. Czymmek, eds. *Advanced Microscopy in Mycology*. Cham: Springer International Publishing, pp. 125–141. Available at: http://dx.doi.org/10.1007/978-3-319-22437-4_7.

Franchi, M. et al., 2004. Osteogenesis and morphology of the peri-implant bone facing dental implants. *TheScientificWorldJournal*, 4, pp.1083–1095.

Francius, G. et al., 2008. Direct observation of Staphylococcus aureus cell wall digestion by lysostaphin. *Journal of Bacteriology*, 190(24), pp.7904–7909.

Francius, G. et al., 2009. Stretching polysaccharides on live cells using single molecule force spectroscopy. *Nature Protocols*, 4(6), pp.939–946. Available at: http://www.nature.com/doifinder/10.1038/nprot.2009.65.

Francius, G. et al., 2013. Thermo-regulated adhesion of the streptococcus thermophilus δrgg0182 strain. *Langmuir*, 29(15), pp.4847–4856.

Fritz, J. et al., 2000. Translating biomolecular recognition into nanomechanics. *Science (New York, N.Y.)*, 288(5464), pp.316–8. Available at: http://www.ncbi.nlm.nih.gov/pubmed/10764640.

Fürst, M.M. et al., 2007. Bacterial colonization immediately after installation on oral titanium implants. *Clinical Oral Implants Research*, 18(4), pp.501–508.

Gaboriaud, F. & Dufrêne, Y.F., 2007. Atomic force microscopy of microbial cells: Application to nanomechanical properties, surface forces and molecular recognition forces. *Colloids and Surfaces B: Biointerfaces*, 54(1), pp.10–19.

Gallo, J., Holinka, M. & Moucha, C.S., 2014. Antibacterial surface treatment for orthopaedic implants. *International Journal of Molecular Sciences*, 15(8), pp.13849–13880.

Geetha, M. et al., 2009. Ti based biomaterials, the ultimate choice for orthopaedic implants - A review. *Progress in Materials Science*, 54(3), pp.397–425.

Gilbert, P. & Moore, L.E., 2005. Cationic antiseptics: Diversity of action under a common epithet. *Journal of Applied Microbiology*, 99(4), pp.703–715.

Gilbert, Y. et al., 2007. Single-Molecule Force Spectroscopy and Imaging of the Vancomycin/D-Ala-D-Ala Interaction. *Nano Letters*, 7, pp.796–801. Available at: http://pubs3.acs.org/acs/journals/doilookup?in_doi=10.1021/nl0700853.

Glaubitz, M. et al., 2014. A novel contact model for AFM indentation experiments on soft spherical cell-like particles. *Soft Matter*, 10(35), pp.6732–6741. Available at: http://pubs.rsc.org/en/content/articlelanding/2014/sm/c4sm00788c%5Cnht

tp://pubs.rsc.org/en/content/articlelanding/2014/sm/c4sm00788c#!divAbstract%5Cnhttp://pubs.rsc.org/en/content/articlepdf/2014/sm/c4sm00788c.

Gordesli, F.P. & Abu-Lail, N.I., 2012. Combined poisson and soft-particle DLVO analysis of the specific and nonspecific adhesion forces measured between L. monocytogenes grown at various temperatures and silicon nitride. *Environmental Science and Technology*, 46(18), pp.10089–10098.

Gordesli, F.P. & Abu-Lail, N.I., 2012. The role of growth temperature in the adhesion and mechanics of pathogenic *L. monocytogenes*: An AFM study. *Langmuir*, 28(2), pp.1360–1373.

Goulter-Thorsen, R.M. et al., 2011. Surface Roughness of Stainless Steel Influences Attachment and Detachment of Escherichia coli O157. *Journal of food protection*, 74(8), pp.1359–63. Available at: http://www.ncbi.nlm.nih.gov/pubmed/21819667.

Groot, P.W.J. et al., 2013. Adhesins in human fungal pathogens: Glue with plenty of stick. *Eukaryotic Cell*, 12(4), pp.470–481.

Grossner-Schreiber, B. et al., 2001. Plaque formation on surface modified dental implants. An in vitro study. *Clinical oral implants research*, 12(6), pp.543–551.

Hall-Stoodley, L. & Stoodley, P., 2009. Evolving concepts in biofilm infections. *Cellular Microbiology*, 11(7), pp.1034–1043.

Hamada, S. et al., 1998. The importance of fimbriae in the virulence and ecology of some oral bacteria. *Oral microbiology and immunology*, 13(3), pp.129–38. Available at: http://www.ncbi.nlm.nih.gov/pubmed/10093527.

Hao, Y. et al., 2010. An electron microscopy study of the diversity of Streptococcus sanguinis cells induced by lysozyme in vitro. *Journal of Electron Microscopy*, 59(4), pp.311–320.

Harimawan, A. et al., 2013. Adhesion of B. subtilis spores and vegetative cells onto stainless steel - DLVO theories and AFM spectroscopy. *Journal of Colloid and Interface Science*, 405, pp.233–241.

Harimawan, A., Rajasekar, A. & Ting, Y.P., 2011. Bacteria attachment to surfaces - AFM force spectroscopy and physicochemical analyses. *Journal of Colloid and Interface Science*, 364(1), pp.213–218.

Harris, L.G., Foster, S.J. & Richards, R.G., 2002. An introduction to Staphylococcus aureus, and techniques for identifying and quantifying S. aureus adhesisn in relation to adhesion to biomaterials: Review. *European Cells and Materials*, 4, pp.39–60. Available at: http://www.ecmjournal.org/journal/papers/vol004/vol004a04.php.

Hartford, O. et al., 1997. The dipeptide repeat region of the fibrinogen-binding protein (clumping factor) is required for functional expression of the fibrinogen-binding domain on the Staphylococcus aureus cell surface. *Molecular microbiology*, 25(6), pp.1065–76. Available at: http://www.ncbi.nlm.nih.gov/pubmed/9350863.

Hassett, D.J. et al., 2010. Pseudomonas aeruginosa biofilm infections in cystic fibrosis: insights into pathogenic processes and treatment strategies. *Expert opinion on therapeutic targets*, 14(2), pp.117–30. Available at: http://www.ncbi.nlm.nih.gov/pubmed/20055712.

Hassett, D.J. et al., 2009. Pseudomonas aeruginosa hypoxic or anaerobic biofilm infections within cystic fibrosis airways. *Trends in Microbiology*, 17(3), pp.130–138.

Heinisch, J.J. et al., 2012. Atomic force microscopy - looking at mechanosensors on the cell surface. *Journal of cell science*, 125(Pt 18), pp.4189–95. Available at: http://www.pubmedcentral.nih.gov/articlerender.fcgi?artid=3516434&tool=pmcentrez&rendertype=abstract.

Helenius, J. et al., 2008. Single-cell force spectroscopy. *Journal of Cell Science*, 121(11), pp.1785–1791. Available at: http://jcs.biologists.org/cgi/doi/10.1242/jcs.030999.

Herman, P. et al., 2013. Forces driving the attachment of staphylococcus epidermidis to fibrinogen-coated surfaces. *Langmuir*, 29(42), pp.13018–13022.

Herman, P. et al., 2014. The binding force of the staphylococcal adhesin SdrG is remarkably strong. *Molecular Microbiology*, 93(2), pp.356–368.

Hermansson, M., 1999. The DLVO theory in microbial adhesion. *Colloids and Surfaces B: Biointerfaces*, 14(1–4), pp.105–119.

Hojo, K. et al., 2009. Bacterial interactions in dental biofilm development. *Journal of*

dental research, 88(11), pp.982–90.

Hu, S. et al., 2014. Rapid detection of isoniazid resistance in Mycobacterium tuberculosis isolates by use of real-time-PCR-based melting curve analysis. *Journal of Clinical Microbiology*, 52(5), pp.1644–1652.

Huebsch, N. & Mooney, D.J., 2009. Inspiration and application in the evolution of biomaterials. *Nature*, 462(7272), pp.426–32. Available at: http://dx.doi.org/10.1038/nature08601.

Huo, K. et al., 2013. Osteogenic activity and antibacterial effects on titanium surfaces modified with Zn-incorporated nanotube arrays. *Biomaterials*, 34(13), pp.3467–3478.

Hwang, G. et al., 2015. Binding Force Dynamics of Streptococcus mutans-glucosyltransferase B to Candida albicans. *J Dent Res*, 94(9), pp.1310–1317. Available at: http://jdr.sagepub.com/content/94/9/1310.full.pdf.

Hyams, C. et al., 2010. The Streptococcus pneumoniae capsule inhibits complement activity and neutrophil phagocytosis by multiple mechanisms. *Infection and Immunity*, 78(2), pp.704–715.

Ivanov, I.E. et al., 2011. Relating the physical properties of pseudomonas aeruginosa lipopolysaccharides to virulence by atomic force microscopy. *Journal of Bacteriology*, 193(5), pp.1259–1266.

Izquierdo-Barba, I. et al., 2015. Nanocolumnar coatings with selective behavior towards osteoblast and Staphylococcus aureus proliferation. *Acta Biomaterialia*, 15, pp.20–28.

Izumida, F.E. et al., 2014. In vitro evaluation of adherence of Candida albicans, Candida glabrata, and Streptococcus mutans to an acrylic resin modified by experimental coatings. *Biofouling*, 30(5), pp.525–33. Available at: http://www.ncbi.nlm.nih.gov/pubmed/24684564.

Jackson, S. et al., 2014. Biofilm development by blastospores and hyphae of Candida albicans on abraded denture acrylic resin surfaces. *Journal of Prosthetic Dentistry*, 112(4), pp.988–993.

Jacquot, A. et al., 2014. Dynamic modulation of fimbrial extension and FimH-mannose binding force on live bacteria under pH changes: A molecular atomic

force microscopy analysis. *Journal of Biomedical Nanotechnology*, 10(11), pp.3361–3372.

Jahed, Z. et al., 2014. Responses of Staphylococcus aureus bacterial cells to nanocrystalline nickel nanostructures. *Biomaterials*, 35(14), pp.4249–4254.

Jakubovics, N.S., Yassin, S.A. & Rickard, A.H., 2014. Community Interactions of Oral Streptococci. *Advances in Applied Microbiology*, 87, pp.43–110.

Jalili, N. & Laxminarayana, K., 2004. A review of atomic force microscopy imaging systems: Application to molecular metrology and biological sciences. *Mechatronics*, 14(8), pp.907–945.

Kabir, M.A., Hussain, M.A. & Ahmad, Z., 2012. Candida albicans: A Model Organism for Studying Fungal Pathogens. *International Scholarly Research Network Microbiology*, 2012, pp.1–15.

Kang, S. & Elimelech, M., 2009. Bioinspired single bacterial cell force spectroscopy. *Langmuir*, 25(17), pp.9656–9659.

Kara, D., Luppens, S.B.I. & Ten Cate, J.M., 2006. Differences between single- and dual-species biofilms of Streptococcus mutans and Veillonella parvula in growth, acidogenicity and susceptibility to chlorhexidine. *European Journal of Oral Sciences*, 114(1), pp.58–63.

Kashef, J. & Franz, C.M., 2015. Quantitative methods for analyzing cell-cell adhesion in development. *Developmental Biology*, 401(1), pp.165–174.

Katsikogianni, M. & Missirlis, Y.F., 2004. Concise review of mechanisms of bacterial adhesion to biomaterials and of techniques used in estimating bacteria-material interactions - True Open Access. *MEu. rKopatesaink oCgeiallnsn ain adn dM Ya.tFe.r iMaliss*, 8(August), pp.37–57. Available at: http://www.ecmjournal.org/journal/papers/vol008/vol008a05.php.

Keane, F.M. et al., 2007. Fibrinogen and elastin bind to the same region within the A domain of fibronectin binding protein A, an MSCRAMM of Staphylococcus aureus. *Molecular Microbiology*, 63(3), pp.711–723.

Khan, M.R. et al., 2012. The enhanced modulation of key bone matrix components by modified Titanium implant surfaces. *Bone*, 50(1), pp.1–8.

Kishen, A. et al., 2008. Influence of Irrigation Regimens on the Adherence of

Enterococcus faecalis to Root Canal Dentin. *Journal of Endodontics*, 34(7), pp.850–854.

Kneidinger, B. et al., 2003. Three Highly Conserved Proteins Catalyze the Conversion of UDP-N-acetyl-d-glucosamine to Precursors for the Biosynthesis of O Antigen in Pseudomonas aeruginosaO11 and Capsule in Staphylococcus aureus Type 5: IMPLICATIONS FOR THE UDP-N-ACETYL-l-FUCOSAMIN. *Journal of Biological Chemistry* , 278(6), pp.3615–3627. Available at: http://www.jbc.org/content/278/6/3615.abstract.

Krasowska, A. et al., 2009. The antagonistic effect of Saccharomyces boulardii on Candida albicans filamentation, adhesion and biofilm formation. *FEMS Yeast Research*, 9(8), pp.1312–1321.

Krieg, M. et al., 2008. A bond for a lifetime: Employing membrane nanotubes from living cells to determine receptor-ligand kinetics. *Angewandte Chemie - International Edition*, 47(50), pp.9775–9777.

Lamont, R.J. et al., 1995. Porphyromonas gingivalis Invasion of Gingival Epithelial Cells. *INFECTION AND IMMUNITY*, 63(10), pp.3878–3885.

Le, D.T.L. et al., 2013. Unraveling the role of surface mucus-binding protein and pili in muco-adhesion of Lactococcus lactis. *PLoS ONE*, 8(11).

Lee, A. & Wang, H.-L., 2010. Biofilm related to dental implants. *Implant dentistry*, 19(5), pp.387–393.

Lee, H. et al., 2007. Mussel-inspired surface chemistry for multifunctional coatings. *Science (New York, N.Y.)*, 318(5849), pp.426–430.

Lindhe, J. & Meyle, J., 2008. Peri-implant diseases: Consensus Report of the Sixth European Workshop on Periodontology. In *Journal of Clinical Periodontology*. pp. 282–285.

Liu, Y., Strauss, J. & Camesano, T.A., 2008. Adhesion forces between Staphylococcus epidermidis and surfaces bearing self-assembled monolayers in the presence of model proteins. *Biomaterials*, 29(33), pp.4374–4382.

Logan, N. et al., 2015. TiO2-coated CoCrMo: Improving the osteogenic differentiation and adhesion of mesenchymal stem cells in vitro. *Journal of Biomedical Materials Research Part A*, 103(3), pp.1208–1217. Available at:

http://dx.doi.org/10.1002/jbm.a.35264.

Logan, N. & Brett, P., 2013. The control of mesenchymal stromal cell osteogenic differentiation through modified surfaces. *Stem Cells International*.

Long, M. & Rack, H.J., 1998. Titanium alloys in total joint replacement--a materials science perspective. *Biomaterials*, 19(18), pp.1621–1639.

Longo, G. et al., 2012. Force volume and stiffness tomography investigation on the dynamics of stiff material under bacterial membranes. In *Journal of Molecular Recognition*. pp. 278–284.

Lorenzetti, M. et al., 2015. The influence of surface modification on bacterial adhesion to titanium-based substrates. *ACS Applied Materials and Interfaces*, 7(3), pp.1644–1651.

Loskill, P. et al., 2014. Reduction of the peptidoglycan crosslinking causes a decrease in stiffness of the staphylococcus aureus cell envelope. *Biophysical Journal*, 107(5), pp.1082–1089.

Louise Meyer, R. et al., 2010. Immobilisation of living bacteria for AFM imaging under physiological conditions. *Ultramicroscopy*, 110(11), pp.1349–1357.

Lower, B.H. et al., 2005. Simultaneous force and fluorescence measurements of a protein that forms a bond between a living bacterium and a solid surface. *Journal of Bacteriology*, 187(6), pp.2127–2137.

Lundgren, D., Rylander, H. & Laurell, L., 2008. To save or to extract, that is the question. Natural teeth or dental implants in periodontitis-susceptible patients: Clinical decision-making and treatment strategies exemplified with patient case presentations. *Periodontology 2000*, 47(1), pp.27–50.

Marco, F. et al., 2005. Peri-implant osteogenesis in health and osteoporosis. *Micron*, 36(7–8), pp.630–644.

Marszalek, P.E. & Dufrêne, Y.F., 2012. Stretching single polysaccharides and proteins using atomic force microscopy. *Chemical Society Reviews*, 41, pp.3523–3534. Available at: http://xlink.rsc.org/?DOI=c2cs15329g.

Mayer, F.L., Wilson, D. & Hube, B., 2013. Candida albicans pathogenicity mechanisms. *Virulence*, 4(2), pp.119–28. Available at: http://www.pubmedcentral.nih.gov/articlerender.fcgi?artid=3654610&tool=p

mcentrez&rendertype=abstract.

McConnell, M.D. et al., 2010. Bacterial plaque retention on oral hard materials: Effect of surface roughness, surface composition, and physisorbed polycarboxylate. *Journal of Biomedical Materials Research - Part A*, 92(4), pp.1518–1527.

Mcdonnell, G. & Russell, A.D., 1999. Antiseptics and disinfectants: Activity, action, and resistance. *Clinical Microbiology Reviews*, 12(1), pp.147–179.

McKendry, R. a, 2012. Nanomechanics of superbugs and superdrugs: new frontiers in nanomedicine. *Biochemical Society transactions*, 40(4), pp.603–8. Available at: http://www.ncbi.nlm.nih.gov/pubmed/22817702.

Mei, H.C. et al., 2000. Direct Probing by Atomic Force Microscopy of the Cell Surface Softness of a Fibrillated and Nonfibrillated Oral Streptococcal Strain. *Biophysical Journal*, 78(5), pp.2668–2674. Available at: http://www.scopus.com/inward/record.url?eid=2-s2.0-0034022186&partnerID=tZOtx3y1%5Cnhttp://linkinghub.elsevier.com/retrieve/pii/S000634950076810X.

Mei, H.C., de Vries, J. & Busscher, H.J., 2010. Weibull analyses of bacterial interaction forces measured using AFM. *Colloids and Surfaces B: Biointerfaces*, 78(2), pp.372–375.

Mei, L. et al., 2011. Influence of surface roughness on streptococcal adhesion forces to composite resins. *Dental materials : official publication of the Academy of Dental Materials*, 27(8), pp.770–8. Available at: http://www.ncbi.nlm.nih.gov/pubmed/21524789.

Mei, L. et al., 2009. Poisson analysis of streptococcal bond-strengthening on saliva-coated enamel. *Journal of dental research*, 88(9), pp.841–5. Available at: http://www.ncbi.nlm.nih.gov/pubmed/19767582.

Méndez-Vilas, A., Gallardo-Moreno, A.M. & González-Martín, M.L., 2007. Atomic force microscopy of mechanically trapped bacterial cells. *Microscopy and microanalysis : the official journal of Microscopy Society of America, Microbeam Analysis Society, Microscopical Society of Canada*, 13(1), pp.55–64.

Metavarayuth, K. et al., 2016. Influence of Surface Topographical Cues on the Differentiation of Mesenchymal Stem Cells in Vitro. *ACS Biomaterials Science &*

Engineering, 2(2), pp.142–151. Available at: http://pubs.acs.org/doi/abs/10.1021/acsbiomaterials.5b00377.

Muller, D.J. et al., 2009. Force probing surfaces of living cells to molecular resolution. *Nat Chem Biol*, 5(6), pp.383–390. Available at: http://www.ncbi.nlm.nih.gov/pubmed/19448607.

Naglik, J.R., Richardson, J.P. & Moyes, D.L., 2014. Candida albicans Pathogenicity and Epithelial Immunity. *PLoS Pathogens*, 10(8).

Navarre, W.W. & Schneewind, O., 1999. Surface proteins of gram-positive bacteria and mechanisms of their targeting to the cell wall envelope. *Microbiology and molecular biology reviews : MMBR*, 63(1), pp.174–229. Available at: http://www.pubmedcentral.nih.gov/articlerender.fcgi?artid=98962&tool=pmcentrez&rendertype=abstract.

Ndieyira, J.W. et al., 2008. Nanomechanical detection of antibiotic-mucopeptide binding in a model for superbug drug resistance. *Nat.Nanotechnol.*, 3(1748–3395 (Electronic)), pp.691–696. Available at: c:%5CKARSTEN%5CPDFs%5CMethodik-PDFs%5CMethodik-2008%5CNdieyira et al.-Nanomechanical detection of antibiotic-mucopeptide binding in a model for superbug drug resistance.pdf.

Nett, J.E. et al., 2010. Development and validation of an in vivo Candida albicans biofilm denture model. *Infection and Immunity*, 78(9), pp.3650–3659.

Núñez, M.E. et al., 2005. Atomic force microscopy of bacterial communities. *Methods in Enzymology*, 397, pp.256–268.

O'Brien, F.J., 2011. Biomaterials & scaffolds for tissue engineering. *Materials Today*, 14(3), pp.88–95.

O'Donnell, L.E. et al., 2016. Dentures are a Reservoir for Respiratory Pathogens. *Journal of Prosthodontics*, 25(2), pp.99–104.

O'Neill, E. et al., 2008. A novel Staphylococcus aureus biofilm phenotype mediated by the fibronectin-binding proteins, FnBPA and FnBPB. *Journal of Bacteriology*, 190(11), pp.3835–3850.

Oh, Y.J. et al., 2009. Effects of substrates on biofilm formation observed by atomic force microscopy. *Ultramicroscopy*, 109(8), pp.874–880.

Okahashi, N. et al., 2010. Pili of oral Streptococcus sanguinis bind to fibronectin and contribute to cell adhesion. *Biochemical and Biophysical Research Communications*, 391(2), pp.1192–1196.

Olivares-Navarrete, R. et al., 2011. Mediation of osteogenic differentiation of human mesenchymal stem cells on titanium surfaces by a Wnt-integrin feedback loop. *Biomaterials*, 32(27), pp.6399–6411.

Otto, M., 2013. Staphylococcal infections: mechanisms of biofilm maturation and detachment as critical determinants of pathogenicity. *Annu Rev Med*, 64, pp.175–188. Available at: http://www.annualreviews.org/doi/abs/10.1146/annurev-med-042711-140023.

Ovchinnikova, E.S. et al., 2012. Evaluation of adhesion forces of Staphylococcus aureus along the length of Candida albicans hyphae. *BMC Microbiol.*, 12(1471–2180 (Electronic)), p.281. Available at: BMC Microbiology.

Ovchinnikova, E.S. et al., 2013. Exchange of adsorbed serum proteins during adhesion of Staphylococcus aureus to an abiotic surface and Candida albicans hyphae-An AFM study. *Colloids and Surfaces B: Biointerfaces*, 110, pp.45–50.

Pan, H. et al., 2015. Cold plasma-induced surface modification of heat-polymerized acrylic resin and prevention of early adherence of *Candida albicans* . *Dental Materials Journal*, 34(4), pp.529–536.

Park, H.S.M. et al., 2001. Structural alterations in a type IV pilus subunit protein result in concurrent defects in multicellular behaviour and adherence to host tissue. *Molecular Microbiology*, 42(2), pp.293–307.

Park, S.E. et al., 2008. Candida albicans adherence to surface-modified denture resin surfaces. *Journal of Prosthodontics*, 17(5), pp.365–369.

Patti, J.M. et al., 1992. Molecular characterization and expression of a gene encoding a Staphylococcus aureus collagen adhesin. *J Biol Chem*, 267(7), pp.4766–4772. Available at: http://www.ncbi.nlm.nih.gov/entrez/query.fcgi?cmd=Retrieve&db=PubMed&dopt=Citation&list_uids=1311320.

Peters, B.M. et al., 2012. Staphylococcus aureus adherence to Candida albicans

hyphae is mediated by the hyphal adhesin Als3p. *Microbiology (United Kingdom)*, 158(12), pp.2975–2986.

Pihl, M. et al., 2013. Biofilm formation by Staphylococcus epidermidis on peritoneal dialysis catheters and the effects of extracellular products from Pseudomonas aeruginosa. *Pathogens and Disease*, 67(3), pp.192–198.

Pillet, F. et al., 2014. Atomic Force Microscopy and pharmacology: From microbiology to cancerology. *Biochimica et Biophysica Acta - General Subjects*, 1840(3), pp.1028–1050.

Pinzón-Arango, P.A., Nagarajan, R. & Camesano, T.A., 2010. Effects of L-alanine and inosine germinants on the elasticity of bacillus anthracis spores. *Langmuir*, 26(9), pp.6535–6541.

Postollec, F. et al., 2006. Interactive forces between co-aggregating and non-co-aggregating oral bacterial pairs. *Journal of dental research*, 85(3), pp.231–4. Available at: http://www.ncbi.nlm.nih.gov/pubmed/16498069.

Powell, L.C. et al., 2013. The effect of alginate oligosaccharides on the mechanical properties of Gram-negative biofilms. *Biofouling*, 29(4), pp.413–21. Available at: http://www.tandfonline.com/doi/abs/10.1080/08927014.2013.777954.

Puckett, S.D. et al., 2010. The relationship between the nanostructure of titanium surfaces and bacterial attachment. *Biomaterials*, 31(4), pp.706–713.

Qu, W. et al., 2012. Bacterial Adhesion Forces to Ag-Impregnated Contact Lens Cases and Transmission to Contact Lenses. *Cornea*, 0(0), p.1.

Qu, W. et al., 2013. Nonadhesive, silica nanoparticles-based brush-coated contact lens cases-Compromising between ease of cleaning and microbial transmission to contact lenses. *Journal of Biomedical Materials Research - Part B Applied Biomaterials*, 101(4), pp.640–647.

Rangel, D.E. et al., 2013. Observation of Bacterial Type I Pili Extension and Contraction under Fluid Flow. *PLoS ONE*, 8(6).

Ratner, B.D. & Bryant, S.J., 2004. Biomaterials: where we have been and where we are going. *Annu Rev Biomed Eng*, 6, pp.41–75.

Renvert, S. et al., 2008. Clinical and microbiological analysis of subjects treated with Branemark or AstraTech implants: a 7-year follow-up study. *Clinical oral*

implants research, 19(4), pp.342–347.

Roberts, C. et al., 2006. Characterizing the effect of the Staphylococcus aureus virulence factor regulator, SarA, on log-phase mRNA half-lives. *Journal of Bacteriology*, 188(7), pp.2593–2603.

Rodríguez-Hernández, A.G. et al., 2011. Streptococcus sanguinis adhesion on titanium rough surfaces: Effect of shot-blasting particles. *Journal of Materials Science: Materials in Medicine*, 22(8), pp.1913–1922.

Rukke, H. V., Hegna, I.K. & Petersen, F.C., 2012. Identification of a functional capsule locus in Streptococcus mitis. *Molecular Oral Microbiology*, 27(2), pp.95–108.

Rupp, F. et al., 2006. Enhancing surface free energy and hydrophilicity through chemical modification of microstructured titanium implant surfaces. *Journal of Biomedical Materials Research - Part A*, 76(2), pp.323–334.

Sakiyama-Elbert, S.E. & Hubbell, J.A., 2001. Functional biomaterials: Design of novel biomaterials. *Annual Review of Materials Research*, 31(1), pp.183–201. Available at: http://www.annualreviews.org/doi/abs/10.1146/annurev.matsci.31.1.183.

Salvatori, O. et al., 2016. Innate Immunity and Saliva in Candida albicans-mediated Oral Diseases. *Journal of dental research*, 95(4), pp.365–371. Available at: http://jdr.sagepub.com/content/95/4/365?etoc.

Schaer-Zammaretti, P. & Ubbink, J., 2003. Imaging of lactic acid bacteria with AFM - Elasticity and adhesion maps and their relationship to biological and structural data. *Ultramicroscopy*, 97(1–4), pp.199–209.

Schmidlin, P.R. et al., 2013. Polyspecies biofilm formation on implant surfaces with different surface characteristics. *Journal of applied oral science: revista FOB*, 21(1), pp.48–55. Available at: http://www.pubmedcentral.nih.gov/articlerender.fcgi?artid=3881803&tool=pmcentrez&rendertype=abstract.

Setzer, F.C. & Kim, S., 2014. Comparison of long-term survival of implants and endodontically treated teeth. *Journal of dental research*, 93(1), pp.19–26.

Setzer, F.C. & Kim, S., 2013. Comparison of long-term survival of implants and endodontically treated teeth. *Journal of dental research*, 93(1), pp.19–26. Available at: http://www.ncbi.nlm.nih.gov/pubmed/24065635.

Shalabi, M.M. et al., 2006. Implant surface roughness and bone healing: a systematic review. *Journal of dental research*, 85(6), pp.496–500.

Sheng, X., Ting, Y.-P. & Pehkonen, S.O., 2007. Force measurements of bacterial adhesion on metals using a cell probe atomic force microscope. *Journal of Colloid and Interface Science*, 310(2), pp.661–669. Available at: http://www.sciencedirect.com/science/article/B6WHR-4MYVG85-3/2/86babc3a32122728be432046e92cc162%5Cn%5C%5CKwi-server%5Cliteratur%5Cedo%5Carticles%5CRES%5CRES_0128.pdf.

Shirley, K.P. et al., 2015. In Vitro Effects of Plantago Major Extract, Aucubin, and Baicalein on Candida Albicans Biofilm Formation, Metabolic Activity, and Cell Surface Hydrophobicity. *Journal of Prosthodontics*.

Silva, A. & Teschke, O., 2003. Effects of the antimicrobial peptide PGLa on live Escherichia coli. *Biochimica et Biophysica Acta - Molecular Cell Research*, 1643(1–3), pp.95–103.

Socransky, S.S. et al., 1998. Microbial complexes in subgingival plaque. *Journal of clinical periodontology*, 25(2), pp.134–144.

Staniszewska, M. et al., 2013. Candida albicans morphologies revealed by scanning electron microscopy analysis. *Brazilian journal of microbiology : [publication of the Brazilian Society for Microbiology]*, 44(3), pp.813–21. Available at: http://www.pubmedcentral.nih.gov/articlerender.fcgi?artid=3910194&tool=pmcentrez&rendertype=abstract.

Storm, C. & Nelson, P., 2003. Theory of high-force DNA stretching and overstretching. *Physical Review E*, 67(5), p.51906. Available at: http://link.aps.org/doi/10.1103/PhysRevE.67.051906.

Strange, A.P. et al., 2017. Quantitative nanohistological investigation of scleroderma: an atomic force microscopy-based approach to disease characterization. *International journal of nanomedicine*, 12, pp.411–420. Available at: https://www.dovepress.com/quantitative-nanohistological-investigation-of-scleroderma-an-atomic-f-peer-reviewed-article-IJN [Accessed February 21, 2017].

Subramani, K. et al., 2009. Biofilm on dental implants: a review of the literature. *The*

International journal of oral & maxillofacial implants, 24(4), pp.616–626.

Sudbery, P.E., 2011. Growth of Candida albicans hyphae. *Nature reviews. Microbiology*, 9(10), pp.737–748. Available at: http://dx.doi.org/10.1038/nrmicro2636.

Sullan, R.M.A. et al., 2015. Binding forces of Streptococcus mutans P1 adhesin. *ACS Nano*, 9(2), pp.1448–1460.

Svensson, S. et al., 2014. Role of nanostructured gold surfaces on monocyte activation and Staphylococcus epidermidis biofilm formation. *International Journal of Nanomedicine*, 9(1), pp.775–794.

Swierkot, K. et al., 2012. Mucositis, Peri-Implantitis, Implant Success, and Survival of Implants in Patients With Treated Generalized Aggressive Periodontitis: 3- to 16-Year Results of a Prospective Long-Term Cohort Study. *Journal of Periodontology*, 83(October), pp.1213–1225.

Sykaras, N. et al., 2000. Implant materials, designs, and surface topographies: their effect on osseointegration. A literature review. *The International journal of oral & maxillofacial implants*, 15(5), pp.675–690.

Tang, L. & Hu, W., 2005. Molecular determinants of biocompatibility. *Expert review of medical devices*, 2(4), pp.493–500.

Taubenberger, A. V, Hutmacher, D.W. & Muller, D.J., 2014. Single-cell force spectroscopy, an emerging tool to quantify cell adhesion to biomaterials. *Tissue engineering. Part B, Reviews*, 20(1), pp.40–55. Available at: http://online.liebertpub.com/doi/abs/10.1089/ten.teb.2013.0125%5Cnhttp://www.ncbi.nlm.nih.gov/pubmed/23688177.

Thomson, D.D., Berman, J. & Brand, A.C., 2016. High frame-rate resolution of cell division during Candida albicans filamentation. *Fungal Genetics and Biology*, 88, pp.54–58.

Tollersrud, T. et al., 2001. Imaging the surface of Staphylococcus aureus by atomic force microscopy. *APMIS : acta pathologica, microbiologica, et immunologica Scandinavica*, 109(7–8), pp.541–5. Available at: http://www.ncbi.nlm.nih.gov/pubmed/11552952.

Touhami, A. et al., 2006. Nanoscale characterization and determination of adhesion

forces of Pseudomonas aeruginosa pili by using atomic force microscopy. *Journal of Bacteriology*, 188(2), pp.370–377.

Tribble, G.D. & Lamont, R.J., 2010. Bacterial invasion of epithelial cells and spreading in periodontal tissue. *Periodontology 2000*, 52(1), pp.68–83. Available at: http://www.ncbi.nlm.nih.gov/pmc/articles/PMC3647226/.

Tsunashima, H. et al., 2012. Organization of the capsule biosynthesis gene locus of the oral streptococcus Streptococcus anginosus. *Journal of Bioscience and Bioengineering*, 113(3), pp.271–278.

Ubbink, J. & Schär-Zammaretti, P., 2005. Probing bacterial interactions: Integrated approaches combining atomic force microscopy, electron microscopy and biophysical techniques. *Micron*, 36(4), pp.293–320.

Uhlen, M., Guss, B. & Nilsson, B., 1984. Complete sequence of the staphylococcal gene encoding protein A. A gene evolved through multiple duplications. *Journal of Biological Chemistry*, 259(3), pp.1695–1702.

Uzunoglu, E. et al., 2014. Biofilm-forming ability and adherence to poly-(methyl-methacrylate) acrylic resin materials of oral Candida albicans strains isolated from HIV positive subjects. *The journal of advanced prosthodontics*, 6(1), pp.30–4. Available at: http://www.pubmedcentral.nih.gov/articlerender.fcgi?artid=3942524&tool=pmcentrez&rendertype=abstract.

Vadillo-Rodriguez, V. et al., 2004. Atomic force microscopic corroboration of bond aging for adhesion of Streptococcus thermophilus to solid substrata. *Journal of Colloid and Interface Science*, 278(1), pp.251–254.

Valderrama, P. et al., 2014. Detoxification of Implant Surfaces Affected by Peri-Implant Disease: An Overview of Non-surgical Methods. *The Open Dentistry Journal*, 8, pp.77–84. Available at: http://www.ncbi.nlm.nih.gov/pmc/articles/PMC4040927/.

Veses, V. & Gow, N.A.R., 2009. Pseudohypha budding patterns of Candida albicans. *Medical mycology*, 47(3), pp.268–75. Available at: http://mmy.oxfordjournals.org/content/47/3/268.full.

Vukosavljevic, D. et al., 2014. Nanoscale Adhesion Forces between Enamel Pellicle

Proteins and Hydroxyapatite. *J Dent Res*, 93(5), pp.514–519. Available at: http://www.ncbi.nlm.nih.gov/pubmed/24591293%5Cnhttp://jdr.sagepub.com/content/93/5/514.full.pdf.

Waar, K. et al., 2005. Atomic force microscopy study on specificity and non-specificity of interaction forces between Enterococcus faecalis cells with and without aggregation substance. *Microbiology*, 151(7), pp.2459–2464.

Wall, I. et al., 2009. Modified titanium surfaces promote accelerated osteogenic differentiation of mesenchymal stromal cells in vitro. *Bone*, 45(1), pp.17–26.

Wang, X. et al., 2012. Correlation of macroscopic aggregation behavior and microscopic adhesion properties of bacteria strains using a dimensionless Tabor's parameter. *Journal of Colloid and Interface Science*, 374(1), pp.70–76.

Wann, E.R. et al., 1999. Genetic analysis of the cap5 locus of Staphylococcus aureus. *FEMS Microbiology Letters*, 170(1), pp.97–103.

Webb, H.K. et al., 2011. Physico-mechanical characterisation of cells using atomic force microscopy - Current research and methodologies. *Journal of Microbiological Methods*, 86(2), pp.131–139.

Weng, Y. et al., 2010. A novel antibacterial dental glass-ionomer cement. *European Journal of Oral Sciences*, 118(5), pp.531–534.

Weng, Y. et al., 2012. A novel antibacterial resin composite for improved dental restoratives. *Journal of Materials Science: Materials in Medicine*, 23(6), pp.1553–1561.

Wennerberg, A. & Albrektsson, T., 2009. Effects of titanium surface topography on bone integration: A systematic review. *Clinical Oral Implants Research*, 20(SUPPL. 4), pp.172–184.

Wennerberg, a et al., 1998. A histomorphometric evaluation of screw-shaped implants each prepared with two surface roughnesses. *Clinical oral implants research*, 9(1), pp.11–9. Available at: http://www.ncbi.nlm.nih.gov/pubmed/11887656.

Wessel, S.W. et al., 2014. Adhesion forces and composition of planktonic and adhering oral microbiomes. *Journal of dental research*, 93(1), pp.84–8. Available at: http://www.ncbi.nlm.nih.gov/pubmed/24186560.

Whitehead, K.A., Colligon, J. & Verran, J., 2005. Retention of microbial cells in substratum surface features of micrometer and sub-micrometer dimensions. *Colloids and Surfaces B: Biointerfaces*, 41(2–3), pp.129–138.

Winkelströter, L.K. et al., 2013. Unraveling Microbial Biofilms of Importance for Food Microbiology. *Microbial Ecology*, 68(1), pp.35–46. Available at: http://link.springer.com/article/10.1007/s00248-013-0347-4.

Wright, B. et al., 2015. A simple and robust method for pre-wetting poly (lactic-co-glycolic) acid microspheres. *Journal of Biomaterials Applications*, 30(2), pp.147–159. Available at: http://www.ncbi.nlm.nih.gov/pmc/articles/PMC4509882/.

Wu, T. et al., 2015. Cellular Components Mediating Coadherence of Candida albicans and Fusobacterium nucleatum. *Journal of Dental Research*, 94(10), pp.1432–1438. Available at: http://jdr.sagepub.com/cgi/doi/10.1177/0022034515593706.

Wu, Y. & Zhou, A., 2010. Fluctuations in adhesion behavior of dividing/budding mycobacterium sp. strains JLS, KMS, MCS: An AFM evaluation. *Micron*, 41(7), pp.814–820.

Wu, Y. & Zhou, A., 2009. In situ, real-time tracking of cell wall topography and nanomechanics of antimycobacterial drugs treated Mycobacterium JLS using atomic force microscopy. *Chemical communications (Cambridge, England)*, (45), pp.7021–3. Available at: http://www.ncbi.nlm.nih.gov/pubmed/19904381.

Xu, C.P. et al., 2008. Staphylococcus aureus-fibronectin interactions with and without fibronectin-binding proteins and their role in adhesion and desorption. *Applied and Environmental Microbiology*, 74(24), pp.7522–7528.

Yamaguchi, M. et al., 2006. Role of Streptococcus sanguinis sortase A in bacterial colonization. *Microbes and Infection*, 8(12–13), pp.2791–2796.

Yang, X. et al., 2010. Atomic force microscopy investigation of the characteristic effects of silver ions on Escherichia coli and Staphylococcus epidermidis. *Talanta*, 81(4–5), pp.1508–1512.

Yang, Y. et al., 2014. In vitro antibacterial activity of a novel resin-based pulp capping material containing the quaternary ammonium salt MAE-DB and Portland cement. *PloS one*, 9(11), p.e112549.

Yarborough, A. et al., 2016. Evidence Regarding the Treatment of Denture Stomatitis. *Journal of Prosthodontics*, 25(4), pp.288–301.

Yongsunthon, R. & Lower, S.K., 2006. Force spectroscopy of bonds that form between a Staphylococcus bacterium and silica or polystyrene substrates. *Journal of Electron Spectroscopy and Related Phenomena*, 150(2–3), pp.228–234.

Younes, J.A. et al., 2012. Adhesion forces and coaggregation between vaginal staphylococci and lactobacilli. *PLoS ONE*, 7(5).

Zengin, H. & Baysal, A.H., 2014. Antibacterial and antioxidant activity of essential oil terpenes against pathogenic and spoilage-forming bacteria and cell structure-activity relationships evaluated by SEM microscopy. *Molecules*, 19(11), pp.17773–17798.

Zhang, T. et al., 2011. Quantification of the lateral detachment force for bacterial cells using atomic force microscope and centrifugation. *Ultramicroscopy*, 111(2), pp.131–139.

Zhang, W., Stack, A.G. & Chen, Y., 2011. Interaction force measurement between E. coli cells and nanoparticles immobilized surfaces by using AFM. *Colloids and Surfaces B: Biointerfaces*, 82(2), pp.316–324.

Zhao, B. et al., 2014. Soft tissue integration versus early biofilm formation on different dental implant materials. *Dental Materials*, 30(7), pp.716–727.

Zhao, G. et al., 2013. Biofilms and Inflammation in Chronic Wounds. *Advances in wound care*, 2(7), pp.389–399. Available at: http://www.pubmedcentral.nih.gov/articlerender.fcgi?artid=3763221&tool=pmcentrez&rendertype=abstract.

Zhao, G. et al., 2005. High surface energy enhances cell response to titanium substrate microstructure. *Journal of Biomedical Materials Research - Part A*, 74(1), pp.49–58.

Zhao, G. et al., 2007. Requirement for both micron- and submicron scale structure for synergistic responses of osteoblasts to substrate surface energy and topography. *Biomaterials*, 28(18), pp.2821–2829.

APPENDIX 1: List of publications

- Aguayo S, Marshall H, Pratten J, Bradshaw D, Brown J.S., Porter S, Spratt D, and Bozec L (2016). *Candida albicans adhesion onto acrylic surfaces at the nanoscale*. Journal of Dental Research. Accepted April 2017.

- Strange A, **Aguayo S**, Ahmed T, Mordan N, Stratton R, Porter S, Parekh S, Bozec L (2016). *Quantitative Nanohistological Investigation of Scleroderma: An AFM-Based Approach to Disease Characterization*. International Journal of Nanomedicine. 2017; 12: 411–420.

- Aguayo S, Strange A, Gadegaard N, Dalby MJ and Bozec L (2016). *Influence of biomaterial nanotopography on the adhesive and elastic properties of Staphylococcus aureus cells. RSC Advances.* 6(92), pp. 89347-89355.

- Aguayo S, Donos N, Spratt D and Bozec L (2016). *Probing the nanoadhesion of Streptococcus sanguinis to titanium implant surfaces by Atomic Force Microscopy*. International Journal of Nanomedicine. 2016 Apr 6;11:1443-50

- Aguayo S and Bozec L (2016). *Mechanics of bacterial cells and initial surface colonisation.* Advances in Experimental Medicine and Biology. 2016;915:245-60

- Aguayo S, Donos N, Spratt D and Bozec L (2015). *Nanoadhesion of Staphylococcus aureus onto Titanium Implant Surfaces*. Journal of Dental Research. 2015;94:1078-1084

- Aguayo S, Donos N, Spratt D and Bozec L (2015). *Single-bacterium nanomechanics in biomedicine: unravelling the dynamics of bacterial cells*. Nanotechnology. Feb 13;26(6):062001.

- Wright B, Parmar N, Bozec L, **Aguayo S** and Day RM (2015). *A simple and robust method for pre-wetting poly (lactic-co-glycolic) acid microspheres*. J Biomater Appl. 2015 Aug;30(2):147-59

APPENDIX 2

International Journal of Nanomedicine

Dovepress
open access to scientific and medical research

Open Access Full Text Article

ORIGINAL RESEARCH

Quantitative nanohistological investigation of scleroderma: an atomic force microscopy-based approach to disease characterization

This article was published in the following Dove Press journal:
International Journal of Nanomedicine
11 January 2017
Number of times this article has been viewed

Adam P Strange[1]
Sebastian Aguayo[1]
Tarek Ahmed[1]
Nicola Mordan[1]
Richard Stratton[2]
Stephen R Porter[3]
Susan Parekh[4]
Laurent Bozec[1]

[1]Department of Biomaterials and Tissue Engineering, UCL Eastman Dental Institute, [2]Centre for Rheumatology and Connective Tissue Diseases, Royal Free Hospital, UCL Medical School, [3]UCL Eastman Dental Institute, [4]Department of Pediatrics, UCL Eastman Dental Institute, London, UK

Abstract: Scleroderma (or systemic sclerosis, SSc) is a disease caused by excess crosslinking of collagen. The skin stiffens and becomes painful, while internally, organ function can be compromised by the less elastic collagen. Diagnosis of SSc is often only possible in advanced cases by which treatment time is limited. A more detailed analysis of SSc may provide better future treatment options and information of disease progression. Recently, the histological stain picrosirius red showing collagen register has been combined with atomic force microscopy (AFM) to study SSc. Skin from healthy individuals and SSc patients was biopsied, stained and studied using AFM. By investigating the crosslinking of collagen at a smaller hierarchical stage, the effects of SSc were more pronounced. Changes in morphology and Young's elastic modulus were observed and quantified; giving rise to a novel technique, we have termed "quantitative nanohistology". An increase in nanoscale stiffness in the collagen for SSc compared with healthy individuals was seen by a significant increase in the Young's modulus profile for the collagen. These markers of stiffer collagen in SSc are similar to the symptoms experienced by patients, giving additional hope that in the future, nanohistology using AFM can be readily applied as a clinical tool, providing detailed information of the state of collagen.

Keywords: rheumatology, adjunct diagnosis, picrosirius red, collagen, nanohistology

Introduction

Scleroderma, or systemic sclerosis (SSc), is a multisystemic collagen disorder of indeterminate etiology.[1,2] It can be characterized primarily by the severe fibrosis of skin and viscera, but widespread vasculopathy and a spectrum of other features can arise.[2] SSc can cause significant physical impairment, reducing the patient's quality of life.[3] SSc occurs globally with females significantly more often diagnosed than males.[4] The precise cause of scleroderma remains unknown, although there can be similarities with exposure to organic solvents.[5,6] There are two broad types of SSc, denoted as limited and diffuse cutaneous SSc.[7–9] Limited cutaneous SSc primarily causes vasculopathy with slow fibrosis, whereas diffuse cutaneous SSc is dominated by the rapid fibrosis of skin and organs. There have been significant advances in the management of SSc over the past 2 decades, and a wide range of new biological agents will hopefully prove to be of clinical benefit. Nevertheless, at present, the disease can lessen life expectancy with 55% of patients dying within 10 years of diagnosis of diffuse SSc.[10,11] While there are a number of biomarkers of SSc (eg, various autoantibodies), there remains no one sensitive diagnostic tool; hence, as a consequence of its relative rarity and the absence of sensitive biomarkers, SSc may go undetected for several years after clinical onset,

Correspondence: Adam P Strange
Department of Biomaterials and Tissue Engineering, UCL Eastman Dental Institute, Gray's Inn Road, London WC1X 8LD, UK
Email adam.strange.13@ucl.ac.uk

http://dx.doi.org/10.2147/IJN.S118690

and thus, opportunities to modify disease progress are lost. Improvements to clinical care and condition management have increased patient life expectancy. The rapid onset of SSc combined with difficulties in early diagnosis is considered to the possible reason for the high mortality rate associated with this condition.[12]

The diagnosis of the disease is performed through clinical investigation via a differential diagnosis approach. To date, there is no conclusive genetic or biomarker diagnosis for SSc.[13] Histological biopsies can prove useful in later-stage SSc, but after the disease has progressed, a visual assessment in clinic is often sufficient. Avoiding the collection of biopsies would avoid the exacerbation of scarring in SSc patients.[14] Currently, the diagnosis of SSc often occurs at a late stage, although there is an ongoing need for earlier-stage diagnosis.[3,6,12] Some advances in the detection of biomarkers have already been made, but these are not suitable for a frontline diagnosis.[3] Similarly, there are very few methods that are used to detect the spread of SSc. Optical coherence tomography (OCT) is a noninvasive tool that could potentially be used to analyze SSc. However, current OCT research is unable to distinguish between the density of healthy skin, keloid scar formation and an SSc lesion.[15]

Although SSc is a collagenous disorder, it is often referred to as a skin condition, and the effects on other tissues can be overlooked.[5,11,12] The effects of SSc on skin are often the first to be noticed by the patient, and skin is an easily accessible and well-characterized tissue. SSc is believed to be associated with an excess of collagen crosslinking from lysyl oxidase and other enzymes noted as a possible cause.[16] The impact of this excessive number of crosslinks within SSc lesions would confer both structural and mechanical abnormalities to collagen fibrils present in these lesions. However, to date, there has been no research effort to investigate the biophysical properties of collagen in relation to SSc patients in order to further understand the onset of this condition. The limited amount of research that has been performed on laboratory cell models is decades old.[17]

In this article, a novel approach is presented to gain further information on the biophysical properties (topographical and nanomechanical) of the collagen network present in the SSc lesions using atomic force microscopy (AFM) combined with histology. The probing of these physical parameters at the scale where the disease is starting to impact the tissue may demonstrate the physical alterations occurring in collagen as a result of SSc. This could provide a future method of assessing disease progress and help to determine if new therapies are having a benefit at the molecular and tissue level.

Materials and methods

All samples were obtained under ethical approval: Research Ethics Committee, Cambridge, UK, 06/6398 and patient consent was obtained following local guidelines. Volunteer patients had a 4 mm punch biopsy taken from the upper forearm in a non-load-bearing area, including the sclerotic lesion where appropriate for this study. One healthy control volunteer and one patient with SSc were included in this study. Both individuals were male white Caucasians, approximately 60 years old. The SSc patient was diagnosed in clinic as being at a severe stage of the disease, ensuring that any samples taken would have sclerotic lesions. Samples were snap-frozen in methyl butane and liquid nitrogen. Samples were histologically cut into 10 μm sections at a clinical laboratory (Blizard Institute – Queen Mary University, London, UK). The sections were subsequently stained with picrosirius red (PS) for collagen after being dried through physisorption onto a glass slide. The prepared sections were then stored at 4°C under Human Tissue Act (2004) guidelines until required for experiments. No further processing was required for light microscopy (LM) histology or AFM characterization. For imaging by electron microscopy (EM), the sections were also fixed for 24 hours in 3% glutaraldehyde (Agar Scientific, Stansted, UK) and dehydrated using an ethanol series, before being coated with Au/Pd.

A Leica (Wetzlar, Germany) light microscope with 4×, 10×, 20× and 50× magnification lenses, equipped with two crossed-light polarizers (90°), was used for polarized LM. At least three images were taken in each location for each sample, with at least three biopsies per patient analyzed. Images were captured using an 8-megapixel digital camera (EOS Rebel 100, Canon).

EM imaging was performed using a Philips XL30 FEG-SEM (FEI, Eindhoven, the Netherlands), at an accelerating voltage of 5 kV. Two AFMs were used to collect imaging and force–displacement (FD) measurement. At least three images were taken in each location for each sample, with at least three biopsies per patient analyzed. A Nanowizard (JPK, Berlin, Germany) with REFSPA tips (k=3 N/m) (Bruker, Santa Barbara, CA, USA) in contact mode in air was used to collect FD. Imaging was also performed on Dimension 3100 (Bruker) AFM in contact mode in air. Both AFMs used MSNL-10 (Bruker) probes in imaging mode. For all AFM measurements, the samples were kept air-dried to avoid the delamination of the sections upon rehydration. FD curves were analyzed on proprietary software (JPK). FD values were

extracted, and the Young's modulus was calculated using the Oliver–Pharr model.[18] These data were statistically analyzed using Kruskal–Wallis analysis of variance and plotted using Origin (OriginCorp, Northampton, MA, USA) processing software. At least three data sets were taken in each location for each sample, with at least three biopsies per patient analyzed, for a minimal of 350 force curves per location. Post-statistical analysis was performed manually by grouping samples into four empirically observed groups (1–5, 5–10, 10–15 and 15–20 GPa), and describing the percentage distribution of n-number values. These were plotted on the previously formed graphs.

Results and discussion

Histological comparison between healthy vs SSc dermal layers

In order to ensure that our approach is clinically relevant, it was essential to start our investigation by using histology as a first approach to compare both healthy and SSc dermal layers. Figure 1A shows the histology of healthy control skin. The epidermal layer is clearly defined as a thick brown-red layer at the top of the skin. The dermoepidermal junction (DEJ) is demarcated by a color change from brown-red to pink-red. The dermal layer is porous with large gaps intercalated between collagen-stratified layers. In healthy dermis, fibrillar collagen aggregates to form larger bundles of fibers and is the structural protein which provides mechanical support to connective tissues throughout the body.[19] The bundles align in register with each other, forming three-dimensional (3D) collagen sheets. These sheets of fibers are found mainly in the reticular dermis of the skin, which is 80% type I collagen.[20] The 3D alignment and order of the collagen provide isotropic mechanical strength to the skin.[21] Collagen can support these mechanical loads due to crosslinking of collagen molecules and the formation of a hierarchal structure.[22] Figure 1B shows the polarized light histology of the healthy skin. The change in color on the control sample is difficult to see, and the dermal layer stained with PS is still pink-red. It is known that staining with PS does not show just collagen, but the register of the collagen.[23] Sirus red, a component of PS, is a strong anionic dye. The sulfonic acid groups on sirus red react with basic groups present in the collagen molecule. Sirus red and collagen align so that their long axes are parallel, which correspond to the long axis of the fibrils. This enhances the birefringence of collagen.[23] As PS aligns to the register of collagen fibrils, any changes from red to another color in the polarized image suggest that the collagen fibrils may no longer be in register and that the collagen scaffold may be structurally disordered (when compared to well-ordered collagen sheet in healthy dermis for example).

Figure 1C shows the histology of SSc. The epidermal layer is colored brown but appears thinner than the control. The DEJ is not well defined, as the dermis appears to bulge into the epidermis. The dermal layer appears denser than the

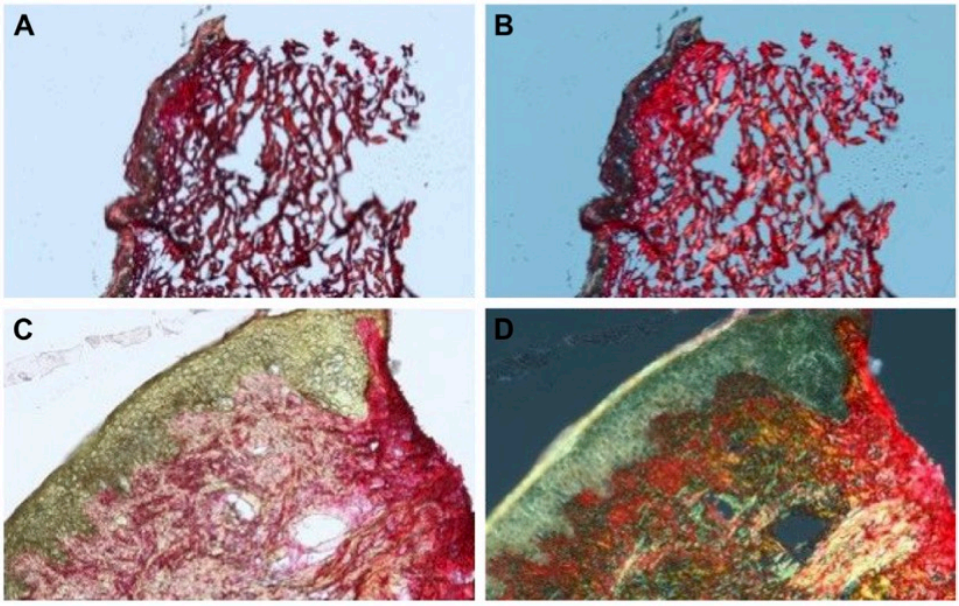

Figure 1 LM images of control (**A** and **B**) and SSc (**C** and **D**) biopsies taken in unpolarized and polarized light (10× magnification).
Abbreviations: LM, light microscopy; SSc, systemic sclerosis.

control, with far fewer gaps between the collagen-stratified layers. The reticular dermis also bulges out past the edge of the epidermis. Collagen production is known to increase in SSc, so the increase in density and loss of gap regions in the SSc sample as viewed under LM is expected. The bulging of the dermis past the edge of the epidermis is known as a "cookie-cutter bulge" and is a reported histological feature of SSc.[13] Figure 1D shows the SSc under polarized light. The color changes are notable, and red, yellow and green regions could be clearly identified, without any color appearing to be more prevalent than another. By combining histological imaging with PS staining, we can observe areas of color change which show different levels of collagen birefringence suggesting different levels of structural ordering of the underlying collagen fibrils. Although this could be sufficient in aiding in a clinical diagnosis, more information about the state of collagen needs to be obtained to explain this lack of structural ordering as a potential marker for SSc.

Structural ordering of collagen fibrils

In order to investigate the structural properties of the collagen scaffold within the dermal layer, the samples were imaged using EM so that both large-field and localized high-resolution images could be obtained on the same samples. Figure 2 shows representative images of skin biopsies obtained through scanning electron microscopy (SEM). The control sample (Figure 2A) shows a representative image from the epidermis. There is a thick sheet-like layer of collagen, with a clearly defined swirling pattern. The swirling pattern has been reported as a sign of dermal aging. The preparation process for SEM caused desiccation cracks, and a small number is visible between the collagen swirls. At this magnification (1,000×), the individual fibrils are not yet fully visible. Figure 2B was imaged at a higher magnification (15,000×), and the collagen fibrils can be seen, and the D-banding periodicity resolved. The collagen fibrils are in register and well ordered, following a clear left–right axis across the image. Figure 2C shows the SSc sample at 1,000× magnification. Larger gaps between the collagen sheets can now be seen, and some individual fibrils may be resolved. Figure 2D was imaged at 15,000× magnification, and there is a notable loss of collagen register. The circled area shows a particular disordered area, where the collagen lacks any register. However, the D-banding periodicity can be clearly resolved confirming the presence of collagen. As far as SEM imaging can tell us, the collagen appears to be well formed

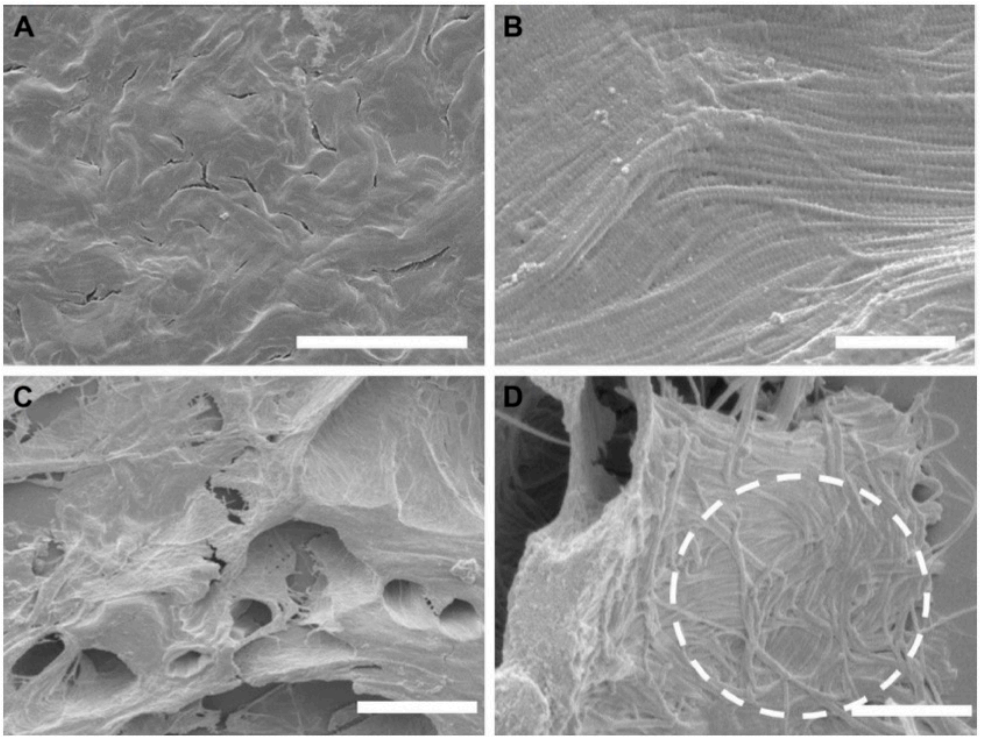

Figure 2 SEM images of control (**A** and **B**) and SSc (**C** and **D**).
Notes: Scale bars of (**A**) and (**C**): 20 µm, 1,000× magnification; scale bars of (**B**) and (**D**): 2 µm, 15,000× magnification. Circled area in (**D**) shows an area of high collagen disorder due to SSc.
Abbreviations: SEM, scanning electron microscopy; SSc, systemic sclerosis.

as the D-banding appears regular, with no pitting, swelling or blebbing observed.[24–26]

SEM allowed for surface topographical analysis over a range of magnifications. When the polarized LM images were used, the color changes seen in the SSc sample implied a loss of collagen register. The control samples lacked a color change, and regular and ordered structure was seen throughout the SEM images at both magnification levels. This reconfirms that the PS stain indicates a change of collagen ultrastructural register. When both the control and SSc images are compared, it becomes evident that the main structural change relates to the lack of interfibrillar registration. Being a connective tissue that is subject to various posttranslational modifications, collagen evolves as we age but also as a result of disease such as SSc. In a healthy tissue, collagen fibrils are stabilized by a series of crosslinks that can be classified as intramolecular, intermolecular (or intrafibrillar) and also interfibrillar. Although at this stage, we have not yet elucidated the crosslinks density on collagen fibrils associated with SSc, we hypothesize two mechanisms that could explain the lack of register between collagen fibrils within an SSc lesion: sclerotic fibrils are unable to adjust their register due to an increase in collagen stiffness caused by excess of intrafibrillar crosslinking. This crosslinking acts as a pathological collagen fixative, keeping the collagen in a disordered state of register. The second hypothesis would suggest that the interfibrillar crosslinks may have become deficient and leads to a loosening of the collagen organization within the dermis. It is known from clinic that SSc causes stiffening in patients, most noticeably in the skin; it is therefore unlikely that the collagen organization loosens due to crosslink weakness. It has therefore been suggested that SSc, in a similar manner to diabetes, arises due to a pathological increase in collagen crosslinking.[27]

Nanomechanics of collagen in dermal layer

Nanoscale analysis can be performed by AFM which has several advantages over SEM in looking at collagen in SSc. AFM can be performed in ambient laboratory conditions and easily allows for mechanical parameters, such as the Young's elastic modulus, to be measured.[18] It is clear that collagen stiffening is an important parameter to take into account while characterizing SSc. In our approach, we have used an AFM to probe the mechanical properties of individual collagen fibrils present in the dermal layer of each series of samples. The AFM probe is small enough so that individual fibrils can be indented separately. Before undertaking this approach to elucidate the collagen stiffening in SSc, it is essential to perform these measurements on the control sample for reference. Figure 3A shows the sample imaged with LM, and four areas were randomly selected and highlighted for further AFM study on a healthy control sample. Figure 3B shows AFM topographical imaging of area D for example. The ultrastructure of collagen fibrils can be identified by means of the D-banding present along the long-fibril axis. In this particular area, three distinct sheets were imaged, appearing in the left, middle and right thirds of the image. This image highlights the structural complexity and isotropy of the dermis in which several collagen sheets may intercept each other, presenting collagen fibrils cross-sections, in-plane section (D-banding) or an oblique section. Thus, to be systematic, only collagen fibrils that were in plane (clear D-banding) with the AFM scan were then mechanically probed using FD. Figure 3C shows the distribution of reduced Young's modulus obtained from the healthy sample after being calculated using the Oliver–Pharr model.[18] Comparing the data obtained from the four different locations probed, it was not possible to observe any meaningful variation in the reduced Young's modulus (Figure 3C). None of the four areas analyzed were statistically different compared to each other ($P>0.05$, Kruskal–Wallis). It is however worth noting that for all the locations tested, it was found that over 60% of the collagen indented ($n\geq225$) had a reduced Young's modulus <10 GPa. The range of reduced Young's moduli values in the skin (Figure 3C) is consistent with published data on collagen fibrils in comparable conditions.[28,29]

Toward quantitative nanohistology

By combining histological imaging, nanoscale imaging and nanoscale indentation, we have created a protocol termed "quantitative nanohistology" (QNH). This allows us to quantify the amount of collagen disorder observed at the nanoscale with no additional sample preparation other than what is commonly used in histology.

Figure 4 demonstrates the imaging part of the QNH profile for the healthy control sample. Figure 4A shows the polarized LM image. It can be seen that the majority of the sample is red in color. There are areas of yellow and green also present. Four areas selected for AFM are highlighted on the image. Figure 4B shows the topographical AFM image of the red area, taken from the highlighted area in Figure 4A. D-banding can be readily observed, confirming that the fibrils are collagen. Figure 4C demonstrates the AFM image of the green area as highlighted in Figure 4A. Some collagen can be seen toward the bottom of the image, but a large section

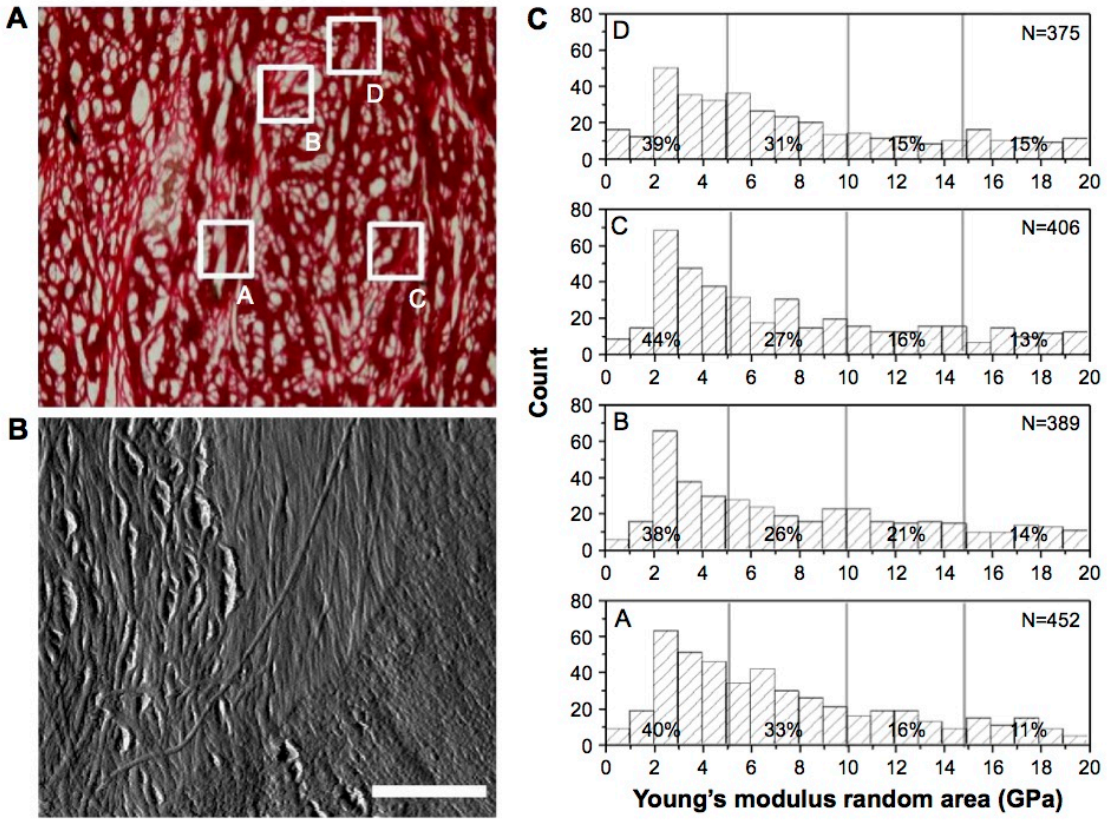

Figure 3 AFM analysis of control skin sample in random locations. (**A**) Standard LM was performed on a healthy control skin sample, and four areas of interest (A–D) were marked (10× magnification). (**B**) AFM image of area D from (**A**), showing interface between three different collagen regions (scale bar 2 μm). (**C**) Young's modulus obtained by transverse collagen on fibrils in locations A–D from (**A**). No areas were significantly different, $P<0.05$ (Kruskal–Wallis).
Abbreviations: AFM, atomic force microscopy; LM, light microscopy.

does not contain D-banded collagen. This is consistent with what is known about PS staining, as the larger amount of non-register collagen caused the green color to be seen under polarized LM.[30] Figure 4D demonstrates a magnified area in Figure 4B. The collagen is in register, and as can be seen in the Figure 4D insert, the D-banding is regular at 65.8 nm periodicity, compared with a reported average of 67 nm.[31] Figure 5A shows the calculated Young's modulus values from the FD curves. Bimodal distribution was seen in the red area, with peaks in the <5 and 10–15 GPa categories (N=312). Bimodal distribution of collagen has been reported previously, with lower Young's moduli values suggested to be newer collagen, and higher Young's moduli values older collagen, when further crosslinking has occurred.[32] Similar bimodal distribution was seen in the red/yellow area. No bimodal distribution was seen in the yellow or green areas, with 72% (N=345) and 83% (N=376) of all values <10 GPa. All colors had their largest percentage values in the 0–5 GPa categories. When analyzed using mean averages as a whole data set using Kruskal–Wallis test, the red (8.81 GPa) and red/yellow (7.56 GPa) areas were not significantly different ($P>0.05$). Significantly lower values ($P\leq0.05$) were found for the red value compared with yellow (6.84 GPa) and green (5.23 GPa).

There were very few red areas under the polarized LM. This is expected for control skin, and following the published literature, it is believed that this region should show collagen that is in register.[23] When looking at the AFM imaging, it was clear that the collagen was not in register. As each individual PS molecule will lie along several collagen molecules, the natural birefringence of collagen is enhanced. When combined with many other PS molecules, this acts as a method of indicating the nanoscale register at the microscale. However, nanoscale-localized imperfections in register would be expected to still show as red under polarized LM. The AFM image of the healthy collagen demonstrates an imperfect collagen register, but one that is nevertheless very well aligned. The significant differences in Young's modulus are

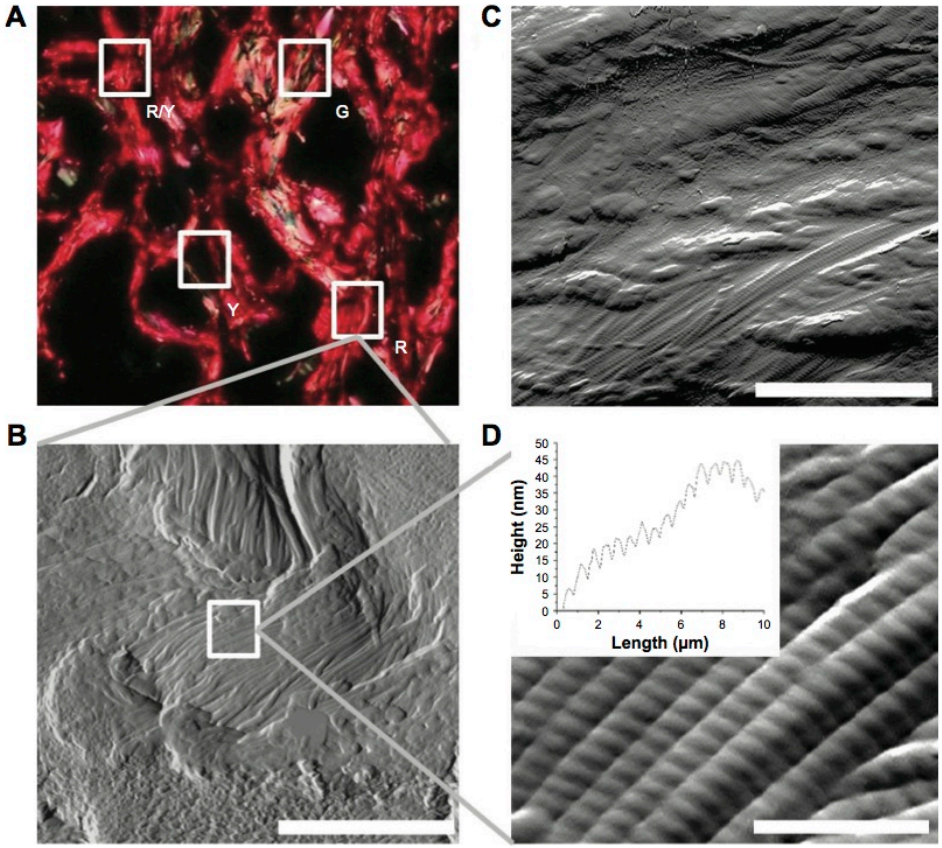

Figure 4 AFM analysis of control skin sample. (**A**) Polarized LM showing red, red/yellow, yellow and green areas of interest (10× magnification). (**B**) AFM error image of red area showing collagen present and highlighting an area of collagen (scale bar 2 μm). (**C**) AFM error image of green area showing minimal intact collagen (scale bar 2 μm). (**D**) AFM error image of highlighted red area with inset showing a line profile from the height image (scale bar 800 nm).
Abbreviations: AFM, atomic force microscopy; G, green; LM, light microscopy; R, red; R/Y, red/yellow; Y, yellow.

consistent with what is known about PS. The Young's moduli for red and red/yellow are consistent with the values given in literature.[28,29] The red collagen, which is the best indication available for healthy in-register collagen, was used as the QNH "fingerprint" for Young's modulus.

QNH – SSc

Figure 6 shows the complete imaging QNH profile for the SSc sample. Figure 6A demonstrates the polarized LM of the SSc sample. It shows no dominant color, with red, yellow and green all present. Four areas for FD are highlighted on the image. Figure 6B shows the topographical AFM image of the red area, highlighted from Figure 6A. The fibrils show D-banding, confirming that the fibrils are collagen. The collagen is not in register, with no discernible directional origination, which is consistent with the SEM data in Figure 2D, specifically the circled area. Figure 6C shows a magnified green area, as indicated in Figure 6A. D-banded collagen can be seen around the edge of the image, with a large amount of protein covering the center of the image. This protein could be hydrolyzed collagen (ie, gelatin) or a non-collagenous protein.[33] Irrespective of its chemical makeup, it covers the underlying collagen and prevents the PS molecules from lying on the collagen D-band. Therefore, this area appears green under polarized microscopy. Figure 6D shows a magnified area of Figure 6B. The collagen, although out of register, has regular D-banding which can be seen in the insert. The average D-band for this area was 64.2 nm, comparing favorably with the reported average of 67 nm.[31] Figure 5B shows the indentation performed on identifiable collagen in the sample. The red area had its largest percentages of values in the 10–15 GPa (32%, N=151) and the 15–20 GPa (30%, N=141) range. The red/yellow area had most of the values (46%, N=178) in the 5–10 GPa category, with 23% (N=89) in the 15–20 GPa category. The yellow and green areas had 89% (N=373) and 94% (N=370) of values <10 GPa.

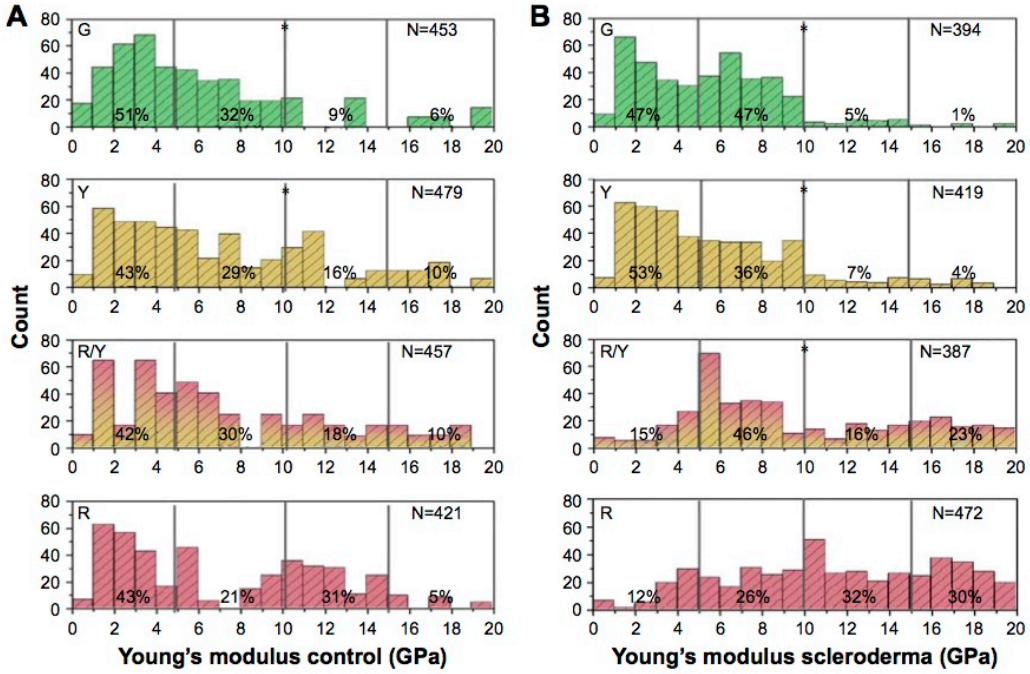

Figure 5 Young's modulus values for control and SSc skin samples. (**A**) Young's modulus obtained by transverse indentation on collagen fibrils in each area. Yellow and green areas are statistically different (indicated with asterisks) compared with red, $P>0.05$ (Kruskal–Wallis ANOVA). (**B**) Young's modulus obtained by transverse indentation on collagen fibrils in each area. Red/yellow, yellow and green areas are statistically different (indicated with asterisks) compared with red, $P>0.05$ (Kruskal–Wallis ANOVA).
Abbreviations: ANOVA, analysis of variance; G, green; R, red; R/Y, red/yellow; SSc, systemic sclerosis; Y, yellow.

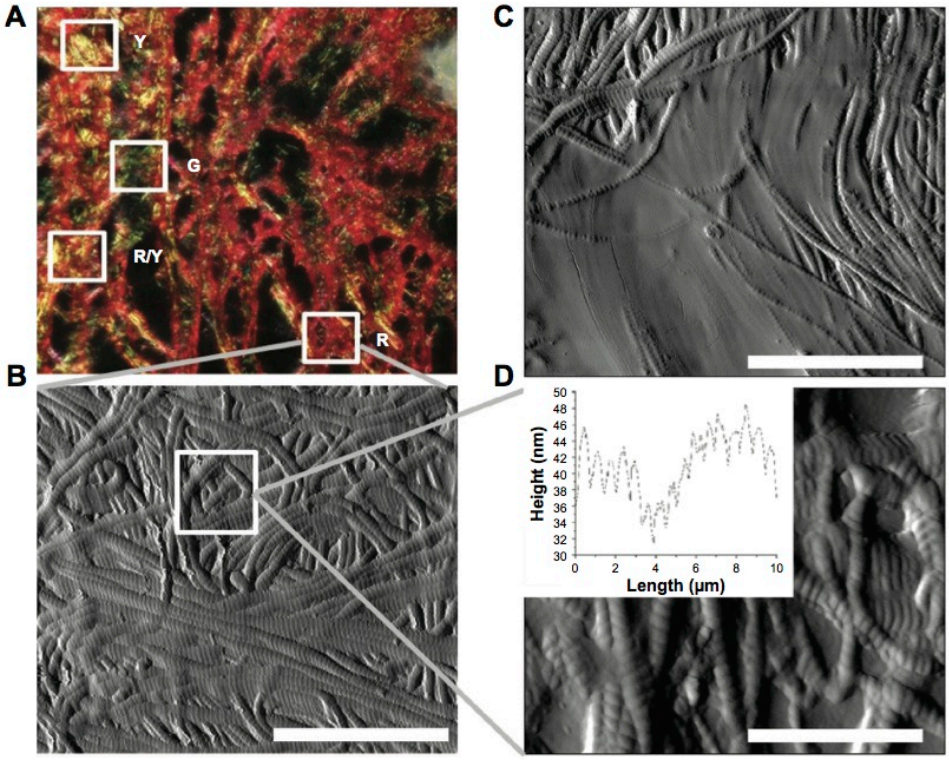

Figure 6 AFM analysis of SSc skin sample. (**A**) Polarized LM showing red, red/yellow, yellow and green areas of interest (10× magnification). (**B**) AFM error image of red area showing collagen present and highlighting an area of collagen (scale bar 2 μm). (**C**) AFM error image of green area showing minimal intact collagen (scale bar 2 μm). (**D**) AFM error image of highlighted red area with inset showing a line profile from the height image (scale bar 800 nm).
Abbreviations: AFM, atomic force microscopy; G, green; LM, light microscopy; R, red; R/Y, red/yellow; SSc, systemic sclerosis; Y, yellow.

There is an immediately noticeable difference in LM between the control and the SSc sample. In the SSc sample, there is no dominant color suggesting a higher level of disorder in the SSc sample compared with the control. The LM provides a direct microscopic analysis of the ordering of the collagen in the sample, but there is no quantification provided by this method. The AFM in the red area also showed marked differences between the control and SSc image. The fibrils in SSc are not in register, and there is localized swelling, while the D-banding is always visible. The lack of register is concerning, as this is not a sign of healthy collagen.[34,35] The Young's modulus values for the red areas were consistently higher for SSc than control. At the macroscale, SSc causes collagen hardening in patients. The green values were not statistically different for both samples (Figure 5A and B). We believe that this is due to the large amount of non-morphologically identifiable collagen seen in the green areas (Figures 4C and 6C). As SSc is only known to affect collagen, it is not unexpected that the non-collagenous regions are similar between healthy individuals and SSc patients.

However, we hypothesize that the disorder seen in SSc patients can be directly linked to the increase in Young's modulus measured for SSc (Figure 5B). The result of this high stiffness is that fibrils are incapable of forming the correct bundling structure; instead, they are not in register and are poorly aligned (Figures 2D and 6B). The severe difference in stiffness seen in the SSc sample could be linked to the severity of the disease in the patient when the sample was obtained. Morphologically, there is also evidence of localized swelling in several fibrils. When the control and SSc are compared morphologically, the differences in the ability of the fibrils to maintain their register can be observed (Figures 4B and D and 6B and D). The D-banding remained similar in appearance for both of the biopsies examined. As the D-band is formed as a result of the amino acid makeup of collagen, this suggests that the collagen is formed correctly, and thus, the excess crosslinking occurs after the formation of collagen. This matches well with what is currently known about SSc, in that there is no known genetic cause.[6,11] If the collagen is formed correctly, we then hypothesize that the crosslinking is interfibrillar.

Conclusion

Imaging using LM currently remains the gold standard in histology for diagnostic medicine, but there are improvements that can be made. The use of PS staining informs the targeting of the AFM measurements, giving rise to QNH adjunct diagnosis. Through nanoscale AFM imaging, it is possible to observe the effects of crosslinking at a point closer to where the changes begin, inside the collagen fibrils. This is then combined with the mechanical measures to provide a detailed indication of the state of the collagen. The nanohistological protocol described here has shown that SSc skin collagen has significantly higher Young's modulus than healthy skin collagen. Having shown this in a case study of SSc, we will then look to expand the number of patients sampled, creating a mechanical and morphological database. Having established a baseline of severe SSc disorder as observed in the clinic and through QNH, we then hope to expand the role of AFM directly into the clinic. It could be expanded to look at less severe cases of SSc, to mark and observe SSc development and activity and to measure patient responses to medical interventions. Finally, QNH may one day be used as an adjunct diagnostic tool in complex cases of collagen-based diseases.

Disclosure

The authors report no conflicts of interest in this work.

References

1. LeRoy EC, Medsger TA Jr. Criteria for the classification of early systemic sclerosis. *J Rheumatol*. 2001;28(7):1573–1576.
2. D'Angelo WA, Fries JF, Masi AT, Shulman LE. Pathologic observations in systemic sclerosis (scleroderma). A study of fifty-eight autopsy cases and fifty-eight matched controls. *Am J Med*. 1969;46(3):428–440.
3. Frech TM, Shanmugam VK, Shah AA, et al. Treatment of early diffuse systemic sclerosis skin disease. *Clin Exp Rheumatol*. 2013;31(2 Suppl 76): 166–171.
4. Englert H, Brennan P, McNeil D, Black C, Silman AJ. Reproductive function prior to disease onset in women with scleroderma. *J Rheumatol*. 1992;19(10):1575–1579.
5. Nietert PJ, Silver RM. Systemic sclerosis: environmental and occupational risk factors. *Curr Opin Rheumatol*. 2000;12(6):520–526.
6. Arnett FC, Cho M, Chatterjee S, Aguilar MB, Reveille JD, Mayes MD. Familial occurrence frequencies and relative risks for systemic sclerosis (scleroderma) in three United States cohorts. *Arthritis Rheum*. 2001; 44(6):1359–1362.
7. Rosenbloom J, Feldman G, Freundlich B, Jimenez SA. Inhibition of excessive scleroderma fibroblast collagen production by recombinant γ-interferon: association with a coordinate decrease in types I and III procollagen messenger RNA levels. *Arthritis Rheum*. 1986;29(7): 851–856.
8. Laxer RM, Zulian F. Localized scleroderma. *Curr Opin Rheumatol*. 2006;18(6):606–613.
9. Peterson LS, Nelson AM, Su WP. Classification of morphea (localized scleroderma). *Mayo Clin Proc*. 1995;70(11):1068–1076.
10. Bernstein EJ, Peterson ER, Sell JL, et al. Survival of adults with systemic sclerosis following lung transplantation: a nationwide cohort study. *Arthritis Rheumatol*. 2015;67(5):1314–1322.
11. Mayes MD, Lacey JV Jr, Beebe-Dimmer J, et al. Prevalence, incidence, survival, and disease characteristics of systemic sclerosis in a large US population. *Arthritis Rheum*. 2003;48(8):2246–2255.
12. Minier T, Guiducci S, Bellando-Randone S, et al; EUSTAR co-workers. Preliminary analysis of the very early diagnosis of systemic sclerosis (VEDOSS) EUSTAR multicentre study: evidence for puffy fingers as a pivotal sign for suspicion of systemic sclerosis. *Ann Rheum Dis*. 2014; 73(12):2087–2093.
13. Katsumoto TR, Whitfield ML, Connolly MK. The pathogenesis of systemic sclerosis. *Annu Rev Pathol*. 2011;6:509–537.

14. Decuman S, Smith V, Verhaeghe ST, Van Hecke A, De Keyser F. Work participation in patients with systemic sclerosis: a systematic review. *Clin Exp Rheumatol*. 2014;32(6 Suppl 86):206–213.
15. Ring HC, Mogensen M, Hussain AA, et al. Imaging of collagen deposition disorders using optical coherence tomography. *J Eur Acad Dermatol Venereol*. 2015;29(5):890–898.
16. Brinckmann J, Neess CM, Gaber Y, et al. Different pattern of collagen cross-links in two sclerotic skin diseases: lipodermatosclerosis and circumscribed scleroderma. *J Invest Dermatol*. 2001;117(2):269–273.
17. Bashey RI, Jimenez SA. Increased sensitivity of scleroderma fibroblasts in culture to stimulation of protein and collagen synthesis by serum. *Biochem Biophys Res Commun*. 1977;76(4):1214–1222.
18. Oliver WC, Pharr GM. An improved technique for determining hardness and elastic modulus using load and displacement sensing indentation experiments. *J Mater Res*. 1992;7(6):1564–1583.
19. Fang M, Goldstein EL, Turner AS, et al. Type I collagen D-spacing in fibril bundles of dermis, tendon, and bone: bridging between nano- and micro-level tissue hierarchy. *ACS Nano*. 2012;6(11):9503–9514.
20. Farage MA, Miller KW, Elsner P, Maibach HI. Characteristics of the aging skin. *Adv Wound Care (New Rochelle)*. 2013;2(1):5–10.
21. van Zuijlen PP, Ruurda JJ, van Veen HA, et al. Collagen morphology in human skin and scar tissue: no adaptations in response to mechanical loading at joints. *Burns*. 2003;29(5):423–431.
22. Ricard-Blum S. The collagen family. *Cold Spring Harb Perspect Biol*. 2011;3(1):a004978.
23. Junqueira LC, Bignolas G, Brentani RR. Picrosirius staining plus polarization microscopy, a specific method for collagen detection in tissue sections. *Histochem J*. 1979;11(4):447–455.
24. Grinnell F, Lamke CR. Reorganization of hydrated collagen lattices by human skin fibroblasts. *J Cell Sci*. 1984;66:51–63.
25. De Paepe A, Malfait F. Bleeding and bruising in patients with Ehlers–Danlos syndrome and other collagen vascular disorders. *Br J Haematol*. 2004;127(5):491–500.
26. Heemskerk JW, Vuist WM, Feijge MA, Reutelingsperger CP, Lindhout T. Collagen but not fibrinogen surfaces induce bleb formation, exposure of phosphatidylserine, and procoagulant activity of adherent platelets: evidence for regulation by protein tyrosine kinase-dependent Ca2+ responses. *Blood*. 1997;90(7):2615–2625.
27. Monnier VM, Glomb M, Elgawish A, Sell DR. The mechanism of collagen cross-linking in diabetes: a puzzle nearing resolution. *Diabetes*. 1996;45(Suppl 3):S67–S72.
28. Wenger MP, Bozec L, Horton MA, Mesquida P. Mechanical properties of collagen fibrils. *Biophys J*. 2007;93(4):1255–1263.
29. Kurland NE, Drira Z, Yadavalli VK. Measurement of nanomechanical properties of biomolecules using atomic force microscopy. *Micron*. 2012;43(2–3):116–128.
30. Montes GS, Junqueira LC. The use of the picrosirius-polarization method for the study of the biopathology of collagen. *Mem Inst Oswaldo Cruz*. 1991;86(Suppl 3):1–11.
31. Holmes DF, Gilpin CJ, Baldock C, Ziese U, Koster AJ, Kadler KE. Corneal collagen fibril structure in three dimensions: structural insights into fibril assembly, mechanical properties, and tissue organization. *Proc Natl Acad Sci U S A*. 2001;98(13):7307–7312.
32. Goh KL, Holmes DF, Lu Y, et al. Bimodal collagen fibril diameter distributions direct age-related variations in tendon resilience and resistance to rupture. *J Appl Physiol*. 2012;113(6):878–888.
33. Eastoe JE. The amino acid composition of mammalian collagen and gelatin. *Biochem J*. 1955;61(4):589–600.
34. Kadler KE, Baldock C, Bella J, Boot-Handford RP. Collagens at a glance. *J Cell Sci*. 2007;120(Pt 12):1955–1958.
35. Kadler KE, Holmes DF, Trotter JA, Chapman JA. Collagen fibril formation. *Biochem J*. 1996;316(Pt 1):1–11.

APPENDIX 3

JOURNAL OF
biomaterials applications

Functional Biomaterials Surfaces

Journal of Biomaterials Applications
2015, Vol. 30(2) 147–159

DOI: 10.1177/0885328215577297
jba.sagepub.com
SAGE

A simple and robust method for pre-wetting poly (lactic-co-glycolic) acid microspheres

Bernice Wright[1], Nina Parmar[1], Laurent Bozec[2], Sebastian D Aguayo[2] and Richard M Day[1]

Abstract

Poly (lactic-co-glycolic) acid microspheres are amenable to a number of biomedical procedures that support delivery of cells, drugs, peptides or genes. Hydrophilisation or wetting of poly (lactic-co-glycolic) acid are an important pre-requisites for attachment of cells and can be achieved via exposure to plasma oxygen or nitrogen, surface hydrolysis with NaOH or chloric acid, immersion in ethanol and water, or prolonged incubation in phosphate buffered saline or cell culture medium. The aim of this study is to develop a simple method for wetting poly (lactic-co-glycolic) acid microspheres for cell delivery applications. A one-step ethanol immersion process that involved addition of serum-supplemented medium and ethanol to PLGA microspheres over 30 min–24 h is described in the present study. This protocol presents a more efficient methodology than conventional two-step wetting procedures. Attachment of human skeletal myoblasts to poly (lactic-co-glycolic) acid microspheres was dependent on extent of wetting, changes in surface topography mediated by ethanol pre-wetting and serum protein adsorption. Ethanol, at 70% (v/v) and 100%, facilitated similar levels of wetting. Wetting with 35% (v/v) ethanol was only achieved after 24 h. Pre-wetting (over 3 h) with 70% (v/v) ethanol allowed significantly greater ($p \leq 0.01$) serum protein adsorption to microspheres than wetting with 35% (v/v) ethanol. On serum protein-loaded microspheres, greater numbers of myoblasts attached to constructs wetted with 70% ethanol than those partially wetted with 35% (v/v) ethanol. Microspheres treated with 70% (v/v) ethanol presented a more rugose surface than those treated with 35% (v/v) ethanol, indicating that more efficient myoblast adhesion to the former may be at least partially attributed to differences in surface structure. We conclude that our novel protocol for pre-wetting poly (lactic-co-glycolic) acid microspheres that incorporates biochemical and structural features into this biomaterial can facilitate myoblast delivery for use in clinical settings.

Keywords

Poly (lactic-co-glycolic) acid microspheres, thermally induced phase separation, thermally induced phase separation microspheres, serum protein adsorption, human skeletal myoblasts and thermally induced phase separation microspheres, poly (lactic-co-glycolic) acid microsphere surface topography, wetting poly (lactic-co-glycolic) acid microspheres

Introduction

Poly (lactic-co-glycolic) acid (PLGA) is a synthetic, biocompatible copolymer that is commonly used as a cell[1] and protein[2] delivery scaffold. Due to intrinsic hydrophobic properties, PLGA polymers require pre-treatment to wet or hydrophilise their surface and thereby allow cell attachment. A number of approaches including ethanol immersion,[3,4] chemical modification with alkaline solutions (e.g. NaOH)[5] and plasma oxygen[6,7] are demonstrated as viable techniques for improving the hydrophilicity, pre-wetting or hydrophilisation of PLGA. The ethanol-mediated pre-wetting method involves the exchange of ethanol for culture medium in microsphere pores to eventually submerge these constructs and enable contact with cells, whereas hydrophilisation involves hydrolysis of the microsphere

[1]Applied Biomedical Engineering Group, Division of Medicine, University College London
[2]Division Biomaterials and Tissue Engineering, UCL Eastman Dental Institute, University College London

Corresponding author:
Richard M Day, Applied Biomedical Engineering Group, Division of Medicine, University College London.
Email: r.m.day@ucl.ac.uk

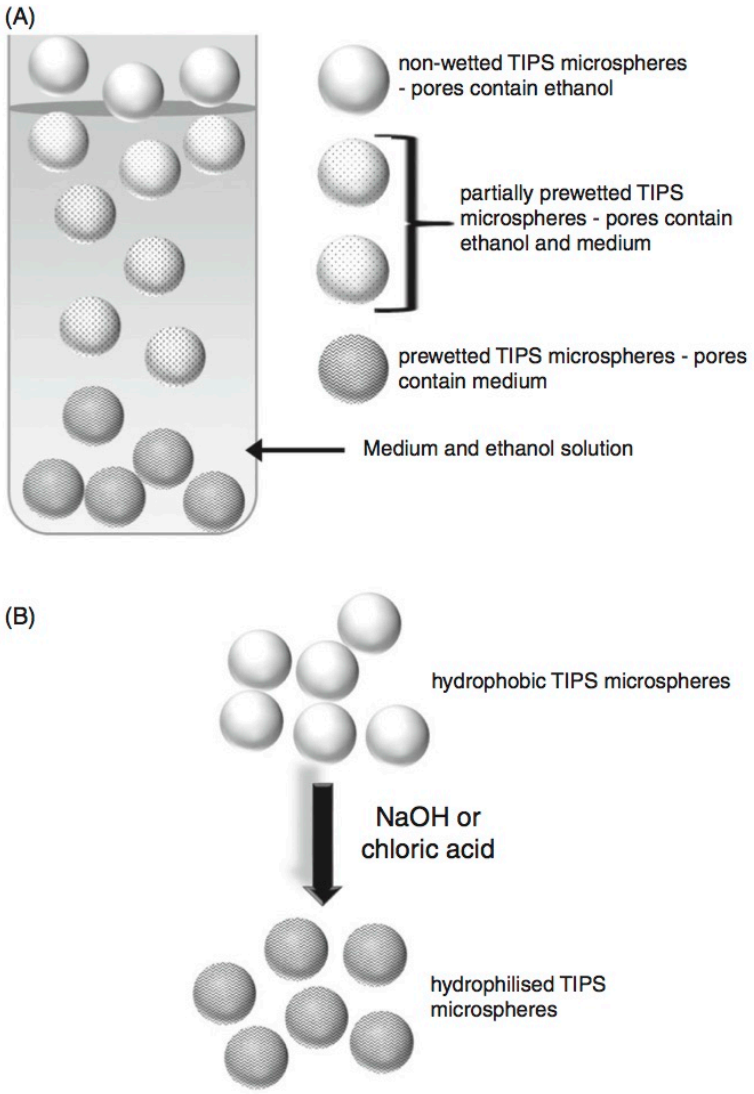

Figure 1. Wetting and hydrophilisation of hydrophobic polymers. Wetting (a) is a simple procedure that is achieved with diluted ethanol. The ethanol is exchanged for culture medium until pore spaces in the polymer are filled with medium, allowing the polymer to become submerged. Hydrophilisation (b) involves hydrolysis of a polymer by a strong alkali (e.g. NaOH) or acid (e.g. chloric acid solution) to create hydroxyl or carboxyl groups on the polymer surface.

surface with strong acids or alkalis (Figure 1). For laboratory and clinical application of PLGA microspheres, the simple, practical, ethanol immersion method for pre-wetting PLGA is the best approach. The aim of the current study is to describe optimal conditions for ethanol-dependent wetting of PLGA microspheres that support efficient loading of human skeletal myoblasts.

In the present study, PLGA microspheres fabricated with the thermally-induced phase separation (TIPS) technology were employed. This specialized technique allows formation of monodisperse, highly porous microspheres via rapid removal of thermal energy in a liquid nitrogen bath.[8] The key advantages of TIPS PLGA microspheres include their open pore structure that facilitates controlled, sustained release of small-molecule drugs (e.g. antibiotics)[9] and antibodies,[2] an external surface that supports adhesion and proliferation of cells[1] and a predictable degradation profile.[10] Moreover, TIPS microcarriers require less initial polymer material to be formed than the more commonly used solid PLGA microspheres, due to their intrinsic

porosity. We have found that *in vivo*, TIPS microspheres can integrate into tissue and are infiltrated by inflammatory cells (unpublished data). The present study will indicate wetting conditions for these scaffolds that will allow optimal loading with human skeletal myoblasts.

Wetting or hydrophilisation of hydrophobic polymers is an essential pre-requisite for cell attachment.[11–14] A previous study demonstrated that poly (glycolic acid) fibre meshes pre-wetted with medium supported attachment of murine hepatocytes.[15] Moderately hydrophilic surfaces rather than those that were hydrophobic or completely hydrophilic were reported to support endothelial cell adhesion on polyethylene (PE) glycol films, and the strength of adhesion was dependent on maintaining partial hydrophilisation.[16] Moderate wetting of hydrophobic methacrylate polymers has been shown to allow efficient adhesion of endothelial cells, but greater numbers of cells adhered in the presence of serum compared to serum-free conditions.[14] A related study showed that moderately wetted polymer surfaces exhibited a serum and cellular protein adsorption pattern that was favorable for attachment of endothelial cells.[13]

Further studies investigating wettability and cell adhesion focused on the use of the wettability gradient of polymers to study the link between protein adsorption and cell adhesion.[11,17] These studies demonstrated that various cell types (Chinese hamster ovary cells, mouse embryo fibroblasts, bovine pulmonary artery cells) adhered, spread and grew in positions along the wettable gradient surface that were moderately hydrophilic on PE films.[11,17] Chargeable functional group gradient surfaces on wetted PE sheets, where the surface density of grafted functional groups (carboxylic acid, sulphonate and amine groups) changed gradually along the sample length, supported the attachment and growth of Chinese hamster ovary cells.[17]

Human albumin adsorption to PE sheets was reported to decrease along the wettability gradient, therefore increasing along the hydrophobic regions of this polymer.[12] Despite this study, human serum adsorption has been correlated to adhesion of human endothelial cells to moderately hydrophilic polymers,[13] possibly due to preferential adsorption of serum proteins to hydrophilic regions.[11]

Structural modifications to PLGA due to polymer composition, method of manufacture and nanostructured surface features were previously shown to influence the binding of serum proteins as well as cells to this polymer. Pluronic® F-108 blended PLGA microfibrous scaffolds adsorbed significantly greater amounts of bovine serum albumin than unblended PLGA.[18] PLGA microspheres fabricated via a water/oil/water (w/o/w) emulsion solvent evaporation method adsorbed greater levels of albumin, IgG, gelsolin and β2-Glycoprotein I than those prepared using a spray-drying technique. The latter technique, however, allowed greater adsorption of apolipoproteins, Ig light chains and IgD.[19] PLGA scaffolds synthesized to present surface features ranging from micron to nanometer, allowed greater adhesion of endothelial and smooth muscle cells compared to unmodified PLGA.[20] Similar topographical changes (submicron to nanometer surface features) to PLGA reduced fibronectin adsorption and platelet adhesion to these proteins on the polymer.[21]

In the present study, TIPS microspheres were wetted to various extents by exposure to different concentrations of ethanol. Serum protein adsorption to TIPS microspheres was shown to accelerate wetting. Human skeletal myoblast attachment to microspheres is influenced by both wetting and the amount of protein adsorbed to these scaffolds, with high amounts of serum protein enhancing the efficiency of cell attachment to less wetted microspheres. We attributed differences in cell attachment to changes in surface topography that demonstrated a more rugose surface structure for more wetted microspheres compared to those that were less wetted.

Taken together, the present study describes a protocol for the preparation of TIPS PLGA microspheres that can be used to facilitate cell delivery with these material scaffolds through dual modification of wetting and protein adsorption parameters.

Materials and methods

Materials

Nutrient mixture F-10 Ham, dexamethasone, antibiotics (penicillin/streptomycin), Trypan Blue dye solution, Tris-base, acetic acid, Trypsin/EDTA solution, sodium dodecyl sulphate (SDS), 2-mercaptoethanol, ammonium persulphate (AMPS), N,N,N′,N′-tetramethylethylenediamine (TEMED), silver nitrate, sodium carbonate, sodium acetate, ethanol, formaldehyde, ethylenediaminetetraacetic acid disodium dehydrate, bovine serum albumin (BSA), the Micro Lowry (Peterson's Modification) total protein assay kit, bromophenol blue, glycerol and sodium thiosulphate were purchased from Sigma-Aldrich (Poole, UK). Industrial methylated spirits (IMS; 99% ethanol) was obtained from Barrettine Industrial Ltd. (Bristol, UK) and human fibroblast growth factor (FGF) basic was acquired from Peprotech (London, UK). Dulbecco's modified eagle's medium (DMEM)/Ham F-12 (1:1), fetal bovine serum (FBS) and the Cyquant® NF assay kit were from Life Technologies (Paisley, UK). Methanol and acetic acid were purchased from Thermo Scientific HyClone (Fisher Scientific: Leicestershire, UK) and acrylamide

(30% acrylamide/Bis solution) was from BioRad (Hertfordshire, UK). The human skeletal myoblasts were from Lonza Biologics (Slough, UK) and the VectorShield mounting medium with 4′,6-diamidino-2-phenylindole (DAPI) was from Vector Laboratories Ltd. (Peterborough, UK). TIPS PLGA (Purasorb PDLG 7507, Purac Biomaterials, Gorinchem, The Netherlands) microspheres (75:25, inherent viscosity approximately 0.6 dl g^{-1}) were prepared as previously described.[1,2]

Methods

Pre-wetting PLGA TIPS microspheres. PLGA TIPS microspheres were fabricated[1,2] using 75:25 poly(D,L-lactide-co-glycolide) (Purasorb PDLG 7507, Purac Biomaterials, Gorinchem, The Netherlands) that was dissolved in dimethylcarbonate (1:25 (w/v), Sigma–Aldrich, UK). Polymer solution was fed into Nisco Encapsulator Unit Var D (Nisco Engineering, Zurich, Switzerland) by a syringe pump (Pump 11, Harvard Apparatus, Kent, UK), connected via a silicone tube, at a constant rate of 3 mL min^{-1}, with vibration frequency of the nozzle at 1.80 kHz and the amplitude of frequency at 100%. Liquid polymer droplets were ejected into a PE beaker containing 250 mL of liquid nitrogen, and frozen droplets were equilibrated in the liquid nitrogen, before samples were freeze dried (Edwards MicroModulyo freeze dryer, Thermo Fisher Scientific, Asheville, NC) for 24 h to allow the sublimation of residual dimethylcarbonate. TIPS microspheres were sieved to produce batches with diameters of 200–300 µm in diameter and scanning electron microscopy confirmed their spherical morphology.

PLGA TIPS microspheres were wetted with industrial methylated spirits (IMS) containing 99% ethanol. IMS was used instead of 100% ethanol as this solution allowed TIPS microspheres to be wetted in a similar manner as ethanol. In future studies where the pre-wetting protocol will be scaled up to a high throughput bioprocess, for large-scale commercial production of wetted TIPS microspheres, the use of IMS for pre-wetting TIPS microspheres will be replaced with ethanol. Dry microspheres were weighed into bijou tubes and 3 mL DMEM/F12 containing 0%, 2%, 10% or 20% FBS was pipetted over the polymer. IMS (600 µL) at 35% (v/v), 70% (v/v) or 100% was mixed into the medium by gentle pipetting. Microspheres were incubated in the medium/IMS solution for 30 min, 3 h and 24 h before the tube was photographed to image the sinking of the polymer from the surface of the solution as it became wetted. After the pre-wetting period, the microspheres were washed with sterile nanopure water – 3 mL and 1 mL of water were used for the first and second washes, respectively. For quantification of proteins adsorbed to the microsphere surface, the individual polymer preparations were suspended in 100 µL of water before the protein assay was performed. PLGA microspheres used for myoblasts attachment studies were prepared using Nutrient medium Ham F-10 instead of DMEM/F12 as the base medium.

Total protein estimations. The micro Lowry protein assay kit was used to measure the amount of serum proteins adsorbed to the surface of PLGA microspheres pre-wetted in the presence of FBS. BSA dissolved in nanopure water was used as a protein standard at 50, 100, 200, 300, 400, 500 and 1000 µg/mL concentrations. The Lowry reagent solution (250 µL) was added to 100 µL of each BSA standard, microsphere preparation (suspended in 100 µL nanopure water) or 100 µL water (blank). The solutions were mixed well by vortexing briefly at high speed and incubated at room temperature for 20 min. Folin and Ciocalteu's phenol reagent working solution (125 µL) was added to each tube with rapid and immediate mixing and the colour was allowed to develop for 30 min. The solutions (100 µL) were transferred to a 96-well plate and absorbance was measured at a wavelength between 500 and 800 nm within 30 min.

One-dimensional gel electrophoresis. Sodium dodecyl sulphate – polyacrylamide gel electrophoresis (SDS-PAGE) was carried out in discontinuous vertical slab gels which contained a final concentration of 15% v/v acrylamide in the resolving gel and 4% (v/v) acrylamide in the stacking gel. The stacking gel contained stacking gel buffer (0.5 M Tris-base; pH 6.8), 30% (v/v) acrylamide, 10% (w/v) SDS, 0.05% (v/v) TEMED and 1.5% (w/v) AMPS. The resolving gel comprised resolving gel buffer (3 M Tris-base and 5 N HCl; pH 8.8), 30% (v/v) acrylamide, 10% (w/v) SDS, 0.08% (v/v) TEMED and 1.5% (w/v) AMPS.

Silver nitrate protein staining. Serum proteins and albumin were stained with silver nitrate. Briefly, proteins immobilized in 15% v/v acrylamide gels were fixed in a solution containing 40% (v/v) methanol, 10% (v/v) acetic acid and 50% (v/v) water. Gels were then washed three times for 5 min each time before they were treated with (5% (w/v) sodium thiosulphate, 30% (v/v/) ethanol and 68 mg/mL sodium acetate) for 30 min. The gel was then washed three times with deionised water for 10 min each time, and stained with 2.5% (w/v) silver nitrate

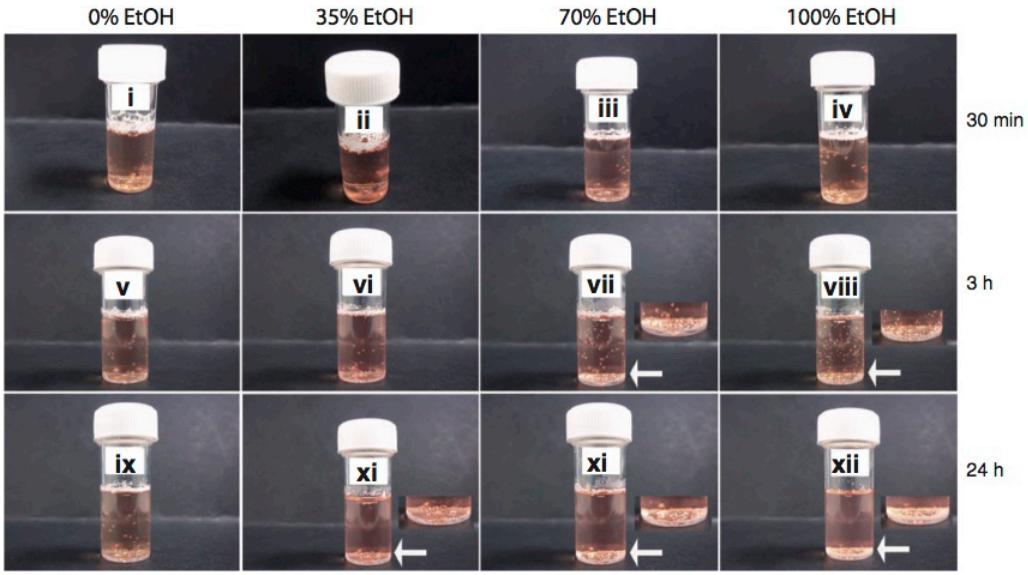

Figure 2. Wetting of TIPS PLGA microspheres by ethanol is dose-dependent. PLGA microspheres were suspended in medium containing 20% FBS and treated with 35% (v/v), 70% (v/v) or 100% ethanol (EtOH), for 30 min, 3 h and 24 h. Arrows and image insets show detailed images of submerged microspheres. Images represent three individual experiments.

for 20 min. Stained gels were washed twice with deionised water (2 min per wash, and the silver stain was developed using a solution of 2.5% (w/v) sodium carbonate and 0.04% (v/v) formaldehyde. When protein bands were visible, development of the stain was stopped using a 1.46% (w/v) EDTA-$Na_{22}H_2O$ solution. The stained gels were washed with water and imaged using an Epson gel scanner. Gels were stored in 5% (v/v) acetic acid at 4°C.

Culture of human skeletal myoblasts. Human skeletal myoblasts (Lonza Biologics) were initially cultured to 70–80% confluency on tissue culture plastic in supplemented (FBS (20%), human FGF-basic (1 µg/mL), dexamethasone (100 µM) and antibiotics (penicillin/streptomycin) (1%)) Nutrient mixture F-10 Ham. Myoblasts were then detached from culture flasks using Trypsin/EDTA solution, counted using a haemocytometer and evaluated for live and dead cell proportions using the Trypan blue exclusion assay (the number of dead cells were negligible). Myoblasts (5×10^4) were seeded onto PLGA TIPS microspheres (approximately 250 microspheres) pre-wetted with 35% or 70% IMS in the presence of 0%, 2% or 20% FBS. The cells and microspheres were cultured in 100 µL supplemented Nutrient mixture F-10 Ham in a 96-well plate for 6 h. The plate was shaken for 10 s every hour at approximately 500 r/min to lift both the myoblasts and the microspheres, to allow the cells to maintain contact with the polymer. After the culture period, the cells that remained unattached to the polymer were washed away with sterile phosphate buffered saline (PBS).

Cell quantification using the Cyquant® NF assay. The number of myoblasts attached to TIPS microspheres pre-wetted under various conditions was measured using the Cyquant® NF assay that determines levels of cellular DNA via fluorescent dye binding. The dye reagent (50 µL) was incubated with PLGA/myoblasts constructs for 1 h at 37°C. Fluorescence was excited at 485 nm and emitted at 530 nm and the signals generated were correlated with that from a standard curve of known cell numbers to determine the number of cells adhered to microspheres.

Fluorescence microscopy. The PLGA/myoblast constructs were fixed with 4% (w/v) for 1 h and mounted with VectorShield containing DAPI on a glass slide. A coverslip was placed over the glass slide prior to analysis. Fluorescence was excited at 358 nm and emitted at 461–488 nm and three-dimensional representations of nuclei from myoblasts attached to the surface of PLGA microspheres were constructed by the generation of layers in the z dimension which were compiled into z-stacks.

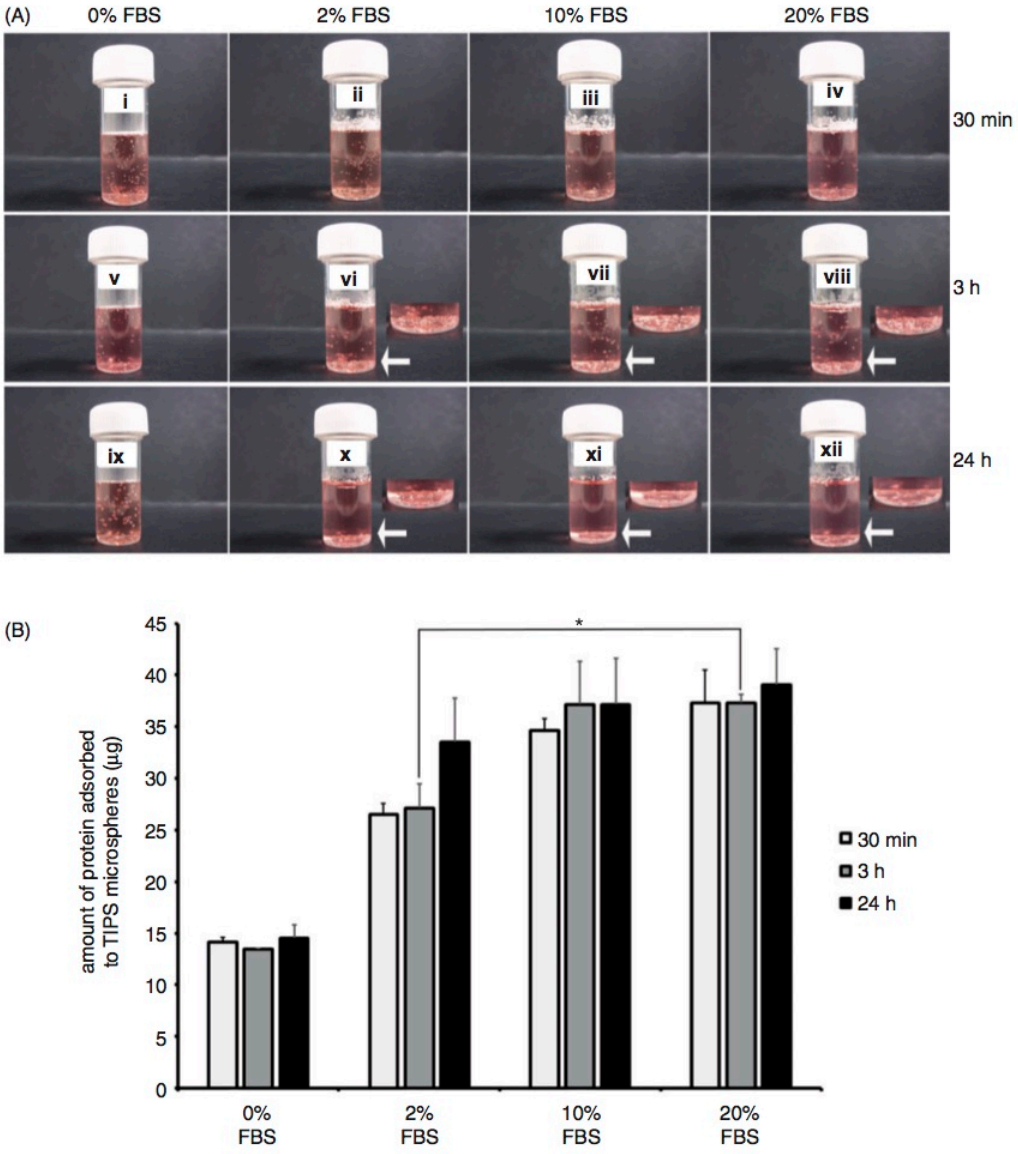

Figure 3. Serum proteins adsorb to wetted TIPS microspheres in a dose-dependent manner. PLGA microspheres were suspended in medium containing 0%, 2%, 10% or 20% FBS and treated 70% (v/v) ethanol (EtOH), for 30 min, 3 h and 24 h (a). Arrows and image insets show detailed images of submerged microspheres. The total amount of serum protein adsorbed to microspheres was measured after each incubation period (b). Data points represent the mean ($n = 3 \pm$ SEM) amount of total protein. *$p \leq 0.05$ indicates differences between wetting conditions. Images represent three individual experiments.

Atomic force microscopy. Pre-wetted TIPS microspheres were mounted on sterile glass slides using super glue and imaged under deionized water in intermittent contact (liquid) mode employing a JPK NanoWizard II AFM (JPK Instruments, Germany) mounted on an Olympus IX71 inverted microscope. MSNL-10 cantilevers (Bruker, Santa Barbara, USA), tuned to a drive frequency of ~46 kHz (nominal resonant frequency 25–50 kHz), were employed with a constant line rate of 0.5 Hz. Gain parameters and set point were adjusted according to each sample. Thermal resonance calibration yielded a cantilever spring constant of 0.11 N/m (nominal value 0.1 N/m). After focusing on an area of interest, images with different scan sizes of 5×5 µm were obtained at random sites of each sample and processed with the Gwyddion 2.37 SPM software.

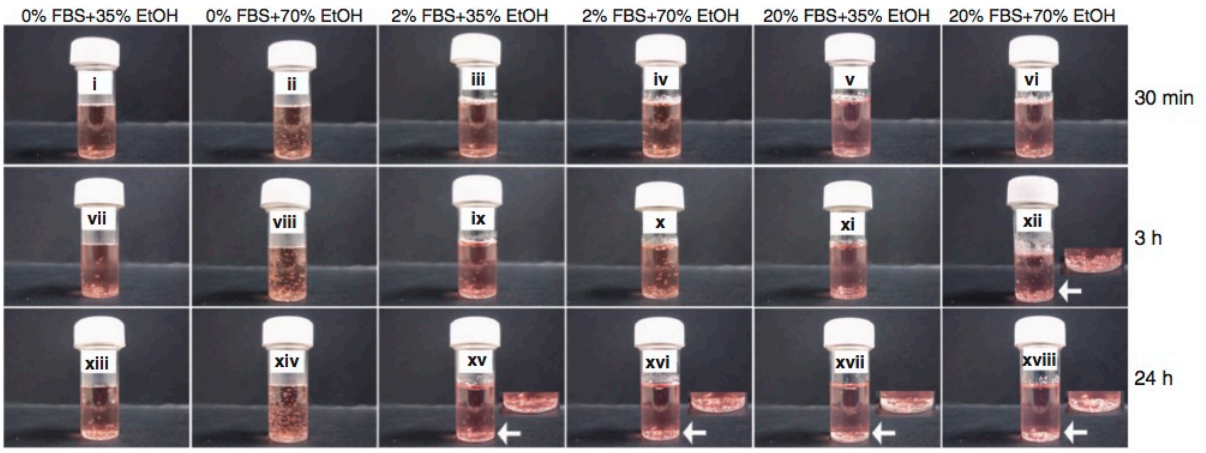

Figure 4. Serum proteins accelerate ethanol-mediated wetting of PLGA microspheres. PLGA microspheres were suspended in medium containing 0%, 2% or 20% FBS and treated with 35% (v/v) or 70% (v/v) ethanol (EtOH), for 30 min, 3 h and 24 h. Arrows and image insets show detailed images of submerged microspheres. Images represent three individual experiments.

Statistical analysis. Unpaired *t*-tests were performed using Microsoft Excel to determine the statistical significance of quantified data. Results are presented as the mean of three individual experiments with standard error of mean (SEM) and p value ≤ 0.05 considered significant.

Results

Wetting of PLGA microspheres is enhanced with exposure to increasing concentrations of ethanol

To wet PLGA microspheres we performed a one-step ethanol immersion method. Ethanol was added to TIPS microspheres suspended in serum-supplemented cell culture medium. The sinking of microspheres in medium was used as an indicator of wetting, as previously described.[22]

Microspheres were wetted with 35% (v/v), 70% (v/v) and 100% industrial methylated spirits (containing 99% ethanol) over 30 min, 3 h and 24 h time periods, under standard culture conditions (37°C, 5% CO_2, 95% humidity). We observed that microsphere pre-wetting was dependent on ethanol concentration and the length (30 min, 3 h and 24 h) of the wetting procedure. Microspheres exposed to 70% (v/v) and 100% ethanol became immersed in medium (containing 20% FBS) after 3 h, but those exposed to 35% (v/v) ethanol required 24 h before they were completely submerged (Figure 2).

These data demonstrated that PLGA microsphere wetting can be modified to various extents by altering ethanol concentrations and exposure times with this solvent. To our knowledge, our study is the first to show that dose- and time-dependent exposure to ethanol can be used to wet PLGA TIPS microspheres.

Serum protein adsorption to PLGA microspheres accelerates wetting

Serum protein adsorption was previously linked to hydrophilisation of hydrophobic polymers.[11,13] We, therefore, investigated the correlation between serum protein adsorption and wetness of PLGA TIPS microspheres. Microspheres were incubated with 35% (v/v) or 70% (v/v) ethanol in medium containing 2%, 10% and 20% serum (FBS).

Microspheres became completely submerged in 20% (v/v) and 10% (v/v) FBS preparations (with 70% (v/v) ethanol for wetting) after 3 h, but those exposed to 2% (v/v) FBS became immersed in medium after 24 h (Figure 3a.). After 3 h microspheres exposed to 20% (v/v) or 10% (v/v) FBS adsorbed similar amounts of protein (approximately 24 µg total protein), and a significantly lower ($p \leq 0.05$) amount of protein (approximately 14 µg total protein) was adsorbed to those exposed to 2% (v/v) FBS (Figure 3b). Under conditions applying 35% (v/v) ethanol, that allowed only partial wetting of microspheres, microspheres did not sink after 3 h (Figure 4). Instead, after 24 h a proportion of microspheres treated with 2% FBS and 35% or 70% ethanol became submerged, but the majority of those treated with 20% FBS including 35% or 70% ethanol sank in medium (Figure 4).

Microspheres treated with 2% FBS + 70% ethanol and those treated with 20% FBS + 35% ethanol adsorbed similar amounts of serum proteins (Figure 5a). By contrast after a 3-h incubation, microspheres treated with 20% FBS + 70% ethanol adsorbed significantly greater ($p \leq 0.01$) amounts of serum protein than those treated with 20% FBS + 35% ethanol, suggesting that the increased wetness of microspheres

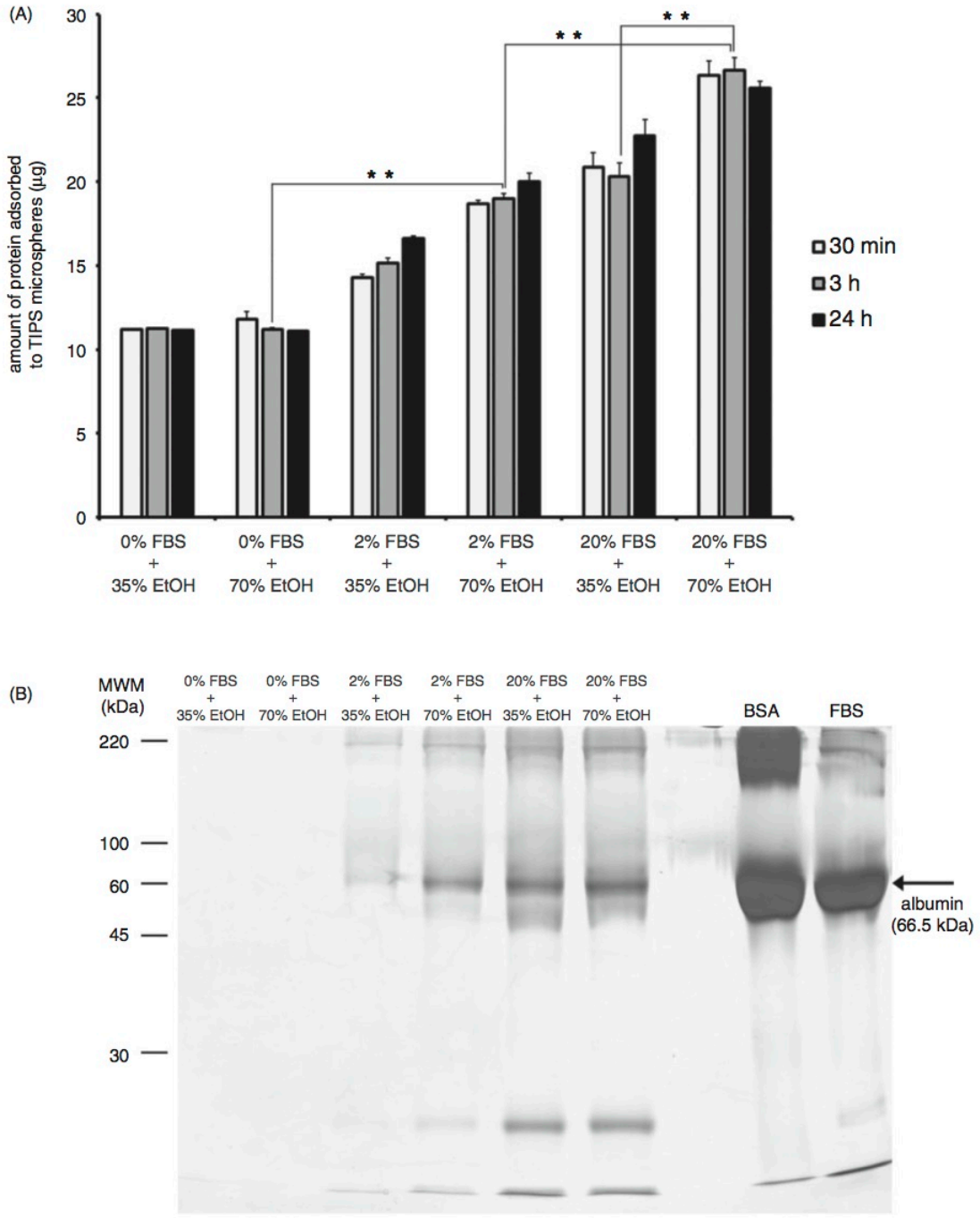

Figure 5. The adsorption of serum proteins to PLGA microspheres is dependent on the extent of pre-wetting. PLGA microspheres were suspended in medium containing 0%, 2% or 20% FBS and treated with 35% (v/v) or 70% (v/v) ethanol (EtOH), for 30 min, 3 h and 24 h. The total amount of serum protein adsorbed to microspheres was measured after each incubation period (a). Serum and EtOH-treated microspheres were heated (95°C) in Laemmli buffer containing the reducing agent β-mercaptoethanol, proteins were separated using 15% acrylamide gels and stained using silver nitrate (b). Bovine serum albumin (BSA) and fetal bovine serum (FBS) were included as external controls. Data points represent the mean ($n = 3 \pm$ SEM) amount of total protein. *$p \leq 0.05$ indicate differences between wetting conditions. Gel represents three individual experiments from three different sets of microsphere-protein adsorption experiments.

conferred by 70% (v/v) ethanol enhanced protein adsorption. The amount of protein adsorbed to microspheres wetted with 70% (v/v) ethanol increased as levels of FBS were raised. 0% FBS + 70% ethanol preparations adsorbed significantly less ($p \leq 0.01$) amounts of protein than 2% FBS + 70% ethanol microspheres, which adsorbed significantly less ($p \leq 0.01$) protein than 20% FBS + 70% ethanol microspheres. In preparations including 2% FBS, levels of albumin adsorbed to microspheres increased as the wetness of the polymers was enhanced, i.e. 70% ethanol allowed more albumin to adsorb than 35% ethanol (Figure 5a and b). Microspheres incubated with 20% FBS adsorbed similar levels of albumin whether they were partially wetted (35% ethanol) or completely wetted (70% ethanol), suggesting that the polymer may be saturated with protein when incubated with 20% FBS.

These data indicated that an additional level of control for wetting PLGA microspheres can involve adsorption of serum proteins.

Human skeletal myoblast attachment to PLGA microspheres is dependent on the extent of wetting and surface topography

Cells have been shown to preferentially bind to wet surfaces[23] and cell adhesion was reported to be dependent on the adsorption of serum proteins to substrates.[24] We therefore investigated the attachment of human skeletal myoblasts to PLGA microspheres treated with 2% and 20% FBS, wetted with 35% and 70% ethanol (during a 3 h period) to determine conditions for optimal loading of these cells on the surface of the polymer scaffold. Myoblasts attached in greater numbers to microspheres wetted with 70% ethanol than those wetted with 35% ethanol regardless of a high serum protein concentration (20% FBS) (Figure 6). Cells were distributed on the peripheral regions of partially wetted microspheres (0% FBS + 70% ethanol (Ai), 2% FBS + 70% ethanol (Aii), 20% FBS + 35% ethanol (Aiii)) and they populated the whole as well as peripheral regions of the microsphere as wetness increased (20% FBS + 70% ethanol (Aiv)) (Figure 6a).

With lower amounts of serum protein (2% FBS) adsorbed to microspheres wetted with 70% ethanol, a significantly lower ($p \leq 0.05$) number of cells attached than those treated with 20% FBS + 70% ethanol (Figure 6b). Greater numbers ($p \leq 0.05$) of myoblasts attached to 20% FBS + 70% ethanol treated microspheres than those incubated with 20% FBS + 35% ethanol. Microspheres treated with 20% FBS + 35% ethanol allowed the attachment of similar numbers of cells as those treated with 2% FBS + 70% ethanol. In the absence of serum proteins and with 70% ethanol for wetting, five times less cells attached to microspheres than to those treated with 2% FBS pre-wetted with 70% ethanol. These data indicated that for skeletal myoblast loading to PLGA TIPS microspheres, wetting precedes the requirement for serum protein adsorption. Increasing the amount of serum proteins (ideally, autologous serum proteins) exposed to partially wet microspheres can, however, enhance cell loading.

A hypothesis of the present study was that the differences observed in the numbers of cells attaching to

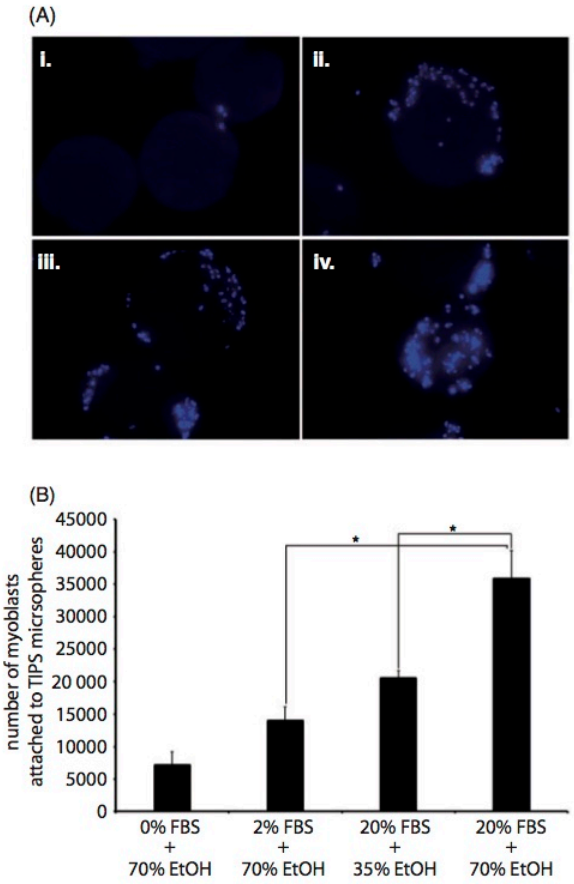

Figure 6. Human skeletal myoblast attachment to PLGA microspheres is dependent on the extent of pre-wetting and serum protein adsorption. Human skeletal myoblasts were subjected to dynamic culture (10 s shaking at approximately 400 r/min, every hour) for 6 h together with PLGA microspheres treated with 0% FBS-70% EtOH (Ai), 2% FBS-70% EtOH (Aii), 20% FBS-35% EtOH (Aiii) or 20% FBS-70% EtOH (Aiv) for 3 h. The nuclei of myoblasts attached to microspheres were stained with DAPI and imaged with excitation at 358 nm and emission at 461–488 nm. The Cyquant assay that measures DNA levels in cells was used to quantify the number of cells (B) attached to microspheres. Data points represent the mean ($n = 3 \pm SEM$) number of cells. *$p \leq 0.05$ indicate differences between cell attachment in various wetting conditions.

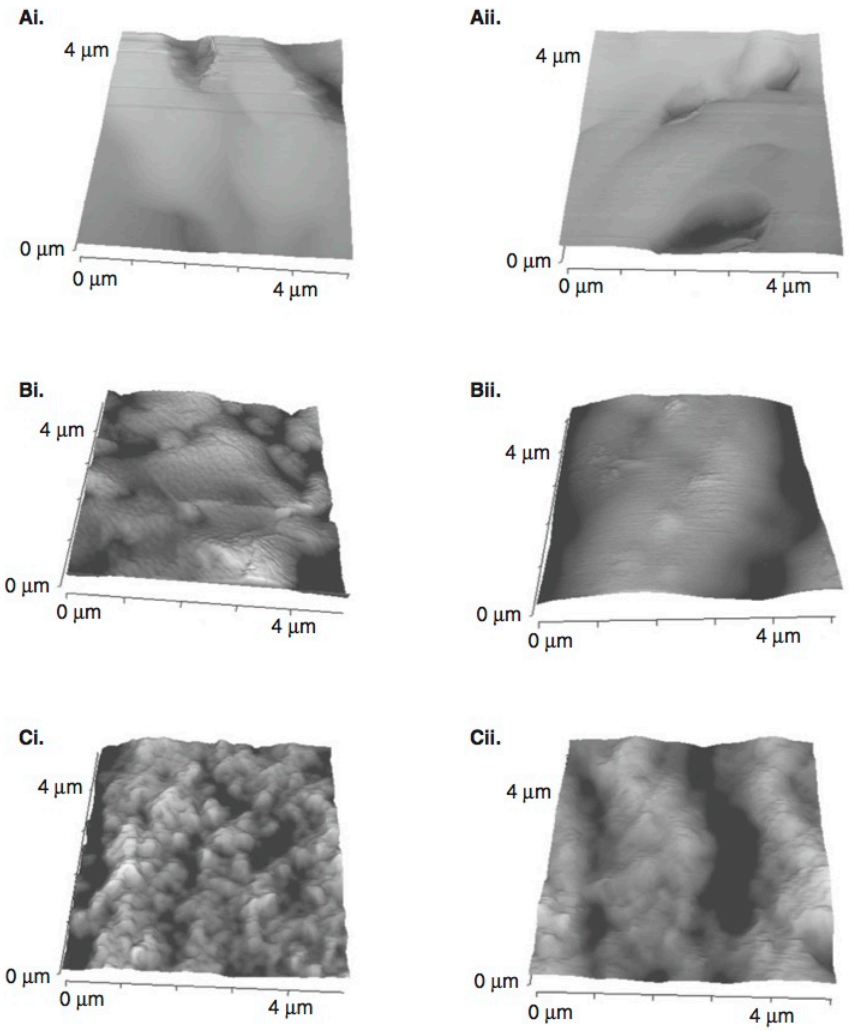

Figure 7. The surface topography of TIPS microspheres is modified by pre-wetting with ethanol. PLGA microspheres treated with 0% FBS and 0% ethanol (ai and aii) 20% FBS and 35% (v/v) (bi and bii) or 70% (v/v) (ci and cii) ethanol (EtOH) for 3 h were attached to metal stubs and imaged with a JPK NanoWizard II AFM mounted on an Olympus IX71 inverted microscope. Images of 5 × 5 µm dimensions were obtained at random sites on each sample. Images represent three individual experiments.

microspheres may be due to changes in the surface topography due to variations in levels of wetting. Previous studies have shown that the addition of nano- and micro-features to PLGA microspheres increases endothelial cell attachment.[20] Certainly, microspheres wetted with 70% (v/v) ethanol (Figure 7Ci and Cii) presented a more rugose surface structure than those treated with 35% (v/v) ethanol (Figure 7Bi and 7Bii), indicating that human skeletal myoblasts adhered more readily to a rough surface than a smooth surface (Figure 7).

The data described in the current study suggest that the surface topography of TIPS microspheres is an important modulator of cell attachment to these copolymers that can be altered with ethanol-mediated wetting and serum protein adsorption to manipulate cell loading efficiency.

Discussion

The clinical delivery of therapeutic cells could be significantly enhanced if they were delivered locally and retained in the tissue area requiring repair. Biocompatible PLGA microspheres were demonstrated to be wetted to various extents with ethanol and serum proteins via a simple method to control human skeletal myoblast loading. These cells may therefore be presented clinically on pre-wetted PLGA microspheres in varying amounts as necessary for specific treatment requirements.

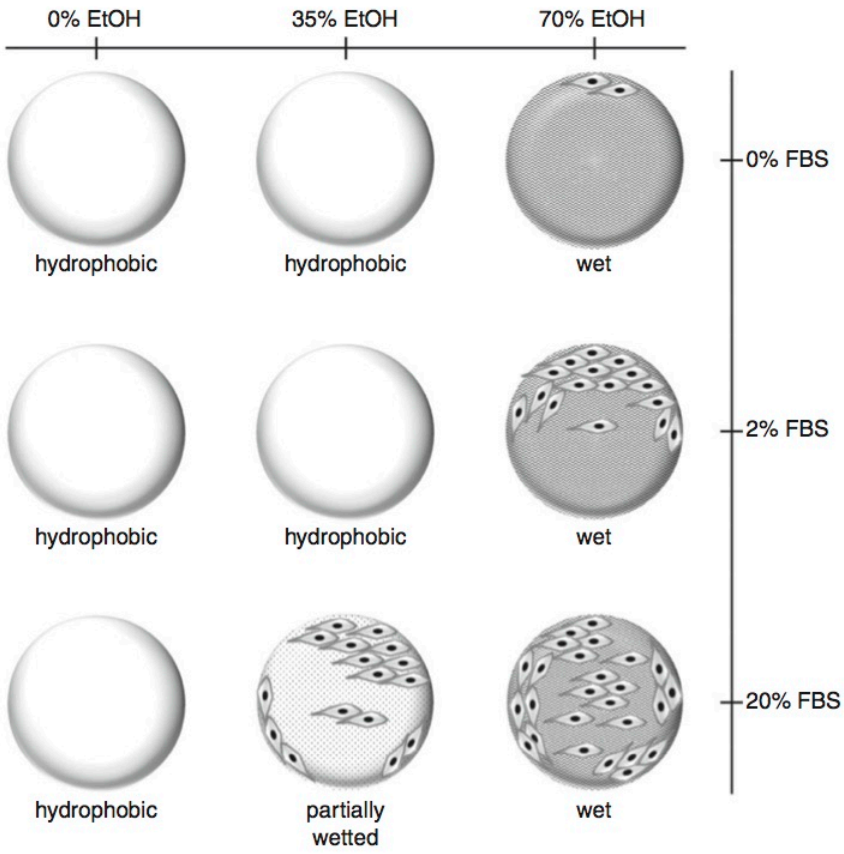

Figure 8. A working model of wetting conditions for attachment of human skeletal myoblasts to PLGA TIPS microspheres. PLGA TIPS microspheres incubated with various concentrations of ethanol (EtOH: 35%–70% (v/v)) and serum proteins (FBS:2–20%) allow the attachment of different numbers of skeletal myoblasts. The number of attached cells increase as the amount of serum protein exposed to microspheres is elevated. Microspheres that are partially wetted (35% EtOH) and incubated with high serum concentrations (20% FBS) allow attachment of similar numbers of cells as microspheres wetted (70% EtOH) under low-serum (2% FBS) conditions.

In the present study, TIPS microspheres that are 4–9 times smaller (200–300 µm in diameter) than PLGA foam disks may be completely wetted with 100% ethanol after 24 h. Mikos et al.[3] showed that 100% ethanol can wet PLGA foams in less than 24 h. This report demonstrated that wetting of PLGA foams in a two-step ethanol and water immersion method, allowed water entry into PLGA foam disks that were 1300–1730 µm in depth, and after only 1 h, water entry was close to its plateau value. The one-step ethanol immersion wetting procedure described in the present study may be suitable for applications requiring degradation of TIPS microspheres, for example, for the in vivo release of attached cells or encapsulated protein from this polymer. Wetting with ethanol in PBS has been shown to increase degradation of PLGA compared to wetting with PBS alone.[4] Another advantage of the one-step method is that it is amenable to high-throughput production of pre-wetted PLGA microspheres that are safe and economically viable. TIPS microspheres were previously shown to present improved water wetting following treatment with atmospheric air plasma (AP: electrical ionization of gas) due to the formation of oxygen- and nitrogen-containing functions.[7] Similar to ethanol-mediated wetting, AP can be applied in a production line setting for rapid treatment of TIPS microspheres, but this method presents safety and cost issues that are obviated by the one-step ethanol immersion protocol.

In line with findings described here, a previous study showed that endothelial adhesion strength is greater on hydrophilic positions on wettable polymers than on the hydrophobic positions.[11] Interestingly, pre-adsorption of different serum proteins on polymers has been shown to cause differential cell adhesion – serum albumin prevented cell adhesion whereas the cell

adhesion protein, fibronectin, enhanced cell adhesion independent of the extent of wetness.[25] The adhesion of myoblasts to pre-wetted myoblasts in the present study may be due to competitive adsorption of cell adhesion proteins from the mixture of serum proteins.[19] The microspheres prepared in the present study may only be moderately wetted, because studies have shown that cells attach to moderately hydrophilic surfaces and they do not attach to hydrophobic or completely hydrophilic surfaces.[11,12]

In the present study, only a proportion of the initial amount of serum protein exposed to TIPS microspheres were adsorbed, indicating that this material could be modified to improve protein adsorption. PLGA blended with Pluronic® F108,[18] PEG[26,27] or chitin[28] were reported to adsorb greater amounts of protein than unmodified PLGA. Moreover, serum proteins adsorbed to TIPS microspheres may not change in structure, as serum albumin bound has been shown to retain its secondary structure and activity whilst bound to PLGA.[18] Serum protein adsorption to PLGA is influenced by the method of manufacture and polymer composition. Differential binding of serum proteins to PLGA was described with albumin, IgG, transferring.[19] Competitive adsorption of serum proteins from a mixture of albumin, IgG and fibronectin showed that the more abundant proteins albumin and IgG were adsorbed to polymers in greater amounts than fibronectin (important for cell adhesion but present at lower concentrations in plasma). In addition to influencing the extent of polymer wetness, protein coating of TIPS microspheres may be useful for *in vivo* transplantation. BSA- (BSA-NP) or transferrin (Tf-NP)-coated PLGA nanoparticles (NP) displayed a greatly prolonged half-life in blood when intravenously injected in rats and mice.[29] *In vivo* targeting of healthy brain tissue was higher with Tf-NP than with BSA-NP and high numbers of both nanoparticles entered brain-developed tumors.

The influence of PLGA scaffold surface topography on cell attachment may be independent to the effects mediated by adsorbed serum protein. Nanostructured PLGA surfaces (cast from silastic molds of NaOH-treated nanostructured PLGA) supported the attachment of increased numbers of vascular cells (endothelial and aortic smooth muscle cells)[5] and bladder smooth muscle cells compared with conventional, unmodified PLGA substrates.[20] PLGA films with surfaces modified by solvent-mediated polymer casting on a master template (nanometer and micrometer features made using UV photolithography or electron beam lithography) were used to investigate the influence of surface topography on thrombogenic potential of PLGA.[21] The study showed that submicron features increased adhesion of fibrinogen and platelets compared to unmodified, pristine PLGA films, so modification of the surface structure can reduce thrombogenicity of PLGA and render the polymer more suitable for use in blood vessels. PLGA membranes modified by oxygen and nitrogen plasma have also been shown to present increased surface rugosity that supported attachment of Vero cells.[6,30]

The extent of wetting mediated by one-step ethanol immersion and serum protein adsorption may benefit the development of PLGA TIPS microsphere scaffolds for improved clinical delivery of human skeletal myoblasts.

Conclusions

A simple one-step protocol has been described for prewetting PLGA TIPS microspheres that incorporates ethanol concentration and exposure time, serum protein adsorption and modifications to surface topography as critical parameters that direct the attachment of human skeletal myoblasts. The wetted TIPS microsphere presents a 3D myoblast culture system that can be tailored to control loading of these cells, indicating the possibility for regulation of the potency of skeletal myoblast therapy. We have devised a working model (Figure 8.) outlining the manner that wetting of TIPS microspheres can produce defined cell attachment profiles through variations to discrete elements of our prewetting procedure. The ultimate aim is to create a process for precision loading of human skeletal myoblasts onto PLGA microspheres. The present study is an important step in the routine clinical application of biocompatible PLGA TIPS microspheres. Wetted, serum protein-coated PLGA microspheres may ameliorate outstanding issues with the therapeutic efficacy of current myoblast transplantation procedures. Prewetted PLGA scaffolds are potentially tractable within high-throughput bioprocesses to create products for the delivery of a range of therapeutic, anchorage-dependent cell types including skeletal myoblasts, osteoblasts, chondrocytes and progenitor cells.

Funding

This project was supported by grants from the UK Medical Research Council (MR/L002752/1) and Sir Halley Stewart Trust. The research was undertaken at UCL/UCLH which receives funding from the Department of Health's NIHR as a Comprehensive Biomedical Research Centre.

Acknowledgements

The authors thank Jaspal Puri for laboratory assistance.

Declaration of conflicting interests

None declared.

References

1. Ahmadi R, Mordan N, Forbes A, et al. Enhanced attachment, growth and migration of smooth muscle cells on microcarriers produced using thermally induced phase separation. *Acta Biomater* 2011; 7: 1542–1549.
2. Foong KS, Patel R, Forbes A, et al. Anti-tumor necrosis factor-alpha-loaded microspheres as a prospective novel treatment for Crohn's disease fistulae. *Tissue Eng Part C-Me* 2010; 16: 855–864.
3. Mikos AG, Lyman MD, Freed LE, et al. Wetting of poly(l-lactic acid) and poly(Dl-lactic-co-glycolic acid) foams for tissue-culture. *Biomaterials* 1994; 15: 55–58.
4. Wu LB, Zhang JC, Jing DY, et al. "Wet-state" mechanical properties of three-dimensional polyester porous scaffolds. *J Biomed Mater Res A* 2006; 76 A: 264–271.
5. Miller DC, Thapa A, Haberstroh KM, et al. Enhanced functions of vascular and bladder cells on poly-lactic-co-glycolic acid polymers with nanostructured surfaces. *IEEE Trans Nanobiosci* 2002; 1: 61–66.
6. Esposito AR, Kamikawa CM, Lucchesi C, et al. Benefits of oxygen and nitrogen plasma treatment in Vero cell affinity to poly(lactide-co-glycolide acid). *Mater Res-Ibero-Am J* 2013; 16: 695–702.
7. Safinia L, Wilson K, Mantalaris A, et al. Atmospheric plasma treatment of porous polymer constructs for tissue engineering applications. *Macromol Biosci* 2007; 7: 315–327.
8. Blaker JJ, Knowles JC and Day RM. Novel fabrication techniques to produce microspheres by thermally induced phase separation for tissue engineering and drug delivery. *Acta Biomater* 2008; 4: 264–272.
9. Blaker JJ, Pratten J, Ready D, et al. Assessment of antimicrobial microspheres as a prospective novel treatment targeted towards the repair of perianal fistulae. *Aliment Pharm Ther* 2008; 28: 614–622.
10. Kim K, Yu M, Zong XH, et al. Control of degradation rate and hydrophilicity in electrospun non-woven poly(D,L-lactide) nanofiber scaffolds for biomedical applications. *Biomaterials* 2003; 24: 4977–4985.
11. Lee JH, Khang G, Lee JW, et al. Interaction of different types of cells on polymer surfaces with wettability gradient. *J Colloid Interf Sci* 1998; 205: 323–330.
12. Lee JH and Lee HB. A wettability gradient as a tool to study protein adsorption and cell-adhesion on polymer surfaces. *J Biomat Sci-Polym E* 1993; 4: 467–481.
13. Vanwachem PB, Beugeling T, Feijen J, et al. Interaction of cultured human-endothelial cells with polymeric surfaces of different wettabilities. *Biomaterials* 1985; 6: 403–408.
14. Vanwachem PB, Hogt AH, Beugeling T, et al. Adhesion of cultured human-endothelial cells onto methacrylate polymers with varying surface wettability and charge. *Biomaterials* 1987; 8: 323–328.
15. Mikos AG, Bao Y, Cima LG, et al. Preparation of poly(glycolic acid) bonded fiber structures for cell attachment and transplantation. *J Biomed Mater Res* 1993; 27: 183–189.
16. Lee JH, Lee SJ, Khang G, et al. The effect of fluid shear stress on endothelial cell adhesiveness to polymer surfaces with wettability gradient. *J Coll Interf Sci* 2000; 230: 84–90.
17. Lee JH, Lee JW, Khang G, et al. Interaction of cells on chargeable functional group gradient surfaces. *Biomaterials* 1997; 18: 351–358.
18. Vasita R and Katti DS. Structural and functional characterization of proteins adsorbed on hydrophilized polylactide-co-glycolide microfibers. *Int J Nanomed* 2012; 7: 61–71.
19. Luck M, Pistel KF, Li YX, et al. Plasma protein adsorption on biodegradable microspheres consisting of poly(D,L-lactide-co-glycolide), poly(L-lactide) or ABA triblock copolymers containing poly(oxyethylene) – influence of production method and polymer composition. *J Contr Release* 1998; 55: 107–120.
20. Miller DC, Thapa A, Haberstroh KM, et al. Endothelial and vascular smooth muscle cell function on poly(lactic-co-glycolic acid) with nano-structured surface features. *Biomaterials* 2004; 25: 53–61.
21. Koh LB, Rodriguez I and Venkatraman SS. The effect of topography of polymer surfaces on platelet adhesion. *Biomaterials* 2010; 31: 1533–1545.
22. Oh SH and Lee JH. Hydrophilization of synthetic biodegradable polymer scaffolds for improved cell/tissue compatibility. *Biomed Mater* 2013; 8: 014101.
23. Grinnell F. Cellular adhesiveness and extracellular substrata. *Int Rev Cytol* 1978; 53: 65–144.
24. Baier RE, Shafrin EG and Zisman WA. Adhesion – mechanisms that assist or impede it. *Science* 1968; 162: 1360–1368.
25. Tamada Y and Ikada Y. Fibroblast growth on polymer surfaces and biosynthesis of collagen. *J Biomed Mater Res* 1994; 28: 783–789.
26. Jeong JH, Lim DW, Han DK, et al. Synthesis, characterization and protein adsorption behaviors of PLGA/PEG di-block co-polymer blend films. *Coll Surf B Biointerf* 2000; 18: 371–379.
27. Tran VT, Karam JP, Garric X, et al. Protein-loaded PLGA-PEG-PLGA microspheres: a tool for cell therapy. *Eur J Pharm Sci* 2012; 45: 128–137.
28. Mi FL, Shyu SS, Lin YM, et al. Chitin/PLGA blend microspheres as a biodegradable drug delivery system: a new delivery system for protein. *Biomaterials* 2003; 24: 5023–5036.
29. Chang J, Paillard A, Passirani C, et al. Transferrin adsorption onto PLGA nanoparticles governs their interaction with biological systems from blood circulation to brain cancer cells. *Pharm Res-Dordr* 2012; 29: 1495–1505.
30. Wan YQ, Yang J, Yang JL, et al. Cell adhesion on gaseous plasma modified poly-(L-lactide) surface under shear stress field. *Biomaterials* 2003; 24: 3757–3764.